

Site-specific Chemistry of Sulfur-containing
Amino Acids on Si(111)- $\sqrt{3}\times\sqrt{3}$ -Ag:
Bioorganic Nanostructured Film Growth and
Adsorbate-induced Metal Cluster Formation
Governed by Surface Defects

by

Hanieh Farkhondeh Borazjani

A thesis
presented to the University of Waterloo
in fulfillment of the
thesis requirement for the degree of
Doctor of Philosophy
in
Chemistry

Waterloo, Ontario, Canada, 2019

©Hanieh Farkhondeh Borazjani 2019

Examining Committee Membership

The following served on the Examining Committee for this thesis. The decision of the Examining Committee is by majority vote.

External Examiner

Prof. Peter Kruse

Associate Professor of Chemistry

McMaster University

Supervisor:

Prof. Kam Tong Leung

Professor of Chemistry

Internal Member:

Prof. Marcel Nooijen

Professor of Chemistry

Internal-external Member:

Prof. John Wen

Associate Professor of Mechanical Engineering

Other Member:

Prof. Daniel Thomas

Professor of Chemistry

University of Guelph

AUTHOR'S DECLARATION

I hereby declare that I am the sole author of this thesis. This is a true copy of the thesis, including any required final revisions, as accepted by my examiners. I understand that my thesis may be made electronically available to the public.

Abstract

The interfacial interactions and film growth mechanisms of sulfur-containing amino acids on Si(111)- $\sqrt{3}\times\sqrt{3}$ -Ag are investigated by using X-ray photoelectron spectroscopy (XPS) and scanning tunneling microscopy (STM) at room temperature and at elevated temperature under ultrahigh vacuum condition. The complementary density functional theory (DFT) calculations with dispersion correction are used to provide precise modeling of the equilibrium adsorption configurations of biomolecules. Cysteine is found to chemisorb initially at surface defects where its island growth fronts further propagate onto terrace regions exhibiting coral-reef-like nanostructures. The lower-step edges and the antiphase boundaries are found to be the preferred adsorption sites followed by upper-step edges and terrace sites. Chemisorption of interfacial cysteine monolayer occurs through S–H cleavage and S–Ag linkage. The zwitterionic hydrogen bonding governs the intermolecular interactions in the interfacial layer, which further grows to zwitterionic multilayer. Our DFT calculations support the experimental results for chemisorption of single molecules to multimers through S–Ag covalent bonding and intermolecular zwitterionic hydrogen bonding. In addition, Ag bridge sites are found to be the most favourable adsorption sites on the surface terraces. At elevated temperatures, cysteine adspecies are found to transform the highly ordered single-atom-thick Si(111)- $\sqrt{3}\times\sqrt{3}$ -Ag overlayer into Ag agglomerates of nanometer sizes. This phenomenon offers an interesting approach to converting monoatomic silver silicide layers to silver nanoclusters and quantum dots for chemical sensing and catalysis applications.

Methionine, on the other hand, does not chemisorb on Si(111)- $\sqrt{3}\times\sqrt{3}$ -Ag due to the termination of its sulfur atom by a methyl group in its methylthio methylene side chain. A minority of methionine adspecies are found to chemisorb through a dehydrogenated amino group most likely at defect sites, step edges and antiphase boundaries. Self-assembled one-dimensional molecular wires are observed at room temperature and at lower temperatures in our variable-temperature STM study, while the chemical state of these molecular wires is found to be zwitterionic by XPS. Our large-scale DFT calculations further support the zwitterionic dimer row structures of the molecular wires. To demonstrate the molecular size effect, the adsorption mechanism of glycine on Si(111)- $\sqrt{3}\times\sqrt{3}$ -Ag is also studied. All three amino acids appear to induce metallic Ag 3d features at elevated temperature, indicating the formation of metallic agglomerates. The Si(111)- $\sqrt{3}\times\sqrt{3}$ -Ag surface offers a unique platform for developing not only self-assembled molecular nanostructures but also metal nanoclusters and agglomerates for potential applications in catalysis.

The Si(111)- $\sqrt{3}\times\sqrt{3}$ -Ag surface contains a number of defects, notably step edges and antiphase boundaries, that could significantly affect the adsorption and other surface properties. Detailed

understanding of the relations between their structural configurations and these surface properties is of fundamental interest to further unraveling the many unique processes found for this intricate surface. Using first-principle quantum mechanical calculations based on DFT, the equilibrium geometries of the step edge and antiphase boundary are calculated and found to exhibit a one-dimensional chain of Ag trimers on both types of defect sites. Unlike the monolayer coverage in the terrace regions, the Ag:Si stoichiometric ratio is found to be 4:3 at the step edge. This ratio is calculated to be 1:1 for the antiphase boundary (and for the terrace). The total densities of states calculated for the step edge, antiphase boundary, and terrace models exhibit surface states near the Fermi level. The mid-gap state found for the step edge appears to have a more intense density of state and to locate closer to the Fermi level. The corresponding calculation of partial densities of states reveals different contributions of Ag and Si atoms at defect sites. Mid-gap states are known to improve the optical properties of materials such as photon absorption and transfer. As the Si(111)- $\sqrt{3}\times\sqrt{3}$ -Ag surface defects promote the mid-gap states and considering their adsorption to be the most favourable, they are expected to play a crucial role in designing applications in (photo) catalysis and chemical sensing.

Acknowledgements

First and foremost, I am deeply indebted to my supervisor, Prof. Kam Tong Leung, for his patience, warm encouragements, thoughtful guidance and valuable insights. He has always been there to listen and give advice. I am sincerely grateful to him for giving me the opportunity to be a part of the WATLab family. I greatly appreciate all the efforts and time he put in formulating this work.

I am very grateful to Prof. Peter Kruse for kindly agreeing to be my external examiner. I would like to thank my advisory committee members, Prof. Dan Thomas, Prof. Scott Hopkins, Prof. John Wen and Prof. Marcel Nooijen for patiently reviewing my work and for serving on my examination committee.

I am very thankful to Dr. Lei Zhang for training me to use the Omicron UHV system in WATLab, and for his kind help and advice throughout the coursework of my Ph.D. research. Also, I would like to thank my former colleague, Dr. Fatemeh Rahnemaye Rahsepar, for her useful comments on my research reports and for training me to use the VASP/MedeA software.

I must thank our science and electronic shop staff, Harmen Vander Heide, Peter Kessel, Jacek Szubra, Zhenwen Wang and Krunomir Dvorski for helping me go on with my experiments by solving technical problems anytime I encountered one.

I would like to thank my former and current colleagues Lei Zhang, Fatemeh Rahnemaye Rahsepar, Marwa Abdellah, Mahdi Beedel, Donal McGillivray, Md Anisur Rahman, Saurabh Srivastava, Jug-Soo Kang, Joseph Palathinkal, Nina Heinig, Shantinaryan Rout, Yan Wang-Duffort, Frank Guan, Qiuyu Shi, Wenyu Gao, Tai Guo and Ying Luo for their continued support and for making it even more joyful to work in the WATLab family.

Last but not least, I thank my family for their endless support and encouragement beyond geographic distances without which this journey would never have been possible.

Dedication

To my mother, Fatemeh, whose unconditional love and support have sustained me throughout my life.

Table of Contents

Examining Committee Membership	ii
Author's Declaration	iii
Abstract	iv
Acknowledgements	vi
Dedication	vii
List of Figures	x
List of Tables	xviii
Chapter 1 Introduction	1
1.1 Surface Science	1
1.2 The Si(111)7×7 Surface as a Template	2
1.3 The Si(111)-√3×√3-Ag Surface	4
1.4 Adsorption of Organic Molecules on Si(111)-√3×√3-Ag	6
1.5 Surface Defects	8
1.6 X-ray Photoelectron Spectroscopy	9
1.7 Scanning Tunneling Microscopy	13
1.8 Scope of Thesis	14
Chapter 2 Experimental and Computational Details	16
2.1 UHV Multitechnique System	16
2.2 MBE Chambers	18
2.3 Analysis Chamber	19
2.3.1 X-ray Photoelectron Spectrometer	20
2.3.2 Variable Temperature Scanning Probe Microscope (VT-SPM)	21
2.4 Sample Preparation and Measurements	22
2.5 Computational Details	23
Chapter 3 Structural and Chemical Evolution of L-Cysteine Nanofilm on Si(111)-√3×√3-Ag: From Preferential Growth at Step-edges and Antiphase Boundaries at Room Temperature to Adsorbate-mediated Metal Cluster Formation at Elevated Temperature	26
3.1 Introduction	26
3.2 Results and Discussion	29
3.2.1 Thiol dissociative adsorption of cysteine and growth of supported cysteine film at room temperature	29
3.2.2 Silver nanocluster formation at elevated temperature	32

3.2.3 Preferential early-stage growth of cysteine at step edges and antiphase boundaries on Si(111)- $\sqrt{3}\times\sqrt{3}$ -Ag.....	37
3.2.4 Formation of silver nanocluster arrays by post-annealing	43
3.2.5 Large-scale DFT calculations of cysteine adsorption on model Si(111)- $\sqrt{3}\times\sqrt{3}$ -Ag surface.....	45
3.2.6 Large-scale DFT calculations of cysteine zwitterionic multimers on model Si(111)- $\sqrt{3}\times\sqrt{3}$ -Ag surface.....	50
3.3 Summary	53
Chapter 4 Development of Aligned Organic Molecular Wires and Silver Metallic Nano-agglomerates in Methionine Nanofilm Supported on Si(111)- $\sqrt{3}\times\sqrt{3}$ -Ag	55
4.1 Introduction.....	55
4.2 Results and Discussion	57
4.2.1 Evolution of chemical-state composition during methionine film growth at room temperature.....	57
4.2.2 Chemical-state evolution of a supported multilayer methionine film upon annealing	60
4.2.3 Metallic silver nanoagglomerate formation induced by methionine nanofilm	62
4.2.4 Formation of methionine molecular wires on Si(111)- $\sqrt{3}\times\sqrt{3}$ -Ag in the early growth stage.....	63
4.2.5 DFT Calculations	69
4.2.6 Comparison of Methionine, Cysteine, and Glycine nanofilms on Si(111)- $\sqrt{3}\times\sqrt{3}$ -Ag and adsorbate-induced formation of Ag-Ag bonds.....	72
4.3 Summary	81
Chapter 5 One-dimensional Defects on Si(111)- $\sqrt{3}\times\sqrt{3}$ -Ag: DFT simulation of the step edge and antiphase boundary	82
5.1 Introduction.....	82
5.2 Simulation Details.....	84
5.3 Results and Discussion	85
5.3.1 Step Edge	85
5.3.2 Antiphase Boundary.....	89
5.3.3 Density of States at Defects	90
5.4 Summary	97
Chapter 6 Conclusions and Future Work	98
Bibliography	103
Appendix A Cysteine on Si(111)- $\sqrt{3}\times\sqrt{3}$ -Ag.....	117
Appendix B Methionine on Si(111)- $\sqrt{3}\times\sqrt{3}$ -Ag.....	130
Appendix C One-dimensional Surface Defects on Si(111)- $\sqrt{3}\times\sqrt{3}$ -Ag	139

List of Figures

Figure 1.1 Top views and side views of the equilibrium geometries of (a) a dimer-atom-stacking fault (DAS) model for Si(111)7×7, (b) a Ag(111) single-crystal surface, and (c) a Si(111)-√3×√3-Ag surface with the honeycomb-chained triangle (HCT) structure. The Si adatoms and restatoms are highlighted in (a) by, respectively, larger green and yellow circles for clarity. Blue and grey circles correspond to Ag and Si atoms, respectively, in (c). The √3×√3 unit cell (diamond) is shown for the model surfaces in (a-c). All the model surfaces are generated by large-scale ab-initio quantum mechanical calculations using a Xeon computer cluster at WATLab.	5
Figure 1.2 Magnified top views of a Si(111)-√3×√3-Ag surface with (a) the honeycomb-chained triangle (HCT) and (b, c) inequivalent triangle (IET) structures, where the (+) and (−) depict the counter-clockwise and clockwise rotational offsets of Ag atoms with respect to their positions in HCT, which results in three of the Ag trimers appear larger than the other three trimers (with the smaller trimers outlined by blue open triangles). Blue and grey circles correspond to Ag and Si atoms respectively.	6
Figure 1.3 Schematic model of a solid surface depicting different types of surface sites. These sites are distinguishable by their nearest neighbours. For a simple cubic lattice used in this model, a terrace atom is bonded to 5 atoms resulting in a coordination number of 5 nearest neighbors. A step atom is the atom at the transition interface between the upper-step and lower-step terraces and is bonded to 4 atoms and hence its coordination number is 4, while a kink is located at a corner of a step edge and exhibits a coordination number of 3. An adatom defect and a vacancy defect correspond to an excess and lack thereof an atom on the surface terrace, respectively.	9
Figure 1.4 Schematic diagram depicting ejection of the 1s electron as the result of absorption of an incident X-ray photon.	10
Figure 1.5 A photograph of the Omicron XPS spectrometer depicting the X-ray source (anode), a quartz-crystal X-ray monochromator, an approximate sample position with respect to the X-ray incident angle and electron emission angle, an electrostatic lens system, a hemispherical analyzer, and a seven-channeltron electron detector.	11
Figure 1.6 The energy level diagram for a conductive sample and the spectrometer. The Fermi levels of the sample and the spectrometer are aligned and the E_B is referenced with respect to E_f . The measurement of E_B is independent of the sample work function but dependent on the spectrometer work function.	12
Figure 1.7 A schematic diagram depicting the principle of the electron tunneling process, where V_t is the tunneling bias voltage (which can be created by applying an external voltage either to the tip or to the sample while keeping the other grounded), z is the vertical distance, E_F is the Fermi level, Φ is the work function, and Ψ is the electron wavefunction.	14

Figure 2.1 (a) A photograph of the multichamber Omicron system consisting of MBE1 for low-temperature organic material deposition and MBE2, for high-temperature metal and inorganic material deposition; and an analysis chamber equipped with an X-ray photoelectron spectrometer (XPS), a variable-temperature scanning probe microscope (SPM), and a low energy electron diffractometer (LEED); as well as a fast entry loadlock (FEL) chamber (out of view) and a center transfer chamber. (b, c) Machine drawings showing the side and top views, respectively (obtained from the Omicron User Manual)..... 17

Figure 2.2 Photographs of (a) MBE1 and (f) MBE2 chambers for deposition of bio/organic materials and metals, respectively. MBE1 chamber was equipped with four low-temperature precision effusion cells (two OME and two NTEZ cells), and a quadrupole mass spectrometer. MBE2 was equipped with two EFM and two WEZ effusion cells, and a RHEED system. Photographs of (b) OME, (c) NTEZ, (g) EFM, and (h) WEZ effusion cells. Schematic diagrams of (d) the OME and (e) NTEZ cells, depicting the crucible, heating system, evaporant (powder), thermocouple and water-cooling mechanism. The photographs in (b, c, g, h) and the diagrams in (d) and (e) were obtained from the MBE effusion cells manual..... 19

Figure 2.3 (a) Photograph of the X-ray Photoelectron Spectrometer, including the Sphera hemispherical analyzer, an X-ray monochromator with an X-ray source, and manipulator. (b) Schematic diagram of the monochromator assembly showing the X-ray source, alignment drives, the crystal mirror housing on the Rowland circle along with the positions of the sample and of the X-ray anode. (c) Photograph of the XM 1000 MKII X-ray source with the aluminum-coated anode, and the long- and short-filament cathodes. The diagram in (b) and the photograph in (c) were obtained from the Omicron User Manual. 21

Figure 2.4 (a) Photograph of the VT-SPM inside its housing chamber, and (b) schematic diagram of the VT-SPM assembly (outside vacuum) with its main components. The diagram in (b) was obtained from the STM system manual..... 22

Figure 3.1 Evolution of O 1s, N 1s, C 1s, and S 2s XPS spectra of cysteine deposited on Si(111)- $\sqrt{3}\times\sqrt{3}$ -Ag as a function of exposure time (30–3600 s) and of the as-grown cysteine multilayer film (obtained with a 3600-s exposure) upon annealing to 85, 175, and 285 °C..... 33

Figure 3.2 XPS spectra of the Ag 3d region for a pristine Si(111)- $\sqrt{3}\times\sqrt{3}$ -Ag surface before and after cysteine exposure for 1200 s and 3600 s, and for the resulting as-grown (3600 s) multilayer film upon annealing to 85 °C, 175 °C, 285 °C and 500 °C. 36

Figure 3.3 Empty-state STM images obtained with a sample bias of +2 V and a constant tunneling current of 0.2 nA for a pristine Si(111)- $\sqrt{3}\times\sqrt{3}$ -Ag surface (a1-a3) before and after cysteine exposure for (b1-b6) 30 s, (c1-c5) 120 s, and (d1-d4) 240 s. The apparent height profiles along the respective lines are

shown in b4, c3, c5 and d4, where the full height and length ranges are given in units of Å and nm, respectively. The arrows in (a1) and (a2) mark examples of antiphase boundaries and adatom defects, respectively. The schematic model of the Ag-Si trimers hexagonal mesh along with three $\sqrt{3}\times\sqrt{3}$ -Ag unit cells are overlaid on the image in (a3), with the Ag and Si atoms represented by blue and grey dots, respectively. 40

Figure 3.4 A schematic illustration (a-c) of the adsorption and growth of the cysteine adspecies on the Si(111)- $\sqrt{3}\times\sqrt{3}$ -Ag surface at room temperature and (d) of metal cluster formation after annealing. Green and yellow balls depict cysteine molecule and thiolated cysteine respectively. The purple layer is the $\sqrt{3}\times\sqrt{3}$ -Ag overlayer which converts to metallic clusters in (d). 42

Figure 3.5 Empty-state STM images obtained with a sample bias of +2 V and a constant tunneling current of 0.2 nA for Ag nanocluster arrays obtained by post-annealing a Si(111)- $\sqrt{3}\times\sqrt{3}$ -Ag surface with cysteine exposures of (a1) 240-s and (b1, c1) 3600-s at (a1) 175 °C, (b1) 285 °C and (c1) 500 °C, respectively. The apparent height profiles along the respective Lines L1, L2 and L3 are shown in (a2), (b2) and (c2), respectively. The x-axis line range for all the height profiles is 65 nm 44

Figure 3.6 (a) Optimized equilibrium structures of three conformers (AH, BH, and CH) of isolated L-cysteine in the gas phase, (b) side view of the adsorption configurations of three dehydrogenated cysteine conformers A, B, and C on the T1 site with the S-C axis along the surface normal, (c) top view of the Si(111)- $\sqrt{3}\times\sqrt{3}$ -Ag surface illustrating prospective adsorption sites, including the threefold hollow sites on Ag trimer (T1) and Si trimer (T2); bridge sites on Ag-Ag (D1), Si-Si (D2) and Ag-Si nearest neighbour pairs or dimer (D3); and atop sites on top of a Ag atom (M1) and a Si atom (M2), (d) three $\sqrt{3}\times\sqrt{3}$ -Ag unit cells overlaid on top of an empty-state STM image of a pristine Si(111)- $\sqrt{3}\times\sqrt{3}$ -Ag surface obtained with a sample bias of +2 V and a constant tunneling current of 0.2 nA and, and (e) calculated adsorption energies of dehydrogenated cysteine conformers A (circles), B (squares) and C (triangles) on adsorption sites M1, M2, D1, D2, D3, T1 and T2 optimized by varying the molecule-to-slab vertical separation while holding all other structural parameters fixed. Green, blue, red, and black balls represent sulfur, nitrogen, oxygen, and carbon, respectively. 46

Figure 3.7 Equilibrium geometries of optimized adsorption configurations after full relaxation of thiolated cysteine conformers A, B, and C initially placed on D1 (top panels) and T1 sites (bottom panels) of the Si(111)- $\sqrt{3}\times\sqrt{3}$ -Ag model surface. The adsorption energies are in unit of eV while the separations $r(X-Y)$ are in unit of Å. To better illustrate the adsorption structure, only part of the slab (corresponding to the 4x4 supercell) for the model surface is shown for each configuration. Green, blue, red, and black balls represent sulfur, nitrogen, oxygen, and carbon, respectively. 49

Figure 3.8 Equilibrium geometries and adsorption energies of optimized adsorption configurations on D1 sites for thiolated Conformer AH with (a) H_{α} up and (b) H_{α} down, (c) hydrogen-bonded dimer containing two thiolated neutral Conformer A with H_{α} up, (e) dimer containing two thiolated zwitterion AH_{ZI} , and (f) trimer containing three thiolated zwitterion AH_{ZI} with H_{α} -up, and (g) hexamer containing six thiolated Conformer AH_{ZI} with H_{α} -up. The equilibrium geometries of isolated zwitterions (ZIs) for Conformers AH, BH and CH are shown in (d). Thiolated zwitterion AH_{ZI} is derived by proton relocation from COOH to NH_2 in a thiolated Conformer AH. To better illustrate the adsorption structure, only part of the slab [corresponding to the 4×4 supercell for (a-c) and (e-f) and to the 8×8 supercell for (g)] for the model surface is shown. 52

Figure 4.1 Ball-and-Stick models for the isolated structures of (a) neutral methionine, (b) zwitterionic methionine, (c) neutral cysteine, (d) zwitterionic cysteine, (e) neutral glycine, and (f) zwitterionic glycine. The models are generated by DFT calculations. In our notation, we identify $-COOH$ as the “head” group and the functional group farthest from the head group as the “tail” group. The long axis is marked by the dashed line. 59

Figure 4.2 Evolution of (a) O 1s, (b) N 1s, (c) C 1s, and (d) S 2s XPS spectra of methionine deposited on $Si(111)-\sqrt{3} \times \sqrt{3}-Ag$ as a function of exposure time (120–7560 s) and of the as-grown multilayer methionine film (obtained with a 7560-s exposure) upon annealing to 85, 175, and 285 °C. In (c) and (d), M is used to represent Si and/or Ag. 60

Figure 4.3 Evolution of Ag 3d XPS spectra of the pristine $Si(111)-\sqrt{3} \times \sqrt{3}-Ag$ surface after deposition of methionine with increasing exposure time and of the as-grown 7560-s methionine film upon annealing to 85, 175, and 285 °C. 63

Figure 4.4 Empty-state STM images of a 30-s exposure of L-methionine on $Si(111)-\sqrt{3} \times \sqrt{3}-Ag$ over (a1) a $200 \times 200 \text{ nm}^2$ area and (b1) a selected $100 \times 100 \text{ nm}^2$ area at a higher magnification. Expanded views of the selected areas (A1, A2, A3) in (a) and (A4, A5) in (b) are shown to illustrate (a2) the emergence of the dimer rows, (a4) directed growth from the step edges, (a5) parallel growth along the step edges, (b2) a “boomerang” nanostructure and (b3) kinks in a nanograting, respectively. The respective height profiles along Line L1 in (a2) and Line L2 in (a5) are shown in (a3) and (a6), respectively. (b4) and (b5) show schematic diagrams of dimer rows superimposed on the corresponding STM images of the respective boomerang and kink structures. The STM images are obtained with a sample bias of +2.0 V and a tunneling current of 0.2 nA with the sample held at 140 K. 67

Figure 4.5 Empty-state STM images of a 120-s exposure of L-methionine on $Si(111)-\sqrt{3} \times \sqrt{3}-Ag$ (a) over a $500 \times 500 \text{ nm}^2$ scan area and (b) a $100 \times 100 \text{ nm}^2$ scan area [area A1 in (a)]. The inset in (a) shows an atomic resolution STM image of the pristine $Si(111)-\sqrt{3} \times \sqrt{3}-Ag$ surface in the approximate orientation as

the substrate in (b) to illustrate the alignment of the molecular wires in nanogratings (marked by rectangles) and triangular nanodomains (the centers of which marked by triangles) along the three equivalent crystallographic directions of the supporting Si(111)- $\sqrt{3}\times\sqrt{3}$ -Ag surface. The STM images are obtained with a sample bias of +2.0 V and a tunneling current of 0.2 nA with the sample held at 140 K. 68

Figure 4.6 (a) A mesh-averaged image (using WSxM) of the atomic-resolution empty-state STM image of the Si(111)- $\sqrt{3}\times\sqrt{3}$ -Ag surface obtained at a sample bias of +1.6 V and a tunneling current of 0.2 nA at room temperature. The hexagon is consisted of three $\sqrt{3}\times\sqrt{3}$ surface unit cells, each with two bright protrusions corresponding to two Ag trimers. The optimized structure of the topmost layer of Si(111)- $\sqrt{3}\times\sqrt{3}$ -Ag is shown along with the corresponding adsorption sites: atop on a Ag monomer (M1), bridge on a Ag dimer (D1) and three-fold hollow on a Ag trimer (T1). Optimized equilibrium structures of (b) a methionine molecule adsorbed with a M1-R115 configuration, (c) an antiparallel dimer with the methionine molecules in an M1-R43 and an M1-R40 configurations, (d) a parallel dimer with methionine in an M1-R74 and an M1-R74 configurations, (e) a tetramer with methionine in the M1-R125, M1-R115, M1-R115, and M1-R125 configurations, and (f) a periodic model of an extended dimer row. The molecular wire can in effect be considered as four antiparallel dimers adsorbed in a dimer row arrangement along the [1-21] direction (dimer row growth direction). The adsorption energy per molecule is also indicated in (b) to (f). Each orange triangle in (b) to (e) corresponds to a single bright protrusion in the STM image in (a). Schematic representations of the calculated dimer rows are superimposed on appropriate STM images to show (g) two separated molecular wires each containing a single dimer row, and (h) two molecular wires containing a single dimer row (top) and a double dimer row (consisting of two single dimer rows side-by-side, bottom)..... 71

Figure 4.7 Evolution of (a) O 1s, (b) N 1s, and (c) C 1s XPS spectra of glycine deposited on Si(111)- $\sqrt{3}\times\sqrt{3}$ -Ag as a function of exposure time (120–3600 s) and of the as-grown 3600-s glycine film upon annealing to 85, 175, and 285 °C..... 74

Figure 4.8 XPS spectra of (a) O 1s, (b) N 1s, and (c) Ag 3d regions of Si(111)- $\sqrt{3}\times\sqrt{3}$ -Ag measured immediately after exposure with glycine for 760 s (top panel) and after subsequent overnight storage for 12 h under ultrahigh vacuum condition (bottom panel). (d) Corresponding empty-state STM image of the overnight sample collected at a sample bias of +1.6 V and a tunneling current of 0.2 nA at room temperature. 75

Figure 4.9 Evolution of Ag 3d XPS spectra of the clean Si(111)- $\sqrt{3}\times\sqrt{3}$ -Ag surface before and after deposition of glycine for 3600 s and of the as-grown glycine film upon annealing to 85, 175, and 285 °C. 78

Figure 4.10 Schematic models for growth evolution of three amino acid films (glycine, cysteine, and methionine) on Si(111)- $\sqrt{3}\times\sqrt{3}$ -Ag, depicting (a) interfacial layer of nanostructures in the early growth stage and (b) multilayer of zwitterions with interlayer and intralayer interactions at room temperature, and (c) metal island/cluster formation after annealing of the as-grown thick multilayer film to 175 and 285 °C. 80

Figure 5.1 Empty-state STM images obtained with a sample bias of +0.9 V and a constant tunneling current of 0.2 nA for a pristine Si(111)- $\sqrt{3}\times\sqrt{3}$ -Ag near a [1-21] step edge for (a) a 10×10 nm² scan area and (b) a magnified area of 3×7 nm² marked in (a). (c) Apparent height profile along the line across points A and B in (b) depicting the well-defined periodicity found for the upper-step and lower-step terraces. The separation between A and B correspond to the run distance and is found to be 7.6 Å..... 86

Figure 5.2 Optimized geometries for two step-edge models with (a1-a3) a Ag₃Si₃ unit cell and (b1-b3) a Ag₄Si₃ unit cell in the step-edge region, each shown in (a1, b1) top view, (a2, b2) side view along SS' direction and (a3, b3) front view along FF' direction. The parallelogram depicts the unit cell of the step edge..... 88

Figure 5.3 (a1) Empty-state STM images obtained with a sample bias of +0.9 V and a constant tunneling current of 0.2 nA for a pristine Si(111)- $\sqrt{3}\times\sqrt{3}$ -Ag near a [1-21] antiphase boundary over a 10×10 nm² scan area. (a2) Apparent height profile along the marked line across the antiphase boundary in (a1). (b1) Top view and (b2) side view of the optimized geometry of the antiphase boundary model showing the periodicity of the antiphase boundary region..... 90

Figure 5.4 Calculated total density of states for the terrace (dashed line), antiphase boundary (grey solid line), and step edge (red solid line) models for (a) the full valence region, and (b) near the Fermi level. . 92

Figure 5.5 (a) A step edge model depicting different Ag and Si atoms at the slope (Ag1-Ag3) and on the upper-step edge (Ag4, Si1) and lower-step edge (Ag5, Si2). Calculated partial density of states for (b) the Ag 4d states of the Ag atoms on the terrace sites, (c-f) the 4d states for Ag1-Ag5 atoms shown in (a), (g) the 3s and 3p states of the Si atoms on the terraces, and (h,i) the 3s and 3p states of the Si1 and Si2 atoms shown in (a). The 4d bands of the Ag atoms connected to each terrace Si sites, Si1, and Si2 are shown in their corresponding panels in (g-i). 94

Figure 5.6 (a) An antiphase boundary model depicting different Ag and Si atoms at (Ag6, Ag7, Ag8, Si3) and near the boundary sites (Ag9, Ag10, Si4, Si5). Calculated partial density of states for (b) the 4d states of the Ag atoms on terrace sites, (c-f) the 4d states for Ag6-Ag10 atoms shown in (a), (g) the 3s and 3p states of the Si atoms on terraces, and (h, i) the 3s and 3p states of the Si3, and Si4 and Si5 atoms shown in (a). The 4d bands of the Ag atoms connected to each terrace Si sites (Si3, and Si4 and Si5) are shown in their corresponding panels in (g-i). 96

Figure A1 Top view (top) and cross sectional view along the C-C' line (bottom) for an unoptimized model of the Si(111)- $\sqrt{3}\times\sqrt{3}$ -Ag surface illustrating the honeycomb-chained trimer on terraces and a tentative geometrical configuration at the step edge along the [1-21] crystallographic direction. The height of the step edge is equal to the height of a Si(111) bilayer, 3.1 Å. The dangling bonds at the step edge are passivated by Ag atoms in this model. Detailed DFT calculations for structural optimization and analysis of the step edge (and antiphase boundary) will be reported elsewhere..... 118

Figure A2 Relative peak areas of O 1s, N 1s, and S 2s features for different cysteine exposures. Solid and dotted lines connecting the respective regular bonding and zwitterionic bonding features are used to guide the eye. 119

Figure A3 Time-sequence empty-state STM images of the Si(111)- $\sqrt{3}\times\sqrt{3}$ -Ag surface after a 30-s cysteine exposure, collected consecutively with a sample bias of +2 V and a tunneling current of 0.2 nA. The circles and the squares mark the adspecies islands that grow slightly bigger in each image, confirming the mobility of the cysteine adspecies at room temperature. The images in (e) correspond to protrusions found in the magnified areas marked by the squares in images (a-d), which show the addition of bright protrusions at marked locations of the adspecies island..... 120

Figure A4 (a) An empty-state STM image obtained with a sample bias of +2 V and a constant tunneling current of 0.2 nA for a Si(111)- $\sqrt{3}\times\sqrt{3}$ -Ag surface after a 240-s cysteine exposure followed by an annealing step at 175 °C. Expanded views of (b) the smooth undisrupted $\sqrt{3}\times\sqrt{3}$ surface terrace and the step edge as in Area A1 and (c) the antiphase boundary in Area A2..... 121

Figure A5 Optimized adsorption configurations of hydrogen-bonded cysteine dimers consisting of (a) two thiolated zwitterionic Conformer A_{ZI}, and (b) two thiolated zwitterionic Conformer B_{ZI}, each adsorbed on the Ag bridge sites of the Si(111)- $\sqrt{3}\times\sqrt{3}$ -Ag model surface. The total adsorption energy of the respective dimer is also indicated. To better illustrate the adsorption structure, only part of the slab for the model surface is shown for each configuration..... 129

Figure B1 Peak areas of O 1s, N 1s, C 1s, and S 2s features (a) as functions of methionine exposure time on Si(111)- $\sqrt{3}\times\sqrt{3}$ -Ag and (b) annealing of the as-grown 7560-s methionine film at 85, 175, and 285 °C.. 130

Figure B2 Empty-state STM image of L-methionine with a 20-s exposure on Si(111)- $\sqrt{3}\times\sqrt{3}$ -Ag at room temperature. Despite the somewhat diffuse features caused by the high mobility of the glycine molecules on the surface at room temperature, self-assembly of distinct molecular wires is clearly observed. The image is obtained with a sample bias of +2.0 V and a tunneling current of 0.2 nA at room temperature.132

Figure B3 Top and side views of the optimized equilibrium adsorption configurations of glycinate at (a) Ag monomer A1, (b) Si monomer A2, and (c) Ag dimer D1 adsorption sites. The adsorption energies are

in unit of eV. A2 appears to be the most favorable adsorption site for glycine bonding through the dissociated amino group in an upright standing configuration. Minor displacements are also observed for the Ag and Si atoms upon chemisorption of glycine. 138

Figure C1 (a) Top view of a Si(111) bilayer. The lighter and darker spheres denote the Si atoms in the top and the bottom layers, respectively. (b) A schematic representation of the major adsorption sites on the Si(111) surface. The square, triangles, and circles denote the H3, T4, and T1 adsorption sites, respectively. (c) A schematic representation of a Si trimer relocated on the T4 adsorption site. (d) A step edge model in which the Si trimers are located on the T4 sites on the upper-step and lower-step terraces of the Si(111) surface. 139

Figure C2 Top views and cross sectional (along the wide side of the slab) views of (a) the step edge slab containing three Si bilayers under the Ag-Si trimers of the upper-step terrace and two Si bilayers under those of the lower-step terraces (576 Si atoms, 96 Ag atoms and 96 H atoms); and (b) the antiphase boundary slab containing three Si bilayers under the Ag-Si trimers. The island model is used to create the step edge slab (672 Si atoms, 96 Ag atoms and 96 H atoms). 140

Figure C3 The optimized adsorption geometries of (a) Ag₃Si₃, (b) Ag₄Si₃, and (c) Ag₅Si₃ step edge models showing most possible adsorption sites around the step edge region. Only the topmost layer (Ag-Si trimers) are shown. Only the Ag bridge sites and Si atop sites are considered. The right panels show the adsorption geometry of a single thiolated cysteine adsorbed at the upper-step edge M2 site on different step edge models. The corresponding adsorption energies are shown in Table C1. 141

List of Tables

Table A1 Binding energies (in eV) of fitted peak maxima of XPS core-level spectra for O1s, N1s, C1s, and S2s regions and their assignments for cysteine films at increasing exposures and after annealing the as-grown thick cysteine film (obtained with the 3600-s exposure) at 85 °C, 175 °C, and 285 °C.	117
Table A2 Adsorption configurations of thiolated cysteine Conformers A, B, and C on T1 sites of the Si(111)- $\sqrt{3}\times\sqrt{3}$ -Ag model surface before (left) and after full optimization of all the atomic positions (right). The adsorption energies are in unit of eV while the separations $r(X-Y)$ are in units of Å. To better illustrate the adsorption structure, only part of the slab for the model surface is shown for each configuration.	122
Table A3 Adsorption configurations of thiolated cysteine Conformers A, B, and C on T2 sites of the Si(111)- $\sqrt{3}\times\sqrt{3}$ -Ag model surface before (left) and after full optimization of all the atomic positions (right). The adsorption energies are in unit of eV while the separations $r(X-Y)$ are in units of Å. To better illustrate the adsorption structure, only part of the slab for the model surface is shown for each configuration.	123
Table A4 Adsorption configurations of thiolated cysteine Conformers A, B, and C on D1 sites of the Si(111)- $\sqrt{3}\times\sqrt{3}$ -Ag model surface before (left) and after full optimization of all the atomic positions (right). The adsorption energies are in unit of eV while the separations $r(X-Y)$ are in units of Å. To better illustrate the adsorption structure, only part of the slab for the model surface is shown for each configuration.	124
Table A5 Adsorption configurations of thiolated cysteine Conformers A, B, and C on D2 sites of the Si(111)- $\sqrt{3}\times\sqrt{3}$ -Ag model surface before (left) and after full optimization of all the atomic positions (right). The adsorption energies are in unit of eV while the separations $r(X-Y)$ are in units of Å. To better illustrate the adsorption structure, only part of the slab for the model surface is shown for each configuration.	125
Table A6 Adsorption configurations of thiolated cysteine Conformers A, B, and C on D3 sites of the Si(111)- $\sqrt{3}\times\sqrt{3}$ -Ag model surface before (left) and after full optimization of all the atomic positions (right). The adsorption energies are in unit of eV while the separations $r(X-Y)$ are in units of Å. To better illustrate the adsorption structure, only part of the slab for the model surface is shown for each configuration.	126
Table A7 Molecular configurations of thiolated cysteine Conformers A, B, and C on M1 sites of the Si(111)- $\sqrt{3}\times\sqrt{3}$ -Ag model surface before (left) and after full optimization of all the atomic positions (right). The adsorption energies are in unit of eV while the separations $r(X-Y)$ are in units of Å. To better	

illustrate the adsorption structure, only part of the slab for the model surface is shown for each configuration.	127
Table A8 Molecular configurations of thiolated cysteine Conformers A, B, and C on M2 sites of the Si(111)- $\sqrt{3}\times\sqrt{3}$ -Ag model surface before (left) and after full optimization of all the atomic positions (right). The adsorption energies are in unit of eV while the separations $r(X-Y)$ are in units of Å. To better illustrate the adsorption structure, only part of the slab for the model surface is shown for each configuration.	128
Table B1 Binding energies (in eV) of fitted peaks for various XPS core-level features and their corresponding assignments for different exposures of L-methionine on Si(111)- $\sqrt{3}\times\sqrt{3}$ -Ag and upon annealing to different temperatures. The notation M represents either Si or Ag or both.....	131
Table B2 Binding energies (in eV) of fitted peaks for various XPS core-level features and their corresponding assignments for glycine on Si(111)- $\sqrt{3}\times\sqrt{3}$ -Ag at different exposures and post-annealing temperatures.	133
Table B3 Top view of the optimized equilibrium adsorption configurations of methionine monomer at different adsorption sites and with different orientations with respect to the surface unit cell. The adsorption energies are in unit of eV while the bond lengths are in unit of Å.....	134
Table B4 Top view of the optimized equilibrium adsorption configurations of methionine antiparallel dimer at different adsorption sites and with different orientations with respect to the surface unit cell. The adsorption energies are in unit of eV while the bond lengths are in unit of Å.....	136
Table B5 Top view of the optimized equilibrium adsorption configurations of methionine parallel dimer at different adsorption sites and with different orientations with respect to the surface unit cell. The adsorption energies are in unit of eV while the bond lengths are in unit of Å.....	137
Table C1 Calculated adsorption energies of thiolated cysteine adsorbed at different adsorption sites, through its sulfur atom, for three step edge models with Ag ₃ Si ₃ , Ag ₄ Si ₃ , and Ag ₅ Si ₃ unit cells. For the structure optimization calculations, the atomic positions of cysteine were relaxed while those of slab were fixed. All the energies are in unit eV.	142
Table C2 Calculated adsorption energies of thiolated cysteine adsorbed at different adsorption sites, through its sulfur atom, for the antiphase boundary model. For structure optimization calculations, the atomic positions of cysteine were relaxed while those of slab were fixed. All energies are in unit eV. ...	143

Chapter 1

Introduction

1.1 Surface Science

Surface science is the study of surfaces and interfacial phenomena at the atomic and molecular level. A combination of a few main factors has given birth to the field of surface science and its continued growth today. The advancement of the vacuum technology and development of the ultrahigh vacuum (UHV) systems, in 1950s, that attain pressure from 10^{-7} to 10^{-11} mbar and allow preparation and maintenance of contamination-free surfaces for an extended period of time for experimentation and studies. The commercial availability of single-crystal samples has enabled researchers to employ high-precision scientific methods that probe various properties of and phenomena on the more well-defined surfaces. The discovery of the wave-particle duality has led to the development of particle-beam-based diffraction techniques such as low energy electron diffraction (LEED) to provide surface-sensitive structural recognition. Near the same time, the discovery of the photoelectric effect has given rise to X-ray photoelectron spectroscopy (XPS) for detailed chemical environment identification based on chemical shifts and their quantitative composition analysis. These developments that begun in the late 1960s have continued and along with other techniques have led to the intense surface science research activities that we know today.¹

The energy crisis is one of the influential factors that drive the surface science field. With increasing global energy consumption and its consequences in environmental pollution and global warming, there is an acute need to develop catalyst-based environmental technologies and sensors. Since 1970s, the contribution of surface science to understanding chemical reactions and to developing catalyst-based environmental technologies has been evermore significant. The three-way catalytic convertor used to clean the automobile exhaust is a shining example of the technological improvements driven by surface science.²

In the discovery of transistor in 1947 and its evolution from large-scale integration to the modern nanoelectronics,³ surface science plays a critical role. The advancement of the semiconductor industry is well foretold by Moore's law, which predicts the doubling of the packing density of the transistors in microelectronic chips every 18-24 months since 1970.⁴ The interest in this trend is two-fold for surface scientists. Firstly, the resolute state of shrinking the feature size of an electronic device in semiconductor industry necessitates better understanding of the surface chemistry of semiconductors and surface chemical reactions for developing new ultra-small patterned templates and devices, which in turn guarantees the technological impact of surface science research. Secondly, the down-scaling of the

microprocessors and computer chips while up-scaling the multitude of functions lead to the growth of computing power available for improving our daily life. As a result, the quantitative predictive power provided by theoretical studies of surface phenomena and supported by increasingly more complex and accurate experimentation has undergone an explosive advancement.

The development of catalysts, sensors, and ever smaller semiconductor-based devices required fundamental understanding and quantitative characterization of surfaces at the atomic and molecular level. Consequently, the need to follow the physical and chemical changes occurring on the surfaces upon stimuli (such as radiation and chemicals) has led to the invention and development of surface-sensitive techniques down to the atomic scale. This has in turn opened up new frontiers in the field of modern surface science, particularly in the more interdisciplinary areas of chemistry, physics, biology, materials science, and nanotechnology.

1.2 The Si(111)7×7 Surface as a Template

Silicon is the most important semiconductor material predominantly used in the field of microelectronics and nanofabrication applications.⁵ Miniaturization of devices require detailed understanding of the fundamental interfacial processes occurring at the Si surfaces in order to enhance their functions and performance for the next-generation Si-based devices. Of all the Si surfaces, the Si(111)7×7 reconstructed surface is one of the most studied surfaces over the past few decades. It has been studied by a wide range of experimental methods and it is the de facto test system for any new emerging surface-sensitive technique. With the advent of scanning tunneling microscopy (STM) in early 1980s, the real space image of the 7×7 reconstruction was realized for the first time with atomic resolution.⁶ Atomically resolved AFM images obtained for this surface⁷ have led to validation of conventional concepts and to new insights. All these studies resulted in reaching a generally accepted dimer-adatom-stacking (DAS) fault model, in which the unit cell is divided into two triangular half unit cells: an unfaulted half and a faulted half that involves a 30 ° rotation in its (unfaulted) stacking sequence.^{8,9} Each half unit cell contains six adatoms and three restatoms with a corner hole, with a total of 19 dangling bonds and featuring dimer rows extended along the boundaries of each half unit cells. A schematic diagram of the Si(111)7×7 surface is shown in Figure 3.1a.

Introducing noble metals onto the Si(111) surface has ushered in a new technological era in the field of microelectronics. Metal silicide thin films have been playing an integral role in new device architecture. With the advances in semiconductor device fabrication, low-dimensional materials with novel properties have attracted a lot of attention particularly for their application in hybrid nanodevices. For that purpose, the Si(111)7×7 surface is a robust template for fabrication of low-dimensional metal

silicide clusters or nanolayers. The formation of metal-semiconductor hybrid systems and their properties are strongly dependent on the choice of the metal and semiconductor and their interactions. The adsorption of a wide range of metal materials has been investigated on the Si(111)7×7 surface at room temperature and at elevated temperature, and they include group IA metals (Li, Na, K, Cs),^{10–13,14,15,16} group IIIA metals (Al, Ga, In, Tl),^{17–20,21,22,23} group VIIB metals (Mn),^{24,25} group VIIIB ferromagnetic metals (Fe, Co, Ni, Pd, and Pt),^{21,26–30,31} group IB metals (Cu, Ag, and Au),^{32–39,40,14,41} group IIB metal (Zn),⁴² and group IVA metals (Ge, Sn, Pb, and Bi).^{43–45,46} While an array of noble metal clusters can be grown on the Si(111)7×7 template at room temperature, smooth two-dimensional metal silicide reconstructed surfaces can be generated at elevated temperature. Various interesting reconstruction phases are produced by this latter approach. Such two-dimensional metal silicide overlayers can exhibit interesting physicochemical properties. For example, in a combined STM and angle-resolved photoemission study of $\sqrt{7}\times\sqrt{3}$ -Pb, $\sqrt{3}\times\sqrt{3}$ -Pb, $\sqrt{7}\times\sqrt{3}$ -In, and $\sqrt{3}\times\sqrt{3}$ -In reconstructed phases on Si(111), superconductivity of their monoatomic layers has been observed, and its origin has been attributed to the metal-metal metallic and metal-Si covalent bondings.⁴⁷ Among all the metal-silicide reconstructions, the $\sqrt{3}\times\sqrt{3}$ phase is the most commonly observed phase in transition metals and is also known to exhibit interesting fluctuation dynamics.⁴⁸

Of the metal-silicide reconstructed surfaces, much of the studies have been devoted to the noble metals (Cu, Ag and Au) on Si due to their interesting applications in nanoelectronics and catalysis. The formation of an ordered array of Cu nanoclusters on Si(111)7×7 has been reported at room temperature at submonolayer coverage (0.4 ML), where identical size magic nanoclusters of Cu occupy both faulted- and unfaulted-half unit cells.⁴⁹ In a recent study in our group, the fabrication of an ordered honeycomb structure of Au monolayers on Si(111)7×7 was successfully achieved for the first time at room temperature.⁵⁰ Interestingly, similar results could not be obtained for Ag overlayers at similar coverages, indicating their different diffusion and growth behavior.⁵¹ At elevated temperatures, Au deposit on Si(111)7×7 evolved to two-dimensional Au-Si $\sqrt{3}\times\sqrt{3}$, 5×2 ,⁵² 5×1 ,⁵³ 6×6 , 5×5 ,⁵⁴ reconstructions. The reconstructed phases for Ag at elevated temperatures including $\sqrt{3}\times\sqrt{3}$, 3×1 , 6×1 , and 5×2 ,⁵⁵ and for Cu the 5×5 ,⁵¹ phase were also obtained. The study of these two-dimensional metal silicide surfaces is interesting not just for their potential implications in nanodevice fabrication but also for their use as prospective model systems in the study of such intricate physical phenomena as correlation effects in reduced dimensions.⁴⁸

1.3 The Si(111)- $\sqrt{3}\times\sqrt{3}$ -Ag Surface

Of particular interest in the wide range of two-dimensional Ag-Si surfaces is the Si(111)- $\sqrt{3}\times\sqrt{3}$ -Ag reconstructed surface. This monoatomic layer superstructure is formed after deposition of 1 monolayer of Ag on Si(111)7 \times 7 followed by annealing to 300-500 °C. Historically, this surface has been one of the most important prototypes for the metal/semiconductor interface. Upon conversion to Si(111)- $\sqrt{3}\times\sqrt{3}$ -Ag, the areal density of Si(111)7 \times 7 changes and the consequent mass transfer results in the formation of “islands” and “holes” above and below the original 7 \times 7 level, respectively.^{41,55-60} Its structure is best described with the “honeycomb-chained triangle” (HCT) model, as shown in Figure 1.1c, in which the Si atoms on the top Si layer form triangles (or trimers) and each Si atom is bonded to one Ag atom creating a honeycomb lattice of equivalent Ag triangles (or trimers) of high symmetry on top.⁶¹ The arrangement of the Ag trimers contains a mirror plane along the [1-21] direction. The HCT model can be used to account for the room-temperature empty-state STM images, in which each protrusion corresponds to the electron density maximum at the center of a Ag trimer. However, at low temperature, a hexagonal lattice in the empty-state image is observed and this so-called “inequivalent triangle” (IET) model is shown in Figures 1.2b and 1.2c. In the IET model, the Ag atoms bonded to each Si atoms are rotated either clockwise or counterclockwise by 6° with respect to their initial positions in HCT. This leads to the creation of an alternating size change of the Ag trimers while the Si trimers are fixed resulting in a breakdown of the mirror symmetry. In other words, the HCT is the fully symmetrical version of the IET.⁶²⁻⁶⁵ Although the coexistence of both HCT and IET structures has been reported at room temperature,⁵¹ we observe only the HCT structure in our experiments.

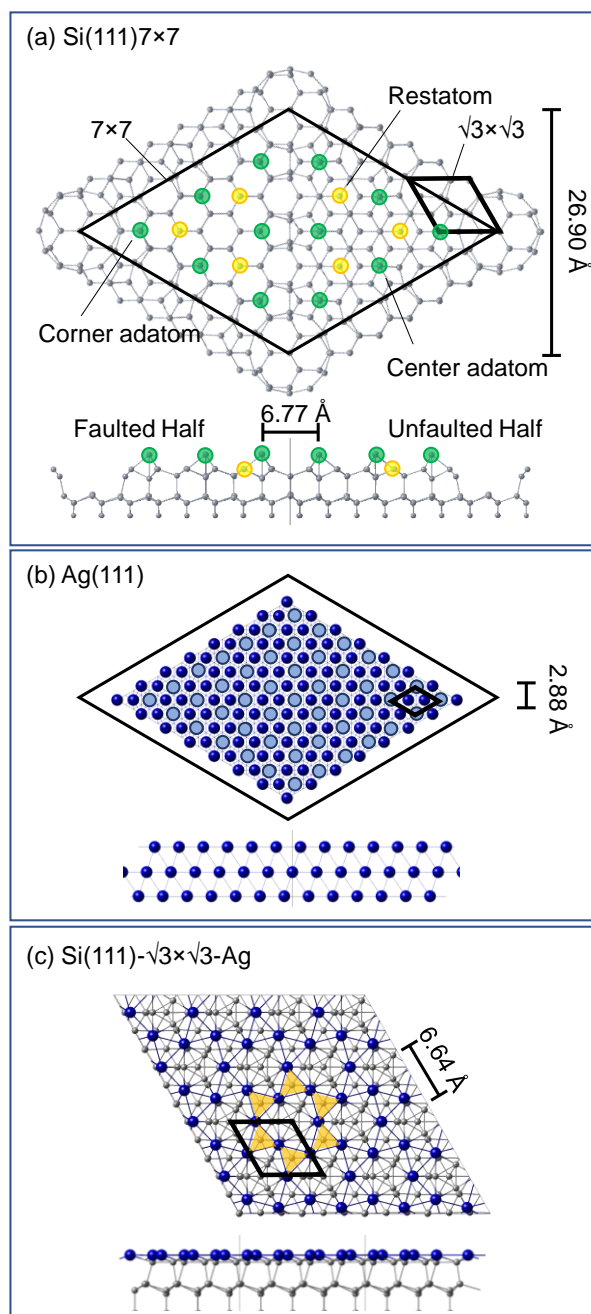


Figure 1.1 Top views and side views of the equilibrium geometries of (a) a dimer-adatom-stacking fault (DAS) model for Si(111)7x7, (b) a Ag(111) single-crystal surface, and (c) a Si(111)- $\sqrt{3}\times\sqrt{3}$ -Ag surface with the honeycomb-chained triangle (HCT) structure. The Si adatoms and restatoms are highlighted in (a) by, respectively, larger green and yellow circles for clarity. Blue and grey circles correspond to Ag and Si atoms, respectively, in (c). The $\sqrt{3}\times\sqrt{3}$ unit cell (diamond) is shown for the model surfaces in (a-c). All the model surfaces are generated by large-scale ab-initio quantum mechanical calculations using a Xeon computer cluster at WATLab.

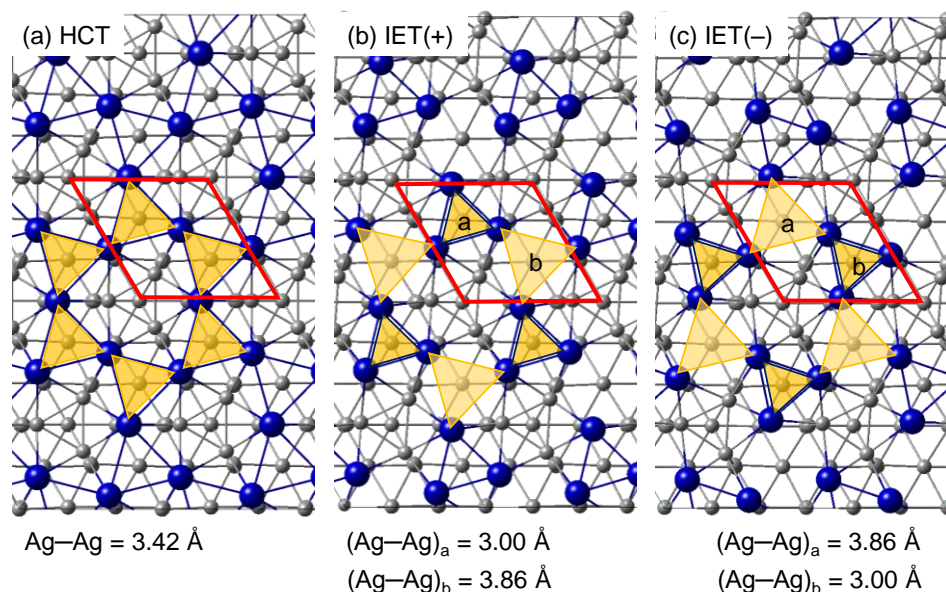


Figure 1.2 Magnified top views of a Si(111)- $\sqrt{3}\times\sqrt{3}$ -Ag surface with (a) the honeycomb-chained triangle (HCT) and (b, c) inequivalent triangle (IET) structures, where the (+) and (-) depict the counter-clockwise and clockwise rotational offsets of Ag atoms with respect to their positions in HCT, which results in three of the Ag trimers appear larger than the other three trimers (with the smaller trimers outlined by blue open triangles). Blue and grey circles correspond to Ag and Si atoms respectively.

1.4 Adsorption of Organic Molecules on Si(111)- $\sqrt{3}\times\sqrt{3}$ -Ag

Molecular interactions of organic components and biomolecules with semiconductor surfaces have attracted a lot of interest because of their potential applications in biosensors, biocompatible materials, and biomolecules-based electronic devices.⁶⁶⁻⁶⁸ The presence of a low diffusion barrier of organic molecules on a (metal) solid surface is essential to form self-assembled molecular architectures on the surface. On a semiconductor surface such as Si(111)7×7, surface diffusion is hindered by the presence of strong directional dangling bonds that enable covalent bonding interaction with organic adsorbates. Passivating the Si(111) surface with Ag atoms not only introduces new physical properties such as high electrical conductivity to the surface,^{69,70} but also creates a platform with a low diffusion barrier for organic molecules to move freely on the surface and aggregate with other molecules forming molecular islands. A number of low-temperature and room-temperature studies have reported the adsorption of large π -conjugated organic molecules on Si(111)- $\sqrt{3}\times\sqrt{3}$ -Ag for the application of organic thin films. These molecules include 3,4,9,10-perylene tetracarboxylic dianhydride (PTCDA),⁷¹ 3,4,9,10-perylene tetracarboxylic diimide (PTCDI),⁷² thiophene,⁷³⁻⁷⁵ metal phthalocyanine,⁷⁶ metal porphyrines,^{77,78} C₆₀,⁷⁹ and pentacene.⁸⁰ Adsorption of smaller molecules such as trimesic acid,⁸¹ terephthalic acid,⁸² and

adenine⁸³ on Si(111)- $\sqrt{3}\times\sqrt{3}$ -Ag have also been studied. According to their STM results, all of the aforementioned molecules lie flat on the surface, where the maximum possible interaction between their π -conjugated rings and the two-dimensional electron system of the surface is obtained. All of the above studies aimed to examine molecular self-assemblies through physisorption. The only experimental study that was focused on chemisorption on Si(111)- $\sqrt{3}\times\sqrt{3}$ -Ag⁸⁴ is for thiol-modified ferrocene. This experimental work was followed by a modelling study that supported their results via quantum mechanical calculations.⁸⁵

In all the aforementioned studies reported to date, the Si(111)- $\sqrt{3}\times\sqrt{3}$ -Ag surface has been used as an alternative substrate to metal substrates, with the focus mainly on the organic film properties. In the present work, we seek to elucidate the evolution of not only the adsorbate film properties but also the substrate properties upon adsorption of the organic adspecies. For this purpose, we employ the two sulfur-containing amino acids, cysteine and methionine, in order to understand their interactions with the Si(111)- $\sqrt{3}\times\sqrt{3}$ -Ag surface, and to investigate the synergetic properties of the functionalized Si(111)- $\sqrt{3}\times\sqrt{3}$ -Ag surface for potential applications. These amino acids were chosen for several reasons: (1) There are extensive amounts of experimental and theoretical data available for these amino acids on the reference Si surface, Si(111)7 \times 7, and on other reference metal surfaces [e.g. Ag(111)]. These data enable us to more readily compare their adsorption properties on Si(111)- $\sqrt{3}\times\sqrt{3}$ -Ag to those on metals and Si(111)7 \times 7. (2) The availability of multiple functional groups typical of amino acids (amino and carboxylic acid groups), in addition to the thiol group in cysteine and methylthio methylene group in methionine, along with their near-proportionate sizes, provide a rich testbed to examine not just the interaction of various functional groups with each other and with the surface but also the influence of molecular size on their adsorption properties on Si(111)- $\sqrt{3}\times\sqrt{3}$ -Ag.

As the smallest building blocks of proteins, amino acids are also fundamentally important in chemistry in general. Understanding their intermolecular interactions and growth processes could provide insights into fundamental interactions of other larger biochemical molecules that are essential for developing bio/nano-devices for biomedical sensing and molecular electronics. This impetus has inspired adsorption studies of a variety of amino acids, including aliphatic amino acids (glycine⁸⁶⁻⁸⁸, alanine,⁸⁹⁻⁹⁴ glutamic acid,⁹⁵⁻⁹⁸ lysine⁹⁹⁻¹⁰¹), sulfur-containing amino acids (cysteine¹⁰²⁻¹⁰⁴ and methionine¹⁰⁵⁻¹⁰⁹), aromatic amino acids (tyrosine^{110,111}), and heterocyclic amino acids (proline^{112,113}), on a number of close-packed single-crystal metal surfaces under UHV condition. Our recent studies in WATLab have been focussing on site-specific surface chemistry of bio/organic molecules including DNA-bases (thymine¹¹⁴ and adenine¹¹⁵), peptides (glycylglycine^{116,117}), and amino acids (glycine,^{116,118-120} alanine, cysteine,¹²¹ and methionine¹²²) on a well-defined semiconductor surface such as Si(111)7 \times 7 using a three-pronged

approach that combines XPS and STM data with large-scale ab-initio quantum mechanical simulations. A universal three-stage growth mechanism has been observed for these proteinogenic amino acids on Si(111)7×7.¹²³ In our latest work, we have also studied the interaction of a sulfur-containing amino acid (cysteine) with a gold honeycomb monolayer supported on Si(111)7×7 at room temperature.¹²⁴ The insights obtained on the adsorption and growth properties of both metal adlayers and (bio) organic films supported on Si surfaces enable us to move one step closer toward not only fabrication of stable hybrid organic/metal/semiconductor surfaces but also extending our understanding of the interfacial phenomena of a more complex hybrid system. The present work seeks to investigate such two-dimensional hybrid systems of higher complexity, which include physical and chemical features found not just on the ideal smooth terraces (that has been the central focus of traditional surface science to date) but indeed on the more reactive surface defects such as step edges and antiphase boundaries.

1.5 Surface Defects

Close-packed flat surfaces are generated by splitting a bulk crystal along its low Miller index planes such as the (100), (110) or (111) surfaces. While these low index surfaces can be used to provide valuable information on prominent surface properties, they are far from true representations of the real surfaces. Whenever technology involves gas-surface interactions, real surfaces come into play. A real surface contains not just low index planes (terraces) but also additional surface defect features such as steps, kinks, adatoms and vacancies. Surface defects could play an important role in the overall properties of the surface. Better understanding the nature and properties of these defects is therefore pivotal in advancing modern surface science. Surface defects are desirable adsorption sites for catalytic reactions on catalyst-relevant metal surfaces often due to the under-coordination of their local atomic sites and hence their higher reactivities. The study of molecular adsorption at these sites is therefore of paramount importance in the areas of catalysis and chemical sensing. A number of experimental and theoretical studies have been reported on the adsorption and reaction behavior of molecules at the step edges on metal surfaces such as Pt(111),¹²⁵ Pt(211) and Pt(311),¹²⁶ Ni(111),¹²⁷ Au(111),^{128,129} and Cu(531),¹³⁰ and on oxide surfaces including TiO₂(110),¹³¹ and Al₂O₃(0001).¹³² Vicinal surfaces of semiconductor materials such as Si contain a high number of dangling bonds at step edges and are good candidates for use as templates for crystal growth

Figure 1.3 shows typical types of defects commonly found on low index surfaces. These defects are distinguished based on the number of their nearest neighbours and include surface adatoms, atom vacancies, kinks, and step edges. The major surface defects of the Si(111)- $\sqrt{3}\times\sqrt{3}$ -Ag surface are step edges and antiphase boundaries. A step edge is the transition interface between the adjacent upper-step

terrace and lower-step terrace, while an antiphase boundary is formed as a result of a registry mismatch between two terraces growing into each other. In the present work, we investigate the electronic structures and geometries of the defects of Si(111)- $\sqrt{3}\times\sqrt{3}$ -Ag surface for the first time using quantum chemical calculations.

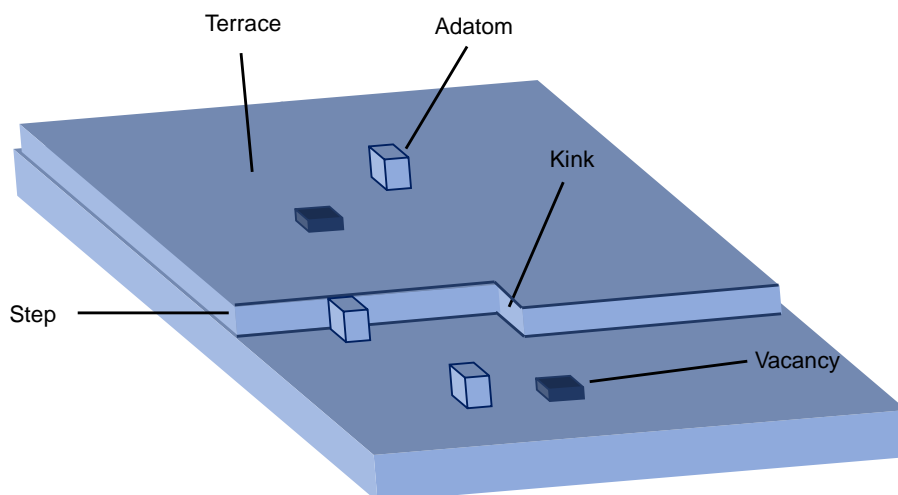


Figure 1.3 Schematic model of a solid surface depicting different types of surface sites. These sites are distinguishable by their nearest neighbours. For a simple cubic lattice used in this model, a terrace atom is bonded to 5 atoms resulting in a coordination number of 5 nearest neighbors. A step atom is the atom at the transition interface between the upper-step and lower-step terraces and is bonded to 4 atoms and hence its coordination number is 4, while a kink is located at a corner of a step edge and exhibits a coordination number of 3. An adatom defect and a vacancy defect correspond to an excess and lack thereof an atom on the surface terrace, respectively.

1.6 X-ray Photoelectron Spectroscopy

X-ray photoelectron spectroscopy (XPS), also known as electron spectroscopy for chemical analysis (ESCA), is one of the most widely used techniques in the field of surface science and it provides quantitative information about the chemical-state composition and the electronic structure of the surface. The working principle of XPS is based on the photoelectric effect, which was discovered by Einstein in 1905¹³³ and was later further developed with the concept of core-level chemical shifts by Siegbahn and coworkers in 1957.¹³⁴ In the photoelectric process, an electron is ejected as a result of absorption of a photon with energy $h\nu$. For an electron to be ejected, the photon energy of the incident X-ray beam must be greater than the surface work function. The kinetic energy (KE) of the emitted photoelectron depends on the energy of the photons through the Einstein equation:

$$KE = h\nu - (E_B + \phi_{sp}) \quad (1.1)$$

where E_B is the binding energy of the electron before photoejection and is measured with respect to the Fermi level, and ϕ_{sp} is the work function of the electron spectrometer that is required to bring the electron from the Fermi level to the vacuum level outside the surface to the spectrometer. The photoemission process is illustrated schematically in Figure 1.4, in which a photoelectron is emitted from the K shell of an atom, upon absorption of a photon. The spectral intensities as functions of kinetic energy (or correspondingly the binding energy) for the photoelectron lines provide a unique signature of individual atoms in their local chemical environment as well as quantitative compositions based on their chemical states. The binding energies of the core-level electrons represent the strength of the Coulombic interactions between the inner-shell electrons and the nuclei, and the local chemical environment exerted by neighbouring atoms. Any change in the chemical environment produces an effect on the electron-nuclei interactions and thus causes a shift in the binding energy of the photoelectron, which is called the chemical shift. Due to the short electron inelastic mean free path, only photoelectrons generated in the top 2-10 nm of the material could escape the surface. XPS is therefore a surface-sensitive technique as it provides quantitative information about not only the surfaces of the inorganic solids but also the organic adsorption layers on surfaces through their respective chemical-state signatures.

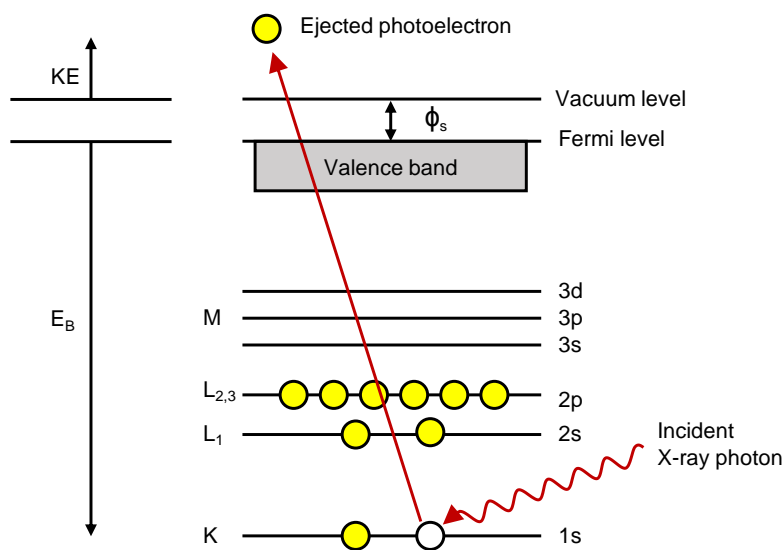


Figure 1.4 Schematic diagram depicting ejection of the 1s electron as the result of absorption of an incident X-ray photon.

In the XPS spectrometer of our Omicron multi-technique system shown in Figure 1.5, the X-ray photons produced by an Al K_α X-ray source (anode) pass through a quartz crystal monochromator and the

resulting monochromatized X-ray beam is focused onto the sample. The monochromator is used to reduce the background produced by the bremsstrahlung scattering and eliminates the unwanted shake-up and shake-off features. The photoelectrons emitted from the sample surface are then collected by electrostatic input lens onto the entrance aperture of a hemispherical deflection electron analyzer (spectrometer). The hemispherical analyzer consists of two concentric hemispherical elements, which are biased with appropriate voltages to allow electrons with the selected kinetic energy to pass through the analyzer. The Gaussian distribution for the transmitted photoelectrons across the exit plane is detected by a high throughput electron detector consisting of multiple channeltrons.

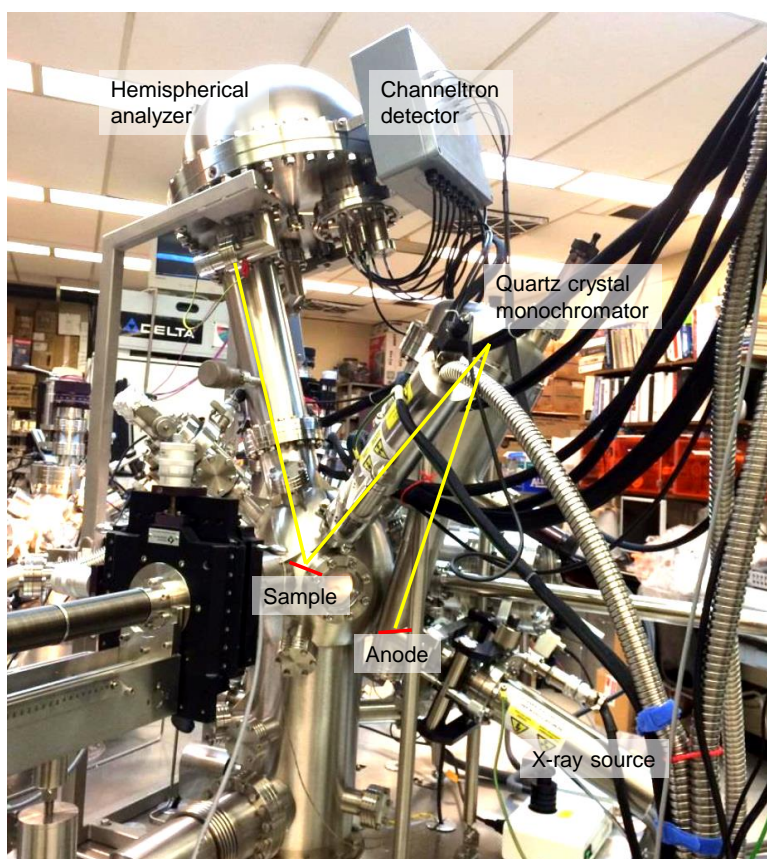


Figure 1.5 A photograph of the Omicron XPS spectrometer depicting the X-ray source (anode), a quartz-crystal X-ray monochromator, an approximate sample position with respect to the X-ray incident angle and electron emission angle, an electrostatic lens system, a hemispherical analyzer, and a seven-channeltron electron detector.

To measure accurately the photoelectron KE (and hence E_B) of various types of samples, a proper referencing of the binding energy is required. After grounding both the sample and the spectrometer, the energy diagram of the sample-spectrometer is shown in Figure 1.6. For conducting samples, the measured

kinetic energy (or binding energy) is independent of the sample work function (ϕ_s), but dependent on the spectrometer work function (ϕ_{sp}), as also implied in the Einstein equation 1.1.

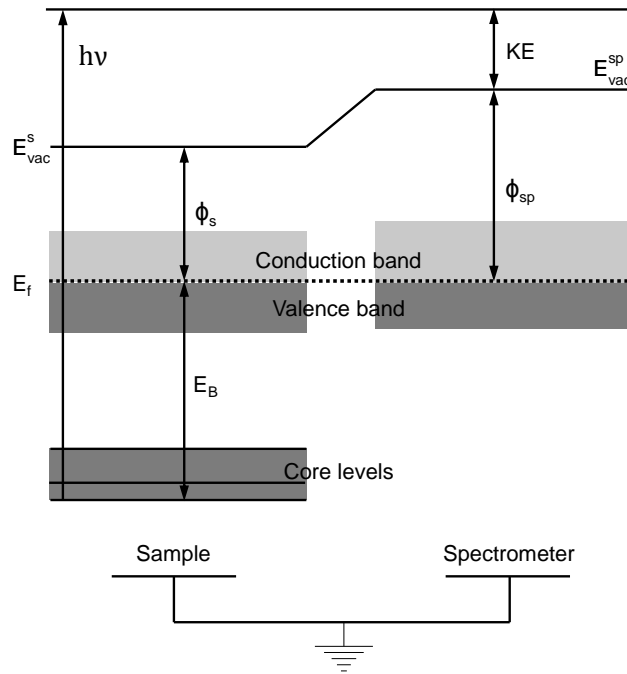


Figure 1.6 The energy level diagram for a conductive sample and the spectrometer. The Fermi levels of the sample and the spectrometer are aligned and the E_B is referenced with respect to E_f . The measurement of E_B is independent of the sample work function but dependent on the spectrometer work function.

1.7 Scanning Tunneling Microscopy

With the invention of the scanning tunneling microscopy (STM) in 1982 by Binnig and Rohrer, not only the morphology of conductive solid surfaces but also their local electronic structure could be investigated at atomic resolution for the first time.¹³⁵ The working principle of STM is based on the quantum-mechanical concept of electron tunneling that involves tunneling of an electron wave through a potential barrier when its classical kinetic energy is lower than the barrier height. The quantum tunneling can occur between two conducting materials (metals or semiconductors) that are separated by a sufficiently small gap where the electron wavefunction can extend out of their classical potential wells. An atomically sharp metallic tip, usually made of platinum/iridium or tungsten, is brought to close proximity of a conductive surface until the tunneling current begins to flow upon applying a voltage. Figure 1.7 illustrates the tunneling effect between the probe tip and a sample surface. Part of the electron wavefunction at the sample surface (Ψ_{sample}) tunnels through the potential barrier where it decays exponentially (Ψ_{barrier}). The amplitude of the pass-through wavefunction at the tip (Ψ_{tip}) is reduced. The fraction of the wavefunction that can tunnel through the potential barrier is described by the transmission coefficient from which the tunneling current can be calculated. The tunneling current can be estimated by Equation 1.2:

$$i \propto U \exp(-2kd) \quad 1.2$$

$$k = \sqrt{\frac{2m_e \Phi}{\hbar^2}} \quad 1.3$$

where Φ is the average barrier height $\frac{1}{2}(\Phi_{\text{sample}} + \Phi_{\text{tip}})$ between the tip (Φ_{tip} is the barrier potential of the tip) and the sample (Φ_{sample} is the barrier potential of the sample), m_e is the electron mass, k is the inverse decay length, and \hbar is Planck's constant divided by 2π . This exponential dependency is the basis of the surface sensitivity of the STM, where a vertical resolution of 0.01 nm and a lateral resolution of 0.1 nm can be achieved. The lateral resolution is determined by the radius of the tip, which ideally corresponds to the size of one tip atom. Furthermore, the tunneling current is proportional to the total (integral) density of states at an energy determined by the applied voltage.

During experiment, a tunneling current is first established at a distance in nm range while a piezoelectric controller enables the tip movement at great precision. The z-piezo is used to adjust the separation between the tip and the surface by applying appropriate voltages, while the x and y piezos provide scanning in the two lateral directions across the sample surface. The STM can be operated in two different modes: the constant height and the constant current modes. Upon moving the tip to the

appropriate tunneling z position, the scanning tip is navigated with a selected bias voltage (typically 5 mV to 2 V) applied to the sample to enable detection of a tunneling current (typically 5 pA to 2 nA). In constant height mode, the tip is scanned over x and y of the specimen surface at a fixed z (constant height). The collected tunneling current is then directly proportional to the local density of electronic states at z above the surface. This mode allows a high scanning speed, but it is limited to very flat surfaces or very small scanning areas (because any surface defects or contamination could potentially crash the tip). Alternatively, in the constant current mode, the tip is scanned over x and y across the surface with z position dynamically adjusted such that a constant tunneling current between the tip and the surface is obtained. In this mode, the tunneling current is proportional to the apparent height of the tip above the surface. A feedback loop is used to control the height of the tip using the z -piezo actuator.

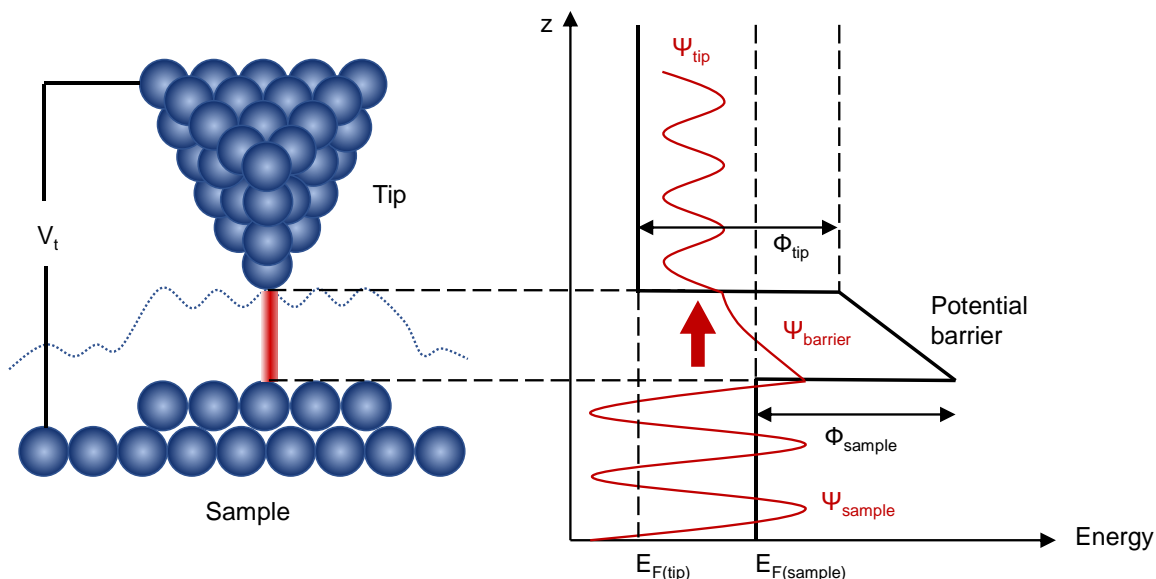


Figure 1.7 A schematic diagram depicting the principle of the electron tunneling process, where V_t is the tunneling bias voltage (which can be created by applying an external voltage either to the tip or to the sample while keeping the other grounded), z is the vertical distance, E_F is the Fermi level, Φ is the work function, and Ψ is the electron wavefunction.

1.8 Scope of Thesis

In the present work, we investigate the molecular interactions of two sulfur-containing amino acids, L-cysteine and L-methionine, with the Si(111)- $\sqrt{3}\times\sqrt{3}$ -Ag surface and follow their growth evolution over not just terraces but also prominent defects including step edges and antiphase boundaries. Using the three-pronged approach of combining chemical-state information provided by XPS and the electronic

density of states images from STM with large-scale quantum mechanical modelling, we seek to investigate their detailed growth and molecular architecture formation at room temperature and after annealing. Our goal is to use an amino acid adsorbate, specifically cysteine with three functional groups, as a probe to identify site-specific phenomena related to surface defects. We also investigate the effect of adsorption on the electronic structure, chemical composition, and morphology of the two-dimensional $\sqrt{3}\times\sqrt{3}$ -Ag surface. We have outlined here in Chapter 1 the motivation and background for the present work, along with a brief literature survey about adsorption of organic and inorganic materials on both Si(111) 7×7 and Si(111)- $\sqrt{3}\times\sqrt{3}$ -Ag surfaces. Chapter 2 provides overviews of the experimental setups for XPS and STM measurements for our amino acid/Ag/Si systems, and of the computational details used for modeling the adsorption on the terraces and surface defects of the Si(111)- $\sqrt{3}\times\sqrt{3}$ -Ag surface. The experimental and computational results of cysteine and methionine on Si(111)- $\sqrt{3}\times\sqrt{3}$ -Ag are given in the next three chapters. In particular, Chapter 3 presents the XPS/STM study of interfacial interactions and growth evolution of cysteine on Si(111)- $\sqrt{3}\times\sqrt{3}$ -Ag, from nucleation at step edges at very low coverages to multilayer growth at room temperature and the subsequent Ag-metal cluster formation after annealing. The large-scale DFT calculation of this system is also presented at the end of Chapter 3 and Appendix A. In Chapter 4, the study on molecular wire formation of methionine and the growth properties of a methionine film on Si(111)- $\sqrt{3}\times\sqrt{3}$ -Ag is presented, using the aforementioned three-pronged approach. We also provide similar experimental measurements performed on glycine adsorption. Along with our data on cysteine and methionine, this data allows us to examine the effect of functional groups and molecular size on the room-temperature adsorption and growth and to investigate their effect on the induced metal cluster formation after annealing. In Chapter 5, we provide a detailed modelling study in which the equilibrium structures of the step edge and antiphase boundary found on Si(111)- $\sqrt{3}\times\sqrt{3}$ -Ag are determined, for the first time, by DFT total energy calculations, and these are corroborated with the experimental data presented in Chapter 3. Finally, the summary and future outlook of the present work are given in Chapter 6. Appendices A, B, and C provide supporting information for Chapters 3, 4, and 5, respectively.

Chapter 2

Experimental and Computational Details

2.1 UHV Multitechnique System

The experiments were carried out in a five-chamber ultrahigh vacuum system (Omicron Nanotechnology, Inc.), shown in Figure 2.1, which consisted of an analysis chamber for X-ray photoelectron spectroscopy (XPS) for chemical composition analysis, variable-temperature scanning probe microscopy (SPM) for atomic-resolution imaging, and low energy electron diffraction (LEED) for surface structure determination; two molecular beam epitaxy (MBE) chambers for organic and inorganic materials deposition, one of which contained a reflection high-energy electron diffraction (RHEED) for in-situ growth monitoring of crystalline materials, and the other one equipped with a quadrupole mass spectrometer for in-situ identification and monitoring of organic materials; a fast-entry loadlock (FEL) chamber for sample loading; and a center transfer chamber connecting the other chambers for sample interchange and storage. Each of the analysis, MBE, and the transfer chambers was pumped by a turbomolecular pump, an ion pump, and a titanium sublimation pump, while the FEL is pumped by a turbomolecular pump. The background pressure of the analysis chamber was better (lower) than 5×10^{-11} mbar, while that of the MBE chambers were better than 1×10^{-10} mbar.

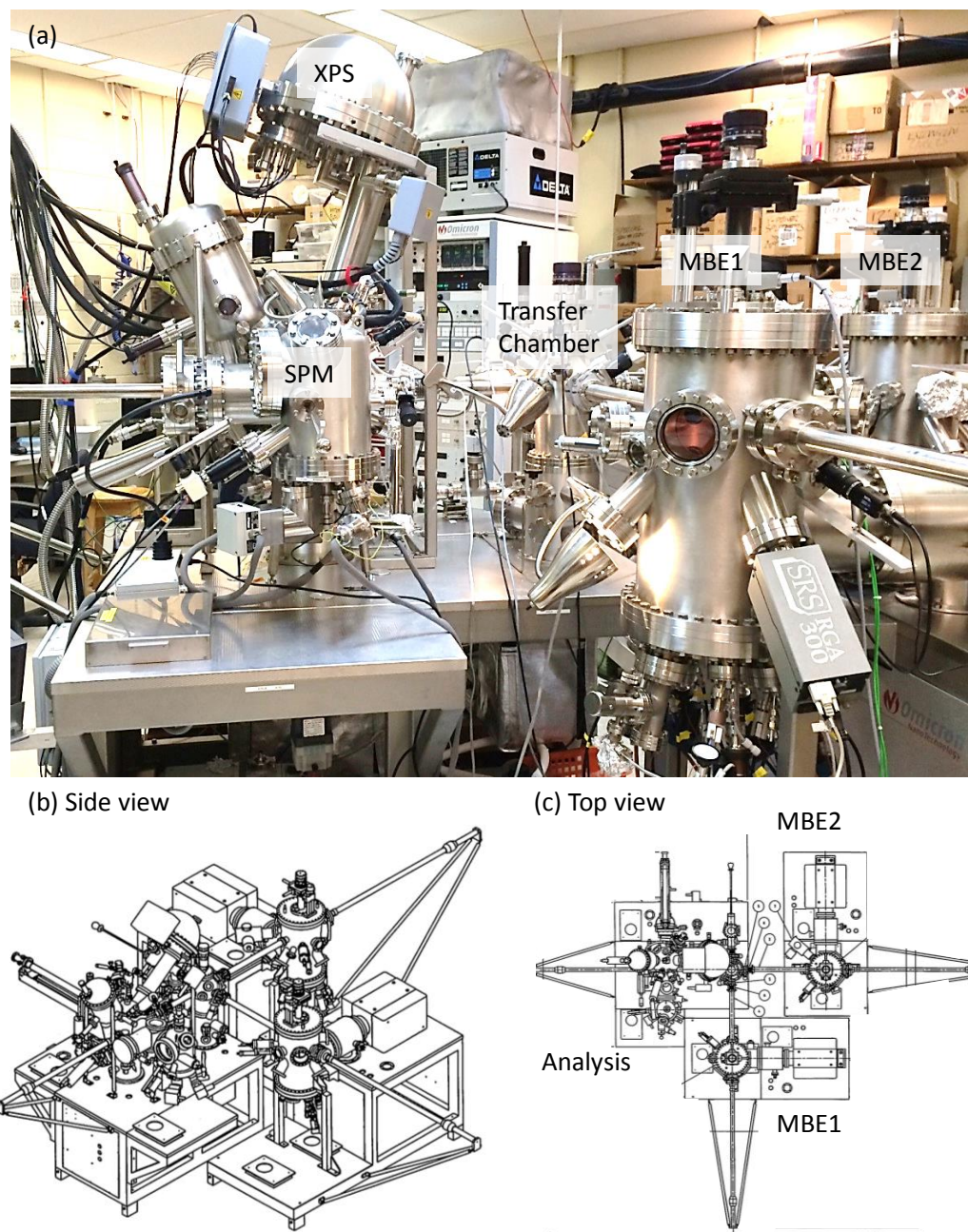


Figure 2.1 (a) A photograph of the multichamber Omicron system consisting of MBE1 for low-temperature organic material deposition and MBE2, for high-temperature metal and inorganic material deposition; and an analysis chamber equipped with an X-ray photoelectron spectrometer (XPS), a variable-temperature scanning probe microscope (SPM), and a low energy electron diffractometer (LEED); as well as a fast entry loadlock (FEL) chamber (out of view) and a center transfer chamber. (b, c) Machine drawings showing the side and top views, respectively (obtained from the Omicron User Manual).

2.2 MBE Chambers

The MBE1 chamber was used to deposit organic materials and was equipped with four specially designed water-cooled low-temperature effusion cells (Dr. Ebert MBE-Komponenten GmbH). To identify the signature of the evaporated molecular vapour, the MBE1 chamber (Figure 2.2a) is also equipped with a 1-300 amu quadrupole mass spectrometer (Stanford Research Systems RGA-300). The effusion cells OME1 and OME2 (Figure 2.2b) were used for thermal evaporation over a relatively low temperature range (15-350 °C), while NTEZ1 and NTEZ2 (Figure 2.2c) were used for evaporating materials at higher temperature (80-700 °C). The bioorganic powder materials were loaded in a quartz crucible and placed inside the effusion cell. The effusion cell (with the crucible filled with powder) was thoroughly outgassed under vacuum to remove any residual absorbants, such as water, in the powder. The powder inside the crucible was heated uniformly along the entire length by a hot Ta-wire heater. The temperature of the crucible was measured by a thermocouple in direct contact with the crucible wall. All effusion cells are equipped with a stainless-steel double-wall cooling shroud (Figures 2.2d and 2.2e) to ensure a uniform temperature distribution along the crucible. The MBE2 chamber (Figure 2.2f) is identical to MBE1 except that it was equipped with two WEZ (200-1300 °C, Figure 2.2h) and two EFM cells (300-2000 °C, Figure 2.2g), and was used to evaporate metals such as Ag, Au, and Fe, and high-temperature materials such as silicon. Both MBE chamber walls were lined inside with a cooling shroud which acted as an additional cryogenic pump when filled with liquid nitrogen. In the present work, liquid nitrogen was used in the cooling shroud of MBE1 chamber to further reduce the background pressure before evaporation of the amino acid powders.

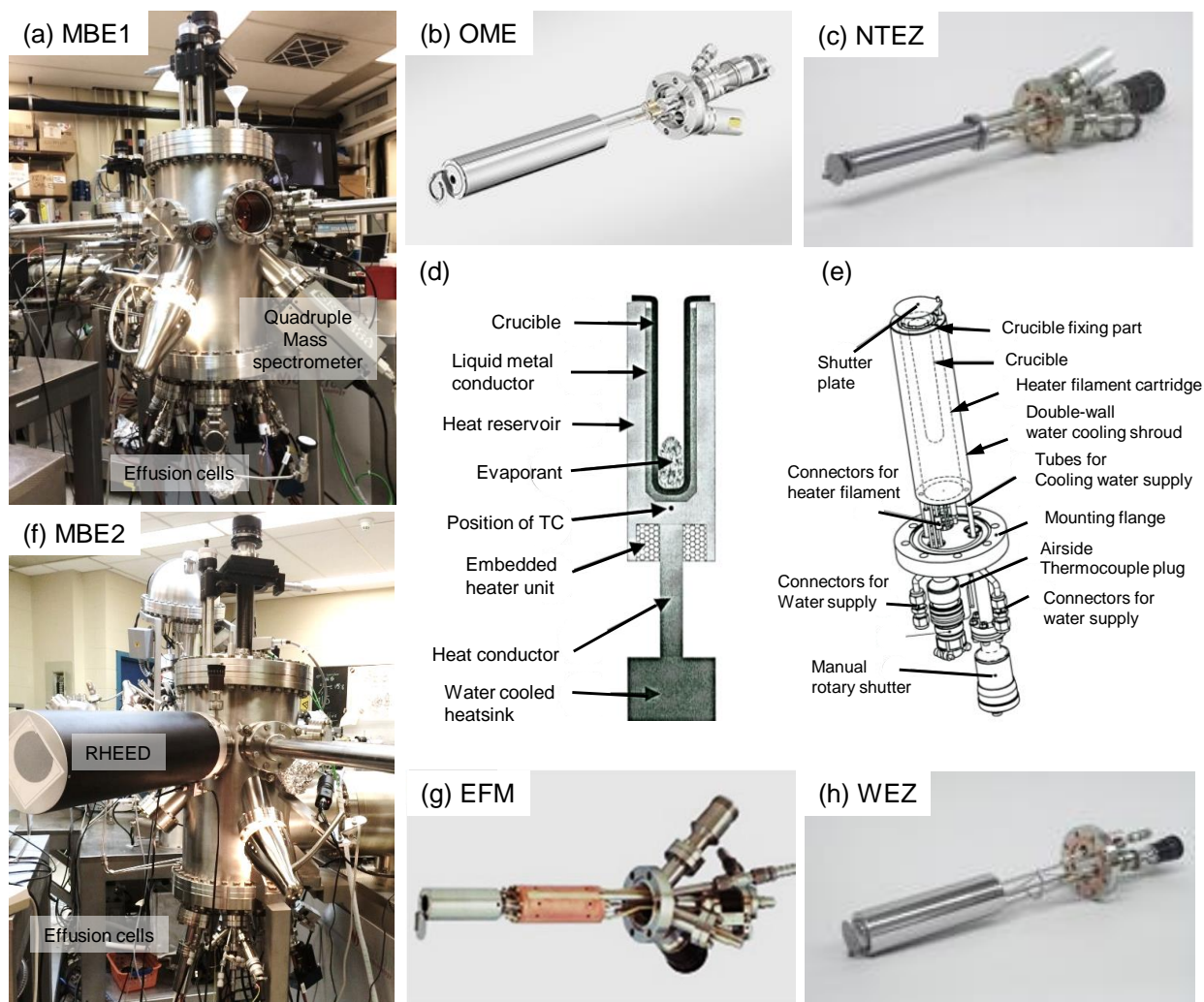


Figure 2.2 Photographs of (a) MBE1 and (f) MBE2 chambers for deposition of bio/organic materials and metals, respectively. MBE1 chamber was equipped with four low-temperature precision effusion cells (two OME and two NTEZ cells), and a quadrupole mass spectrometer. MBE2 was equipped with two EFM and two WEZ effusion cells, and a RHEED system. Photographs of (b) OME, (c) NTEZ, (g) EFM, and (h) WEZ effusion cells. Schematic diagrams of (d) the OME and (e) NTEZ cells, depicting the crucible, heating system, evaporant (powder), thermocouple and water-cooling mechanism. The photographs in (b, c, g, h) and the diagrams in (d) and (e) were obtained from the MBE effusion cells manual.

2.3 Analysis Chamber

The analysis chamber was equipped with XPS, SPM, and LEED used for chemical composition analysis, atomic-resolution imaging, and surface structure characterization, respectively.

2.3.1 X-ray Photoelectron Spectrometer

The XPS spectrometer consisted of a monochromatized Al K α (photon energy = 1486.6 eV) X-ray source (XM 1000 MkII), a SPHERA hemispherical electron analyzer, and a 7-channeltron detector assembly (Figure 2.3a). Figure 2.3b shows a schematic diagram of the X-ray monochromator assembly with its three major components: electron source and alignment manipulator of the cathode, X-ray anode, and the quartz-crystal mirror assembly (monochromator). The sample, X-ray anode, and the quartz-crystal mirror (of the monochromator) were positioned appropriately on the Rowland circle. The relative orientation of the monochromator axis (photon direction) and the entrance lens direction of the analyzer (photoelectron emission direction) was fixed at the magic angle (of 54.7°). The X-ray source, shown in Figure 2.3c, consisted of an Al-coated anode and two, one short and one long, filaments used as cathodes. The short cathode (~ 1mm) operated at a higher power density (300 W at 15 kV) could deliver a more focused X-ray beam spot, while the longer cathode operated at a lower power density (600 W at 16 kV) produced a larger and more diffuse X-ray beam spot (~ 4mm) on the sample. The resulted photoemission signal was directly proportional to the brightness of the X-ray spot. The control units for both X-ray source and the analyzer were fully under computer control. The XPS spectra were fitted with Gaussian-Lorentzian (70% Gaussian and 30% Lorentzian) lineshapes along with appropriate Shirley background by using the Casa-XPS data analysis software.

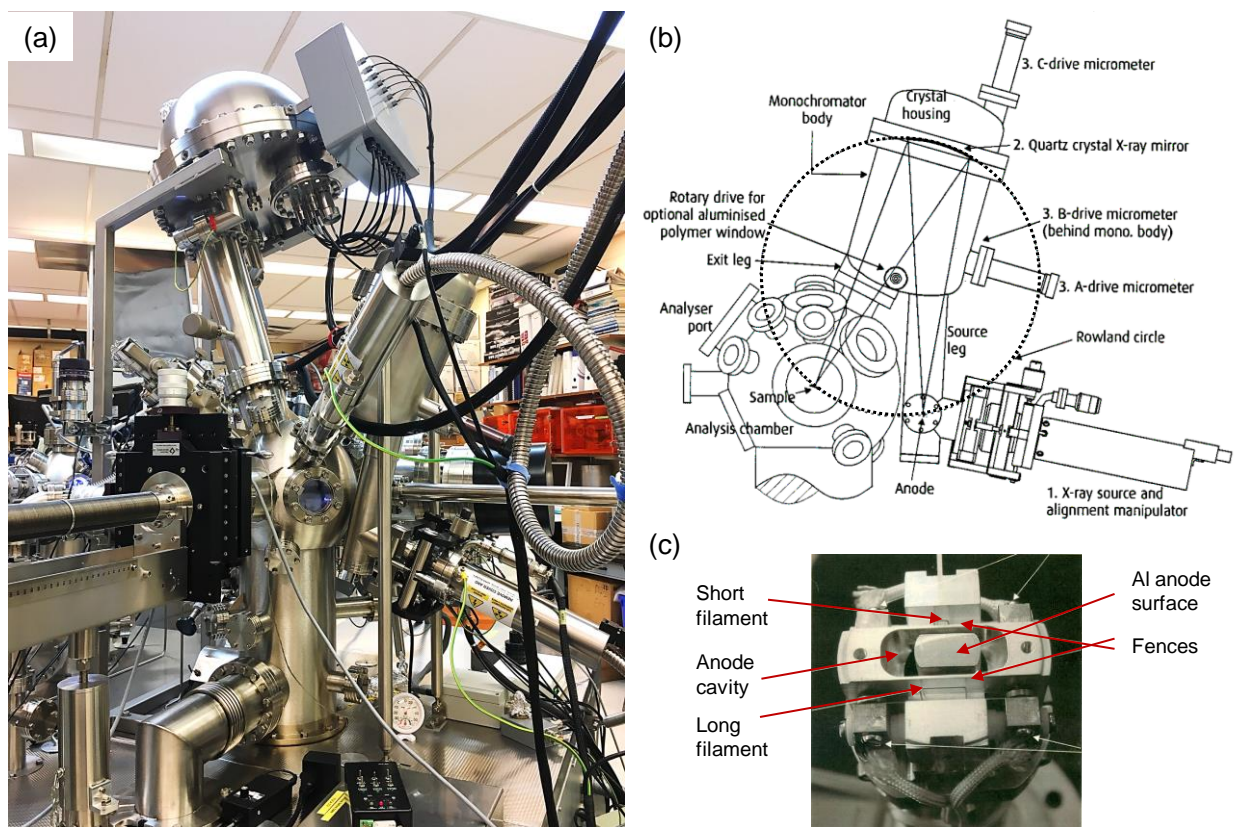


Figure 2.3 (a) Photograph of the X-ray Photoelectron Spectrometer, including the Sphera hemispherical analyzer, an X-ray monochromator with an X-ray source, and manipulator. (b) Schematic diagram of the monochromator assembly showing the X-ray source, alignment drives, the crystal mirror housing on the Rowland circle along with the positions of the sample and of the X-ray anode. (c) Photograph of the XM 1000 MKII X-ray source with the aluminum-coated anode, and the long- and short-filament cathodes. The diagram in (b) and the photograph in (c) were obtained from the Omicron User Manual.

2.3.2 Variable Temperature Scanning Probe Microscope (VT-SPM)

The variable-temperature scanning probe microscope was installed in the analysis chamber (Figure 2.4a) and is capable of both STM and atomic force microscopy measurements over a wide temperature range between -203 and 227 °C when used with appropriate cooling and heating facilities. Figure 2.4b shows a schematic view of the VT-SPM and its anti-vibration suspension mechanism. An effective noise reduction system was provided by a unique vibration decoupling technique. The base plate is suspended by four springs and vibrations of the suspension system were prevented by using a non-periodic eddy-current damping mechanism. This was achieved by a set of copper plates seated in between permanent magnets and positioned around the perimeter of the VT-STM base plate. To transfer the sample or the tip, the spring suspension was locked with a push-pull motion drive (Figure 2.4b). The sample transfer was

performed by using a wobble stick (Figure 2.4a). During measurement, the STM stage was released and suspended again with the push-pull motion drive. The tip approach of moving the tip holder to the sample stage was controlled with a remote-control box. After tunneling current was achieved, the measurements can be started in the MATRIX control software. In our experiments, an atomically sharp, chemically etched W wire was used as the STM tip to probe the surface in the constant current mode.

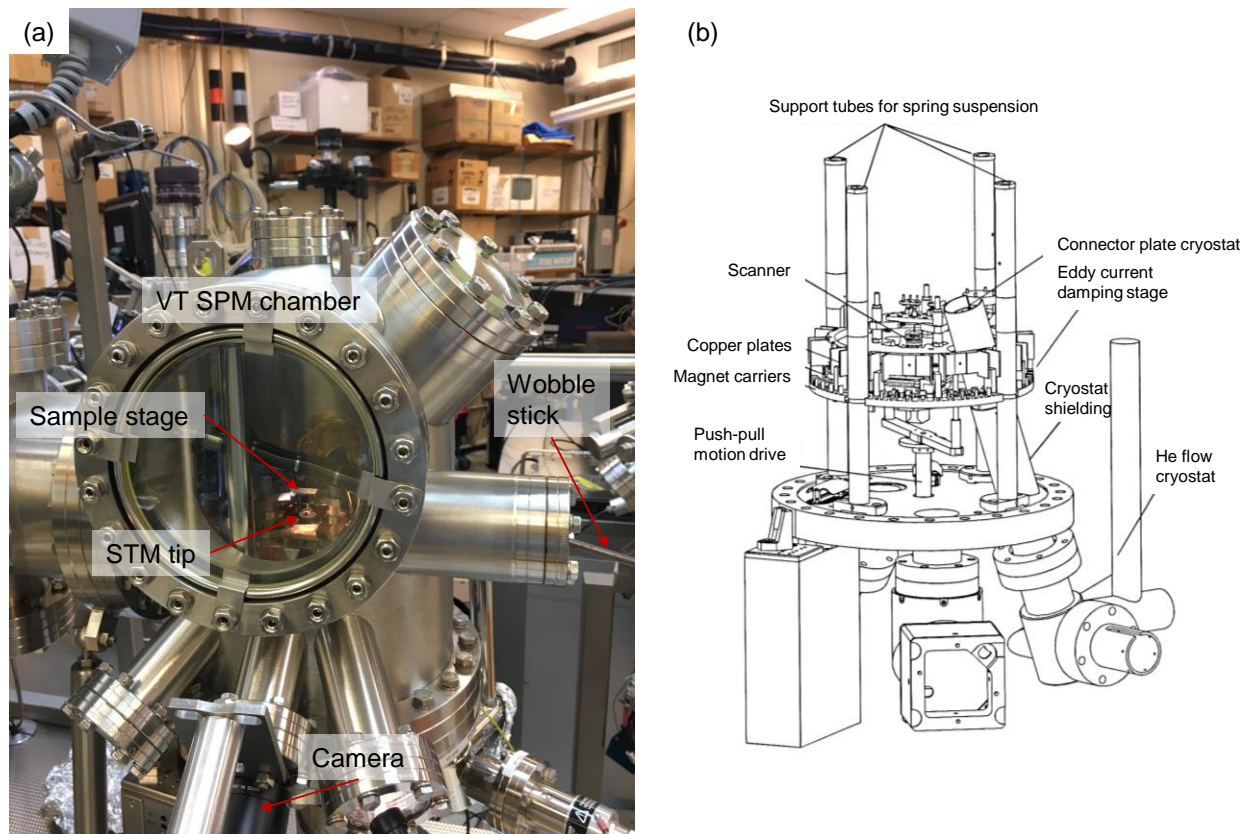


Figure 2.4 (a) Photograph of the VT-SPM inside its housing chamber, and (b) schematic diagram of the VT-SPM assembly (outside vacuum) with its main components. The diagram in (b) was obtained from the STM system manual.

2.4 Sample Preparation and Measurements

The substrate was a single-side polished, n-type Si(111) chip ($11 \times 2 \text{ mm}^2$, 0.3 mm thick) with a resistivity of $5 \text{ m}\Omega \text{ cm}$ (Virginia Semiconductor, Inc.). After cleaning with acetone and ethanol in an ultrasound cleaner, the sample was introduced into the FEL chamber and transferred to the analysis chamber using the appropriate magnetic transfer rods. After the Si substrate was thoroughly degassed by

direct-current heating at 400 °C for 12 h, an atomically clean Si(111)7×7 surface was prepared by a repeated flash-annealing procedure, in which the outgassed sample was heated to ~1200°C rapidly and held at that temperature for ~5 s, and then rapidly cooled to ~800 °C followed by a slow cool-down to room temperature at a 4-5 °C/s. The clean Si(111)7×7 substrate was then transferred to the MBE2 chamber for Ag deposition. Silver was deposited from a WEZ effusion cell at a cell temperature of 870 °C onto the Si substrate for 120 s, and then followed by direct-current annealing to 500 °C for 120 s to produce the Si(111)-√3×√3-Ag surface after cool-down.⁵⁵ The cleanliness of both the Si(111)7×7 surface before Ag deposition and the resulting Si(111)-√3×√3-Ag surface was then verified by STM and XPS before deposition of the appropriate amino acid of interest. For STM measurements, all the images in this work were obtained with the tip grounded while maintaining a constant tunneling current of 0.2 nA at a sample bias of either -2 V for filled-state imaging or +2 V for empty-state imaging. The organic vapour depositions were performed with the low-temperature organic effusion cells (Dr. Ebert, MBE-Komponenten GmbH) in the MBE1 chamber.

For the amino acid films studied in Chapters 3 and 4, cysteine or methionine (both 99.5% purity, Fluka) was exposed to the Si(111)-√3×√3-Ag surface by increasing the effusion cell temperature to 130 °C for cysteine and 120 °C for methionine. During deposition, the background pressure of the chamber was 2×10^{-9} mbar. To confirm the purity of the amino acid powder, the cracking pattern was monitored in-situ by using a quadrupole mass spectrometer (Stanford Research Systems RGA-300) and was found to be in good accord with the literature.¹³⁶ To obtain sub-monolayer to multilayer films, cysteine or methionine was evaporated onto the Si(111)-√3×√3-Ag surface at room temperature with different exposure times. For cysteine film preparation, each exposure was performed on a freshly prepared Si(111)-√3×√3-Ag surface, while for methionine the exposure procedure was performed cumulatively. For the surface covered with a thick cysteine or methionine film, the sample was annealed sequentially to 85 °C, 175 °C, and 285 °C, each for 600 s, by using resistive heating. The sample was then allowed to cool back to room temperature after each annealing step before characterization. All the STM and XPS experiments were conducted with the sample held at room temperature. The XPS spectra were recorded at a pass energy of 20 eV with an energy resolution of 0.7 eV full width at half maximum (fwhm) for the Ag 3d_{5/2} photoline at 368.3 eV. Using the Casa XPS software, Gaussian-Lorentzian line shapes were employed to fit the spectra after appropriate correction with the Shirley background.

2.5 Computational Details

The goal of computational surface science is to provide fundamental understanding of the basic principles that govern the physical and electronic structures of surfaces and their relations to chemical and

other properties and related processes (structure-property relations). Despite their inherent complexities, there has been a tremendous amount of progress in the theoretical treatment of surface structures and processes. There is now a large class of systems that can be addressed quantitatively based on first-principle electronic structure methods. This progress is mainly driven by advances in computing power and development of efficient electronic structure algorithms. Classical and quantum mechanical techniques can be used to model a wide range of surface processes. Electronic structure calculations for surface problems are dominated by methods based on the density functional theory (DFT), which can also be used to predict various molecular structures and properties such as magnetic properties and vibrational frequencies in chemistry. DFT-based methods solve the many-electron system by using functionals, i. e. functions of another function, which in this case is the electron density. Various properties of the bulk can be described by using local density approximation (LDA)^{137,138}, where the electron density is approximated to have the same value at every position in the system. However, LDA is not an appropriate approximation in cases such as molecules, where the electron density is clearly not uniform. Generalized gradient approximation (GGA) has been developed to address the shortcomings of LDA. There are a large number of GGA¹³⁹ functionals based on different ways of generating the gradients of electron density. The Perdew-Wang functional (PW91)¹⁴⁰ and Perdew-Burke-Ernzerhof (PBE)¹⁴¹ functional are two of the more popular ones. In spite of great developments in constructing specific functionals in the last decade, the problem of van der Waals interactions or dispersion forces in intermolecular interactions remains a big challenge. To alleviate this problem, an additional term has been added to the conventional DFT energy.¹⁴² Dispersion-corrected DFT-D2 and DFT-D3 methods by Grimme¹⁴³⁻¹⁴⁵ have been shown to give quite accurate thermochemistry for both covalently bonded systems and systems dominated by dispersion forces.

In the present work, we used an optimized structure of the honeycomb-chained trimer model for the Si(111)- $\sqrt{3}\times\sqrt{3}$ -Ag substrate, in which each unit cell contained three Ag atoms (in the topmost layer) and three Si atoms underneath. Unless otherwise stated, a periodic 4×4 slab with sixteen 1×1 unit cells of Si(111)- $\sqrt{3}\times\sqrt{3}$ -Ag was used as the model surface. This slab (supercell) consisted of a topmost layer of Ag trimers (48 Ag atoms) bonded to a layer of Si trimers underneath and three underlying Si bilayers (336 Si atoms in total) with a lattice constant of 5.41 Å, as well as a vacuum gap of 10 Å. The bottom layer of Si atoms in the slab was terminated with 48 H atoms.

The first-principle total energy calculations were performed within the projector augmented wave (PAW) potentials and the generalized gradient approximation (GGA) based on the Perdew-Burke-Ernzerhof (PBE) exchange-correlation functional. The Vienna Ab-initio Simulation Package (VASP, version 5.4) with the Materials Exploration and Design Analysis platform (MedeA, version 2.19,

Materials Design, Inc.) was used. The plane wave expansion cutoff energy was set to 400 eV and the surface Brillouin zone was sampled at the Γ point with a k-point spacing of 0.5 \AA^{-1} for all DFT-D2 calculations. The structures of all stationary points were obtained with the conjugate-gradient algorithm. Further details of specific adsorption structure calculations are given in Chapters 3-5.

Chapter 3

Structural and Chemical Evolution of L-Cysteine Nanofilm on Si(111)- $\sqrt{3}\times\sqrt{3}$ -Ag: From Preferential Growth at Step-edges and Antiphase Boundaries at Room Temperature to Adsorbate-mediated Metal Cluster Formation at Elevated Temperature

3.1 Introduction

The study of physical and chemical phenomena occurring at the interface between organic molecules and a solid surface has attracted much interest due to their wide range of applications in optics, electronics, biotechnology and nanoscience. Understanding such interfacial interactions at the molecular level is pivotal to the design and development of emerging devices such as hybrid organic-semiconductor devices, biological and chemical sensors, and catalysts. There have been numerous studies on the interface between an organic adlayer and a metal or semiconductor substrate. Metal surfaces are interesting because they offer a two-dimensional electron gas system to effect weak physical interactions with organic molecules. On the other hand, semiconductor surfaces such as Si(111) 7×7 contain reactive dangling bonds that make possible directional covalent bonding with organic molecules. Semiconductor surfaces are therefore great candidates for organic functionalization in bio or chemical sensing and nanoelectronics applications. Hybrid metal-semiconductor surfaces are another class of solid surfaces that have attracted a lot of recent attention due to the provision of the structural and electronic properties from both metal and semiconductor surfaces and to the potential creation of synergetic properties.

The Si(111)- $\sqrt{3}\times\sqrt{3}$ -Ag surface has been one of the most studied hybrid surfaces by various surface-sensitive techniques. One technical significance of this type of substrates is that an usually well-ordered, two-dimensional, single-atom thick metal overlayer is supported on the Si(111) substrate, making it readily customizable for applications in molecular devices appropriate for large-scale integration and other thin-film fabrication protocols. It has also been historically one of the most important prototypes for the metal/semiconductor interfaces, because of the interesting physics revealed in its atomic arrangements, surface electronic states, and electronic transport phenomena.¹⁴⁶ Silver-passivated silicon surface is obtained by depositing one monolayer of Ag atoms on the Si(111) 7×7 substrate, thereby terminating all the dangling bonds perfectly and making the surface inert. Upon annealing to the appropriate temperature, the surface is composed of ordered Si and Ag trimers in an alternating island (upper terrace) and hole (lower terrace) pair arrangement. The resulting atomic structure of the Si(111)- $\sqrt{3}\times\sqrt{3}$ -Ag surface is best described by honeycomb-chained triangle and inequivalent triangle structures,

which are closely related to each other such that the former is a fully symmetrical version of the latter.^{61-65,147,148} The Ag atoms are arranged on the top layer with a three-fold rotational symmetry and the Ag-Si bonding in the honeycomb-chained triangle configuration has been reported to be heteropolar in character, with considerable charge transfer from the Ag adlayer to the Si substrate.¹⁴⁹ The most abundant surface defects of Si(111)- $\sqrt{3}\times\sqrt{3}$ -Ag include the step edges and antiphase boundaries. A step edge is the transitional interface between the upper terrace and the lower terrace (shown in a schematic model in Figure A1) while an antiphase boundary is the phase boundary between terraces of the same height.

A number of studies have focused on the adsorption of large π -conjugated organic molecules on the Si(111)- $\sqrt{3}\times\sqrt{3}$ -Ag surface for organic thin film applications, which include 3,4,9,10-perylene tetracarboxylic dianhydride (PTCDA),⁷¹ 3,4,9,10-perylene tetracarboxylic diimide (PTCDI),⁷² thiophene,⁷³⁻⁷⁵ metal phthalocyanine,⁷⁶ metal porphyrines,^{77,78} C₆₀,⁷⁹ and pentacene,⁸⁰ as well as of smaller molecules such as trimesic acid,⁸¹ terephthalic acid,⁸² and adenine,⁸³ at both low temperature and room temperature. All of these molecules adsorb in a flat configuration via weak molecular coupling with the surface, as realized by physisorption through the interaction of their π -conjugated rings with the two-dimensional electron gas of the surface. The focus of these physisorption studies has been the nature of self-assembly into molecular structures. To date, there is only one study on chemisorption of organic molecules on Si(111)- $\sqrt{3}\times\sqrt{3}$ -Ag, in which thiol-modified ferrocene molecules are reported to undergo S-H dissociation and chemisorption via S-Ag linkage preferentially on defect sites and occasionally on terrace sites at room temperature.⁸⁴ Chemisorption is arguably a more important alternative mechanism for immobilizing molecules, allowing more robust modification of the electronic properties of Si-based surfaces and development of more stable devices with organic molecules to enable operation at a more desirable temperature such as room temperature.

The objective of the present study is two-fold: (1) to understand the interactions between the Si(111)- $\sqrt{3}\times\sqrt{3}$ -Ag surface and a prototypical amino acid with multiple functional groups, such as cysteine (C _{β} OOHC _{α} HNH₂C _{γ} H₂SH), at room temperature and at elevated temperature, and (2) to investigate any potential synergetic properties of the Si(111)- $\sqrt{3}\times\sqrt{3}$ -Ag surface functionalized with these S-containing amino acid molecules for potential applications. As the building blocks of proteins, amino acids represent one of the most important classes of small organic molecules. They are also of special interest to the engineering of biomimetic materials because their different functional groups (carboxylic acid group, amino group, and thiol group in the case of cysteine) could link to one another and to the surface, making them ideal molecular systems for studying various types (and their combinations) of long-range and short-range interactions. Understanding these important interactions will enable efficient construction and manipulation of their supramolecular architectures on metal surfaces crucial for the performance of

bioanalytical devices and biocompatible materials.^{150–160} Among the twenty naturally occurring amino acids, cysteine is the only “biogenic” amino acid that contains a thiol side chain. Cysteine is known to be a strong ligand for transition metals, making it a potential candidate as a chemical receptor for metal ions. It is also widely used not only for anchoring larger biomolecules to metal nanoparticles in bioanalytical and drug delivery protocols but also for molecular electronics development by taking advantage of its dissociated thiol group (thiolate) to produce strong covalent bonding with noble metals. A variety of ordered structures of cysteine has been obtained on different metal surfaces of Cu,^{130,161,162} Ag,^{103,163–165} and Au,^{102,162,163,166–181} through both physisorption and chemisorption at various temperatures as characterized by scanning tunneling microscopy (STM), X-ray photoelectron spectroscopy (XPS), and quantum mechanical calculations based on the density functional theory (DFT).

Previous experimental and theoretical studies of our group have shown that cysteine adsorbs on Si(111)7×7 in the initial growth stage through dehydrogenation of the thiol and amino groups and formation of both S–Si and N–Si (unidentate and bidentate) covalent bonding. This is followed by lateral and vertical intermolecular hydrogen bonding at the interfacial and transitional layers for low cysteine exposures and by zwitterionic interactions for thicker layers.¹²¹ Here, we report a comprehensive approach to determine the chemical nature of L-cysteine adsorption on the Si(111)-√3×√3-Ag surface and their pertaining implications for surface functionalization. Our combined STM and XPS measurements, complemented by large-scale DFT calculations, reveal a clear bonding picture of interfacial layer formation and film growth of cysteine at and above room temperature. Our XPS data show that cysteine chemisorbs on the surface through S–H bond cleavage and S–Ag anchorage while zwitterionic interactions dominate even at lower coverages. Our STM results depict preferential nucleation of cysteine adspecies near step edges and their growth into disordered coral-reef shaped islands on the terraces of the Si(111)-√3×√3-Ag surface. Our DFT calculations confirm cysteine chemisorption through S–Ag linkage and further determine the most favorable adsorption configurations involving single and multiple molecules on the surface. We also identify the processes occurring at the interface between the molecules and the substrate from the early growth stage to the multilayer regime at room temperature, as well as the structural and chemical evolution of the cysteine on Si(111)-√3×√3-Ag upon annealing to elevated temperatures. Of particular interest is our first observation of adspecies-induced formation of Ag clusters above 175 °C.

The experimental procedure and theoretical details are given in Chapter 2, sections 2.4, 2.5.1.

3.2 Results and Discussion

3.2.1 Thiol dissociative adsorption of cysteine and growth of supported cysteine film at room temperature

In addition to the carboxylic acid and amino groups common in the 20 proteinogenic amino acids, cysteine is one of two sulfur-containing amino acids and it is the only amino acid that contains a thiol group. Cysteine is found in its neutral form in the gas phase, while it exists in its zwitterionic form with a protonated amino group and a deprotonated carboxylic acid group in both aqueous solution and solid state.¹⁸² To analyze the evolution and stability of chemical states of cysteine during nanofilm growth, we conduct XPS measurements on films obtained with low to high cysteine exposures at room temperature and on the as-grown multilayer film at elevated temperatures. Figure 3.1 shows the XPS spectra of the O 1s, N 1s, C 1s, and S 2s regions of cysteine on the Si(111)- $\sqrt{3}\times\sqrt{3}$ -Ag surface as a function of exposure time. It should be noted that since the S 2p peak at 164.0 eV partially overlaps with the broad Si plasmon peak near 168.0 eV, we have chosen the S 2s peak to monitor the change in the S chemical-state composition in the present work. To compare our results of the interface adsorption with the bulk, we use the cysteine multilayer grown on the Si(111)- $\sqrt{3}\times\sqrt{3}$ -Ag surface after the 3600-s exposure, for which the peak positions closely resemble those observed for the cysteine multilayer film on Si(111)7 \times 7 and for the cysteine powder in the solid phase.¹²¹ In the multilayer regime (3600-s exposure in Figure 3.1), we find that the S 2s peak appears predominantly at 228.6 eV, indicating the presence of an intact thiol group. The single O 1s peak at 532.0 eV and the N 1s peak at 402.0 eV correspond to, respectively, the deprotonated carboxylic acid group ($-\text{COO}^-$) and protonated amino group ($-\text{NH}_3^+$) in the zwitterions. The C 1s signal can be fitted with three main components at 286.3 eV, 287.0 eV, and 289.0 eV, corresponding to the alkyl carbon atoms in C-SH and C-NH₃⁺ moieties and to the carboxylate group, respectively.

In the low-exposure regime of 30-120 s, the S 2s spectra show only one peak at 226.6 eV, which is 2.0 eV lower in binding energy than the multilayer thiol peak. This feature is clearly related to the chemisorption of cysteine through the dehydrogenated thiol group. In our previous study on the adsorption of cysteine on Si(111)7 \times 7,¹²¹ we found the S 2s feature of the S-Si bond to be located at 227.4 eV. The lower binding energy by 0.8 eV for the observed S 2s feature therefore indicates S-Ag rather than S-Si linkage.¹⁸³ In the N 1s region, two well-defined peaks are observed at 399.5 eV and 402.0 eV, with the former being less intense than the latter. The N 1s peak at 402.0 eV is consistent with the protonated amino group in the zwitterionic adspecies. The position of deprotonated amino (and N-Si linkage) has been reported to downshift by 3.2 eV with respect to the protonated amino group, while the intact amino group is known to be located at 1.8 eV lower than the position of zwitterionic N 1s

feature.^{121,170} Since the separation between the two N 1s features in our current results is 2.5 eV, the peak at the lower binding energy can be attributed to the intact amino group that is likely closer to the surface to enable its interaction with the surface Ag atoms through its lone-pair electrons. The presence of the deprotonated amino group, however, cannot be ruled out, because given that the NH–Si feature has been observed for the adsorption of cysteine on Si(111)7×7, the presence of the NH–Si linkage on Si-rich defect sites is plausible and should be expected. The interaction of the intact amino group through its lone-pair electrons has also been reported for cysteine adsorption on the Ag(111) surface.¹⁰³ The sharper O 1s feature at 531.7 eV (fwhm = 1.4 eV) agrees well with the deprotonated carboxylic acid group position, while the broader O 1s peak at 532.9 eV (fwhm = 1.9 eV) can be attributed to the carbonyl oxygen and hydroxyl oxygen atoms in the carboxylic acid group. The presence of two well-defined neutral and zwitterionic features in the N 1s and O 1s regions, along with the single thiolate feature in the S 2s region, indicate the presence of two types of cysteine adspecies on the surface at the same time. The neutral adspecies could represent single cysteine molecules bonded to the surface through their dehydrogenated thiol group in an upright configuration or in a nearly flat configuration with the amino and carboxylic acid functional groups leaning towards the surface. The latter configuration is expected to be viable at very low coverages due to the absence of neighboring molecules, where the individually adsorbed molecules have enough space to exert their interactions with the surface through all their available free functional groups. On the other hand, the presence of the zwitterionic species suggests the formation of small clusters (or islands) of two or more cysteine molecules with zwitterionic intermolecular interactions between the protonated amino group and deprotonated carboxylic acid group while chemically bonded to the surface through the dehydrogenated thiol group. The peak maxima and the peak assignments of the fitted peaks for individual components are given in Table A1 and their relative intensities are shown in Figure A2.

Further increasing the exposure time to 180 s leads to the emergence of a second peak in the S 2s region at 228.7 eV corresponding to an intact thiol group. Both the thiol (at 228.7 eV) and thiolate features (at 226.6 eV) further develop with increasing exposure time until the thiol feature becomes dominant at 1200 s. Concurrently, the N 1s and O 1s peaks grow in intensity with the zwitterionic features becoming more prominent. This can be attributed to the growth of the existing chemisorbed cysteine islands and to increased non-dissociative adsorption of cysteine molecules simultaneously, both of which involve zwitterionic intermolecular coupling. Our companion STM study of Si(111)- $\sqrt{3}\times\sqrt{3}$ -Ag before (i.e. pristine surface) and after cysteine exposure (results discussed below) shows that for exposure up to 240 s the coverage of cysteine adspecies appear to be less than one monolayer, where we define one monolayer as a fully covered Si(111)- $\sqrt{3}\times\sqrt{3}$ -Ag surface in the STM image. Physisorption of incoming

cysteine species could occur directly on both the uncovered terraces of the Si(111)- $\sqrt{3}\times\sqrt{3}$ -Ag surface and the existing cysteine islands. Using the adsorbate-induced attenuation of the Si 2p signal and the calculated electron mean free path in a uniformly thick organic film,¹⁸⁴ we estimate the thickness of the organic layer for the 1200-s exposure to be 1.1 nm. The S 2s spectrum for the 1200-s exposure (Figure 3.1d) consists of 42% thiolate species and 58% thiol species. As the thickness of a chemisorbed molecular layer (1 ML) is estimated to be 0.51 nm (discussed further in our DFT study below), the relative intensity of the thiolate S 2s feature therefore indicates an approximate coverage of 0.86 ML of chemisorbed species in the interfacial layer. Since the amount of thiol species in the S 2s region is higher than the chemisorbed ones, the rest of the interfacial layer is composed of adspecies on top of the interfacial layer bound not directly to the surface but to one another through zwitterionic interlayer interactions or weak van der Waals forces. Using the relative intensities of the thiolate feature in the other S 2s spectra (Figure A2) and the calculated thicknesses of their films, we estimate the cysteine layer coverage for each exposure time. Accordingly, the weakly bound species (with the thiol feature) start to appear at the 180-s exposure where the coverage is estimated to consist of 0.36 ML of chemisorbed species adsorbed directly on the surface and 0.16 ML of weakly bound species on the top side of the interface layer. Similarly, the coverage of the chemisorbed species for the 240-s exposure is calculated to be 0.47 ML while that for the weakly bound species both on the top side of the interfacial layer and in the second adlayer is estimated to be 0.29 ML.

Interestingly, while the intensity change of the N 1s feature attributed to the amino group (at 399.5 eV) generally follows an increasing trend with increasing exposure time, it is less discernible than the trend observed for the S 2s features (Figure A2). The minor fluctuation in the intensity change with increasing exposure supports our hypothesis that this feature is connected to preferential adsorption on surface defect and other non-terrace sites. As a freshly Si(111)- $\sqrt{3}\times\sqrt{3}$ -Ag surface is prepared for each cysteine exposure, each preparation could lead to a slightly different amount of surface defects and a different extent of terrace sizes. The lack of a well-defined trend with increasing exposure found for this N 1s feature for the amino group therefore supports adsorption on defect and non-terrace sites. At the 1200-s exposure, since the estimated thickness of the molecular adlayer (1.1 nm) remains less than the photoelectron escape depth (~9.00 nm), the S 2s features in the interfacial layer remain easily detectable. However, the $-\text{NH}_2$ feature related to the interfacial layer is not present anymore, suggesting that the $-\text{NH}_2$ moieties that are not involved in the zwitterionic interactions have most likely been protonated with additional H atoms originating from the breakage of the S-H bonds. The increase in the O 1s intensity for the carboxyl component ($-\text{COOH}$) up to the 1200-s exposure can also be explained in a similar way.¹⁰³ At lower coverages, on the other hand, the presence of the $-\text{COOH}$ component is related to either the

isolated cysteine molecules adsorbed on surface defects or the free $-\text{COOH}$ groups at the outer region of the cysteine islands.

The corresponding C 1s spectra for the 30-120 s exposures consist of two broad bands, with three peaks at lower binding energies of 285.3 eV, 286.1 eV and 286.7 eV, and two peaks at higher binding energies of 288.4 eV and 289.3 eV, which can be attributed to $-\text{CH}_2-\text{S}-\text{Ag}$, $-\text{CH}_2-\text{NH}_2$, and $-\text{CH}_2-\text{NH}_3^+$ and to $-\text{COO}^-$ and COOH moieties, respectively.¹⁰³ For higher exposures of 180-1200 s, a new peak at 286.3 eV corresponding to the $-\text{CH}_2-\text{SH}$ moiety (with an intact thiol group) in the zwitterionic layer^{103,121} is observed. The growth of this feature appears to overtake the intensity of the nearby $-\text{CH}_2-\text{NH}_2$ feature (at 286.1 eV). At the 3600-s exposure, the S 2s feature of the $-\text{CH}_2-\text{SH}$ component at 228.3 eV, along with the C 1s features for the $-\text{CH}_2-\text{NH}_3^+$ component at 287.0 eV and the $-\text{COO}^-$ component at 289.0 eV, have become the predominant features, consistent with the emergence of a zwitterionic film.

3.2.2 Silver nanocluster formation at elevated temperature

Our observation of the zwitterionic intermolecular interactions in the cysteine multilayer film on $\text{Si}(111)-\sqrt{3}\times\sqrt{3}-\text{Ag}$ is consistent with the adsorption of a cysteine zwitterionic film found on other noble metal single-crystal surfaces, including $\text{Ag}(111)$, $\text{Au}(111)$, $\text{Au}(110)$, and $\text{Cu}(110)$, at submonolayer and monolayer coverages.^{170,185-187} To further understand the nature of the interactions of cysteine with the $\text{Si}(111)-\sqrt{3}\times\sqrt{3}-\text{Ag}$ surface and to investigate the stability of the supported cysteine multilayer film, thermal treatment is performed on a supported multilayer film obtained with a 3600-s cysteine exposure (Figure 3.1). The top three spectra shown in Figure 3.1 correspond to the spectral evolution of the as-grown cysteine film obtained with a 3600-s exposure upon sequential annealing to 85 °C, 175 °C, and 285 °C for 600 s each (followed by cool-down back to room temperature before the XPS measurement). Annealing at 85 °C appears to cause discernible intensity reduction for the zwitterionic features and reappearance of the minor $-\text{COOH}$ O 1s and $-\text{NH}_2$ N 1s features, which could be due to partial desorption of the film thereby exposing free amino and carboxylic acid groups. The peak positions and widths of the predominant features remain unchanged with respect to the as-deposited multilayer zwitterionic film. Further annealing to 175 °C has led to desorption of ~80% of the original film, as shown by the significant intensity reduction found in the thiol S 2s feature. Furthermore, the thiolate S 2s feature of the interfacial layer has re-emerged at 226.6 eV (Figure 3.1d).

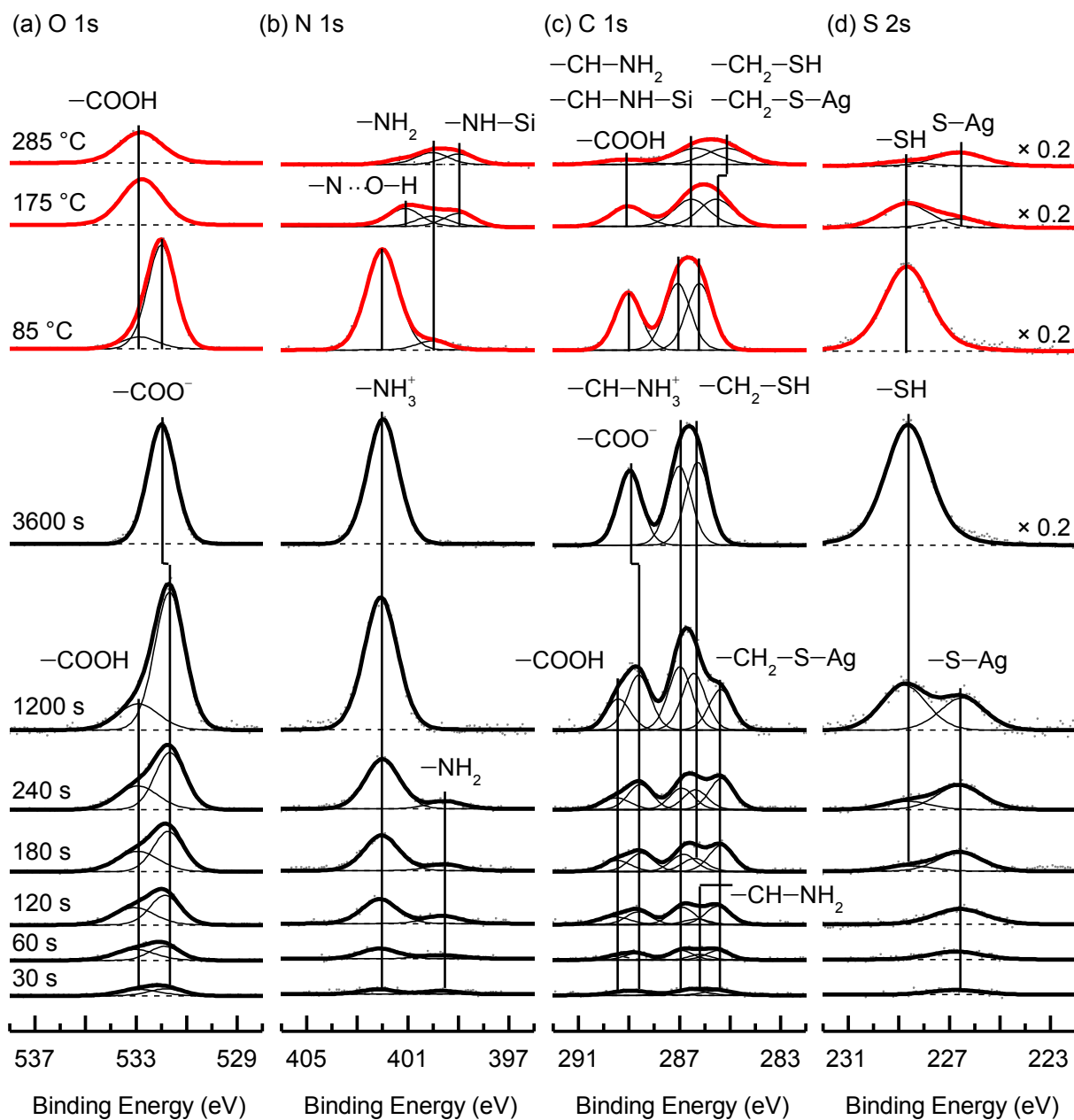


Figure 3.1 Evolution of O 1s, N 1s, C 1s, and S 2s XPS spectra of cysteine deposited on Si(111)- $\sqrt{3}\times\sqrt{3}$ -Ag as a function of exposure time (30–3600 s) and of the as-grown cysteine multilayer film (obtained with a 3600-s exposure) upon annealing to 85, 175, and 285 °C.

The O 1s spectrum shows a single broader feature at 532.5 eV, which corresponds to the carboxylic acid group. On the other hand, the N 1s spectrum can be fitted with three new features at 399.1 eV, 400.1 eV, and 401.1 eV, which can be assigned to $-\text{NH}-\text{Si}$, $-\text{NH}_2$, and $\text{N}\cdots\text{O}-\text{H}$ (or $\text{N}\cdots\text{S}-\text{H}$) moieties, respectively.¹²¹ The C 1s spectrum is found to consist of two broad bands. The lower-binding-energy band can be fitted with two components corresponding to S-containing moieties such as $-\text{CH}_2-\text{S}-\text{Ag}$ and $-\text{CH}_2-\text{SH}$ (at 285.5 eV) and to N-containing moieties such as $-\text{C}-\text{NH}-\text{Si}$ and $-\text{C}-\text{NH}_2$ (at 286.5 eV), while the higher-binding-energy band at 289.0 eV corresponds to the $-\text{COOH}$ feature.

In the study of cysteine adsorption on $\text{Si}(111)7\times 7$, we conclude that the cysteine zwitterionic structure could exist up to 85 °C, while the transitional layer (second adlayer) consisting of interlayer hydrogen bonds are stable even after annealing to 175 °C.^{121,123} In the present work, no transitional layer is observed and physisorption is found to occur at the second adlayer on the as-formed chemisorbed layer. However, after annealing, the chemical composition of the cysteine film on $\text{Si}(111)-\sqrt{3}\times\sqrt{3}-\text{Ag}$ appears to resemble that of cysteine on $\text{Si}(111)7\times 7$, which suggests the presence of a transitional layer on the interfacial layer. We propose the following mechanism for the formation of the transitional layer. Upon annealing the cysteine film on $\text{Si}(111)-\sqrt{3}\times\sqrt{3}-\text{Ag}$, the interfacial layer undergoes a structural and chemical change during annealing and desorption of the thick zwitterionic film, which results in disruption of the zwitterionic intermolecular interactions (in the first adlayer). Through their free amino and carboxylic acid groups, the cysteine molecules in the disrupted interfacial layer could interact vertically with the second layer leading to the formation of interlayer H-bonds. This in effect results in the formation of the transitional layer between the newly formed H-bonded layer and the zwitterionic layer on top. This process may also propagate to the third or higher adlayer, depending on the original thickness of the zwitterionic film and the heating and desorption rates of the film. Our proposed mechanism is supported by the presence of both $-\text{COOH}$ and $-\text{NH}_2$ features and the corresponding $-\text{COO}^-$ and $-\text{NH}_3^+$ (H-bond related) features in the O 1s and N 1s regions. Formation of H-bonded groups has also been observed in the transitional layer of a cysteine film on $\text{Si}(111)7\times 7$.¹²³

Upon annealing to 285 °C, the $-\text{COOH}$ C 1s feature (at 289.0 eV) has been reduced in intensity discernibly more than the N- and S-related C 1s peaks, indicating the decomposition of the cysteine film. However, the positions of the $-\text{NH}-\text{Si}$ (Figure 3.1b) and $-\text{S}-\text{Ag}$ peaks (Figure 3.1d) remain unchanged, suggesting the presence of intact chemisorbed (thiolated) cysteine or its decomposition fragments. This is consistent with the decomposition of cysteine powder over the temperature range of 185-280 °C.¹⁸⁸ The presence of atomic S (and S-containing fragments) has also been reported for thermal evolution of thiophene adsorbed on $\text{Si}(100)$ and $\text{Pt}(111)$ and for cysteine adsorption on $\text{Si}(111)7\times 7$ upon annealing at 285 °C.^{121,189,190}

To investigate the influence of cysteine adsorption and thermal treatment on the $\sqrt{3}\times\sqrt{3}$ -Ag overlayer itself, we show in Figure 3.2 the corresponding XPS spectra of the Ag 3d region for the Si(111)- $\sqrt{3}\times\sqrt{3}$ -Ag surface before and after the exposure of cysteine for 1200 s and 3600 s and upon annealing of the as-grown 3600-s cysteine multilayer film on the surface. The pristine Si(111)- $\sqrt{3}\times\sqrt{3}$ -Ag surface exhibits a sharp Ag 3d_{5/2} (Ag 3d_{3/2}) feature at 369.0 eV (375.0 eV, fwhm = 0.85 eV), which corresponds to the Si–Ag bonds in the Ag trimers of the $\sqrt{3}\times\sqrt{3}$ surface template. Cysteine exposure for 1200 s results in the broadening of the overall Ag 3d band, which can be fitted with two Ag 3d_{5/2} (Ag 3d_{3/2}) peaks with the same widths at 369.0 eV (375.0 eV) and 368.5 eV (374.5 eV). The additional peak at the lower binding energy can be attributed to the Ag–S component, in agreement with the corresponding S 2s chemical state of chemisorbed species (Figure 3.1d).^{191,192} Not surprisingly, cysteine exposure for 3600 s leads to a general reduction of the Ag 3d intensity due to the attenuation of the Ag 3d photoelectrons through a thicker cysteine multilayer film on the surface. After annealing at 85 °C, there appears to be no discernible change in the Ag 3d peak widths, while the Ag 3d_{5/2} (Ag 3d_{3/2}) peak at 368.5 eV (374.5 eV) shifts slightly to a lower binding energy of 368.4 eV (374.4 eV). The corresponding intensities for both Si–Ag and Ag–S features, however, increase due to partial desorption of the thick cysteine film. As desorption of the cysteine film continues upon further annealing to 175 °C and to 285 °C, the Si–Ag feature appears to reduce in intensity while the Ag 3d_{5/2} lower-binding-energy feature has further relocated to a slightly lower binding energy of 368.3 eV, which corresponds to the well-known metallic Ag–Ag (in the bulk).¹⁹³

In a separate control experiment, we perform the same annealing procedure on a pristine Si(111)- $\sqrt{3}\times\sqrt{3}$ -Ag surface (i.e. without any cysteine exposure). Evidently, the Ag 3d peak positions and areas of the single Ag–Si feature for Ag trimers of the pristine surface remain unchanged after each annealing step. There is no additional Ag–Ag feature emerged at a lower binding energy for this pristine Si(111)- $\sqrt{3}\times\sqrt{3}$ -Ag sample. These XPS results lead us to hypothesize the following model to account for the changes occurring to the cysteine multilayer film on the Si(111)- $\sqrt{3}\times\sqrt{3}$ -Ag surface upon thermal evolution. In particular, chemisorption of cysteine on the Si(111)- $\sqrt{3}\times\sqrt{3}$ -Ag surface creates Ag–S bonds involving a fraction of the Ag atoms on the surface. The formation of Ag–S bonds results in weakening of the Ag–Si bonds underneath and near the adsorption areas, potentially producing tension and strain. Annealing provides sufficient energy to overcome the activation barrier to further weaken and displace the Ag–Si bonds, creating interface defects. Meanwhile, reorganization of the cysteine molecules results in agglomeration of the displaced Ag atoms, leading to the formation of Ag clusters (or islands) with metallic Ag–Ag bonds.

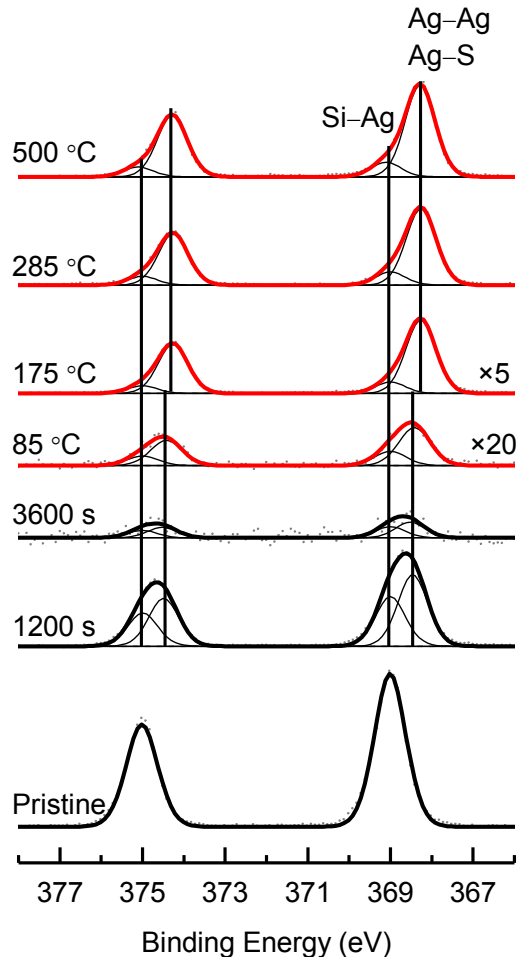


Figure 3.2 XPS spectra of the Ag 3d region for a pristine Si(111)- $\sqrt{3}\times\sqrt{3}$ -Ag surface before and after cysteine exposure for 1200 s and 3600 s, and for the resulting as-grown (3600 s) multilayer film upon annealing to 85 °C, 175 °C, 285 °C and 500 °C.

The formation of Ag clusters could account for the observed shift to a lower binding energy from the Ag 3d binding energy position of the Ag-S feature to that of the Ag-Ag feature upon annealing to 175 °C and 285 °C in Figure 3.2. Assuming no desorption and decomposition occurs at the interfacial layer (at 175 °C), the newly formed Ag clusters can be functionalized (either on top or around their perimeters) with the surrounding cysteine molecules of the interfacial layer. The disruption of the Si(111)- $\sqrt{3}\times\sqrt{3}$ -Ag surface has also been observed for the adsorption of H atoms on the Si(111)- $\sqrt{3}\times\sqrt{3}$ -Ag surface, in which the formation of Ag(111) agglomerates induced by the adsorption of H atoms at room temperature has also been reported.¹⁹⁴ It was claimed that the process of $\sqrt{3}\times\sqrt{3}$ -Ag to Ag metallic cluster formation could be reversed after (recombinative) desorption of H atoms at 500 °C. In our experiment, increasing the

annealing temperature to 500 °C shows no change in the Ag 3d spectra in Figure 3.2, which suggests that the H atoms resulted from dehydrogenation of cysteine are not the only cause of induced cluster formation. The passivation of S or S-containing fragments enables the Ag clusters to remain stable to 500 °C. This is a significant result because thermal annealing of cysteine film on the $\sqrt{3}\times\sqrt{3}$ -Ag overlayer provides a viable, non-reversible pathway of producing stable Ag nanoclusters. Further details of the surface morphology after annealing are discussed below.

3.2.3 Preferential early-stage growth of cysteine at step edges and antiphase boundaries on Si(111)- $\sqrt{3}\times\sqrt{3}$ -Ag

STM measurements have also been performed to investigate changes in the morphology of the Si(111)- $\sqrt{3}\times\sqrt{3}$ -Ag surface upon low cysteine exposures, focussing on notable adsorption features particularly near step edges and antiphase boundaries in the early growth stage. Figure 3.3a1 shows the empty-state STM images of a pristine Si(111)- $\sqrt{3}\times\sqrt{3}$ -Ag surface (i.e. before any cysteine exposure). The brighter and darker areas correspond to the upper-step and lower-step terraces, respectively, that are typically found on the Si(111)- $\sqrt{3}\times\sqrt{3}$ -Ag surface.^{56,57} In addition to these terraces, discernible step edges (between the upper-step and lower-step terraces), antiphase boundaries (on the same terrace), and adatom and vacancy defects are also observed (Figures 3.3a1 and 3.3a2).⁵⁵ The high-resolution STM image of the surface shown in Figure 3.3a3 illustrates the expected honeycomb structure of the $\sqrt{3}\times\sqrt{3}$ surface reconstruction of Ag on Si(111). The Si(111)- $\sqrt{3}\times\sqrt{3}$ -Ag surface structure has an oblique unit cell with side-length $a = b = 0.7$ nm. Each unit cell contains three Ag atoms and three underlying Si atoms (appropriately arranged as illustrated in Area A2, Figure 3.3a3). The step edge appears in the [1-21] and [110] directions and the height of the step (or the rise) is 0.31 nm.^{61,195} The step edges could appear either curved or straight with sharp angles depending on the surface preparation procedure.⁶⁰ The antiphase boundaries appear as straight bright lines in the STM image (Figure 3a1). The width of a typical antiphase boundary is 0.75 nm.¹⁹⁶

After cysteine exposure for 30 s, the most significant changes can be found at the defect sites, which appear to be energetically the most favorable adsorption sites. As shown in Figure 3.3b1, the antiphase boundaries for the unoccupied surface states that usually appear brighter than their surrounding terrace sites have now become darker, indicating the changes in their electronic distribution upon cysteine adsorption. In addition, bright protrusions, attributed to cysteine adspecies, are found at step edges and antiphase boundaries. The adspecies are observed mostly at the lower-step edges rather than the upper-step ones, indicating the higher reactivity of the lower-step edges and the absence of Ehrlich-Schwoebel barrier at the upper-step edges. All of the areas in the immediate proximity of the lower-step edges are

consistently populated with adspecies with a nearly uniform width, suggesting continuous diffusion and adsorption, and consequently leading to nearly the same growth rates in all directions. In the magnified Area A3 (Figure 3.3b2), the majority of the adsorbates at the lower-step edge appear as clusters, while Area A6 on the lower-step terrace (and other upper-step terrace, Figure 3.3b2) appears to contain isolated bright protrusions and isolated dark depressions (Figure 3.3b6). The majority of the clusters in Area A4 appear to aggregate into a ring with a depression at the center (Figure 3.3b3). According to the height profile along Line L1 (Figure 3.3b4), the size of its constituent moieties is consistent with the size of those measured on the isolated single bright protrusions in Area A6 and elsewhere (Figures 3.3b2 and 3b6). These isolated single bright protrusions may therefore be considered as the building blocks of the ring-like clusters, and the apparent depression in the center (Figure 3.3b3) could indicate the gap between the adsorbates. Similar to the lower-step edges, antiphase boundaries also appear to be more favourable to adsorption than the upper-step edges and bare terraces. Similar behaviour of cluster formation is observed at the edges of the antiphase boundaries in Area A5 (Figures 3.3b2 and 3.3b5). The chain-like structure of the antiphase boundaries appears to be affected by the adsorbates as manifested through reduction of their apparent height. A closer look at the terrace sites in Area A6 (Figures 3.3b2 and 3.3b6) reveals the presence of individual dark depressions that are similar in size to those of individual bright protrusions. These dark depressions can also be found near the perimeters of the adsorbate islands at the step edges and antiphase boundaries. As in an earlier report on the chemisorption of ferrocene on Si(111)- $\sqrt{3}\times\sqrt{3}$ -Ag, both the presence of individual dark depressions on the terrace sites and a lower apparent height at the antiphase boundaries could be attributed to chemisorption of the adspecies.⁸⁴

Not surprisingly, the bright protrusions corresponding to the cysteine adspecies increase in population and become more extended in size with increasing cysteine exposure from 30 s (Figure 3.3b1) to 120 s (Figure 3.3c1) and 240 s exposures (Figure 3.3d1). Evidently, the adsorbate islands become larger both in area and in apparent height, and they appear grainier and more porous in texture with increasing exposure time. The most prominent feature of the adsorbate islands appearing at these intermediate coverages is the spreading of the networks of protrusions interconnecting to one another forming a porous structure that resembles the coral reef. The grainy protrusion appearance of the adsorbate islands leads to pores that could potentially include both the gaps in the ring-like clusters and the chemisorption-induced dark depression areas (Figures 3.3c2 and 3d2). In Area A7 (Figures 3.3c1 and 3c2), the entire region along the lower-step edge is covered with adspecies, while only a few small islands are found at the upper-step edge. The height profile along Line L2 over a chain of dark depressions on the adsorbate island near the lower-step edge (Figure 3.3c3) illustrates the typical roughness of the adsorbate island. Interestingly, there appears to be some approximate regularity in the spacing between the pores,

which suggests possible short-range ordering in the adsorption induced by the step edge. The widths of the islands near the step edges increase by nearly the same extent on both the lower-step terraces and upper-step terraces after the 240-s exposure (Figure 3.3d1). As the lower-step terraces occupy smaller footprints of the overall surface (depending on the sample preparation), these terraces are completely occupied by the adspecies first before the upper-step terraces (Figure 3.3d1).

As the island growth extends deeper into a terrace region and away from the nearby step-edge or antiphase boundary region, a lower density of dark depressions and an apparently much smoother appearance for the areas (marked with dotted circles in both Area A7 in Figure 3.3c2 and Area A9 in Figure 3.3d2) are found, confirming that a higher number of adsorbate-induced pores are formed largely on the terrace regions near the step edges. This in turn suggests that the nature and morphology of the step-edge sites play an important role in imprinting structural relations in the adsorption pattern of these adspecies near the step edges. Indeed, the pore sizes of the ring-like clusters in Area A4 (Figure 3.3b3) and in Area A10 (Figures 3.3d2 and 3.3d3) are found to be quite similar, as shown in their respective height profiles along Lines L1 (Figure 3.3b4) and L4 (Figure 3.3d4). This suggests similar nature of these ring-like clusters, with their formation likely induced by adsorption near the step edges and their growth in population with increasing exposure. This in turn supports the notion of the presence of a structural relation near the step edges. On the other hand, this structural relation becomes weaker and is lost for adspecies located farther and farther away from the step edges. For the smoother island far away from the step edges in Area A8 (Figures 3.3c1 and 3.3c4), the height profile along Line L3 (Figure 3.3c5) shows mainly two different apparent heights of adsorbates suggesting the presence of a second adlayer in this area similar to the areas near the step edges.

Nucleation and growth of cysteine islands do not appear to initiate on the generally defect-free terraces, which could be caused by the large diffusivity of the cysteine molecules at room temperature (due in part to the high activation barrier for dehydrogenation of the thiol group) and to the relatively small size of the terraces when compared to the large transport length of surface diffusion on the Si(111)- $\sqrt{3}\times\sqrt{3}$ -Ag surface.^{84,197} The initial adsorption at non-terrace sites indicates that defect sites are energetically more favourable to activate dehydrogenation of the thiol group. In Figure 3.4, we show a schematic model of the adsorption mechanism for cysteine on the Si(111)- $\sqrt{3}\times\sqrt{3}$ -Ag surface, which we consider to involve four main structural components: lower-step terrace, upper-step terrace, step edge and antiphase boundary (as illustrated in Figure 3.4a).

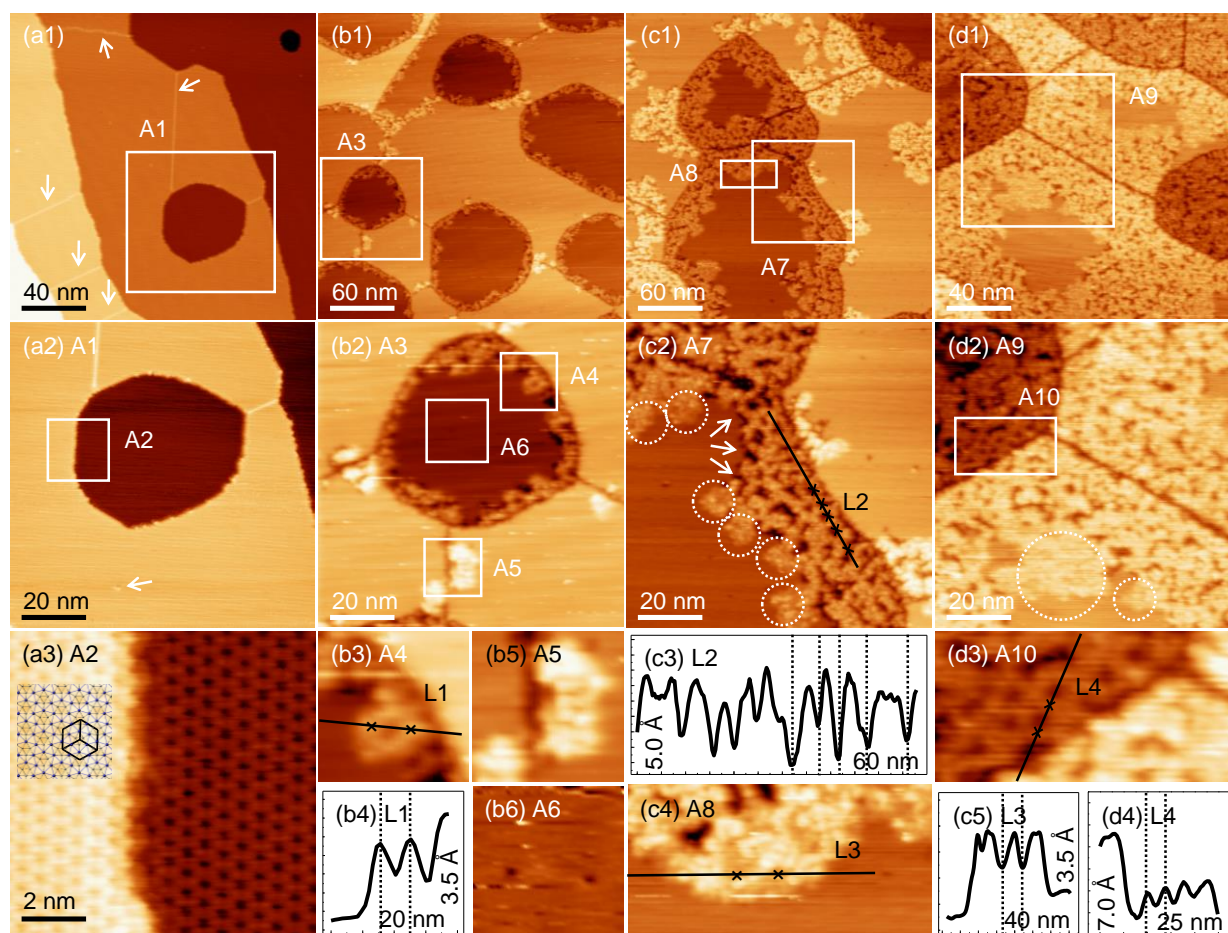


Figure 3.3 Empty-state STM images obtained with a sample bias of +2 V and a constant tunneling current of 0.2 nA for a pristine Si(111)- $\sqrt{3}\times\sqrt{3}$ -Ag surface (a1-a3) before and after cysteine exposure for (b1-b6) 30 s, (c1-c5) 120 s, and (d1-d4) 240 s. The apparent height profiles along the respective lines are shown in b4, c3, c5 and d4, where the full height and length ranges are given in units of Å and nm, respectively. The arrows in (a1) and (a2) mark examples of antiphase boundaries and adatom defects, respectively. The schematic model of the Ag-Si trimers hexagonal mesh along with three $\sqrt{3}\times\sqrt{3}$ -Ag unit cells are overlaid on the image in (a3), with the Ag and Si atoms represented by blue and grey dots, respectively.

For the step edge, we could consider adsorption on the lower-step edge, upper-step edge and the slope surface [where the slope corresponds to the rise (vertical displacement) over the run (horizontal displacement)]. Upon arriving on the terraces (both lower-step and upper-step terraces), the cysteine molecules are free to diffuse on the terrace sites until they arrive at the step edges or antiphase boundaries (Figure 3.4a). We obtain more direct evidence of this surface diffusion in a series of time-sequence STM images in Figure A3, which shows the addition of bright protrusions to the edges of the adspecies islands at room temperature over the collection time of a set of STM images collected one after another. Cysteine molecules undergo dissociative adsorption with S–H bond cleavage and S–Ag bond formation, and the resulting dehydrogenated adspecies (thiolated cysteine) become trapped at these defect sites (Figure 3.4b). Anchoring to the surface through their thiolate groups, the dehydrogenated cysteine adspecies with their free amino and carboxylic acid groups provide new linkage points for further attachment of other molecules through zwitterionic interactions and thus propagate growth of the adspecies islands both laterally and vertically (Figure 3.4c). Our XPS results show that loosely bound species start to appear at the submonolayer coverage, which we attribute to the onset of second-layer adsorption while the interfacial layer chemisorption is still developing. The emergence of second-layer adspecies is corroborated by our STM measurement. Among all the defect sites, the lower-step edges provide the most reactive sites for adsorption, followed by the antiphase boundary sites and then the upper-step edges. Figure 3.4d shows a schematic model of the as-grown cysteine thick film surface after annealing. STM images of the surface morphology obtained after annealing will be shown in the following section.

The high mobility of the molecular building blocks is a prerequisite for the formation of self-assembled nanostructures on the terraces of solid surfaces. On the other hand, the reactivity of the molecule (arising from different functional groups) and its size relative to the separations of various available adsorption sites play an important role in the competition between molecule-molecule and molecule-substrate directional interactions for constructing the supramolecular architectures.¹⁹⁸ On the semi-metallic Si(111)- $\sqrt{3}\times\sqrt{3}$ -Ag surface, no ordered nanostructure is seen in the interfacial layer (from our STM images). However, the imprinting of the Si(111)- $\sqrt{3}\times\sqrt{3}$ -Ag surface template is observed in areas near the step edges as irregular ring-like clusters that contribute to the porous (coral reef like) morphology at higher coverages. To understand the adsorption of the cysteine molecules in more detail, we perform DFT calculations to determine its adsorption configurations on the terrace sites of the Si(111)- $\sqrt{3}\times\sqrt{3}$ -Ag surface. More detailed calculations about the adsorption on the defect sites on step-edges and antiphase boundaries of the surface will be given elsewhere.

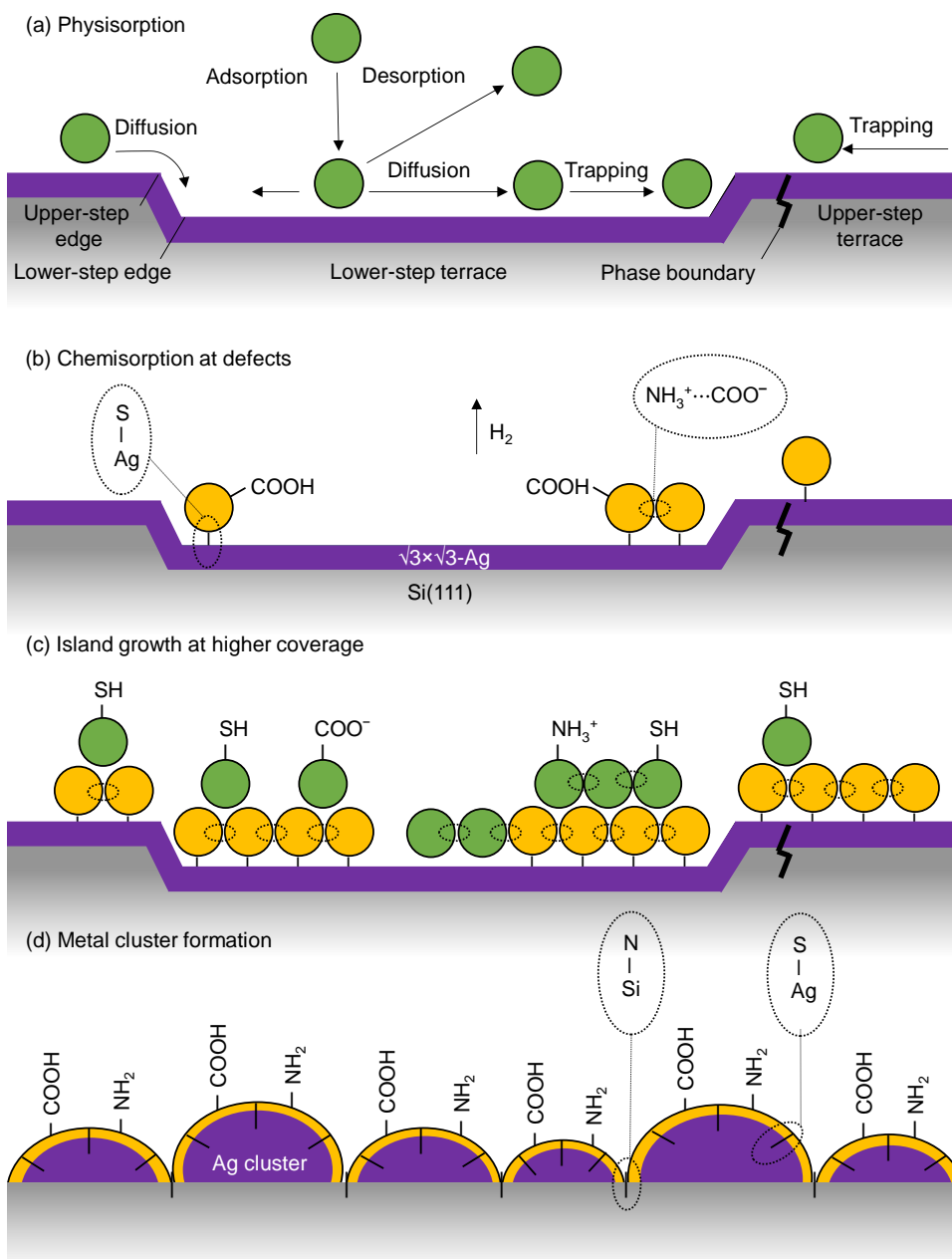


Figure 3.4 A schematic illustration (a-c) of the adsorption and growth of the cysteine adspecies on the Si(111)- $\sqrt{3}\times\sqrt{3}$ -Ag surface at room temperature and (d) of metal cluster formation after annealing. Green and yellow balls depict cysteine molecule and thiolated cysteine respectively. The purple layer is the $\sqrt{3}\times\sqrt{3}$ -Ag overlayer which converts to metallic clusters in (d).

3.2.4 Formation of silver nanocluster arrays by post-annealing

Our XPS results show that annealing the Si(111)- $\sqrt{3}\times\sqrt{3}$ -Ag surface pre-exposed with cysteine at elevated temperatures leads to emergence of the Ag metallic state, indicating significant changes in the electronic structure of the $\sqrt{3}\times\sqrt{3}$ -Ag surface template. To confirm our Ag 3d XPS results (Figure 3.2), we collect the STM images after annealing the as-grown cysteine films with submonolayer and multilayer coverages supported on the $\sqrt{3}\times\sqrt{3}$ -Ag surface. Figure 3.5a1 shows the morphology of the surface with a 240-s cysteine exposure (a submonolayer coverage) upon annealing at 175 °C. The porous coral-reef-like nanostructures of the cysteine adsorbate islands initially observed before annealing (Figure 3.3d1) is no longer present after annealing. Instead, the surface is partly covered with larger bright protrusions with an apparent diameter of 3.2-10.5 nm, as illustrated in the height profile along Line L1 in Figure 3.5a2. Since the adspecies coverage is less than one monolayer initially, some parts of the pristine $\sqrt{3}\times\sqrt{3}$ surface are not covered by adspecies and are therefore exposed. These areas remain intact after annealing as evidenced by the appearance of smooth terraces (marked by $\sqrt{3}\times\sqrt{3}$) and typical antiphase boundaries (marked by arrows) in Figure 3.5a1. Selected magnified areas of Figure 3.5a1 showing the smooth $\sqrt{3}\times\sqrt{3}$ surface terrace, the step edge and the antiphase boundary are illustrated in Figure A4. This therefore indicates that only the areas covered by the cysteine adsorbate islands are affected by annealing at an elevated temperature. The clusters (bright protrusions) appear to have agglomerated to form larger clusters or islands. The appearance of these new STM features, i.e. clusters and islands, are corroborated with the emergence of the metallic Ag 3d_{5/2} peak at 368.3 eV after annealing at 175 °C (Figure 3.2), which can therefore be used to validate the metallic nature of these clusters. Annealing the Si(111)- $\sqrt{3}\times\sqrt{3}$ -Ag surface covered with a multilayer of cysteine (with a 3600-s exposure) at a higher temperature of 285 °C results in a much denser layer of bright protrusions without any part of the smooth $\sqrt{3}\times\sqrt{3}$ -Ag surface visible, which is consistent with the surface fully covered by cysteine before the annealing (Figure 3.5b1). Evidently, these bright protrusions exhibit a narrow size distribution, with the larger clusters formed by agglomeration of the smaller clusters. The majority of the clusters appear to exhibit an apparent size of 10.5-15.3 nm, as illustrated by the height profile along Line L2 in Figure 3.5b2. In order to compare our STM results with those reported for cluster formation induced by hydrogen adsorption,^{199–201} we increase the annealing temperature to 500 °C and the result is shown in Figure 3.5c1. Evidently, the metal clusters persist and do not disappear after annealing at 500 °C. It should be noted that 500 °C corresponds to the nominal annealing temperature required to produce the $\sqrt{3}\times\sqrt{3}$ Ag overlayer from an as-deposited monolayer of Ag on Si(111). In marked contrast to adsorbed H induced clusters reported earlier,^{199–201} the smooth $\sqrt{3}\times\sqrt{3}$ structure cannot be restored by annealing and the present cluster formation is therefore robust and not reversible. This indicates the encapsulation of the Ag metallic

clusters and the local passivation of the underlying Si layer by S (from the dehydrogenated thiol group) and N (from the dehydrogenated amino group) consistent with our XPS results. This further suggests that the supported metal clusters resulted from cysteine adsorption and the subsequent annealing process are stable even at higher temperature.

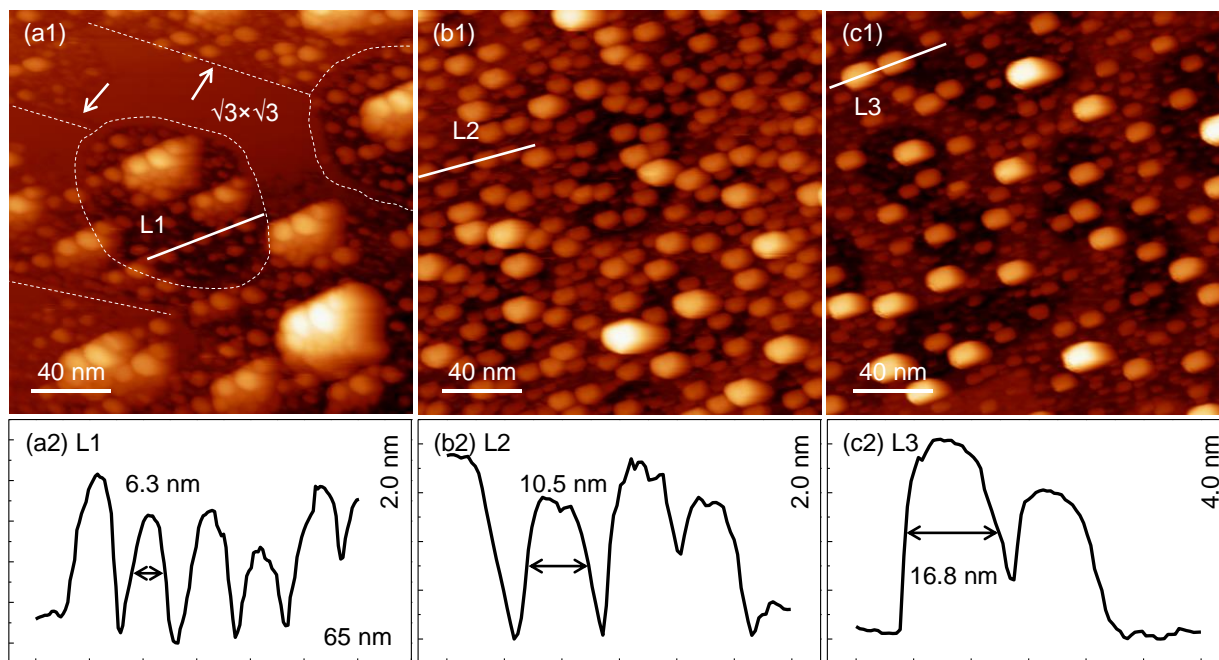


Figure 3.5 Empty-state STM images obtained with a sample bias of +2 V and a constant tunneling current of 0.2 nA for Ag nanocluster arrays obtained by post-annealing a Si(111)- $\sqrt{3}\times\sqrt{3}$ -Ag surface with cysteine exposures of (a1) 240-s and (b1, c1) 3600-s at (a1) 175 °C, (b1) 285 °C and (c1) 500 °C, respectively. The apparent height profiles along the respective Lines L1, L2 and L3 are shown in (a2), (b2) and (c2), respectively. The x-axis line range for all the height profiles is 65 nm

The clusters also appear to organize with short-range alignment in a preferred direction as shown in Figure 3.5a1 to 3.5c1. This limited directionality is likely guided by both the imprinting effect of the underlying Si surface and the presence of cysteine adspecies (molecules or decomposition fragments) in between or at the perimeters of the clusters. The alignment of Ag clusters along the crystallographic directions of the Si(111) surface has also been reported for adsorption of Ag on H-terminated Si(111) surface.²⁰² As the metal clusters are functionalized (at their perimeters) by cysteine adspecies, the interactions among these adspecies could enable semi-ordering among the clusters along certain preferred directions. The use of cysteine to generate aligned nanocluster arrays on Si(111) promises a new approach to synthesize nanocatalysts and/or nanocluster templates.

3.2.5 Large-scale DFT calculations of cysteine adsorption on model Si(111)- $\sqrt{3}\times\sqrt{3}$ -Ag surface

Cysteine exists as a free molecule in numerous stable structures in the gas phase. Of the 324 possible conformers calculated for both L- and D-cysteine, 42 are considered the most stable due to the presence of different types of internal hydrogen bonding among its functional groups.²⁰³ Through interaction with different surface atoms of the substrate (at different surface sites), some of these cysteine conformers may become more favorable for direct adsorption while others may undergo rearrangement upon adsorption on the $\sqrt{3}\times\sqrt{3}$ -Ag surface. A variety of adsorption structures/configurations at the substrate sites could provide local energy minima and are therefore energetically plausible. Given the inherent complexity of the system at hand and the lack of information about preferred orientations of the functional groups with respect to a specific surface site, we begin our calculations by first selecting three energetically most stable L-cysteine conformers. Figure 3.6a shows the equilibrium structures for three isolated L cysteine conformers, with conformer AH being 0.06 eV and 0.13 eV more stable than conformers BH and CH, respectively. In accord with our XPS results that show the adsorption being dominated by bonding to the surface through the dissociated thiol group, we therefore only consider anchoring the S end to the surface in our adsorption configuration calculations. After removing the H from the thiol group, we orient the three gas-phase thiolated conformers with their respective S–C axis perpendicular to the $\sqrt{3}\times\sqrt{3}$ -Ag surface to obtain three initial adsorption structures with the carboxylic acid group pointing upward (Conformer A), parallel (Conformer B) and downward (Conformer C) with respect to the surface plane, as shown in Figure 3.6b. To qualitatively identify the more stable surface adsorption sites, we place a single thiolated cysteine conformer at a selected adsorption site through its thiolate group. A near-optimized adsorption configuration is then obtained by relaxing just the separation between the adspecies and the site in the z direction while keeping the adspecies and the slab frozen at their separately optimized equilibrium structures.

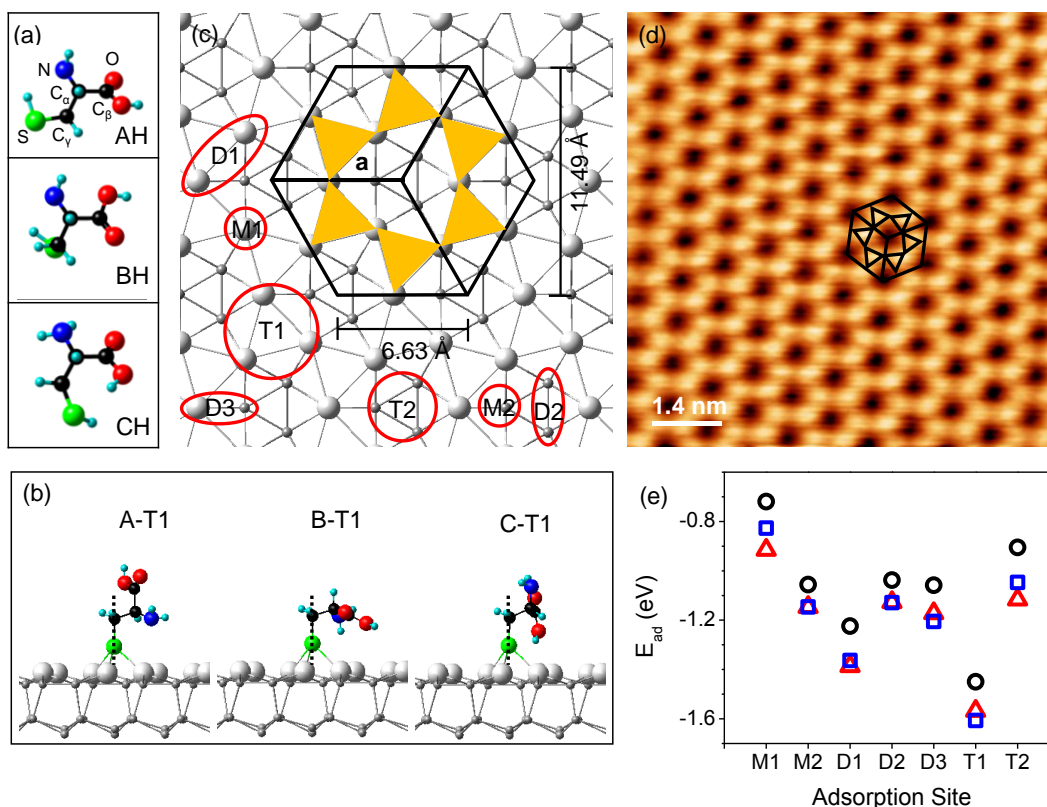


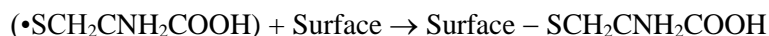
Figure 3.6 (a) Optimized equilibrium structures of three conformers (AH, BH, and CH) of isolated L-cysteine in the gas phase, (b) side view of the adsorption configurations of three dehydrogenated cysteine conformers A, B, and C on the T1 site with the S–C axis along the surface normal, (c) top view of the Si(111)- $\sqrt{3}\times\sqrt{3}$ -Ag surface illustrating prospective adsorption sites, including the threefold hollow sites on Ag trimer (T1) and Si trimer (T2); bridge sites on Ag-Ag (D1), Si-Si (D2) and Ag-Si nearest neighbour pairs or dimer (D3); and atop sites on top of a Ag atom (M1) and a Si atom (M2), (d) three $\sqrt{3}\times\sqrt{3}$ -Ag unit cells overlaid on top of an empty-state STM image of a pristine Si(111)- $\sqrt{3}\times\sqrt{3}$ -Ag surface obtained with a sample bias of +2 V and a constant tunneling current of 0.2 nA and, and (e) calculated adsorption energies of dehydrogenated cysteine conformers A (circles), B (squares) and C (triangles) on adsorption sites M1, M2, D1, D2, D3, T1 and T2 optimized by varying the molecule-to-slab vertical separation while holding all other structural parameters fixed. Green, blue, red, and black balls represent sulfur, nitrogen, oxygen, and carbon, respectively.

Figure 3.6c shows the probable adsorption sites that include the atop sites on top of a Ag monoatom (M1) and a Si monoatom (M2); the bridge sites on a Ag-Ag dimer (D1), a Si-Si dimer (D2) and a Ag-Si dimer (D3); and the threefold hollow sites on a Ag trimer (T1) and a Si trimer (T2). The hexagon pictogram containing three $\sqrt{3}\times\sqrt{3}$ surface unit cells, each with two constituent Ag trimers, are highlighted on the surface model in Figure 3.6c and on our atomically resolved STM image in Figure 3.6d. It should be noted that a bright protrusion in the honeycomb network observed in the STM image (Figure 3.6d) corresponds to a Ag trimer as marked by a solid triangle in Figure 3.6c. The calculated adsorption

energies for the three thiolated cysteine conformers on these adsorption sites are compared in Figure 3.6e. The adsorption energy (E_{ad}) of a thiolated cysteine conformer on a selected site of the slab is given by:

$$E_{\text{ad}} = E_{\text{M-slab}} - E_{\text{slab}} - E_{\text{M}}$$

where $E_{\text{M-slab}}$, E_{slab} , and E_{M} are, respectively, the equilibrium energies of the adsorbate-substrate system, the slab (used as the model substrate), and the thiolated cysteine radical ($\bullet\text{SCH}_2\text{CNH}_2\text{COOH}$) in the gas phase. This definition of the adsorption energy corresponds to the bond formation between the thiolated cysteine radical and the surface, i.e.:



In the present definition, we have avoided the need to consider the dissociation energies of cysteine and hydrogen molecules. As the main goal of the present computational study is to identify notable trends in the adsorption configurations of plausible thiolated cysteine conformers, this definition of the adsorption energy is more practical. Evidently, the most favorable adsorption site (with the most negative adsorption energy) for all three conformers is found to be the T1 site, followed by the D1 site, with a 0.2 eV less negative adsorption energy. The energy differences among the three conformers for a particular site are generally small. While the adsorption energies of Conformers B and C on the T1, D1, D2, D3, and M2 sites are nearly the same (within 0.06 eV), those of Conformer A are discernibly higher (by 0.2 eV). Conformer A is also the least stable one for all the adsorption sites, which confirms that orienting the carboxylic acid group upright and away from the surface (without benefiting from auxiliary interactions of the carboxylic acid and amino groups as in Conformers B and C) would lead to less stable adsorption configurations. Cysteine also prefers adsorption on a bridge or three-fold hollow Ag sites rather than the corresponding Si sites, which is supported by the observed shift in the S 2s binding energy to a lower energy. This is, however, in marked contrast to the bond energy of S–Si (617 ± 5 kJ/mol) being almost 3 times higher than that of S–Ag (216.7 ± 14.6 kJ/mol).²⁰⁴ This apparent bond energy advantage is not relevant here because of the relative position of the Ag trimers being 0.8 \AA above the Si trimers (on the terraces) and of the steric hindrance of the cysteine molecules, making the Si sites less accessible for adsorption. In addition, the dangling bonds of Si atoms are already saturated through bonding with other Si atoms and Ag atoms and therefore not available to interact with any adspecies.

In order to determine the effect of the other two functional groups on the stabilization of the adsorption energy, we re-optimize the adsorption geometries with the structures of both the slab and the adsorbate fully relaxed. Tables A2-A8 show the adsorption configurations and adsorption energies before and after relaxation for Conformers A, B, and C at the trimer, dimer and monomer sites, respectively. Interestingly, all three conformers have relocated to the D1 sites when initially placed on the M1, M2, D1, and D3 sites. Initial placement on D2 and T2 has changed to M1 for all three conformers, except for

Conformer C initially on T2 which has changed to D1. Initial placement on T1 sites remain the same for Conformers B and C while Conformer A has moved to D1 after full geometry optimization. Clearly, none of the Si related sites (M2, D2, T2) has led to stable adsorption upon complete optimization for all three conformers. For the Ag related sites (M1, D1, D3, T1), the D1 site has become the most favorable adsorption site after relaxation for all three conformers (with small variations in the structural parameters), with 67% of all the adsorption configurations relaxed into the D1 configurations. We have summarized the most stable, fully optimized adsorption geometries of all three conformers on the D1 sites in Figure 3.7. While the adsorption energies for the A-D1 and B-D1 configurations are within 10% of each other, that for the C-D1 configuration is discernibly less negative (i.e. less stable). For Conformers B and C initially placed on the T1 sites, complete optimization has not affected the adsorption sites (T1) but has improved the adsorption energies (Figure 3.7). Not surprisingly, the fully optimized configurations for all three conformers on the M1 site, with the adsorption energy of A-M1 being the least negative, are generally less stable than those on the T1 and D1 sites. On Ag(111), the stability of the thiolated cysteine adsorption has been found to increase from the atop, to bridge, and to three-fold hollow sites.¹⁶⁵ A detailed DFT study of L-cysteine adsorption at the bridge sites of the Ag(111) surface has revealed a complicated interplay between sp and d states of silver in the bond formation between the adsorbate and the surface. Bridge sites have also been reported to be the most favourable adsorption sites for thiolated cysteine on Au(111)^{177,178} and Au(110),^{102,171} where flat adsorption configurations with S–Au at an off-bridge site and NH₂–Au at an off-atop site were found to be energetically more favourable on the Au(111) surface.

According to the adsorption energies for all three conformers after full relaxation, Conformer A has become the most favorable conformer of thiolated cysteine for adsorption on these sites, which suggests that complete geometry optimization (relaxation) allows thiolated cysteine to be repositioned to enable the amino group to play a stabilizing role. The magnitudes of the adsorption energies of the conformers appear to follow a trend [A (most negative and most stable) < B < C (least negative and least stable)] that is opposite to that of the separations between the amino groups in these conformers and the surface. Upon relaxation of the atomic positions, the S-C axis that is set initially perpendicular to the surface plane is now tilted, enabling the amino group to lean toward the Ag atoms of the surface. The tilt in the S-C axis is also found for Conformer B, while it remains unchanged for almost all adsorption configurations of Conformer C, which could account for the lower stability of Conformer C as compared to other two conformers.

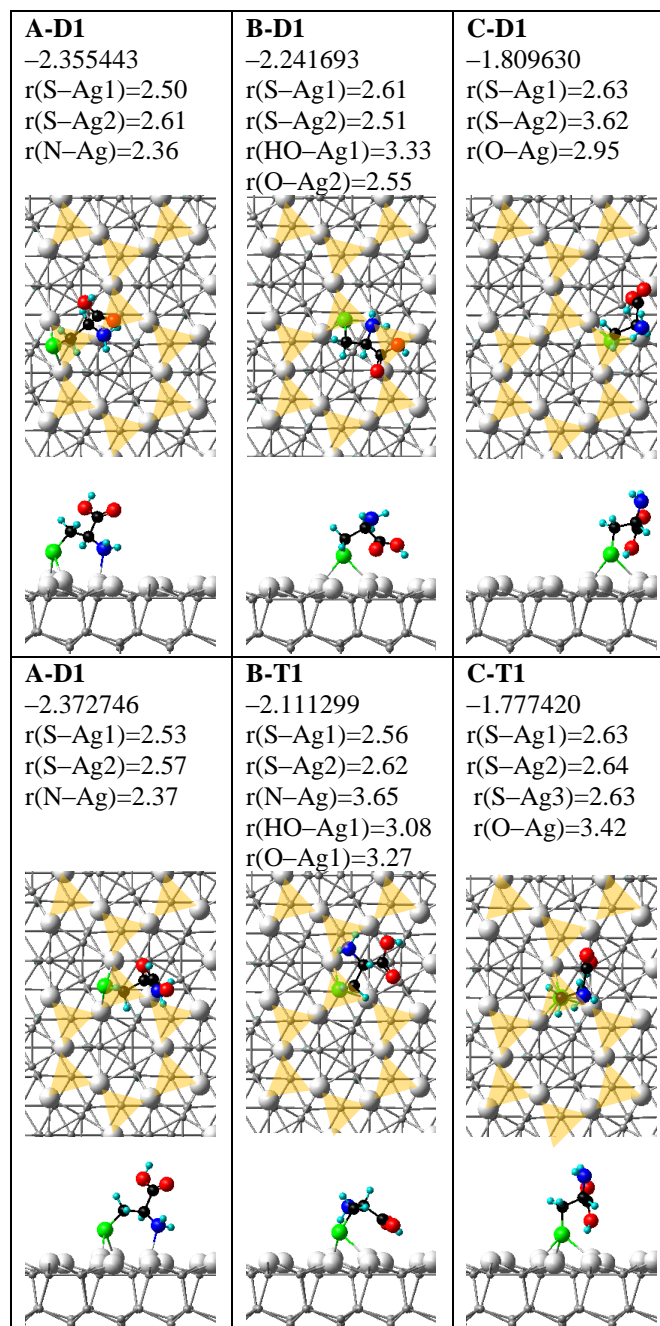


Figure 3.7 Equilibrium geometries of optimized adsorption configurations after full relaxation of thiolated cysteine conformers A, B, and C initially placed on D1 (top panels) and T1 sites (bottom panels) of the Si(111)- $\sqrt{3}\times\sqrt{3}$ -Ag model surface. The adsorption energies are in unit of eV while the separations $r(\text{X-Y})$ are in unit of Å. To better illustrate the adsorption structure, only part of the slab (corresponding to the 4×4 supercell) for the model surface is shown for each configuration. Green, blue, red, and black balls represent sulfur, nitrogen, oxygen, and carbon, respectively.

3.2.6 Large-scale DFT calculations of cysteine zwitterionic multimers on model Si(111)- $\sqrt{3}\times\sqrt{3}$ -Ag surface

To investigate the effect of intralayer bonding involving other functional groups that are not used for direct attachment to the surface on the adsorption, we perform calculation of other plausible adsorption geometries in which either the amino or carboxylic acid or both groups are initially close to the surface. This type of calculations could provide some insights into the early formation of the zwitterionic layer of cysteine on the Si(111)- $\sqrt{3}\times\sqrt{3}$ -Ag surface. While the A-D1 configuration with the carboxylic acid group pointing away from the surface is more conducive to initiating bonding with the second adlayer, a small rotation of the C_{α} -C bond could reposition the carboxylic acid group such that it becomes more accessible to intralayer bonding in the first adlayer. Figures 3.8a and 3.8b show the optimized geometries of the most favorable A-D1 adsorption configurations where the C-C $_{\alpha}$ -C plane is tilted parallel to the surface, with H $_{\alpha}$ (the H atom connected to C $_{\alpha}$) pointing up away from and down towards the surface, respectively. The separations between the functional groups and the respective underlying silver atoms are: r(S-Ag1)=2.54 Å, r(S-Ag2)=2.64 Å, r(N-Ag)= 2.42 Å, and r(O-Ag)=3.52 Å for the H $_{\alpha}$ -up configuration, and r(S-Ag1)=2.57 Å, r(S-Ag2)=2.57 Å, r(N-Ag)=2.41 Å, and r(HO-Ag)=3.32 Å for the H $_{\alpha}$ -down configuration. Both A-D1 configurations in Figures 3.8a and 8b as well as the upright A-D1 configuration in Table A4 are consistent with our XPS data, which support the presence of free amino and carboxylic acid groups at low coverages. As expected, the configuration with the molecular plane more surface parallel (Figure 3.8a) is energetically more stable (by 0.1 eV) due to the potential interaction of lone-pair electrons of the amino group with the surface Ag atoms. Such a more surface-parallel A-D1 configuration is a strong candidate for cysteine adsorption at very low coverage, in good accord with experimental and theoretical reports of cysteine on Au(110)¹⁷¹ and Ag(111) surfaces¹⁶⁵ at low coverages.

Using the A-D1 surface-parallel adsorption configuration (Figure 3.8a), we calculate the adsorption configuration for cysteine dimer obtained with the addition of a thiolated cysteine conformer (A) in appropriate orientation (Figure 3.8c). On the Au(111) and Au(110) surfaces, cysteine dimer formation has been reported to be as favourable as the single molecule adsorption at low coverages.^{171,177,178,181} The cysteine dimer in Figure 3.8c is therefore another prospective candidate for adsorption at lower coverages, in good accord with our XPS results in which both zwitterionic and neutral states are observed. Under UHV condition, zwitterions have been observed at higher coverages, where their formation is driven by the intermolecular proton transfer between the hydroxyl group of one molecule and the amino group of a neighboring molecule.^{163,164,176,177} A common DFT approach used to determine the coverage-dependent zwitterionic structure formation is to first calculate the adsorption configuration of a single molecule on the surface in a sufficiently large supercell corresponding to the low coverage regime. Decreasing the cell

size appropriately would then promote highly ordered zwitterionic intermolecular interactions and therefore can be used to mimic the higher coverage regime. In our system, however, the zwitterionic chemical state is observed even at very low coverages due to the presence of high densities of step edges and small terraces as well as to the high diffusivity of cysteine on Si(111)- $\sqrt{3}\times\sqrt{3}$ -Ag. As we do not observe any ordered structure of cysteine at any coverage, the aforementioned approach of calculating the zwitterionic intermolecular interaction is less effective. We have therefore used a thiolated form of the zwitterion of Conformer AH_{ZI} (shown in Figure 3.8d) as the initial form of the adsorbate to redo the calculation for the adsorption configuration of the cysteine dimer (involving zwitterionic interactions between deprotonated carboxylic acid and protonated amino groups of one cysteine zwitterion with the respective protonated amino and deprotonated carboxylic acid groups of a neighbouring cysteine zwitterion). We obtain the equilibrium geometry of an adsorption configuration (Figure 3.8e) that is similar to that shown in Figure 3.8c, with slight differences in the orientation of the $-\text{NH}_3^+\cdots\text{COO}^-$ components and their separations. The corresponding adsorption energy is found to be more negative by 0.75 eV relative to the non-zwitterionic dimer, which confirms that the zwitterionic dimer form is more stable than the neutral dimer form. This is reasonable because the cysteine dimer in Figure 3.8e is stabilized by two mutual zwitterionic hydrogen bonding while the one in Figure 3.8c contains only one hydrogen bond. Using the latter approach, we also calculate other possible zwitterionic dimers, including dimer of Conformer AH with H_a down and dimer of Conformer BH (Figure A5), which are found to have less negative adsorption energies than that shown in Figure 3.8e. Figures 3.8f and 8g show the calculated adsorption configurations of the zwitterionic trimer and zwitterionic hexamer, respectively. These zwitterionic structures of cysteine dimer, trimer and hexamer found in our calculations are consistent with some of the notable protrusion features observed in our STM data, Figures 3.3b3 and 3.3d3. The respective $-\text{NH}_3^+\cdots\text{COO}^-$ bond lengths of these zwitterionic bonds are found to be 1.67 Å (dimer), 1.55 Å (trimer), and 1.73 Å (hexamer), which are in general accord with previous DFT calculations of cysteine on other surfaces.^{163,181} Using the vertical separation between the topmost O atom of the cysteine adsorbates and the Ag atom underneath, the thickness of the interfacial layer with flat configuration is calculated to be 5.13 Å (Figure 3.8g). This estimate of the interfacial layer thickness is used for calculating the coverage of chemisorbed species in the interfacial layer based on our XPS data discussed above. It should be noted that minor displacements in the Ag positions in the $\sqrt{3}\times\sqrt{3}$ -Ag template are also observed for dimer, trimer and hexamer adsorption configurations.

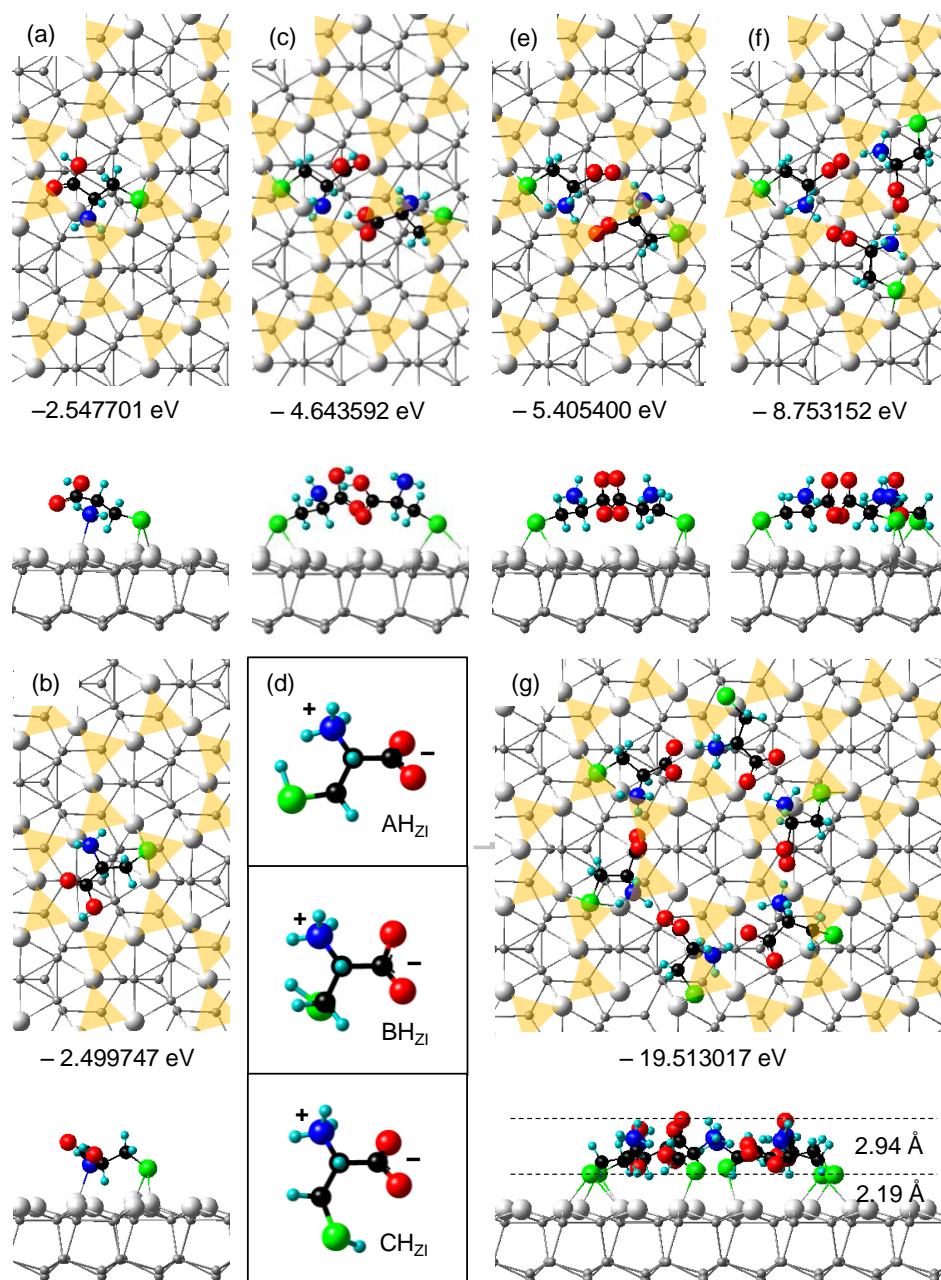


Figure 3.8 Equilibrium geometries and adsorption energies of optimized adsorption configurations on D1 sites for thiolated Conformer AH with (a) H_{α} up and (b) H_{α} down, (c) hydrogen-bonded dimer containing two thiolated neutral Conformer A with H_{α} up, (e) dimer containing two thiolated zwitterion AH_{ZI} , and (f) trimer containing three thiolated zwitterion AH_{ZI} with H_{α} -up, and (g) hexamer containing six thiolated Conformer AH_{ZI} with H_{α} -up. The equilibrium geometries of isolated zwitterions (ZIs) for Conformers AH, BH and CH are shown in (d). Thiolated zwitterion AH_{ZI} is derived by proton relocation from $COOH$ to NH_2 in a thiolated Conformer AH. To better illustrate the adsorption structure, only part of the slab [corresponding to the 4×4 supercell for (a-c) and (e-f) and to the 8×8 supercell for (g)] for the model surface is shown.

The calculated hexamer structure (and larger multimer structures – not shown) for the D1 site on the terrace is therefore inspired by the ring-like structures at low coverage found in our STM images in Figures 3.3b3 and 3.3d3. While individual cysteine adspecies involved in forming each ring are too small to be resolved in our STM images, the calculated adsorption configurations shown in Figure 3.8 illustrate the viability of zwitterionic multimer structures for use as the building blocks in the cysteine film growth on the Si(111)- $\sqrt{3}\times\sqrt{3}$ -Ag surface. This type of large-scale DFT calculations is therefore especially important for verifying the presence of zwitterionic intermolecular interactions, in addition to the molecule-to-substrate covalent bonding at the interfacial layer, for corroborating with both our XPS and STM results.

3.3 Summary

The $\sqrt{3}\times\sqrt{3}$ -Ag reconstruction on the Si(111)7 \times 7 surface offers a unique, single-atom-thick, two-dimensional metal silicide platform to investigate the surface chemistry of biomolecules. With a variety of bonding sites available not just on its lower-step terraces and upper-step terraces but also on step edges and antiphase boundaries, the Si(111)- $\sqrt{3}\times\sqrt{3}$ -Ag surface provides a rich testbed for studying site-specific chemistry, particularly the role of defects. As one of two natural S-containing amino acids, cysteine offers three important functional groups to explore the surface chemistry of these bonding sites. In the present work, we follow the growth of a cysteine nanofilm and study their interfacial interactions with the Si(111)- $\sqrt{3}\times\sqrt{3}$ -Ag surface and their molecule-to-molecule interactions. By combining the results from our XPS and STM experiments with complementary large-scale DFT calculations, we are able to decipher the chemical nature of the interface and reach a molecular level understanding of the physical processes occurring in such an intricate system. Adsorption of cysteine is found to begin on the lower-step edge and antiphase boundary sites and the adsorption fronts propagate from these defect sites out to the terrace regions with increasing exposure. This result suggests the viability of preferential site functionalization by manipulating the formation of and adsorption on specific defect sites of the Si(111)- $\sqrt{3}\times\sqrt{3}$ -Ag surface. We propose a plausible diffusion-driven adsorption model for the observed growth evolution. Unlike the cysteine film growth on Si(111)7 \times 7, no transitional layer is observed on Si(111)- $\sqrt{3}\times\sqrt{3}$ -Ag at room temperature, as supported by the absence of hydrogen bonding found in our XPS spectra obtained at low exposures. The zwitterionic structures therefore start on the interfacial layer and grow directly onto the multilayer. The lack of a transitional layer is therefore similar to that found on metal surfaces, which is in good accord with the semi-metallic nature of the $\sqrt{3}\times\sqrt{3}$ -Ag template. Our DFT calculations show that a bridge site provides the most stable adsorption site for cysteine when compared to the three-fold hollow or atop site on a $\sqrt{3}\times\sqrt{3}$ -Ag terrace surface. As the availability of other

types of bridge sites is expected to be more prevalent at the step edges (and other defects), our DFT result is consistent with the observed initial growth first on step edges. The formation of a S-to-metal bond allows at most one additional functional group to be sufficiently close to enable interaction with a second surface atom (due to the inherent structure of cysteine itself), thus favouring the bridge site. This also leaves the remaining (third) functional group free to undergo further interaction with other incoming adspecies. At elevated temperatures, cysteine adspecies are found to transform the monoatomic Ag layer of $\sqrt{3}\times\sqrt{3}$ -Ag into Ag agglomerates of nanometer sizes by cleavage of Ag–Si bonds and formation of Ag–S and Si–NH bonds. This is an important result because cysteine-induced cluster formation at elevated temperature offers a new approach of using adsorbates to convert a two-dimensional, single-atom-thick $\sqrt{3}\times\sqrt{3}$ -Ag overlayer to, in effect, zero-dimensional nanoclusters. The present work further highlights the possibility of taking advantage of the unique surface chemistry on this and similar intricate two-dimensional metal overlayers as templates to grow nanoclusters or quantum dots for chemical sensing and catalysis applications.

Chapter 4

Development of Aligned Organic Molecular Wires and Silver Metallic Nano-agglomerates in Methionine Nanofilm Supported on Si(111)- $\sqrt{3}\times\sqrt{3}$ -Ag

4.1 Introduction

Understanding the interactions between biomolecules and solid surfaces in the atomic scale and the mechanism of nanofilm growth is of paramount importance to not just expanding the boundaries of our basic knowledge about these benchmark biological materials but also enabling technological applications that exploit the hybrid organic-inorganic interactions in the design of next-generation catalysts, biosensors and nanoelectronic devices. The adsorption of biomolecules on metal and semiconductor surfaces has been studied extensively due to their applications particularly in surface functionalization and molecular self-assembly.²⁰⁵ Detailed understanding of the physical and chemical phenomena at the interface between biomolecules and solid surfaces can lead to better control of the self-assembly and self-organization processes in synthesizing multifunctional materials based on two-dimensional nanostructures and to the development of the promising biocompatible nanomaterials. Bio-organic molecules such as amino acids play a particularly important role in these fields. As the smallest building blocks of peptides and proteins, amino acids are among the most fundamental model systems for elucidating the interactions of these complex molecules with surfaces. They also offer potential biological functionalities in addition to powerful chemical and physical properties, making them good candidates for functionalization of solid surfaces, often serving as the first step in building a biocatalyst or bioactive device.

Of the 20 proteinogenic amino acids (that are used in the genetic code), methionine is one of two sulfur-containing amino acids that comprises of a methythio methylene end group. Methionine is important in molecular biosynthesis in human body, and due to its antioxidant properties, it is known to prevent cell damage resulting from cancer treatments without delaying antitumor activity.²⁰⁶ The self-assembly of methionine on metal surfaces offers a promising approach to design drug delivery carriers and bio-architectures with customizable nanostructures. Fundamental understanding of their self-assembly properties on metal surfaces is therefore of particular interest. Among the large volume of research on benchmark amino acids on metal surfaces,²⁰⁵ only a few have focused on methionine, despite the aforementioned potential applications. Two-dimensional molecularly ordered structures of L-methionine have been reported to form on Ag(111), and holding the surface at 320 K during deposition was used to promote the formation of regular gratings.¹⁰⁸ On Au(111),^{106,109} D- and L-methionine were

found to form parallel chains or zipper-like dimer rows in the formation of hydrogen-bonded zwitterionic layers at room temperature. Furthermore, steering chiral organization of L-methionine on Cu(111)¹⁰⁷ was found to be strongly affected by the substrate reactivity and thermal activity.

The configuration of a stable two-dimensional structure at thermodynamic equilibrium can be controlled by not only the lateral interactions, but also the nature of the chemical and structural characteristics of the underlying support. In our previous work, the formation of self-organized methionine trimers on a Si(111)7×7 surface at room temperature is found to be governed by the N–Si covalent bonding at the center adatoms of the Si substrate surface and by the intermolecular hydrogen bonding that leads to the formation of Y-shaped trimers.¹²² While the two-dimensional electron gas of a metallic surface facilitates fast diffusion of organic molecules and hence promotes the fabrication of molecular self-assembly, the strong directional dangling bonds of the semiconductor surfaces [such as Si(111)7×7] favor trapping of molecules in a diffusion-limited state, thereby potentially inhibiting the long-range self-assembly of small amino acids. One advantage of Si-based substrates over metal substrates is that they are fundamentally essential for fabricating electronic devices by large-scale integration techniques. Passivation of Si surfaces with metal atoms therefore offers a promising approach to altering the surface diffusion properties of the adsorbed molecules and hence promoting the equilibrium-state formation of self-assembled molecular structures. Among all metal-passivated Si surfaces, Si(111)-√3×√3-Ag is one of the most studied prototypical metal/semiconductor interfaces. It is formed by deposition of one monolayer of Ag atoms on the Si(111) surface followed by annealing at an elevated temperature. The parabolic surface band structure of Si(111)-√3×√3-Ag near the Fermi level resembles that of a typical metal surface. While the Si(111)-√3×√3-Ag surface properties are more similar to those of metal surfaces than Si surfaces, there are significant structural distinctions between the two. Notable differences between the Si(111)-√3×√3-Ag surface and the Ag(111) single-crystal surface are found in their unit cell sizes and surface Ag–Ag separations. Furthermore, while the topmost layer of the Si(111)-√3×√3-Ag surface is composed of Ag atoms, the underlying layers are comprised of Si atoms, leading to the surface electronic states containing Ag–Si components, as opposed to the Ag–Ag surface states on the Ag(111) surface.

Here, we study the interface and growth properties of methionine from sub-monolayer to multilayer coverages on Si(111)-√3×√3-Ag at room temperature and follow their thermal evolution under ultrahigh vacuum condition. Our goal is to determine the changes in the chemical states of methionine at notable adsorption sites of the Ag silicide surface. Our combined scanning tunneling microscopy (STM) and X-ray photoelectron spectroscopy (XPS) data provide a comprehensive picture of the nature of molecule-molecule and molecule-substrate interactions both at the interface and during the early nanofilm growth.

These data are supported by complementary quantum mechanical calculations based on density functional theory (DFT) that enable us to identify the chemical state of the adspecies and their most probable adsorption configurations, and two-dimensional surface assembly at the interface. We also perform a comparative analysis on the nanofilm formation and growth of glycine, cysteine, and methionine on Si(111)- $\sqrt{3}\times\sqrt{3}$ -Ag at and above room temperature in order to establish notable trends in the interfacial processes of these benchmark biomolecules. Of particular interest is the formation of metal agglomerates mediated by the adspecies of these amino acids at elevated temperature.

The details of the experimental procedure and the computational details are given in Chapter 2.

4.2 Results and Discussion

4.2.1 Evolution of chemical-state composition during methionine film growth at room temperature

Similar to all other proteinogenic amino acids, methionine is found in a neutral form in the gas phase and a zwitterionic form in the liquid and solid phases. Figure 4.1 compares the ball-and-stick models of neutral and zwitterionic structures of an isolated methionine molecule with those of cysteine (the smallest sulfur-containing amino acid) and glycine (the smallest amino acid). Starting from glycine ($C_{\beta}OOHC_{\alpha}H_2NH_2$), cysteine is obtained by replacing an alpha H with a thiol methylene group ($-CH_2SH$). The difference between the two S-containing amino acids is that the thiol group ($-SH$) in cysteine ($C_{\beta}OOHC_{\alpha}HNH_2C_{\gamma}H_2SH$) is replaced by a methylthio methylene group ($-CH_2SCH_3$) in methionine ($C_{\beta}OOHC_{\alpha}HNH_2C_{\gamma}H_2C_{\delta}H_2SC_{\epsilon}H_3$). The carbon chain backbone increases in length from 2 C atoms in glycine to 3 C atoms in cysteine and to 4 C atoms in methionine. The termination of the S atom by a methyl group in the methylthio methylene group also makes methionine less reactive than cysteine (with the highly reactive thiol group).

Figure 4.2 shows the O 1s, N 1s, C 1s, and S 2s spectra of methionine as a function of exposure time on Si(111)- $\sqrt{3}\times\sqrt{3}$ -Ag at room temperature and of the thickest as-grown methionine film upon annealing to elevated temperatures. The corresponding peak positions and assignments obtained for the fitted features are summarized in Table B1, while the changes in their relative intensities are given in Figure B1. Increasing the exposure from 120 s to 360 s generally increases the intensities of all the components in the XPS region spectra (Figure 4.2). The predominant N 1s peak appeared at 401.8 eV can be assigned to the protonated amino group, while the weak N 1s feature at 398.7 eV is in good agreement with the N–Si linkage reported for methionine adsorbed on the Si(111) 7×7 surface. Formation of the N–Si bond could arise from N–H dissociative adsorption of methionine at defect sites such as step edges and

antiphase boundaries of the Si(111)- $\sqrt{3}\times\sqrt{3}$ -Ag surface.^{122,123} The O 1s spectra can be fitted with a main peak at 531.7 eV assigned to the deprotonated carboxylic acid group and a weaker one at 532.7 eV assigned to the neutral carboxylic acid group. This latter feature likely corresponds to the adsorbed species at defect sites. The single S 2s peak located at 228.4 eV can only be attributed to the sulfur atoms in the methylthio methylene group. The four C 1s features at 285.5 eV, 285.9 eV, 286.9 eV, and 288.7 eV can be assigned to $-\text{CH}_3$, $-\text{CH}_2-\text{S}-\text{CH}_3$, $-\text{C}-\text{NH}_3^+$, and $-\text{COO}^-$, respectively. Indeed, the presence of deprotonated carboxylic acid group ($-\text{COO}^-$) and protonated amino group ($-\text{NH}_3^+$) along with the intact methylthio methylene group indicates non-dissociative adsorption of methionine in their zwitterionic state. Physisorption of zwitterionic methionine on the Ag(111)¹⁰⁸ and Au(111)^{109,207} surfaces has also been reported at cryogenic temperature and up to room temperature. On Cu(111),¹⁰⁷ methionine was found to adsorb in both anionic and zwitterionic states, while the adsorption state on the Cu(110)¹⁰⁵ surface is only anionic with stronger interaction of oxygen atoms with copper.

Increasing the exposure to 840 s and 1800 s further increases the intensities of all the peaks. For the 1800-s exposure, the O 1s feature for the zwitterionic moiety and its corresponding C 1s features are found to undergo small shifts to higher binding energies by 0.3 eV, while the N 1s and S 2s positions of the respective protonated amino and methylthiol methylene groups stay unchanged. The carboxylate shift to a higher binding energy with increasing exposure can be due to an electrostatic effect arising from the formation of a thicker film. Finally, extending the exposure time to 3720 s leads to further increase in the intensities of the peaks in all four regions with no additional chemical shifts. The peak positions of XPS spectra for the methionine multilayer obtained for the 7560-s exposure to Si(111)- $\sqrt{3}\times\sqrt{3}$ -Ag are found to be similar to those for methionine powder in the solid phase. Comparing the XPS spectra of the methionine multilayer with those of the lower exposures shows that intermolecular zwitterionic interactions are clearly present even at the lowest coverage (120 s exposure). The majority of the adsorbate species are therefore physisorbed on the surface as no significant chemical shift is observed in the dominant peaks of all regions. Indeed, only a small fraction of the adsorbate is found to be chemisorbed most likely at defect sites through N-H bond cleavage.

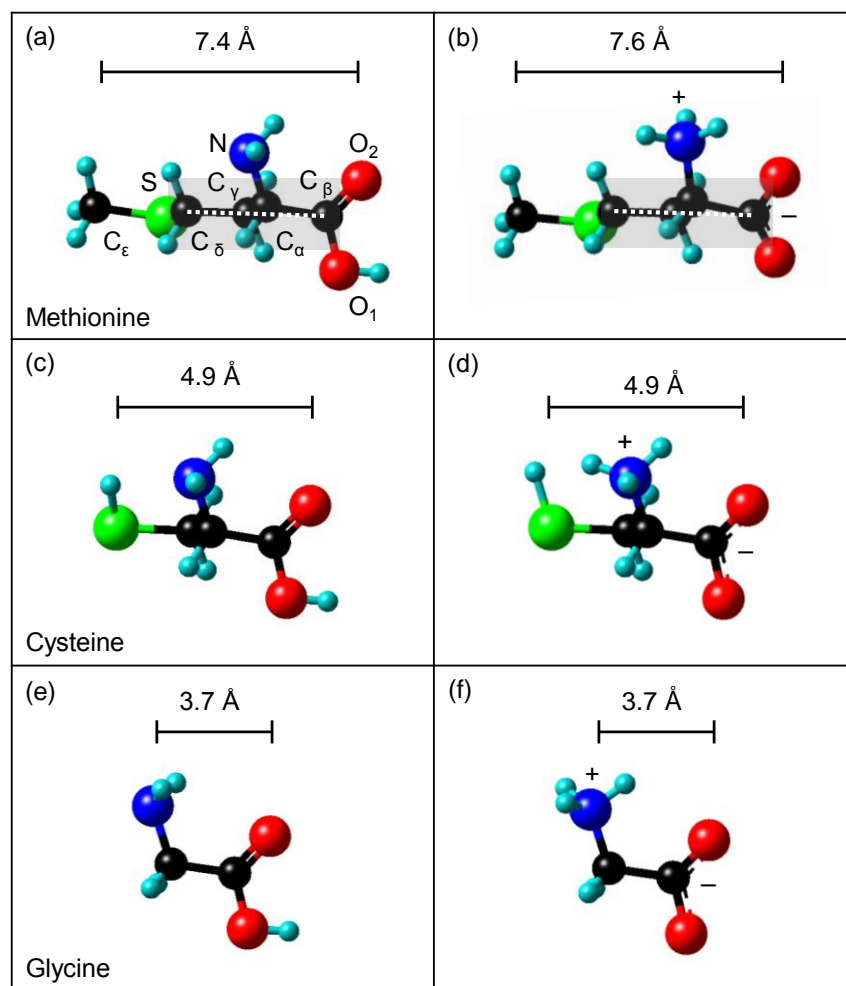


Figure 4.1 Ball-and-Stick models for the isolated structures of (a) neutral methionine, (b) zwitterionic methionine, (c) neutral cysteine, (d) zwitterionic cysteine, (e) neutral glycine, and (f) zwitterionic glycine. The models are generated by DFT calculations. In our notation, we identify -COOH as the “head” group and the functional group farthest from the head group as the “tail” group. The long axis is marked by the dashed line.

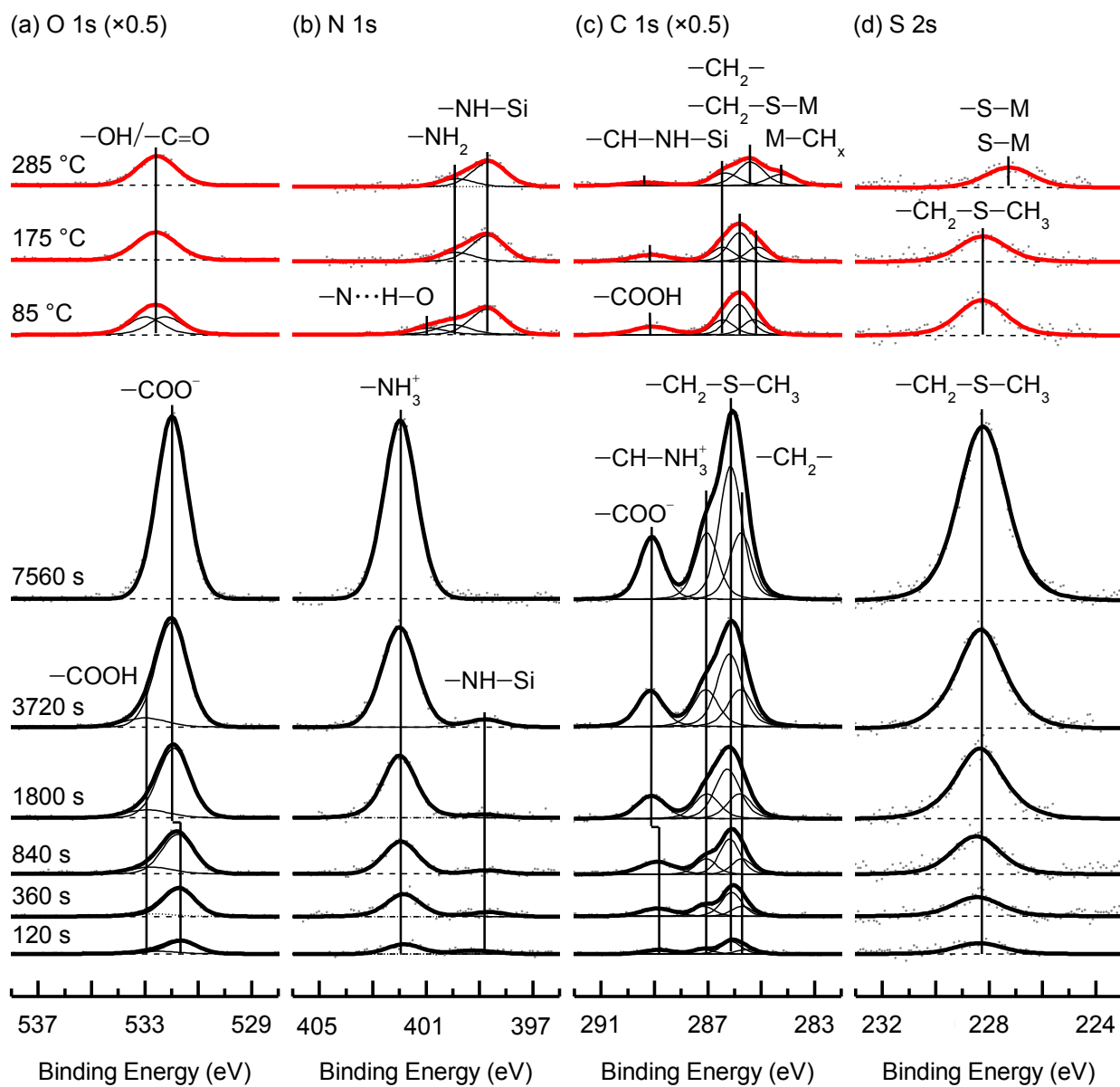


Figure 4.2 Evolution of (a) O 1s, (b) N 1s, (c) C 1s, and (d) S 2s XPS spectra of methionine deposited on Si(111)- $\sqrt{3}\times\sqrt{3}$ -Ag as a function of exposure time (120–7560 s) and of the as-grown multilayer methionine film (obtained with a 7560-s exposure) upon annealing to 85, 175, and 285 °C. In (c) and (d), M is used to represent Si and/or Ag.

4.2.2 Chemical-state evolution of a supported multilayer methionine film upon annealing

To examine the thermal stability of the methionine film and the underlying interface, we anneal the as-deposited multilayer methionine film (obtained with the 7560-s exposure) sequentially to 85 °C, 175

°C, and 285 °C, each for 600 s, followed by cooling to room temperature before XPS measurement after each annealing step. The corresponding XPS spectra depicting the changes in the chemical-state compositions after each annealing-cooling cycle are shown in Figure 4.2. Annealing the film to 85 °C appears to reduce the peak intensities by 80%, indicating that the majority of methionine in the film has been desorbed. Moreover, the chemical states of the remaining features closely resemble those of the non-zwitterionic adspecies. The single O 1s band has shifted to a higher binding energy (532.4 eV), which is attributed to the neutral carboxylic acid group (–COOH). The N 1s broad band can be deconvoluted into three features at 398.8 eV, 399.9 eV, and 401.0 eV, assigned respectively to the dehydrogenated amino group (–NH), neutral amino group (–NH₂), and the amino group involved in hydrogen bonding (–N···HO, where “···” is used to denote a hydrogen bond). Annealing has therefore led to dehydrogenation of the amino group and chemisorption of the methionine adspecies through NH–Si linkage, as its binding energy is closer to that observed on methionine adsorption on Si(111)7×7,^{122,123} most likely near the defect sites at which the N–Si chemisorption has already initiated at room temperature. Upon annealing to 175 °C, we observe no further shift in the binding energy positions in all the spectra, while the intensities are slightly lowered due to desorption of the non-chemisorbed species as evidenced by the removal of the hydrogen bonding N 1s feature at 401.0 eV. Finally, upon annealing to 285 °C, the intensities and positions of both the N 1s and O 1s features for the chemisorbed species remain essentially unchanged, while major changes are observed in the S 2s and C 1s regions. The S 2s signal has undergone a major shift to a lower binding energy (227.2 eV), which indicates the breakage of either the S–C_α or C_β–S (or both) and chemisorption of the resulting S-containing fragments or S atoms on the Si or Ag atoms.^{121,208,209} The dissociation of the S–C bond and deposition of atomic S have also been observed in the study of thiol alkanes and thiophene on Au(111),^{208,210} Cu(111),²⁰⁹ Pt(111) and Ni(111).²¹¹ In the C 1s region, the –COOH peak is weakened while the major band at the lower binding energy is broadened. As the –CH–NH–Si C 1s feature remains unchanged in both energy position and intensity, a new peak is found to emerge at 284.7 eV (the lowest C 1s binding energy). This new feature can be assigned to the decomposition fragments –CH_x (adsorbed most likely on the Si or Ag atoms),²¹² and the peak at 285.5 eV can now be attributed to both –CH₂–S–M (where M is Si or Ag) and –CH₂– moieties. This is in good accord with our previous studies on cysteine adsorption on Si(111)-√3×√3-Ag and on Si(111)7×7,¹²¹ both of which show decomposition of cysteine molecules to dissociated S atoms and/or S-containing fragments on the surface at 285 °C. Similar decomposition of methionine at ~285 °C has also been observed on Si(111)7×7. The N 1s position of the chemisorbed feature after annealing is close to that of the methionine interfacial layer on Si(111)7×7.¹²⁴ Chemisorption of the resulting methionine fragments would therefore more likely involve the underlying Si atoms of the Si(111)-√3×√3-Ag surface via N–Si

linkage rather than the Ag atoms on the Ag silicide surface. It should be noted that while deprotonation of the amino group on Si surfaces has been observed,^{205,213} it has not been found to occur on any of the Ag surfaces at room temperature.

4.2.3 Metallic silver nanoagglomerate formation induced by methionine nanofilm

After observation of the significant changes in the methionine nanofilm upon annealing to 285 °C, examination of the corresponding Ag 3d spectra could provide additional insight to understanding the interface between the methionine nanofilm and the Si(111)- $\sqrt{3}\times\sqrt{3}$ -Ag surface. Figure 4.3 shows the corresponding Ag 3d spectra of the pristine Si(111)- $\sqrt{3}\times\sqrt{3}$ -Ag surface before and after methionine deposition at room temperature, and of the supported multilayer methionine upon annealing to higher temperatures. The pristine Si(111)- $\sqrt{3}\times\sqrt{3}$ -Ag surface exhibits well-defined Ag 3d_{5/2} and Ag 3d_{3/2} peaks at 369.0 eV and 375.0 eV, respectively, the separation of which is in good accord with the Ag 3d spin-orbit splitting of 6.0 eV. The binding energy position of the Ag 3d_{5/2} (Ag 3d_{3/2}) peak corresponds to that reported for Ag silicide. Upon exposure to methionine, the peak positions remain unchanged while the intensities decrease, consistent with the increasing thickness of the methionine film (and the finite electron inelastic mean free path). Increasing the exposure time to 7560 s leads to a small gradual increase in the Ag 3d_{5/2} (Ag 3d_{3/2}) line width. After annealing the 7560-s film at 85 °C, a new Ag 3d_{5/2} (Ag 3d_{3/2}) feature emerges at 368.4 eV (374.4 eV), which corresponds to the Ag–Ag metallic state of the bulk Ag. This feature appears to increase in intensity at the expense of Ag–Si peak upon further annealing to 175 °C and to 285 °C. This is an important result because it shows that the population of the Ag–Si moieties of Si(111)- $\sqrt{3}\times\sqrt{3}$ -Ag is reduced while that for the Ag–Ag metallic state increases, likely in the form of metal agglomerates. Furthermore, it should be noted that the aforementioned annealing does not have any effect on the pristine Si(111)- $\sqrt{3}\times\sqrt{3}$ -Ag surface because the surface alone is known to be stable in this temperature range due to its preparation that requires annealing at 300-500 °C. We have also independently verified the absence of the Ag–Ag metallic state in a separate control experiment performed on a pristine Si(111)- $\sqrt{3}\times\sqrt{3}$ surface (i.e. without any methionine exposure) under similar annealing conditions.

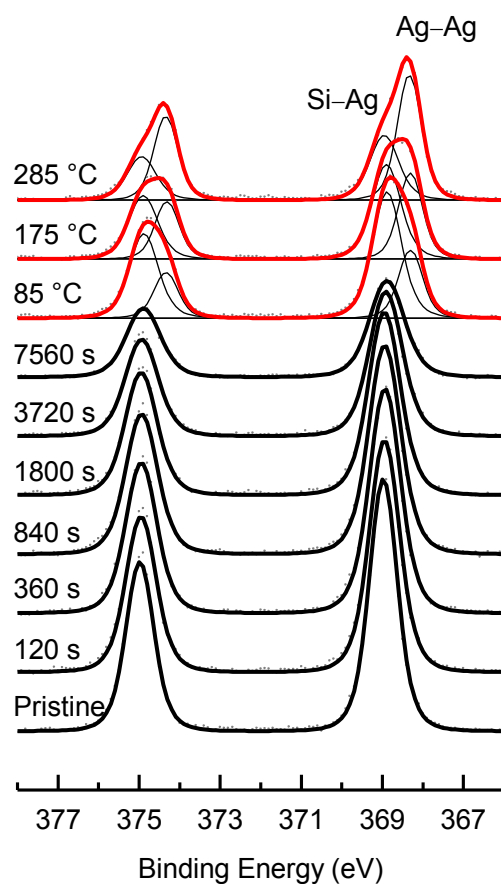


Figure 4.3 Evolution of Ag 3d XPS spectra of the pristine Si(111)- $\sqrt{3}\times\sqrt{3}$ -Ag surface after deposition of methionine with increasing exposure time and of the as-grown 7560-s methionine film upon annealing to 85, 175, and 285 °C.

4.2.4 Formation of methionine molecular wires on Si(111)- $\sqrt{3}\times\sqrt{3}$ -Ag in the early growth stage

In order to take advantage of the well-defined $\sqrt{3}\times\sqrt{3}$ -Ag overlayer as a reference template on Si(111), we focus our STM studies in the early growth stage of the methionine film. For a very low exposure (20 s) of methionine on Si(111)- $\sqrt{3}\times\sqrt{3}$ -Ag, STM measurement at room temperature shows mostly “fuzzy” protrusion features, along with a number of one-dimensional (1D) stripes (Figure B2). The diffuse molecular-wire features represent mobile molecules that are in rapid motion too fast for the STM to resolve, confirming the weak molecule-substrate interactions at room temperature at very low coverages. In order to investigate these organized adsorbate nanostructures in more detail, we perform STM measurements at a lower temperature. Figure 4.4a1 shows the STM image of the surface after a 30-s

exposure of methionine with the surface held at 140 K. Unlike cysteine, methionine forms well-defined 1D extended ordered structures with distinct widths. The 1D extended molecular stripes are formed on surface terraces with three distinct orientations 120° from one another. Interestingly, a large number of these stripes tend to align in parallel to the step-edge directions. As the step-edge directions are known to be along the $[110]$ and $[1\bar{2}1]$ directions,¹⁹⁶ the orientations of these molecular wires are likely along the $[110]$ or $[1\bar{2}1]$ direction.

As illustrated in Area A1 (Figures 4.3a1 and 4.3a2) and the corresponding height profile along Line L1 (Figure 4.4a3), the molecular wires appear to have three different widths 1.9 nm, 3.4 nm, and 4.7 nm. The width of the thinnest molecular wire is close to that of a methionine dimer with a head-to-head configuration (discussed further in the calculation section) and is in good accord with the observation of 1D extended structures of methionine on Ag(111).¹⁰⁸ Considering the theoretical value of a dimer width to be 1.5 nm (as discussed in the calculations section), the widths of the molecular wires are found to be 1.2, 2.3, and 3.1 times that of a theoretical dimer. In other words, the thicker stripes can be considered 2 and 3 such molecular wires located side by side next to each other. The highlighted circles in Figure 4.4a1 mark the edges of the single dimer rows grown next to another molecular wire, creating thicker stripes. This “merging” of multiple molecular wires into stripes with integral widths is clearly observed in Figure 4.4a2 (from top to bottom: single, triple, and double dimer rows). Furthermore, there appears to be an inter-stripe surface-mediated long-range interaction leading to the one-dimensional extended ordering among a number of stripes with well-defined spacings between them.^{108,214} The spacing between the molecular stripes varies from 2.1 nm to 21.2 nm. However, the long-range order is disrupted occasionally when another stripe with a different orientation starts growing nearby, which leads to the formation of inter-stripe joints with 60° and 120° angles.

Similar type of linear structures has been observed on the Ag(111) surface,¹⁰⁸ where aligned 1D structures were extended on the large surface terraces with defined and equal inter-stripe separations. In this Ag(111) study, the STM data were collected at 15 K and the so-called nanograting was shown to be stable up to room temperature with molecular desorption occurring above 370 K. Formation of the 1D molecular grating has also been reproduced on Cu(111)¹⁰⁷ under ultrahigh vacuum condition, and on graphite^{215,216} under ambient conditions, at various temperatures up to room temperature. On Ag(111), the nanowires were oriented along the high-symmetry substrate directions, while on the more reactive Cu(111) surface the assembly of the nanowires was oriented with an angle of -10° with respect to the $\langle 110 \rangle$ axes below 273 K and $+10^\circ$ above 283 K. These studies proposed that a single nanowire corresponds to a dimer row of methionine molecules extended along a direction that is in registry with the substrate crystallographic directions. The dimerization was shown to be mediated by zwitterionic

intermolecular hydrogen bonding of methionine on Ag(111) and a combination of anionic and zwitterionic intermolecular bonding on Cu(111). The zwitterionic molecular dimerization leading to the formation of 1D nanowires being commensurate with the underlying atomic lattice was also reported for L-tyrosine on Ag(111),¹¹⁰ which has further been proposed as a universal bonding scheme for 2D zwitterionic systems. Indeed, this bonding picture is consistent with our STM images of methionine molecular wires on Si(111)- $\sqrt{3}\times\sqrt{3}$ -Ag.

Some of the molecular wires appear to be nucleated at the step edges, while others are formed on the surface terraces, where the number of molecular wires unattached to the step edges is evidently less than the attached ones. This confirms that, although nucleation at the step edges is more probable, it can also occur on the defect-free terraces, which is likely driven by the presence of intermolecular attractive forces. The higher likelihood of nucleation at the step edges could be due to the molecules becoming trapped at these defect sites more easily than the terrace sites. To illustrate the effect of other surface features, such as defects, on the adsorption properties, we show a magnified image of a step edge in Area A2 (Figure 4.4a1) in Figure 4.4a4. The single bright protrusions on the upper-step edge (marked by arrows) can be attributed to single molecules and dimers, while the white stripe appears to resemble a dimer row conforming to and along the upper-step edge. A dashed line is drawn alongside the step edge to highlight the change in the step edge direction and to illustrate the close alignment of the molecular wire to the step edge. On the lower-step terrace shown in Figure 4.4a4, the molecular wires appear to originate from the kink (molecular wire W1) and the straight part of the step edge (molecular wire W2). While the double dimer row in molecular wire W2 extends perpendicularly to the step edge, wire W1 is directed 120° from the left side and it emerges perpendicularly to the right side of the step edge. The lower-step edge sites between W1 and W2 wires are filled with discrete bright protrusions, corresponding to individual dimer units that nucleate along a similar growth direction as the W1 and W2 molecular wires. Originated at the lower-step edge as a single dimer row and grown with a 120° step-edge angle initially, wire W3 then changes its growth path and becomes parallel with wires W1 and W2. All the wires nucleated at the step edges extend further onto the terrace following the direction of the underlying $\sqrt{3}\times\sqrt{3}$ -Ag template. Another adsorption morphology near the upper-step and lower-step edges is observed in Area A3 (Figures 4.3a1 and 4.3a5). Near the upper-step edge, the single bright protrusions marked by arrows likely represent the single and dimer methionine adsorbates. The bright stripes running parallel along the upper-step edge (wire W4) and lower-step edge (wire W5) are as wide as the single stripe on the lower-step terrace (wire W6), as shown in the height profile along Line L2 (Figure 4.4a6). Given their similar widths (1.9 - 2.1 nm), they can therefore be considered as single molecular wires.

Like the step edges, the antiphase boundaries also appear to confine the stripes, as supported by the presence of the stripes either formed parallel along or nucleated at and extended from an antiphase boundary. No molecular wires are found to grow across an antiphase boundary. Both step edges and antiphase boundaries provide favourable trapping sites for the methionine admolecules due to their lower coordination numbers (as revealed in the perpendicular and 120° growth directions) and to the perturbation of the electronic density of states as manifested in the alignment of molecular wires along the step edges and antiphase boundaries, i.e. parallel growth.

Figure 4.4b1 shows an STM image of a typical nanoscale grating of dimer rows with defined width and spacing on a lower-step terrace. Similar gratings can also be found on the upper-step terraces. The nano-grating arises as the result of collective alignment of the molecular wires in registry with preferred crystallographic directions of the $\sqrt{3}\times\sqrt{3}$ -Ag surface terraces. These molecular wires are found to originate from one edge of the terrace and extend across the terrace to the opposite edge. Two of the molecular wires orientate from two nearby points at the step edge, P1 and P2, and grow along the directions 60° and 120° , respectively, from the step-edge. The molecular wire at P1 is found to grow with no change in direction and connects at the other end to another step edge, while the one started at P2 evidently changes its direction by 120° after a short distance (3-4 nm) and becomes parallel to the first one (started at P1) and terminates at the opposite step edge. The growth pattern of these molecular wires suggests that their growth directions critically depend on the $\sqrt{3}\times\sqrt{3}$ -Ag surface. The presence of defects on the $\sqrt{3}\times\sqrt{3}$ -Ag template could redirect the growth direction of a molecular wire. In Figure 4.4b1, the larger number of molecular wires along a particular direction may be related to the smaller area of the terrace. In Area A4 (Figure 4.4b1), a short stripe grown on the surface terrace (marked by B) along the dominant direction of the longer stripes is terminated at the junction of another stripe (of nearly the same length) with a 120° rotated growth direction. Closer examination of this “boomerang” structure in Area A4 (Figure 4.4b2) and the individual lines in the nano-grating in Area A5 (Figure 4.4b3) reveals that a slight change in their adsorption sites to the nearest most favorable adsorption sites could lead to notable defects in the molecular wire. These include bends that redirect the growth direction of the molecular wires (leading to the “boomerang” structure (Area A4, Figure 4.4b1) or kinks in the molecular wires (Area A5, Figure 4.4b3). In Figures 4.3b4 and 4.3b5, we overlay schematic models of the dimer rows on the respective STM images of the boomerang and kink structures, in order to illustrate the effects of the minor underlying imperfections in the nanowire growth. Interestingly, the kinks (or dislocations) in the parallel wires of the nano-grating, marked by circles in Area A5 (Figure 4.4b3), all seem to be aligned (and connectable) on a straight line, which suggests the presence of a correlation between the dimer rows

that could be related to the confinement of the surface electronic states between the stripes.^{214,217} More details about the molecular configurations of the molecular wires are given in our DFT study below.

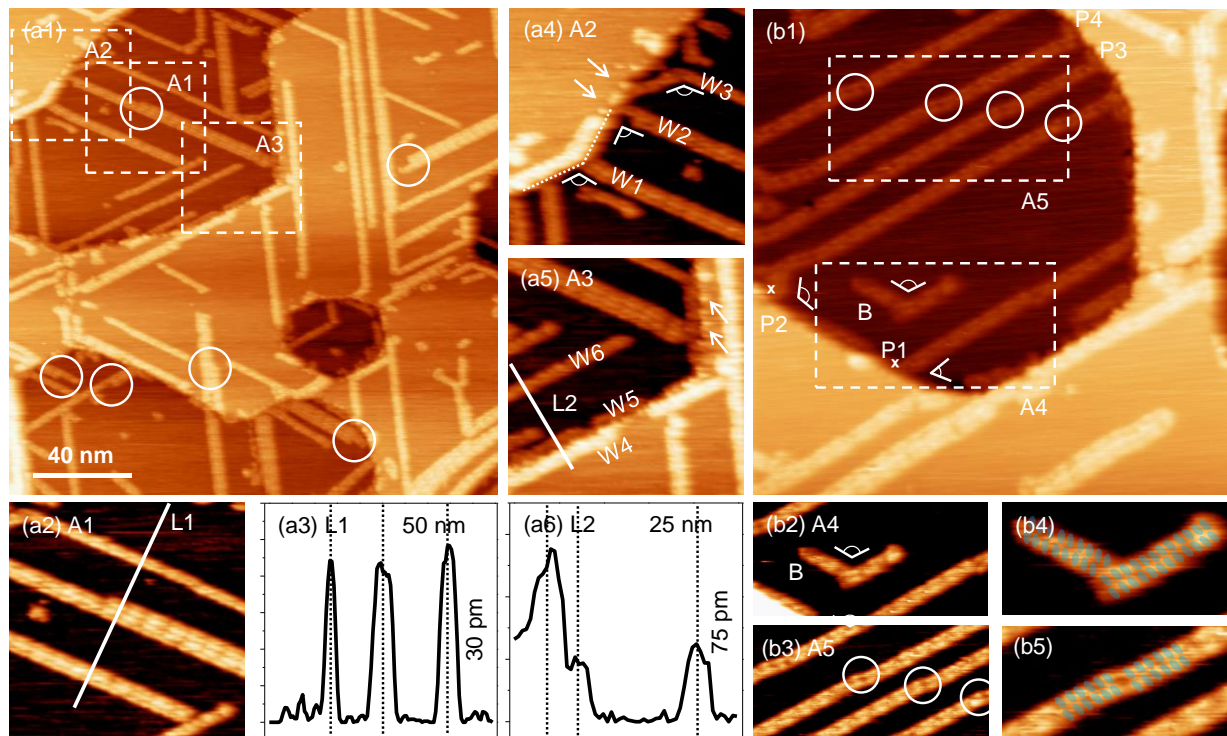


Figure 4.4 Empty-state STM images of a 30-s exposure of L-methionine on Si(111)- $\sqrt{3}\times\sqrt{3}$ -Ag over (a1) a 200×200 nm² area and (b1) a selected 100×100 nm² area at a higher magnification. Expanded views of the selected areas (A1, A2, A3) in (a) and (A4, A5) in (b) are shown to illustrate (a2) the emergence of the dimer rows, (a4) directed growth from the step edges, (a5) parallel growth along the step edges, (b2) a “boomerang” nanostructure and (b3) kinks in a nanograting, respectively. The respective height profiles along Line L1 in (a2) and Line L2 in (a5) are shown in (a3) and (a6), respectively. (b4) and (b5) show schematic diagrams of dimer rows superimposed on the corresponding STM images of the respective boomerang and kink structures. The STM images are obtained with a sample bias of +2.0 V and a tunneling current of 0.2 nA with the sample held at 140 K.

Figure 4.5a shows the STM images of Si(111)- $\sqrt{3}\times\sqrt{3}$ -Ag upon a higher exposure (120 s) of methionine collected at 140 K. Evidently, all the upper-step and lower-step surface terraces are densely covered with adsorbate islands. The island orientations can be seen more clearly in the magnified Area A1 (Figure 4.5b). While the majority of the molecular wires appear to connect to the step edges and antiphase boundaries, not all the molecular wires initiate the growth at these defect sites. Indeed, the dimer stripes growing along three equivalent directions appear to meet at the interception points forming concentric equilateral triangular nanostructures well inside the terraces. In addition to these concentric

triangular nanodomains, nanograting structures (strips of parallel molecular wires) located well inside the terraces (and not connecting to the step edges or antiphase boundaries) are also found when one or more growth directions are disrupted. Other than the increase in the density of these nanostructures, the three-fold symmetry of these oriented adsorbate structures remains unchanged from the structures obtained at a lower coverage (Figure 4.4).

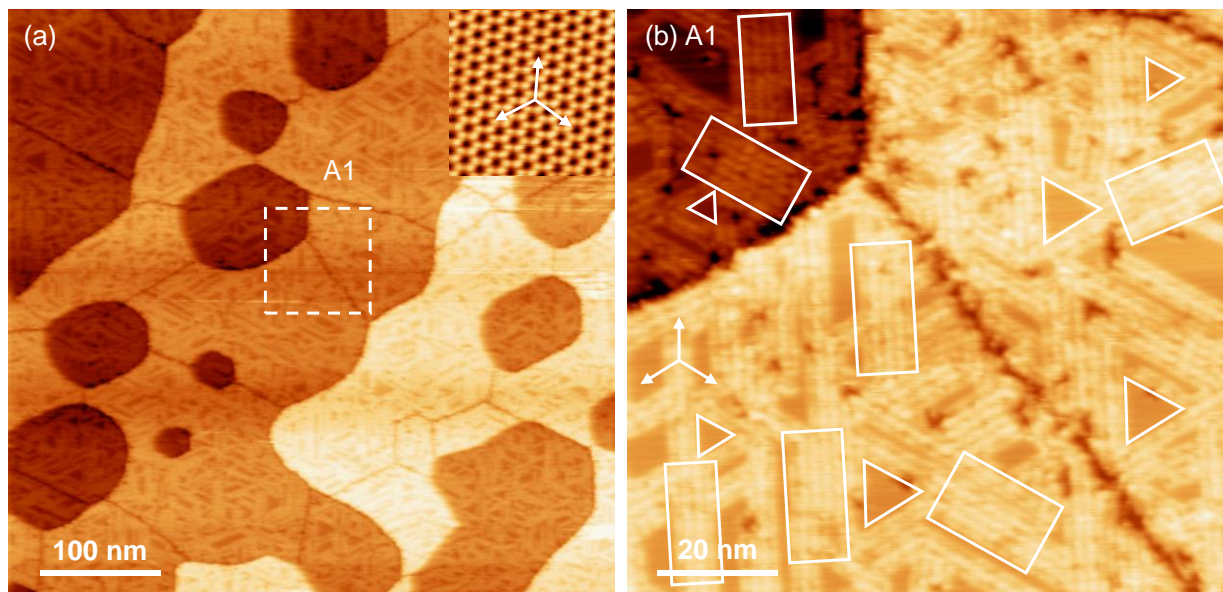


Figure 4.5 Empty-state STM images of a 120-s exposure of L-methionine on Si(111)- $\sqrt{3}\times\sqrt{3}$ -Ag (a) over a $500\times 500\text{ nm}^2$ scan area and (b) a $100\times 100\text{ nm}^2$ scan area [area A1 in (a)]. The inset in (a) shows an atomic resolution STM image of the pristine Si(111)- $\sqrt{3}\times\sqrt{3}$ -Ag surface in the approximate orientation as the substrate in (b) to illustrate the alignment of the molecular wires in nanogratings (marked by rectangles) and triangular nanodomains (the centers of which marked by triangles) along the three equivalent crystallographic directions of the supporting Si(111)- $\sqrt{3}\times\sqrt{3}$ -Ag surface. The STM images are obtained with a sample bias of +2.0 V and a tunneling current of 0.2 nA with the sample held at 140 K.

At this higher exposure, the step edges and antiphase boundaries are still visible, indicating that the growth of the molecular wires does not extend across and cover these defect structures. However, the extent of long-range order seems to be reduced when the merged stripes of variable orientations grow in close proximity creating an increased number of intersections. There are no discernible differences in the morphology, density and distribution of these molecular wire nanostructures between the upper-step terrace and lower-step terrace.

4.2.5 DFT Calculations

To further investigate the dimer-row nanostructures observed in our STM images in more detail, we perform large-scale DFT calculations to discover and optimize the equilibrium geometries of plausible adsorption configurations. To determine the most favorable adsorption site, we begin by placing a single methionine molecule in different configurations on plausible adsorption sites of the surface terrace: Ag monomer (M1), Ag dimer (D1), and Ag trimer (T1), as shown in Figure 4.6a. Since the lone-pair electrons of the S atom in the methylthio methylene group could potentially undergo long-range interactions with the surface states, we orient the methionine molecule with its S atom pointing to the selected adsorption site. For each adsorption site, the molecule is positioned with its long axis (defined in Figure 4.1) rotated around the selected adsorption site counter-clockwise from the surface unit cell axis *a*. After geometry optimization, the resulting adsorption configuration is then denoted by the adsorption site and the degree of counter-clockwise rotation. For example, the adsorption configuration on a Ag dimer site (D1) with the long axis rotated 60° counter-clockwise from *a* is denoted as D1-R60.

Figure 4.6b illustrates the most stable structure of an isolated methionine molecule adsorbed on the Si(111)- $\sqrt{3}\times\sqrt{3}$ -Ag surface near the atop position of an Ag atom (M1) with the long axis rotated 15° counter-clockwise from the *a* axis (R15). An adsorption energy (E_{ad}) of -1.38 eV is found for this a flat-on adsorption configuration (M1-R15), in which the S and N atoms are located approximately above the monomer sites (M1) of a Ag trimer with the methyl group lying flat parallel to the surface. The relatively long separations of Ag-S (2.65 Å) and Ag-N (2.54 Å), compared with their respective nominal covalent radii of 2.35 Å and 2.09 Å,^{218,219} indicate the presence of dative bonding involving the lone-pair electrons of the S and N atoms with the Ag atoms of the surface. As the dispersion force contribution represents 79% (-1.09 eV) of the calculated adsorption energy (-1.38 eV), the molecule-substrate interaction is governed mainly by van der Waals forces.

Using their most stable zwitterionic structure, we optimize the equilibrium adsorption geometries of zwitterionic methionine dimers in antiparallel and parallel configurations, illustrated in Figures 4.5c and 5d respectively. The respective total adsorption energies per molecule for the antiparallel and parallel dimers are -1.29 eV and -1.49 eV, while the contribution due to dispersion forces per molecule in each dimer is -1.07 eV for the antiparallel configuration and -1.09 eV for the parallel configuration. The energy difference between the dimers is most likely originated from the intramolecular stabilization (inside the molecule) via the OH \cdots N hydrogen bonding in the parallel dimer after relaxation. In addition, while the S atoms of both molecules in the dimers are still located on their respective M1 positions, the orientations of the individual molecules in the antiparallel or parallel dimer are different from that in the

most stable configuration of the monomer. The adsorption energies and adsorption configurations of single molecules are therefore compensated by the intermolecular interactions in the methionine dimers.

Based on our STM and XPS results that show extended 1D nanostructures with intermolecular zwitterionic interactions and on previous studies that suggest universality of the intermolecular bonding scheme of amino acids on noble metal surfaces,^{107,108,110} we search for a stable ordered structure of methionine adspecies. We first optimize the geometry of a tetramer (consisting of two antiparallel dimers) oriented along the [1–21] direction, as shown in Figure 4.6e. The corresponding adsorption energy per molecule is found to be more negative by 0.3 eV compared to the monomer and by 0.39 eV and 0.19 eV relative to the antiparallel and parallel dimers respectively. This suggests that the formation of an ordered assembly of dimers could further enhance the adsorption stability with respect to the monomer and dimers. To simulate the adsorption configuration of an extended assembly of 1D molecular dimers, a row of 4 antiparallel methionine dimers (with 8 molecules total in the cell) is placed on an expanded supercell consisting of a 4×4 slab of Si(111)- $\sqrt{3}\times\sqrt{3}$ -Ag in the [1–21] direction. The initial parameters of the dimer row are based on those obtained from the adsorption configurations of the single, dimer, and tetramer, where the S atom of each molecule is positioned near an M1 position. Figure 4.6f shows the optimized structure of the resulting 1D dimer row. Interestingly, the periodicity of the dimer row is in near-perfect match with that of the slab. The corresponding calculated adsorption energy is 1.84 eV per molecule, which shows that the ordered structure is stabilized considerably by, on average, 0.47 eV per molecule due to the intermolecular interactions. The formation of the ordered dimer rows therefore enhances the adsorption stability with respect to the monomer and dimers. The contribution from the dispersion forces remains essentially unchanged at -1.07 eV to the total adsorption energy (per molecule), and it is still the main stabilizing factor of the dimer row. The separation between the S atom and the underlying Ag atom of the M1 site (2.83 Å) has become larger by 0.18 Å, indicating that the stronger intermolecular interaction in the dimer row could also cause a slight reduction in the molecule-substrate interactions.

To illustrate the plausible adsorption configurations of the correlated molecular wires (that are separately aligned in parallel), we superimpose simulated molecular wires on appropriate STM image features in Figure 4.6g. The width of the calculated molecular wires is found to be in excellent accord with the one measured by STM (Figure 4.6g), which in turn affirms that the observed molecular wire does indeed correspond to the dimer row structure. To simulate a thicker molecular wire with double width, two dimer rows (with appropriately optimized geometries) are placed side-by-side on the nearest neighbor adsorption sites as shown in Figure 4.6h. The nearest neighbor adsorption site for a dimer is defined as an adsorption site where both dimers are adsorbed at equivalent adsorption sites (e. g. M1) with a minimum separation between the innermost methyl groups of the opposite dimer rows.

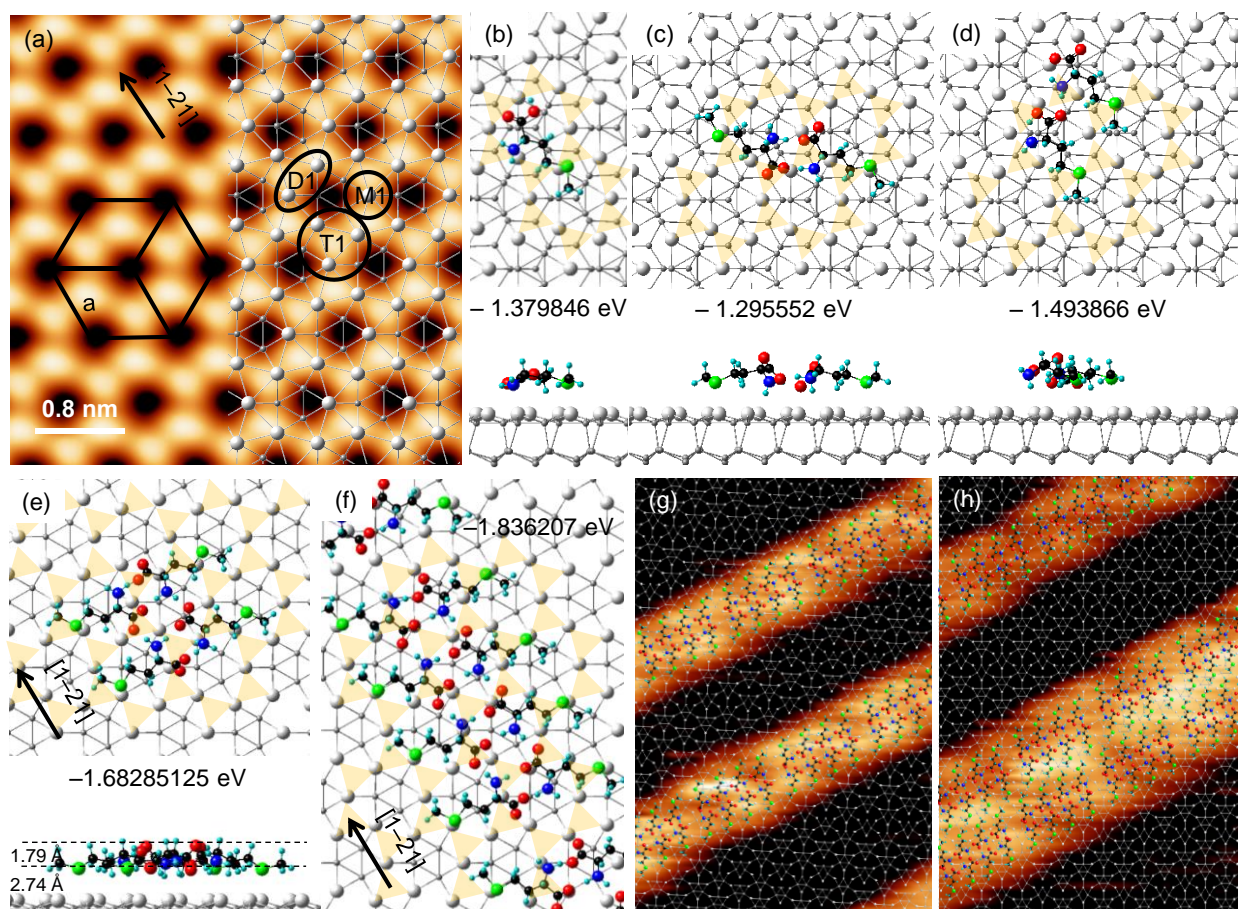


Figure 4.6 (a) A mesh-averaged image (using WSxM) of the atomic-resolution empty-state STM image of the Si(111)- $\sqrt{3}\times\sqrt{3}$ -Ag surface obtained at a sample bias of +1.6 V and a tunneling current of 0.2 nA at room temperature. The hexagon is consisted of three $\sqrt{3}\times\sqrt{3}$ surface unit cells, each with two bright protrusions corresponding to two Ag trimers. The optimized structure of the topmost layer of Si(111)- $\sqrt{3}\times\sqrt{3}$ -Ag is shown along with the corresponding adsorption sites: atop on a Ag monomer (M1), bridge on a Ag dimer (D1) and three-fold hollow on a Ag trimer (T1). Optimized equilibrium structures of (b) a methionine molecule adsorbed with a M1-R115 configuration, (c) an antiparallel dimer with the methionine molecules in an M1-R43 and an M1-R40 configurations, (d) a parallel dimer with methionine in an M1-R74 and an M1-R74 configurations, (e) a tetramer with methionine in the M1-R125, M1-R115, M1-R115, and M1-R125 configurations, and (f) a periodic model of an extended dimer row. The molecular wire can in effect be considered as four antiparallel dimers adsorbed in a dimer row arrangement along the [1-21] direction (dimer row growth direction). The adsorption energy per molecule is also indicated in (b) to (f). Each orange triangle in (b) to (e) corresponds to a single bright protrusion in the STM image in (a). Schematic representations of the calculated dimer rows are superimposed on appropriate STM images to show (g) two separated molecular wires each containing a single dimer row, and (h) two molecular wires containing a single dimer row (top) and a double dimer row (consisting of two single dimer rows side-by-side, bottom).

The minimum separation of the carbon atoms of the methyl groups in an end-to-end configuration of an isolated dimer is calculated to be 4.29 Å in our DFT calculations. In the double dimer row model (Figure 4.6h), this separation is found to be 3.88 Å. This proximity of the methyl groups could lead to an increase in the electronic density of states at the center of the double dimers, as exhibited by an increase in the apparent protrusion intensity at the center of the double dimer rows in the STM image (Figure 4.6h). Indeed, this correlation can be used to explain the intensity profiles of molecular wire structures observed at higher coverages in our STM results, where a greater number of dimers are located side-by-side together to form molecular wires of multiple widths (Figure 4.5). For an n number of increased 1D apparent protrusion intensity (as compared to the protrusion intensity at the wire edge), there are $n+1$ dimer rows in a unidirectional nanodomain (nanograting) in the STM image (Figure 4.5b).

4.2.6 Comparison of Methionine, Cysteine, and Glycine nanofilms on Si(111)- $\sqrt{3}\times\sqrt{3}$ -Ag and adsorbate-induced formation of Ag-Ag bonds

In the study of the adsorption behavior of amino acids on solid surfaces, there are two fundamental areas of interest: (1) the chemical state of the adsorbates, and (2) the driving force in the growth to a thick nanofilm. Amino acids are found mostly in their zwitterionic state in solid or liquid phase, while their chemical state is neutral in the gas phase. On the other hand, their chemical state on a solid surface depends on the nature of the surface states of the substrate, particularly the availability of directional dangling bonds in semiconductors [e.g. Si(111)7×7] or delocalized electron gas in metals [e.g. Ag(111)]. Since a metal silicide surface such as Si(111)- $\sqrt{3}\times\sqrt{3}$ -Ag does not have dangling bond states, it should behave more like a metal surface. After the initial deposition of bioorganic adspecies on a surface, the driving force for growth to a thicker layer depends on the chemical state of the already adsorbed interfacial layer. In our previous studies, we show that the adsorption and film growth of proteinogenic amino acids on the Si(111)7×7 surface generally follow a common three-stage growth mechanism: (1) formation of an interfacial monomolecular layer through directional covalent bonding with the surface dangling bonds and through intermolecular N···HO H-bonds, (2) adsorption of a second molecular layer (the transitional layer) driven by the characteristic interlayer interaction of N···HO H-bonds, and (3) formation and growth of a zwitterionic (multi)layer through additional O···H–N and O···H–O bonds between the transitional layer and zwitterionic layer and through intralayer zwitterionic hydrogen bonding (involving O···H–N H-bonds).^{123,116–120,220,221} The directional dangling bonds and their distribution on the semiconductor surface play a key role in the molecular orientations and intermolecular interactions of the adspecies, and ultimately their adsorption in the neutral state in the interfacial layer. Due to the presence of the free functional groups in the interfacial layer, the gas-phase molecules approaching the surface

could orient themselves to access the free functional groups through H-bond formation, which becomes the main driving force for further growth of the transitional layer. On a metal surface, on the other hand, amino acids are reported to adsorb in neutral, anionic, and zwitterionic forms, depending on the reactivity of the substrate.²⁰⁵ In the case of a zwitterionic interfacial layer on the metal surface, the protonated amino group and deprotonated carboxylic acid group predominantly form intralayer zwitterionic H-bonding, leaving essentially no free functional groups. There is no transitional layer and the growth continues from interfacial layer directly onto the zwitterionic multilayer.

To investigate the effects of different functional groups and of molecular length on the adsorption and film growth behavior on Si(111)- $\sqrt{3}\times\sqrt{3}$ -Ag, we compare the XPS results of methionine with those of cysteine (as the smallest S-containing amino acid) and glycine (as the smallest amino acid) during their nanofilm growth. If we define the molecular length as the separation between the hydroxyl O atom and the farthest non-H atom along the carbon chain backbone in the molecule, then these three amino acids cover a wide range of molecular lengths, from glycine (3.7 Å), to cysteine (4.9 Å), and to methionine (7.4 Å) (Figure 4.1). The lengths of these molecules are obtained for their most stable conformers in the isolated molecule case (in the gas phase) by quantum mechanical calculations. It is of interest to note that the molecular length of methionine is twice that of glycine and 1.5 times that of cysteine, and it is only 12% larger than the length of the $\sqrt{3}\times\sqrt{3}$ -Ag unit cell. The XPS data and the detailed assignments of respective XPS features for cysteine on Si(111)- $\sqrt{3}\times\sqrt{3}$ -Ag have been provided in our recent work and those for glycine on Si(111)- $\sqrt{3}\times\sqrt{3}$ -Ag are given below.

Partial desorption of a glycine film has been observed during the XPS measurements. For the XPS spectra in Figure 4.7, the peak intensities with increasing exposure time may not represent the intensities of a freshly deposited film on the surface. However, we are able to measure all the spectra before desorption of the film, which closely follow the expected N:O:C ratio of 1:1:2. We therefore focus only on evolution of the peak positions and shapes with increasing coverage. It should be noted that the exposure of the X-ray beam to the sample is not the cause of the glycine film desorption because intensity reduction is also observed after storing the sample in ultrahigh vacuum condition for a few hours even without X-ray exposure. Evidently, the prominent features of glycine at 532.0 eV (fwhm=1.4 eV) in the O 1s region, 402.0 eV (fwhm=1.5 eV) in the N 1s region, and 287.0 eV and 289.1 eV (fwhm=1.2 eV) in the C 1s region exhibit chemical-state evolution characteristic of a zwitterionic film with increasing exposure (Figure 4.7). Even at the very early growth stage (the 120-s exposure), zwitterionic intermolecular bonding is clearly present. As no dissociative chemisorption feature is observed in the N 1s region immediately after the deposition, the molecule-substrate interactions are mainly driven by weak van der Waals forces.

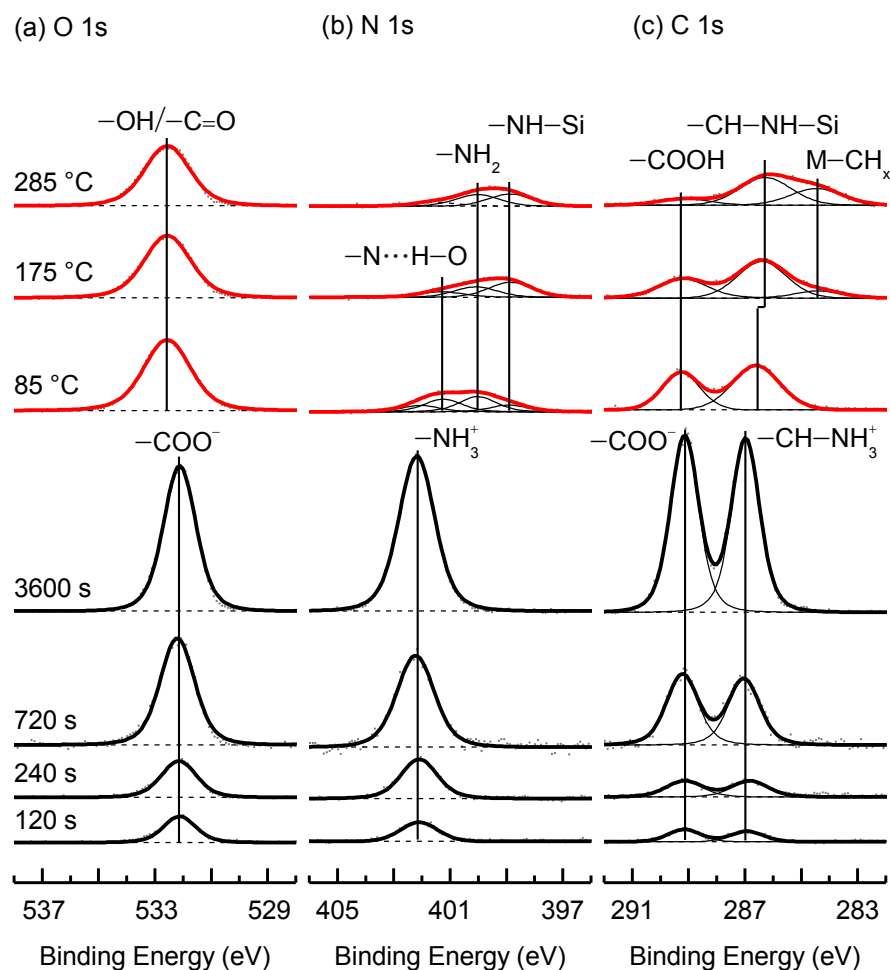


Figure 4.7 Evolution of (a) O 1s, (b) N 1s, and (c) C 1s XPS spectra of glycine deposited on Si(111)- $\sqrt{3}\times\sqrt{3}$ -Ag as a function of exposure time (120–3600 s) and of the as-grown 3600-s glycine film upon annealing to 85, 175, and 285 °C.

Interestingly, the spectra recorded after storage of the sample for 12 h show no evidence of zwitterionic related peaks. Instead, we observe features typical of the deprotonated amino group and a neutral carboxylic acid group. As an example, the spectra recorded after 12 h storage of the sample with a 720-s glycine exposure is shown in Figures 4.8a-c (lower panel). The corresponding STM image in Figure 4.8d shows dark depression areas near the lower-step edges and antiphase boundaries. There are also a few dark depressions on the terraces. The upper-step edges appear to have also been modified. The dark depression areas can be attributed to the chemisorption of glycine molecules through N–Si linkage as supported by the presence of the –NH–Si N 1s feature at 398.8 eV in Figure 4.8b.

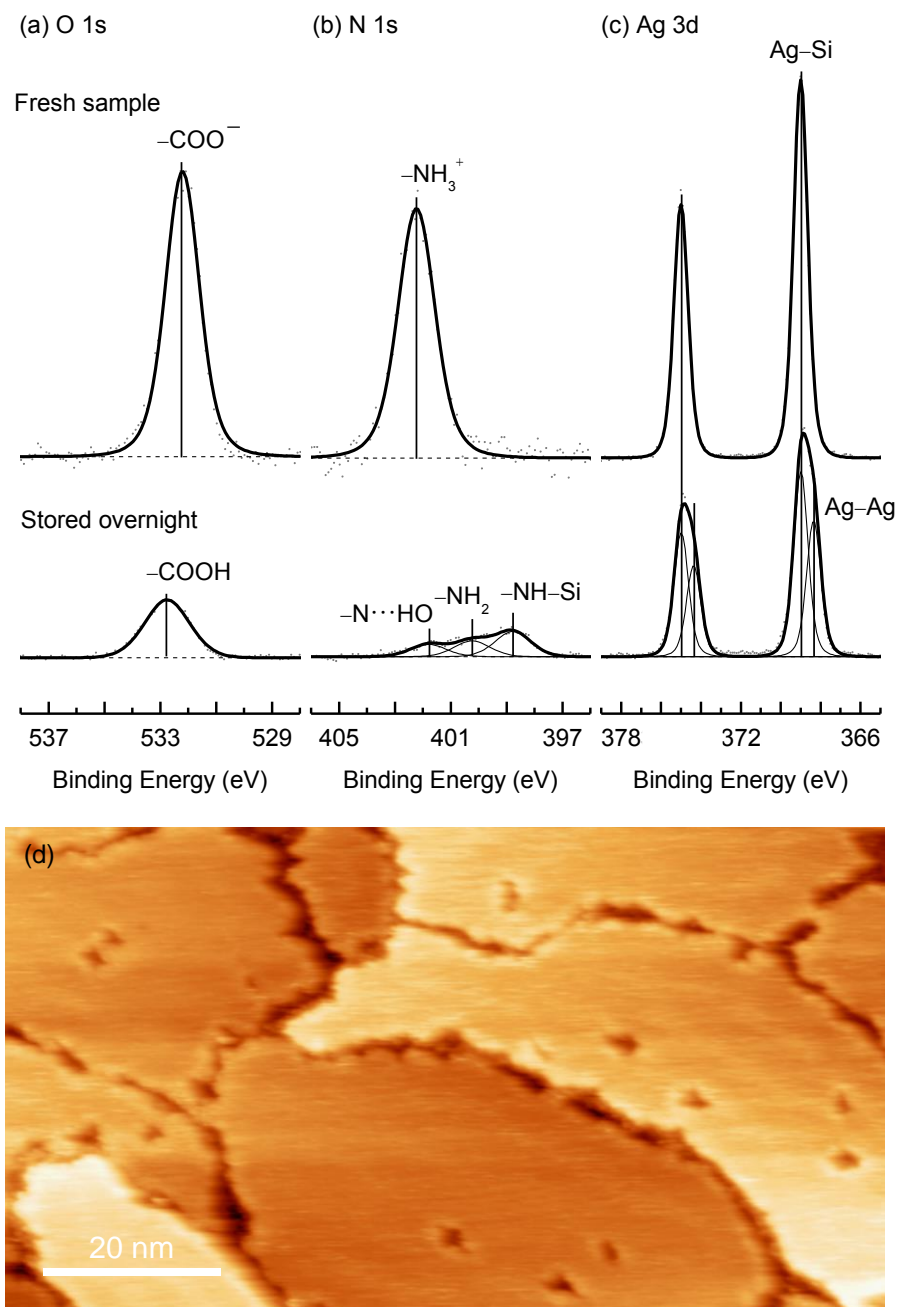


Figure 4.8 XPS spectra of (a) O 1s, (b) N 1s, and (c) Ag 3d regions of Si(111)- $\sqrt{3}\times\sqrt{3}$ -Ag measured immediately after exposure with glycine for 760 s (top panel) and after subsequent overnight storage for 12 h under ultrahigh vacuum condition (bottom panel). (d) Corresponding empty-state STM image of the overnight sample collected at a sample bias of +1.6 V and a tunneling current of 0.2 nA at room temperature.

The concomitant appearance of this chemisorbed N 1s feature (Figure 4.8b) and the Ag 3d shoulder on the lower binding energy side (Figure 4.8c) suggests chemisorption that occurs through either the N–Ag linkage or; or N–Si linkage, or both. In the former case, the Ag 3d_{5/2} feature at 368.4 eV could correspond to the emergence of the –N–Ag moiety. In the latter case, the N–Si linkage would require Ag–Si bond breakage that leads to the accumulation of the dislodged Ag atoms near the adsorption areas and the Ag 3d_{5/2} feature at 368.4 eV and the bright ridges near the dark region in the STM image could correspond to the accumulated Ag atoms. The limited adsorption of glycine on Si(111)-√3×√3-Ag is consistent with earlier studies on a pristine Ag surface, on which chemisorption of glycine is found to be limited due to the apparent inability of this substrate to deprotonate glycine into glycinate at room temperature.^{205,213} In contrast, chemisorption of glycine has been commonly observed on Si surfaces at room temperature through N–Si bond formation.^{116,118–120,220} In addition, we have calculated the adsorption energy of a single glycine molecule on different Ag and Si terrace sites involving a dissociated amino group (Figure B4). The results again support the preference of N–Si linkage rather than the N–Ag linkage, in general accord with the deprotonation of an amino group in proteinogenic amino acids reported on Si surfaces,¹²³ but not on noble metal single crystal surfaces (Cu, Ag, Au) at room temperature.²⁰⁵ Our combined XPS and STM data therefore support weak physisorption of glycine on terraces and chemisorption at exposed Si sites at the step edges and antiphase boundaries (following metal ridge formation near the chemisorption areas). The presence of defects provides trapping sites for glycine molecules, where glycine can overcome the deprotonation barrier through interaction with Si atoms. The small size of the glycine molecule (3.7 Å) relative to the cavity size of the Si trimer (6.6 Å) near the step edge enables glycine to reach closer to a Si atom to facilitate the deprotonation process.

Zwitterionic chemical states corresponding to the O 1s and C 1s features of a deprotonated carboxylic acid group (–COO[–]) and to the N 1s feature of a protonated amino group (–NH₃⁺) are observed in all three amino acids (methionine, cysteine and glycine) from sub-monolayer to multilayer coverages. The only notable exception is the presence of the O 1s feature for the neutral carboxylic acid group (–COOH) found for cysteine. In the case of cysteine, we are able to estimate the extent of zwitterionic adspecies in the second adlayer adsorption using the S 2s spectrum. However, this is not possible for methionine because there is no chemisorption involving S in their interfacial layer (Figure 4.2), and for glycine due to the absence of a S component. In contrast to the adsorption of amino acids on Si surfaces, formation of a transitional layer does not occur in the growth mechanism of all three amino acids on Si(111)-√3×√3-Ag. This is consistent with the formation of a zwitterionic layer already initiated in the interfacial layer and continued adsorption to form the second adlayer. The latter could occur through either the interlayer zwitterionic H-bonding or physisorption of the (non-zwitterionic) molecules or both.

The occurrence of the interlayer zwitterionic H-bonding depends on the orientation of their amino and carboxylic acid groups with respect to the surface. While a flat configuration of the COO^- group is generally required for intralayer zwitterionic H-bonding on metal surfaces, a more upright orientation of COO^- could facilitate both intralayer and interlayer zwitterionic H-bonding.

The nature of the molecule-substrate interactions in all three amino acids control their respective thermal stabilities on the $\text{Si}(111)\text{-}\sqrt{3}\times\sqrt{3}\text{-Ag}$ surface. For all three molecules, the nature of adsorption on surface terraces is markedly different from that at defect sites. On terrace sites, the presence of the thiol group enables chemisorption of cysteine in the interfacial layer, which in turn provides sufficient stability at room temperature and at elevated temperatures. In contrast, glycine adsorption is hardly possible on surface terraces at room temperature. For methionine, the S atom is connected to a methyl group making the methylthio methylene group an inert side chain for chemisorption on the surface. Although weak van der Waals forces (physisorption) govern the molecule-substrate interactions, the large size of the methionine molecules and their flat-lying adsorption configuration provide sufficient dispersion forces (between the adsorbates and the substrate) for them to be stable at room temperature. Moreover, the intermolecular zwitterionic hydrogen bonding of the dimer rows further helps to stabilize the adsorbate film at room temperature. The van der Waals forces are, however, not strong enough to withstand the thermal activation upon annealing the methionine film. On the other hand, chemisorption at defect sites is found to be viable for all three amino acids, with the dominant chemisorption features S–Ag for cysteine and N–Si for both methionine and glycine. After annealing to 175 °C, all chemisorbed species remain trapped on the $\text{Si}(111)\text{-}\sqrt{3}\times\sqrt{3}\text{-Ag}$ surface for all three amino acids, following a similar trend seen in the annealing of these amino acid nanofilms on the $\text{Si}(111)7\times 7$ surface.

Figure 4.9 shows the Ag 3d spectra of a glycine multilayer film (obtained with a 3600-s exposure) on $\text{Si}(111)\text{-}\sqrt{3}\times\sqrt{3}\text{-Ag}$ before and after annealing. Interestingly, the presence of each of the three amino acid nanofilms on the $\text{Si}(111)\text{-}\sqrt{3}\times\sqrt{3}\text{-Ag}$ surface has a similar effect of inducing formation of metallic agglomerates (islands or clusters) as supported by the emergence of the metallic Ag $3d_{5/2}$ (Ag $3d_{3/2}$) features at 368.3 eV (374.3 eV) after annealing. This is a significant result as there has been no report to date on metal cluster formation induced by organic adsorbates on the $\text{Si}(111)\text{-}\sqrt{3}\times\sqrt{3}\text{-Ag}$ surface. The present work therefore illustrates the potential of using these amino acids to transform a two-dimensional metal overlayer into metallic agglomerates appropriate for catalysis, sensing and nanopatterning applications. Figure 4.10 illustrates a schematic model of the three amino acids film growth at room temperature (Figure 4.10a and b) and their induced cluster formation after annealing (Figure 4.10c).

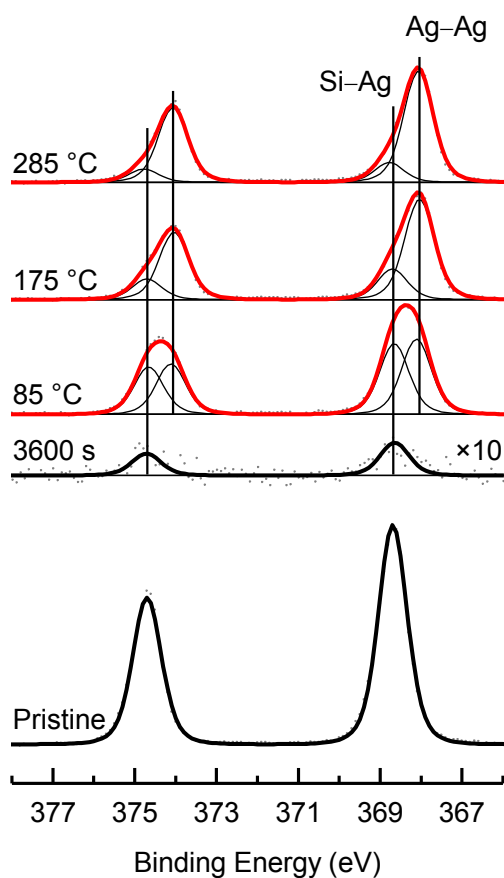


Figure 4.9 Evolution of Ag 3d XPS spectra of the clean Si(111)- $\sqrt{3}\times\sqrt{3}$ -Ag surface before and after deposition of glycine for 3600 s and of the as-grown glycine film upon annealing to 85, 175, and 285 °C.

The formation of metallic agglomerates appears to depend on the coverage of the chemisorbed species on the surface. As observed in the case of glycine adsorption, the terraces are largely uncovered (Figure 4.8b), and they remain intact after annealing (not shown). The presence of the organic molecules, adsorbed in close proximity to one another on the surface, confines the diffusion of the dislodged Ag atoms guiding them to agglomerate and form metal islands and clusters. When chemisorption occurs only around the defects (low coverage), the dislodged Ag atoms form only metallic ridges and metal adatom gas. On single-crystal metal surfaces such as Au(110),²²² the adsorption of amino acids induces reconstruction that causes reordering and faceting of the surface.^{96,223} While in most cases this phenomenon is observed through chemisorption after annealing, it could also occur at room temperature involving physisorption in rare cases. Induced formation of metal clusters on the Si(111)- $\sqrt{3}\times\sqrt{3}$ -Ag^{194,199-201,224} and Si(111)- $\sqrt{3}\times\sqrt{3}$ -In²²⁵ surfaces has been reported through adsorption of hydrogen atoms at room temperature. An early study also showed that NH₃ dissociative adsorption on Si(111)- $\sqrt{3}\times\sqrt{3}$ -Al and

Si(111)- $\sqrt{3}\times\sqrt{3}$ -Ag surfaces could cause structural transformation of the reconstructed surface on the former but not the latter surface.²²⁶ The (dissociated) hydrogen atoms could cause breakage of the Si–Ag bonds, freeing the Ag adatoms on the Si(111)1 \times 1-H surface to migrate and nucleate into metallic clusters in a commensurate fashion with the underlying surface orientation.^{194,200–202,224,225} Despite the strong covalent bonding in the Ag–Si moieties arising from saturation of the Si dangling bonds, the presence of any amount of surface strain on the Ag overlayer could weaken the Ag–Si bonds. In addition to organic adspecies, the transformation of highly ordered $\sqrt{3}\times\sqrt{3}$ -Ag structure to metallic agglomerates after annealing in the present work can therefore also be caused by hydrogen atoms resulted from thermally activated dehydrogenation of the amino group as evidenced in the N 1s region (Figure 4.2b).

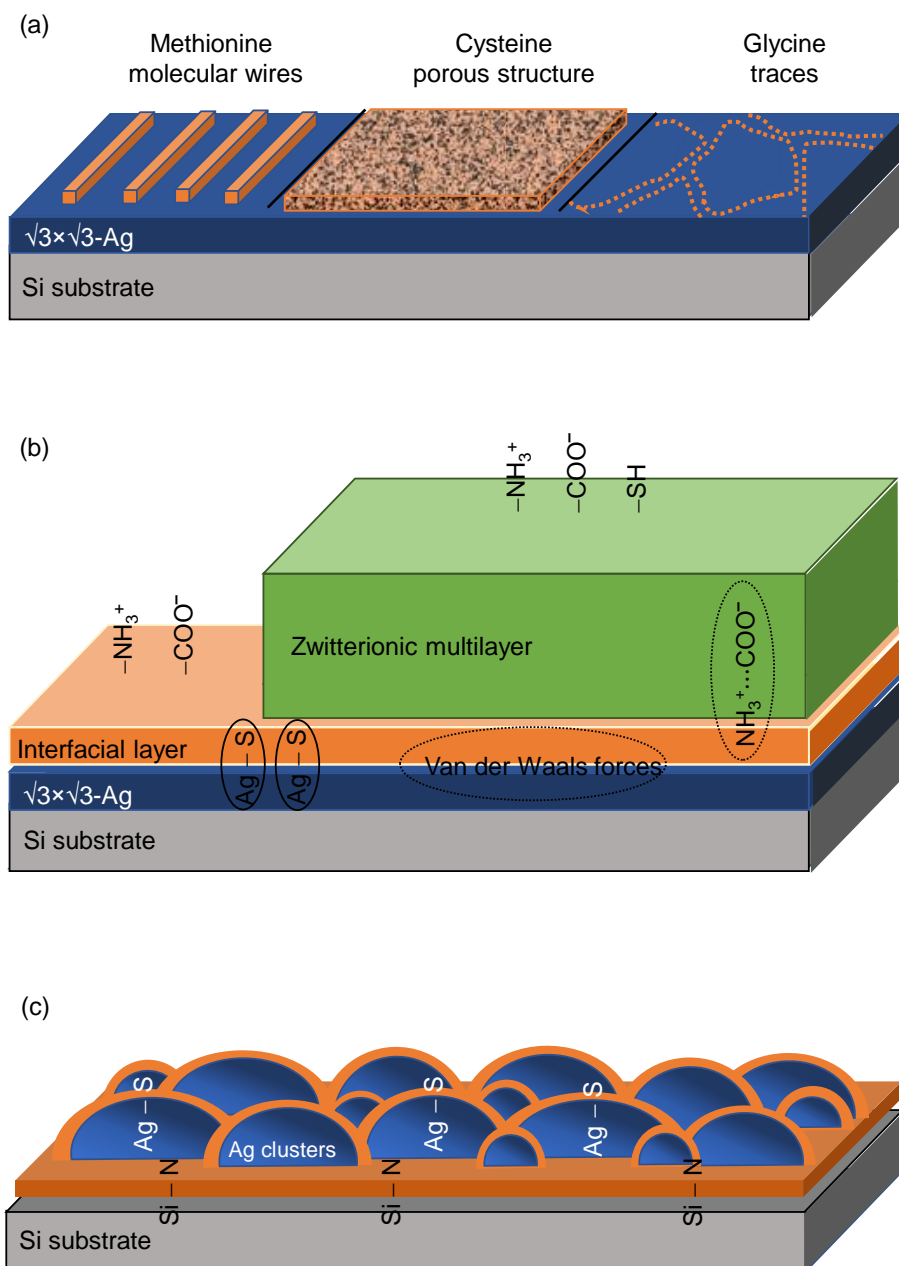


Figure 4.10 Schematic models for growth evolution of three amino acid films (glycine, cysteine, and methionine) on Si(111)- $\sqrt{3}\times\sqrt{3}$ -Ag, depicting (a) interfacial layer of nanostructures in the early growth stage and (b) multilayer of zwitterions with interlayer and intralayer interactions at room temperature, and (c) metal island/cluster formation after annealing of the as-grown thick multilayer film to 175 and 285 °C.

4.3 Summary

We have investigated nanofilm growth of methionine on Si(111)- $\sqrt{3}\times\sqrt{3}$ -Ag at room temperature and at 140 K. XPS and STM analyses provide a coherent film growth picture that involves the formation of the interfacial first-adlayer followed by zwitterionic multilayer. These results are complemented with our DFT calculations to provide further insights into the interfacial processes. Adsorption of methionine on a supported two-dimensional metal silicide overlayer like $\sqrt{3}\times\sqrt{3}$ -Ag is found to follow the two-stage growth mechanism found on a single-crystal metal surface [e.g., Ag(111)] rather than the three-stage growth on a semiconductor surface [e.g. Si(111)7 \times 7] (Figure 4.3). We observe self-assembly of zwitterionic dimer rows of methionine along the surface close-packed directions at room temperature, which becomes more pronounced and well-defined at low temperature. These results are consistent with our DFT calculations that show the viability of the formation of methionine dimers and tetramers and the emergence of the dimer row as the molecular wire. We also demonstrate the molecular size effect by following the glycine adsorption on Si(111)- $\sqrt{3}\times\sqrt{3}$ -Ag with XPS, and compare the results with those of cysteine and methionine. Nanofilm growth of these three amino acids on Si(111)- $\sqrt{3}\times\sqrt{3}$ -Ag at room temperature and their evolution after annealing follow similar trends. Despite the difference in the nature of the initial adsorption, physisorbed glycine and methionine and chemisorbed cysteine all induce surface structural transformation of the $\sqrt{3}\times\sqrt{3}$ -Ag substrate overlayer at elevated temperatures. The presence of metallic Ag 3d features indicates the formation of metallic nanoclusters and/or nanostructures (or agglomerates with 3-dimensional geometry) induced by these amino acids (Figure 4.3). The Si(111)- $\sqrt{3}\times\sqrt{3}$ -Ag therefore offers a rather unique testbed for developing not only self-assembled amino acid nanowires but also metal nanoclusters and agglomerates for potential applications in catalysis and sensing as well as molecular photonics, plasmonics.

Chapter 5

One-dimensional Defects on Si(111)- $\sqrt{3}\times\sqrt{3}$ -Ag: DFT simulation of the step edge and antiphase boundary

5.1 Introduction

Investigation of surface defects is a big challenge in the study of solid surfaces. Beside close-packed flat surfaces, nearly all real surfaces exhibit some forms of defects, such as steps and kinks, which can influence the overall surface properties. The physical and electronic properties of defect sites could deviate significantly from the terrace sites. Studies on surface defects, particularly those on step edges, are especially important to their applications in catalysis and in film deposition and growth. There are various experimental and theoretical studies on the adsorption and reaction behavior of molecules at the step edges on metal surfaces such as Pt(111),¹²⁵ Pt(211) and Pt(311),¹²⁶ Ni(111),¹²⁷ Au(111),^{128,129} and Cu(531),¹³⁰ and on oxide surfaces including TiO₂(110)¹³¹ and Al₂O₃(0001).¹³² The step-edge configuration on the high-index vicinal surfaces of metal single crystals is defined by the cutting (misorientation) angle of the bulk material, and it corresponds to the bulk-terminated arrangement on the microfacets. For example, a Au(310) surface consists of (100) terraces and (110) steps. On semiconductor surfaces, on the other hand, the presence of a high density of dangling bonds along with the surface strains lead to the reconstruction of the semiconductor surfaces in order to minimize the surface energy. At the step edges, the two-dimensional periodicity of the surface structure is interrupted, resulting in a higher number of dangling bonds, which enhances many important surface phenomena including adsorption and crystal growth. These step-edge sites are therefore good candidates for use as templates for guiding the formation of self-organized quantum wires and quantum dots in nanomaterials synthesis and nanofabrication.

The Si(111)- $\sqrt{3}\times\sqrt{3}$ -Ag is one of the most important prototypical metal-semiconductor hybrid surfaces. It is formed by deposition of one monolayer of Ag on the Si(111)7×7 surface followed by annealing to 500 °C. The Ag-induced surface reconstruction is known to change the Si atomic density, i.e. the presence of Ag atoms at an elevated temperature causes restructuring of the 7×7 periodicity by removing the stacking fault to produce a pristine (111) surface. This process involves ejection of the Si adatoms in the Si layer underneath (called hole) and their relocation/accumulation as an island near the ejected area (called island), creating an island-hole pair. The topmost Si layer consisting of these island-hole pairs is then reconstructed to a network of Si trimers, where each Si atom is bonded to one Ag atom, creating Ag trimers located in between the Si trimers (in x-y coordination) and 0.8 Å higher than the Si trimers in the z-direction.^{61,195} The formation mechanism and the surface structure have been investigated

extensively and there is a general consensus for two surface models: the honeycomb chain trimer (HCT) model and the inequivalent triangle (IET) model, of which the IET is known to be an asymmetrical variant of the HCT.^{61,147,63,227} It has been claimed that thermal averaging of the trimer fluctuations results in the HCT appearance of the surface at room temperature.²²⁸ The Si trimers occupy the T4 sites (Figure C1) of the underlying Si bilayer on both islands and holes, creating only one type of the $\sqrt{3}\times\sqrt{3}$ domain.⁵⁹ As the dispersion corrected calculation methods (e. g. DFT-D2) do not lead to an optimized equilibrium IET structure and since these methods are required to obtain accurate organic molecular adsorption geometries, all calculations have been performed based on the HCT model.

The Si(111)- $\sqrt{3}\times\sqrt{3}$ -Ag surface contains various types of defects including step edges, antiphase boundaries, adatom and vacancy defects.¹⁹⁶ A step edge represents the transitional interface between the island and hole pairs and is usually 3.1 Å high.¹⁹⁵ An antiphase boundary is formed when two islands (or holes) located at different T4 adsorption sites grow into each other, creating a boundary caused by a “T4-T4 shift”.¹⁹⁶ Among the reported experimental and theoretical studies on the atomic structures of surface terraces and defects and in spite of the desire to understand surface defects in the early days of discovering this prototypical surface, there is no theoretical studies on the structure and configuration of the surface step edges, arguably the most important type of surface defects on the Si(111)- $\sqrt{3}\times\sqrt{3}$ -Ag surface because of their high density. With the advancement of technology to date, we are able to elucidate complex reconstructions on a larger scale using plane wave basis sets in advanced quantum mechanical computational software such as VASP. In addition, the adsorption behavior of atoms and molecules and the morphology of the resulting as-grown film on the $\sqrt{3}\times\sqrt{3}$ -Ag surface are strongly dependent on these defects, because the geometrical and physical properties of the surface terrace sites usually deviate significantly from those at the step-edge sites, which affect the overall electronic and other properties of the $\sqrt{3}\times\sqrt{3}$ -Ag surface. Detailed understanding of the electronic properties of these defect sites also promises new insights for developing applications based on the Si(111)- $\sqrt{3}\times\sqrt{3}$ -Ag surface. Here, we provide, for the first time, large-scale ab-initio calculations to determine the step-edge and antiphase boundary configurations of the Si(111)- $\sqrt{3}\times\sqrt{3}$ -Ag surface using computational methods based on the density functional theory (DFT). We show that the geometry of the step edge depends on the stoichiometric ratio of the number of Ag atoms to that of Si atoms at the step edge. We further show that there are no Si dangling bonds at the step edge and antiphase boundary. We illustrate the electronic effect at the step edge and the antiphase boundary based on their calculated total and partial density of states.

5.2 Simulation Details

The geometry of a step edge on the Si(111)- $\sqrt{3}\times\sqrt{3}$ -Ag surface critically depends on the formation mechanism of the surface because it involves a change in density of Si atoms and the formation of Si trimers and Ag trimers. Step edges of the Si(111)- $\sqrt{3}\times\sqrt{3}$ -Ag surface are found to extend along the [1-21] and [110] crystallographic directions.^{59,196} In this work, we have chosen to focus on the configurations of step edges along the [1-21] direction. There are two approaches to building the model: the periodic high index slab model and the island model. We employ both models to determine the structures of the step edges. However, the island model appears to be closer in geometry to that we observe experimentally as our STM result shows that the terrace corresponds to a combination of alternating island and hole pairs and not to a high-index stepped surface. A periodic slab of two Si bilayers (192 Si atoms) with an x-y dimension equivalent to $8\times 4\sqrt{3}\times\sqrt{3}$ unit cells is used. The bottom layer of the slab is terminated with 96 H atoms. An island-hole pair with equal island and hole sizes is created by stacking one Si bilayer of 4×4 dimension (96 Si atoms) on top of the already built 8×4 slab. The Si trimers are then added on top of the T4 adsorption sites of the topmost Si bilayer on both islands and holes. Finally, each Si atom in the trimer is bonded to one Ag atom in a Ag trimer, creating a honeycomb of trimers with one monolayer coverage. A vacuum gap of 10 Å is chosen in the z direction for the supercell. To build the antiphase boundary, a surface terrace of an already optimized $\sqrt{3}\times\sqrt{3}$ structure containing 8×4 unit cells and three Si bilayers is used. The antiphase boundary is created by translating half of the Si-Ag trimer layer (in the [1-21] direction) to the neighboring equivalent T4 sites on the Si bilayer. The completed slab models are shown in Figure C2.

The geometries of the slabs in both cases are optimized after each aforementioned step in building the slabs. Density functional theory calculations including the effect of dispersion correction (DFT-D2) are employed using the generalized gradient approximation (GGA) with the Perdew-Burke-Ernzerhof (PBE) exchange correlation functional and projector augmented wave (PAW) potentials. All calculations are performed by using the Vienna Ab-initio Simulation Package (VASP, version 5.4) with the MedeA platform (Materials Design, version 2.19). The surface Brillouin zone is sampled at the Γ point with a k-point spacing of 0.5 \AA^{-1} , and the plane wave expansion cutoff is set to 400 eV. The conjugate-gradient algorithm is used to optimize the geometry of the stationary points. The self-consistency convergence criterion is set to 10^{-5} eV, while the Si and Ag atoms are relaxed until the forces on all atoms are less than 0.05 eV/\AA .

5.3 Results and Discussion

5.3.1 Step Edge

The STM measurements on the step edges have been performed with variable contrasts in both filled-state and empty-state imaging modes. The presence of a ridge of increased protrusion is clearly observed near the upper-step edge of the step in the filled-state images (not shown), while its contrast is considerably less apparent in the corresponding empty-state images.^{59,196} This phenomenon has therefore been correlated with electronic effects rather than the topological ones.¹⁹⁶

Figure 5.1a shows an empty-state STM image of the surface with a step edge along the [1–21] direction. A hexagonal mesh containing red triangles is superimposed on top of the dark depressions of the upper-step terrace of the image, which mark the positions of the Si trimers on the T4 adsorption sites of the topmost Si bilayer. The major adsorption sites of a Si(111) bilayer are illustrated in Figure C1. While the positions of the red triangles perfectly match those of the Si trimers on the upper-step terrace, they appear to be located on the H3 adsorption sites of the Si bilayer on the lower-step terrace, which is in good accord with the earlier reports on the island-hole pair structures.^{55,56,59} Since the stacking of the Si bilayers follows an A-B-C stacking sequence, the H3 sites of the upper bilayer (on the island) are equivalent to the T4 sites of the lower bilayer (on the hole), i.e., the adsorption sites of the Si trimers are always located at T4 sites on both lower-step and upper-step terraces. We further confirm the validity of this model by DFT calculations, which show that the total energy of the terrace slab with the T4 adsorption sites is 0.2 eV per unit cell more negative than the one with the H3 adsorption sites. We therefore construct our step edge models based on Si trimers located on the T4 sites.

Figure 5.1b shows a magnified area of the step edge in Figure 5.1a, and a corresponding apparent height profile along a line across the step edge (connecting points A and B) is shown in Figure 5.1c. The separations of the features shown in the apparent height profile (Figure 5.1c) will be used as a guide to build and validate our model. The coverage of the terrace sites is known to be 1 monolayer, with a Si-to-Ag stoichiometric ratio of 1:1. On the other hand, the areal ratio of the upper-step terrace to the lower-step terrace has been reported to be ~ 1 ideally, and it changes (to usually less than 1) depending on the surface preparation procedure.⁶⁰ In addition, the shape of the step edges varies from sloping and blunt to straight and sharp according to the details of the preparation procedure (such as the deposition and annealing temperatures, and the amount of deposition time). It has been reported that the step edges of the Si(111)- $\sqrt{3}\times\sqrt{3}$ -Ag surface serve as reservoirs of excess Ag atoms to provide further growth and extension of the lower-step terrace regions upon further annealing.²²⁹ It is also known that, in general, the number of dangling bonds is higher at the step edges of a Si(111) surface than those on terraces sites due to the

truncation in the x-y direction.²³⁰ It is therefore reasonable to expect a higher density of Ag adatom adsorbates at the step edges. Since the electronic density morphology of the step edges cannot be observed with STM measurements due to its sloping plane with respect to the x-y plane of the surface, a trial-and-error method is used to search for the most reasonable (realistic) step edge configuration. Given the 1:1 areal ratio of upper-step and lower-step terraces and the overall single monolayer coverage observed experimentally, we start our trial quest with building an idealized step edge in which the numbers of Si and Ag atoms on upper-step and lower-step terraces are equal, and the Si trimers are located on the T4 adsorption sites on both upper-step and lower-step terraces. In our model, we have adopted the periodicity of the honeycomb chain trimer model to continue to the step edges. Each of the peak maxima in the apparent height profile in Figure 5.1c (and the centers of protrusions in Figure 5.1b) can therefore be attributed to the (empty-state) electron density maximum at the center of three Ag atoms (i.e. the Ag trimer).

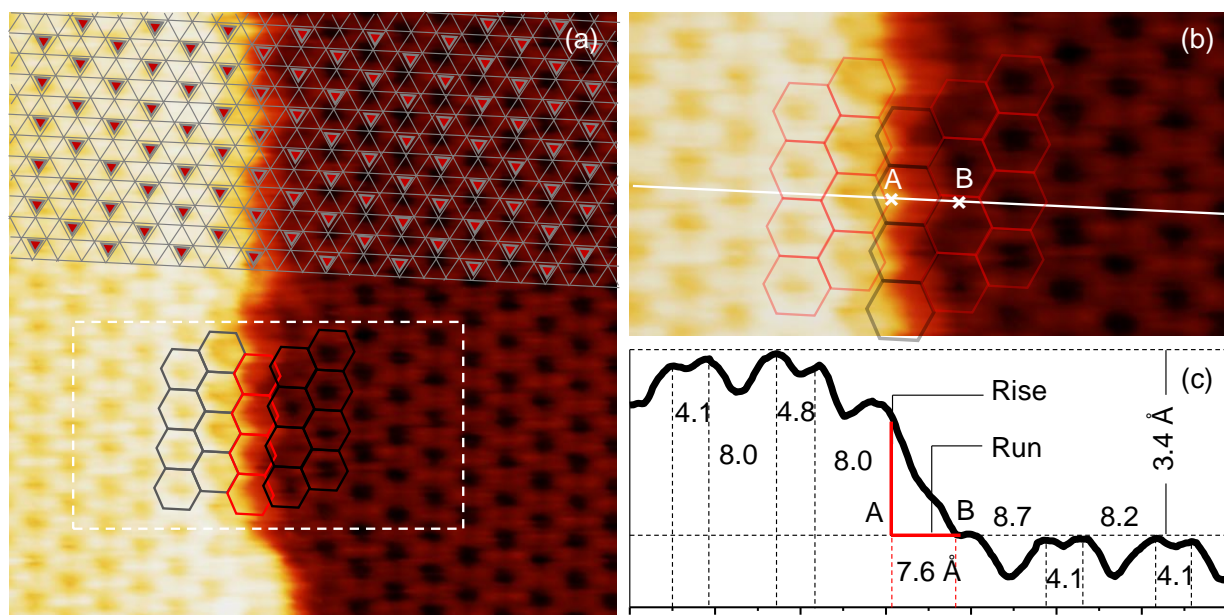


Figure 5.1 Empty-state STM images obtained with a sample bias of +0.9 V and a constant tunneling current of 0.2 nA for a pristine Si(111)- $\sqrt{3}\times\sqrt{3}$ -Ag near a [1-21] step edge for (a) a 10×10 nm² scan area and (b) a magnified area of 3×7 nm² marked in (a). (c) Apparent height profile along the line across points A and B in (b) depicting the well-defined periodicity found for the upper-step and lower-step terraces. The separation between A and B correspond to the run distance and is found to be 7.6 Å.

The optimized equilibrium geometry of this model is shown in Figure 5.2a1. In the top view, the upper-step terrace and lower-step terrace of the honeycomb chain trimer structure are highlighted with

light blue and dark blue circles, respectively, which correspond to the maxima of the bright protrusions in our STM image in Figure 5.1b. The hexagonal symmetry of these trimer maxima is illustrated by red hexagonal meshes overlaid on both terraces. Figure 5.2a2 shows the side view of the slab, of which the step-edge region is marked by a wedge consisting of the rise, the run, and the slope. The horizontal width of the step-edge region (the run) is 6.54 Å and its height (the rise) is 3.1 Å. This is in good agreement with the apparent height profile of our STM result shown in Figure 5.1c, where the run and the rise are estimated to be 7.6 Å and 3.4 Å, respectively. It should be noted that the STM images shown in Figure 5.1 contain minor distortions (caused by the tip) as the separation between two Ag trimer maxima should be 3.0 Å. The step edge can be considered a nearly one-dimensional (1D) structure extended along the step slope. The front view of the step edge shown in Figure 5.2a3 indicates that the parallelogram unit cell of this 1D structure (as projected on the rise plane) consists of three Si atoms and three Ag atoms creating a 1:1 stoichiometry at the step edge. The dangling bonds of each Si atom at the upper-step edge and lower-step edge of the step edge are passivated as each Si atom is bonded to one Ag atom, consistent with the unity Si:Ag stoichiometric ratio on the terraces.

The adsorption sites for chemisorption at the slope of the step edge region can generally be categorized as monomers of Ag (labelled as M1) and Si (M2), dimers Ag–Ag (D1) and Si–Si (D2) and Ag–Si (D3), and trimers of Ag atoms (T1). Using cysteine as a “probe” adsorbate, our calculation shows that cysteine adsorption (through a dehydrogenated thiol group) at the M2 (Si monomer) site at the upper-step edge (of the step) is the most favorable adsorption site. This is, however, in marked contrast to our STM and XPS experimental results, which show that the adsorption is preferred on the Ag atoms and at the lower-edge of the step edge. One possible cause for this apparent inconsistency is that there are excess Ag atoms on the surface used in our experiments. However, we have reproduced the experimental results on the surfaces with several different Ag coverages up to 1 monolayer, which show that the upper-step edges remain intact and free of adsorbates especially at lower coverages. This leads us to believe that the model in Figures 5.2a1-5.2a3 could be inadequate. Although the Si dangling bonds at the step edge are passivated by Ag atoms in our model, their coordination number at the upper-step edge is smaller than those on the terraces and the lower-step edge. While each Si atom is surrounded by three Si atoms and three Ag atoms on the terraces and the lower-step edge, the number of Ag atoms surrounding a Si atom is just two on the upper-step edge.

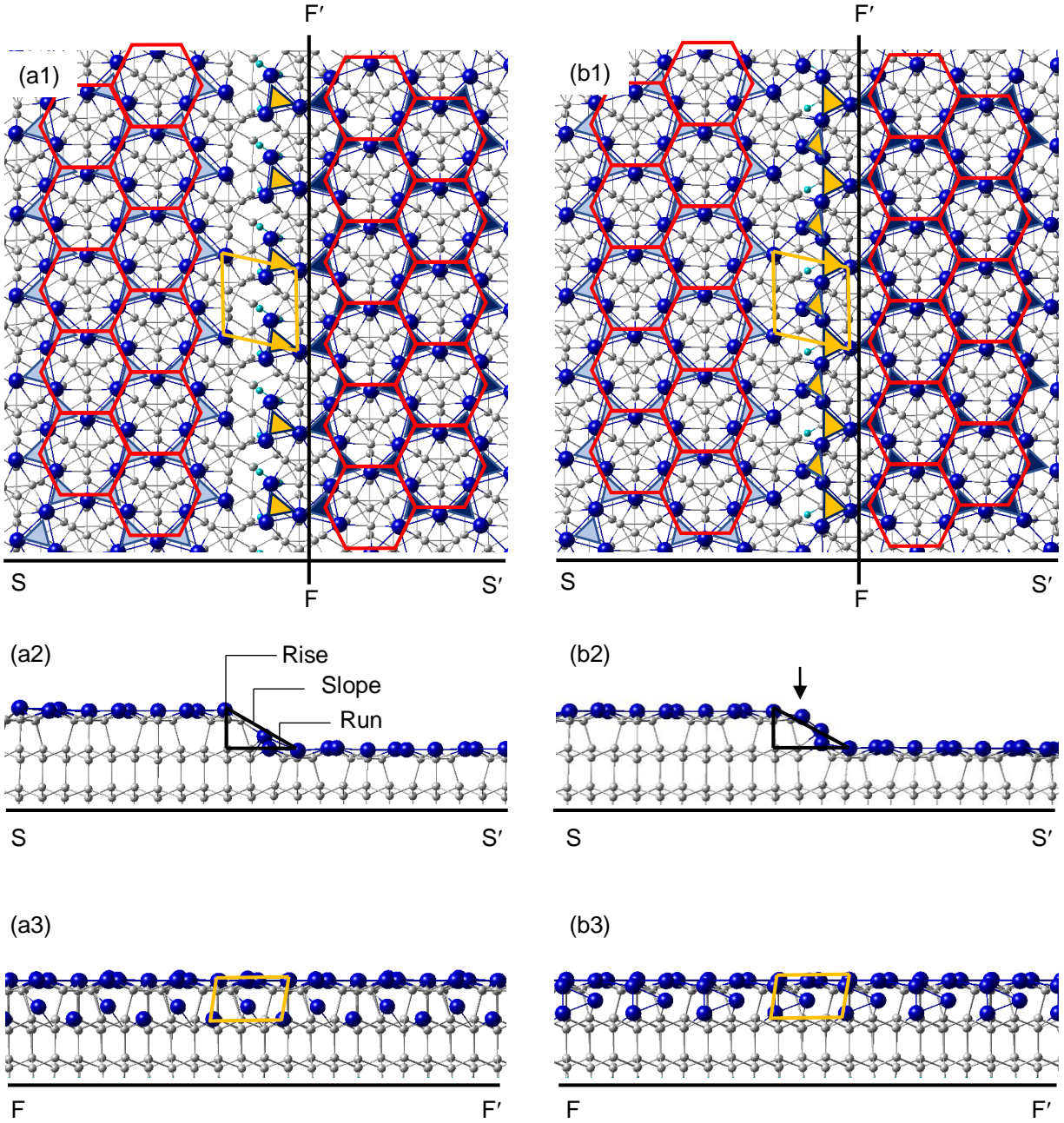


Figure 5.2 Optimized geometries for two step-edge models with (a1-a3) a Ag_3Si_3 unit cell and (b1-b3) a Ag_4Si_3 unit cell in the step-edge region, each shown in (a1, b1) top view, (a2, b2) side view along SS' direction and (a3, b3) front view along FF' direction. The parallelogram depicts the unit cell of the step edge.

In addition, the geometric effect may play an important role as the Si atoms on the upper-step edge are more exposed and open to the incoming adsorbates geometrically, when compared to Si atoms on the

terrace sites. To correct for the coordination number and the geometric effect, we add one more Ag atom neighbour to each of the exposed Si atoms located at the upper-step edge. Figure 5.2b shows the optimized structure of the improved model, which consists of periodically repeating Ag triangles with a unit cell containing 3 Si atoms and 4 Ag atoms. The number of Ag atoms surrounding each Si atoms at the upper-step now becomes the same as that on the terraces and the lower-step edge. As the under-coordination of the atoms at the step edge is now compensated for the Si dangling bonds, there is no electronic effect associated with the Si dangling bonds at the step edge. We further check the viability of the new model by performing geometry optimization on a cysteine molecule initially placed at a Si atom at the upper-step edge (before optimization) and obtain its equilibrium adsorption geometry on an upper-step edge D1 (Ag dimer) site (after optimization). The calculated adsorption energies for various adsorption sites on both models are presented in Table C1. Furthermore, as the Ag atom is under-coordinated and surrounded by 3 Ag atoms at both upper-step and lower-step edges relative to a Ag atom at the terraces (surrounded by 4 Ag atoms), the Ag atoms at the step edges therefore offer more probable adsorption sites for chemisorption.

5.3.2 Antiphase Boundary

Another common one-dimensional defect observed on the Si(111)- $\sqrt{3}\times\sqrt{3}$ -Ag surface is created when two island-hole pairs with different T4 adsorption sites grow into each other, forming a dislocation caused by the T4-T4 shift.¹⁹⁶ Previous studies have proposed plausible models for this type of defects without providing structural optimization. Figure 5.3a1 shows an empty-state STM image of the Si(111)- $\sqrt{3}\times\sqrt{3}$ -Ag surface with a typical antiphase boundary. The chain of bright protrusions aligned along the boundary in the empty-state image would become dark in the filled-state image (not shown), consistent with that reported in previous studies.¹⁹⁶ The holes in the hexagonal mesh superimposed on the image mark the positions of the Si trimers on both sides of the antiphase boundary. The separation between the nearest Si trimers across the antiphase boundary is 7.8 Å as shown in the corresponding apparent height profile along the relevant line in Figure 5.3a2. The optimized equilibrium geometry of the antiphase boundary shown in Figures 5.3b1 (top view) and 5.3b2 (side view) corroborates well with the STM results, with the calculated separation between the Si trimers across the antiphase boundary (7.6 Å) found to be in good accord with the STM apparent height profile (Figure 5.3a2). The Burgers vector associated with the dislocation is 3.8 Å, also in accord with that reported in previous studies.¹⁹⁶ The 1D chain structure of the antiphase boundary is composed of Ag trimers with a periodicity of 6.6 Å along the antiphase boundary and a unit cell containing 2 Ag atoms and 2 Si atoms. The remaining dangling bonds

resulted from the T4-T4 shift are each passivated with three Ag atoms (in the middle of Ag trimers in Figure 5.3b1) with Ag–Si bond lengths of 2.4 Å.

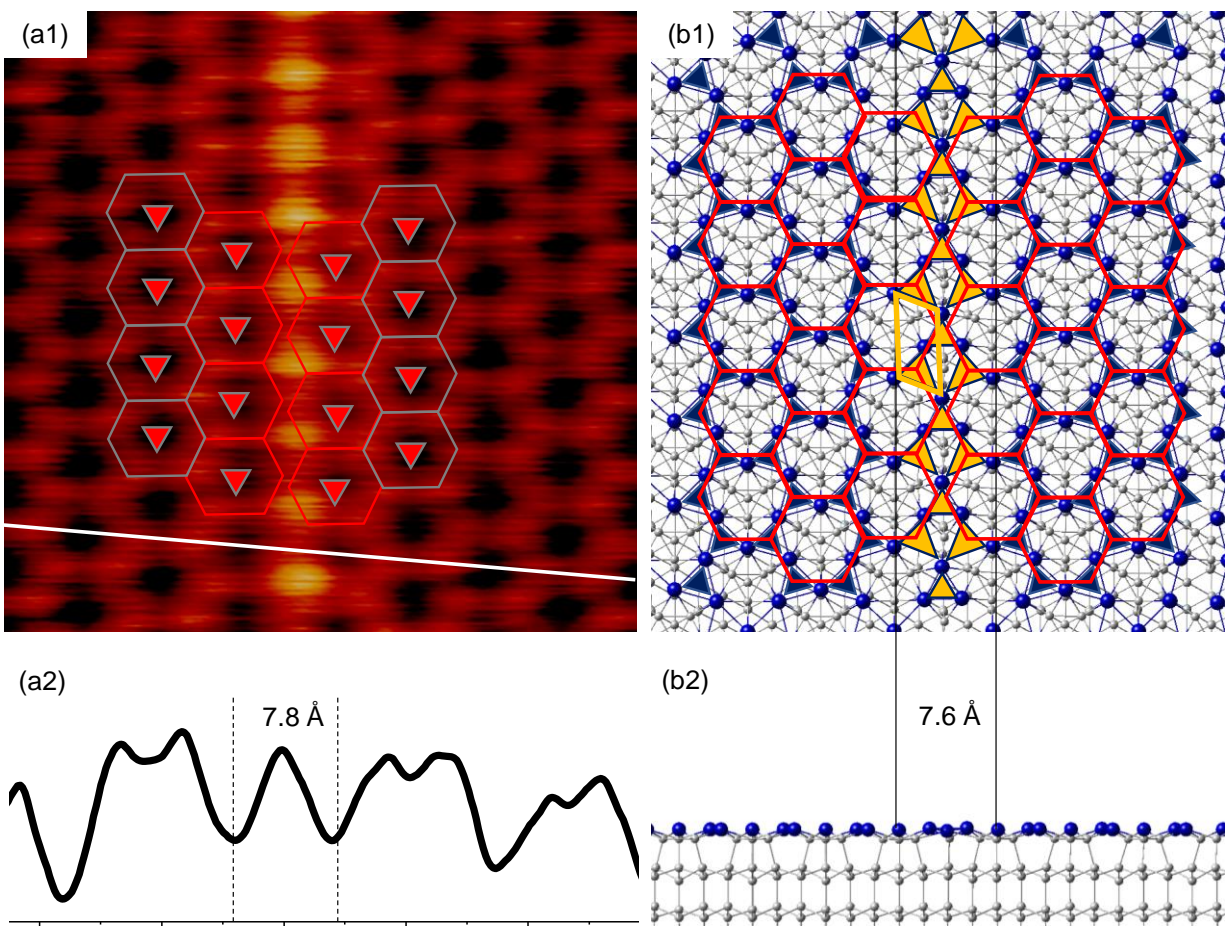


Figure 5.3 (a1) Empty-state STM images obtained with a sample bias of +0.9 V and a constant tunneling current of 0.2 nA for a pristine Si(111)- $\sqrt{3}\times\sqrt{3}$ -Ag near a [1–21] antiphase boundary over a 10×10 nm² scan area. (a2) Apparent height profile along the marked line across the antiphase boundary in (a1). (b1) Top view and (b2) side view of the optimized geometry of the antiphase boundary model showing the periodicity of the antiphase boundary region.

5.3.3 Density of States at Defects

To further investigate the electronic effect at defect sites, we calculate the electronic density of states (DOS) of the model surfaces containing the step edge and antiphase boundary. It should be noted that the x-y dimensions of the slabs are kept the same in all three models for the terrace, step edge and antiphase boundary. The number of Si bilayers (3) and hence the total number of atoms are also the same in the

terrace and antiphase boundary models. In the step edge model, there are three Si bilayers underneath the island and two bilayers underneath the hole sites (Figure C2a). The latter difference in the number of Si bilayers underneath the hole sites could affect the calculated results for the total density of states, most likely in their intensities. We also employ a less dense k-mesh of the Brillouin zone ($1 \times 2 \times 1$) in order to provide, without extended computation time, sufficiently accurate results for the purpose of comparison between different models in our system. The calculated total DOS spectra for the surface terrace, step edge, and antiphase boundary are shown in Figure 5.4. A wide unoccupied band observed at 1-3.5 eV above the Fermi level could be considered the conduction band, while the band extending from the Fermi level to -4.0 eV can be considered the valence band. The occupied and unoccupied states are separated by a band gap of 0.9 eV. The prominent sharp feature of high DOS located near -4.0 eV can be attributed to the Ag 4d-bands. The entire DOS spectrum of the antiphase boundary is found to be shifted to a lower energy by ~ 0.1 eV from that of the terrace model, while a larger downshift of the total DOS (0.4 eV) is observed for the step edge model. A closer examination of the states near the Fermi level in Figure 5.4b reveals three peaks located within 2 eV below the Fermi level for the terrace and antiphase boundary models. Both models also exhibit a small peak (at 0.7 eV above the Fermi level) within the band gap near the conduction band minimum. There are discernible differences in the DOS spectrum for the step edge model. Relative to the terrace and antiphase boundary DOS spectra, a general shift to a lower energy and a broadening with less intense maximum is found in the two peaks closest to the Fermi level in the step edge spectrum. More importantly, a well-defined broad peak at 0.5 eV above the Fermi level inside the band gap is clearly observed, which confirms the existence of the so-called mid-gap states in the case of step-edge defects.

Various experimental and theoretical efforts have been made to identify the nature of the surface states near the Fermi level. In earlier photoemission studies of $\text{Si}(111)-\sqrt{3} \times \sqrt{3}-\text{Ag}$, three distinct surface states were clearly observed within 2 eV below the Fermi level. Among these, the so-called S1 state appears within the band gap. The metallic nature of the S1 band has been attributed to the presence of excess Ag adatoms donating electrons to the Ag trimers, which results in a partial occupation of an unoccupied band.^{61,231-233} There have been no studies on the contribution of the electronic states of the one-dimensional surface defects. Since the amount of these typical surface defects is relatively high as observed in the STM measurements, proportional contribution from these states to the total DOS can be expected. The origin of the S1 state could therefore be attributed, at least in part, to the step edges on the surface.

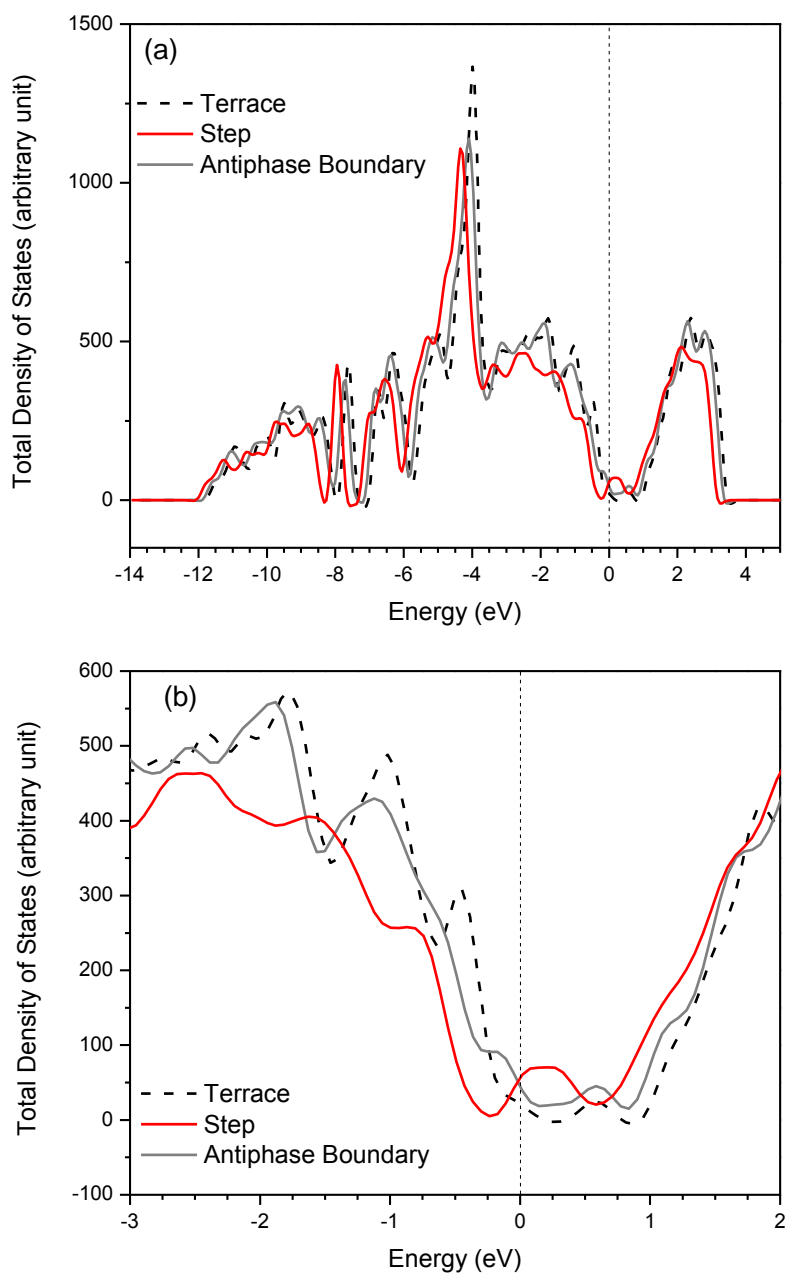


Figure 5.4 Calculated total density of states for the terrace (dashed line), antiphase boundary (grey solid line), and step edge (red solid line) models for (a) the full valence region, and (b) near the Fermi level.

To further distinguish the contribution of Ag and Si states and the effect of defect sites on the total DOS, we also calculate the partial density of states of the Ag 4d bands and the Si 3s and 3p bands. The Ag (Ag1 to Ag5) and Si (Si1 and Si2) atoms contributing to the partial DOS are marked with different colors on the step edge model in Figure 5.5a. Figures 5.5c-f show the corresponding partial DOS profiles of the Ag 4d bands for the respective Ag atoms at the step edge. As a reference, the Ag 4d partial DOS for the Ag trimer atoms on the surface terraces is also shown in Figure 5.5b. Among all the Ag atoms of the step-edge trimer chain, the Ag atom located near the lower-step edge (Ag3, Figure 5.5e) exhibit a discernible change in the partial DOS spectrum, with the center of the d-band appeared to have shifted to a lower energy by ~ 1.0 eV from that of a terrace Ag atom (Figure 5.4b). The 4d bands associated with the upper-step Ag atom (Ag1, Figure 5.5c) in the step-edge trimer chain are shifted to a higher energy by ~ 0.3 eV. There seems to be only minor shifts for the center of the d-states for the remaining Ag atoms, including that at the center of the step edge (Ag2, Figure 5.5d), and those next to the trimer chain on the upper-step edge (Ag4, Figure 5.5f) and lower-step edge (Ag5, Figure 5.5f). The 4d partial DOS spectra of these latter Ag atoms (Ag4 and Ag5) are found to be generally similar to those for Ag atoms on the terrace (Figure 5.5b).

To identify the Ag-Si states, Figure 5.5g shows a magnified view of partial DOS for both the Ag 4d states and the considerably weaker Si 3s and Si 3p partial DOS spectra of a Si atom at the terrace. The Ag 4d, Si 3s, and Si 3p states appear to overlap in the energy ranges: -5.8 eV to -8.8 eV (s-p-d), -0.2 eV to -3.6 eV (p-d), and that of the conduction band (s-p-d), and they can be identified as hybridized states. Evidently, some Ag-Si mixed levels are present within the band gap region (0 eV to $+1$ eV) of Si at the lower-step edge (Si2, Figure 5.5i), while no such band gap states exist on terrace sites (Figure 5.5g). The partial DOS of the hybridized p-d states of Si2 (Figure 5.5i) near the Fermi level in the valence band (at -0.8 eV) is higher in intensity than that of the terrace sites (Figure 5.5g), while that of Si1 (Figure 5.5h) is lower than that of the terrace sites. This is consistent with the observation that the adsorption at the lower-step edge Si site is more probable than that of the upper-step edge Si site. Furthermore, both Si1 and Si2 and their connecting Ag atoms (Ag1 and Ag4 are connected to Si1, Ag3 and Ag5 are connected to Si2) contribute to the mid-gap states near 0.2 eV (Figures 5.5h and 5.5i).

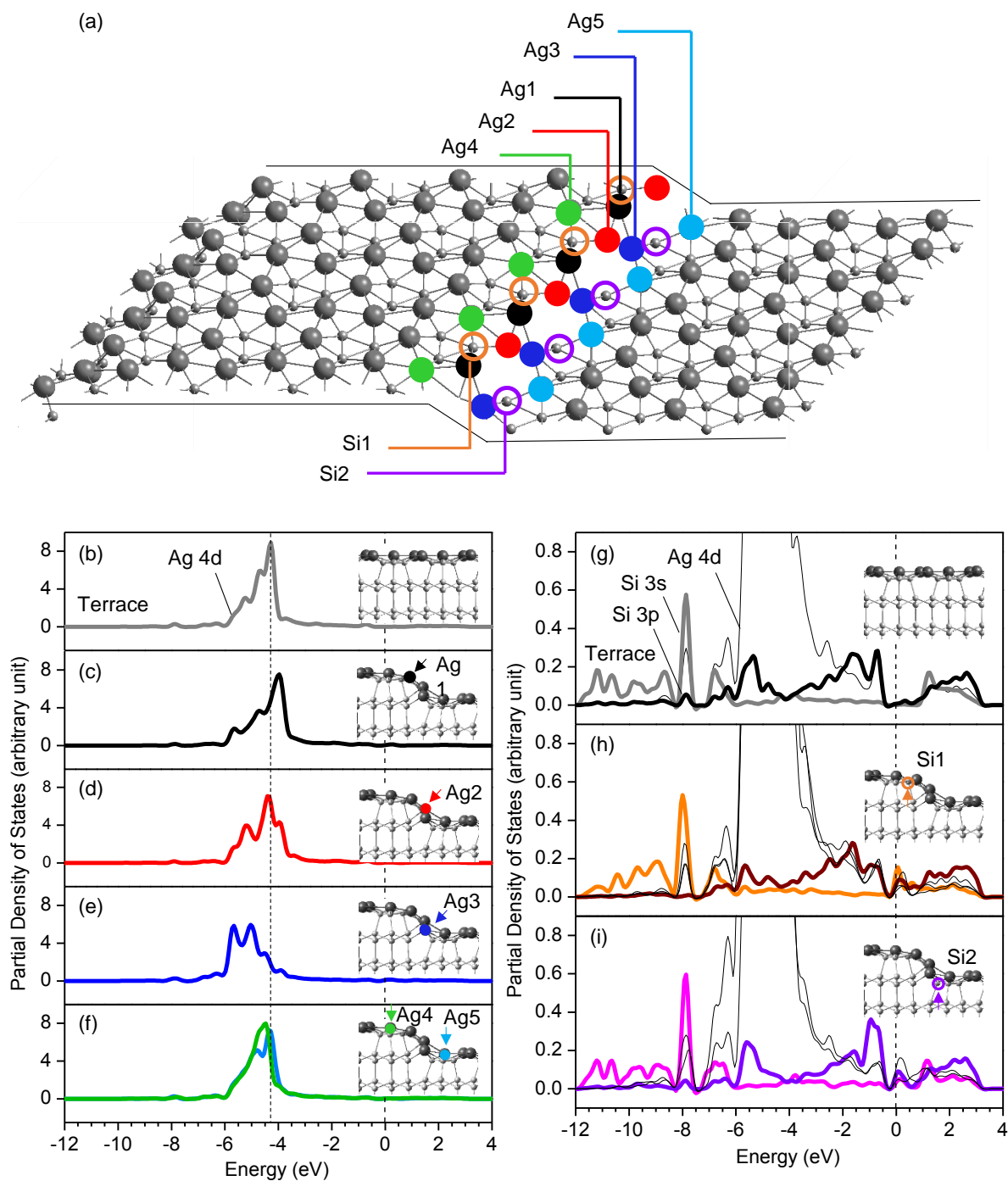


Figure 5.5 (a) A step edge model depicting different Ag and Si atoms at the slope (Ag1-Ag3) and on the upper-step edge (Ag4, Si1) and lower-step edge (Ag5, Si2). Calculated partial density of states for (b) the Ag 4d states of the Ag atoms on the terrace sites, (c-f) the 4d states for Ag1-Ag5 atoms shown in (a), (g) the 3s and 3p states of the Si atoms on the terraces, and (h,i) the 3s and 3p states of the Si1 and Si2 atoms shown in (a). The 4d bands of the Ag atoms connected to each terrace Si sites, Si1, and Si2 are shown in their corresponding panels in (g-i).

Figure 5.6 shows the contributing Ag and Si atoms at and around the antiphase boundary and their corresponding partial DOS spectra. The partial DOS of the Ag 4d states of the middle Ag atom in the trimer chain (Ag6, Figure 5.6c) is shifted to a higher energy by 0.1 eV and is more similar in shape to those of the Ag trimers on the terraces (Figure 5.6b). On the other hand, the corresponding partial DOS spectra of the other two Ag atoms in the trimer chain (Ag7, Figure 5.6d and Ag8, Figure 5.6e) appear to be distributed between two bands with almost the same intensities, the center of which is shifted to a lower energy with respect to the middle Ag atom (Ag6, Figure 5.6c). The Ag atoms neighboring the trimer chain (Ag9 and Ag10, Figure 5.6f) exhibit DOS spectra that are similar to those of the Ag trimers on the terraces (Figure 5.6b) but are shifted to a lower energy by 0.1 eV. There is also a more noticeable change in the distribution of the p states of the Si atoms in the middle of the trimer chain (Si3, Figure 5.6h) compared to those of the Si trimers on the terraces (Figure 5.6g). Two prominent hybrid Ag-Si features also emerge at 0 eV and within the band gap (0.6 eV), which also appear more intense than those contributed by the step-edge Si atoms (Si4, Figure 5.6i), due most likely to the presence of three dangling bonds of Si3 that are saturated by three Ag atoms (Ag6, Ag7, and Ag8).

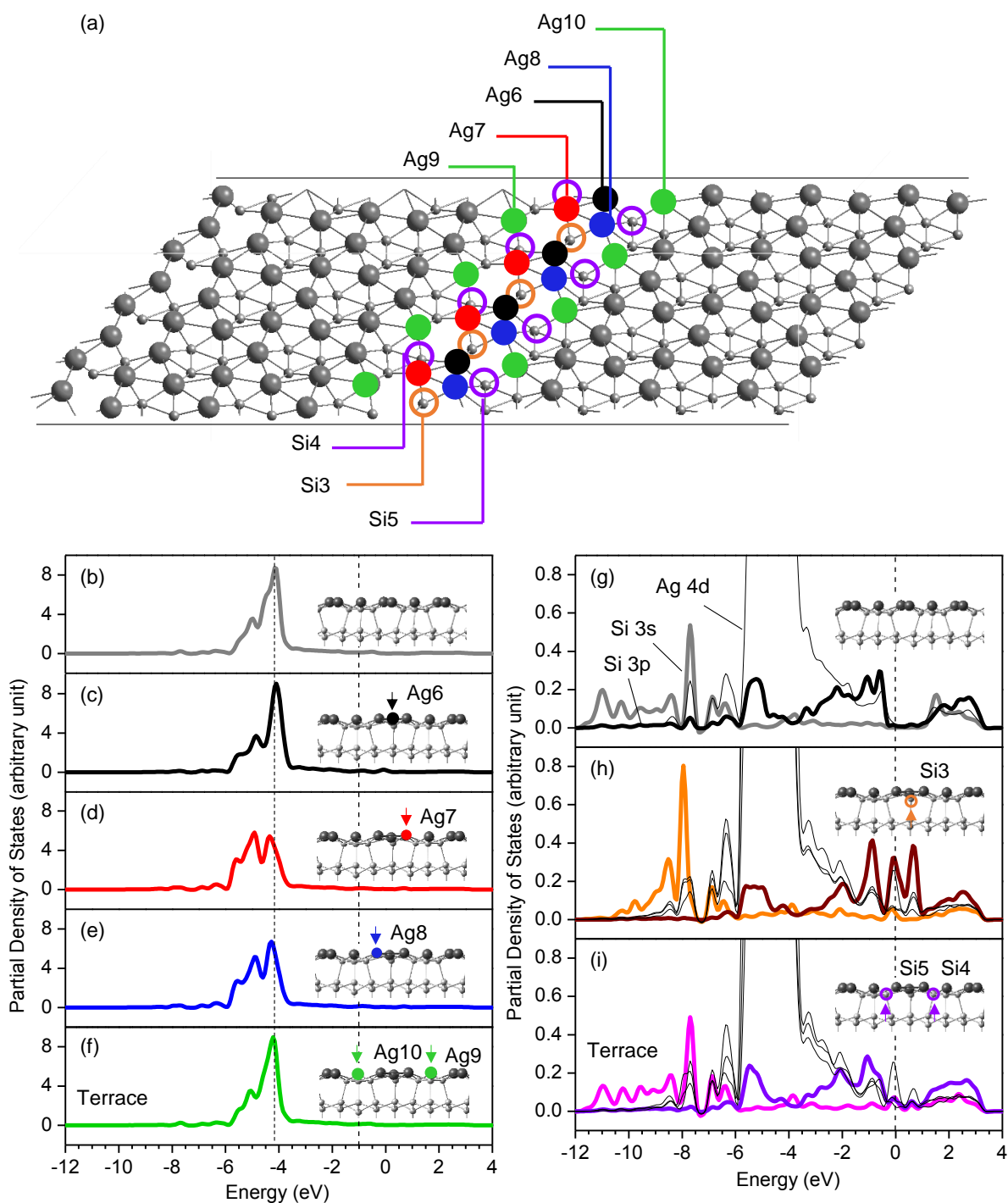


Figure 5.6 (a) An antiphase boundary model depicting different Ag and Si atoms at (Ag6, Ag7, Ag8, Si3) and near the boundary sites (Ag9, Ag10, Si4, Si5). Calculated partial density of states for (b) the 4d states of the Ag atoms on terrace sites, (c-f) the 4d states for Ag6-Ag10 atoms shown in (a), (g) the 3s and 3p states of the Si atoms on terraces, and (h, i) the 3s and 3p states of the Si3, and Si4 and Si5 atoms shown in (a). The 4d bands of the Ag atoms connected to each terrace Si sites (Si3, and Si4 and Si5) are shown in their corresponding panels in (g-i).

5.4 Summary

The Si(111)- $\sqrt{3}\times\sqrt{3}$ -Ag surface structure and properties have been the subject of extensive research in the past few decades. The anomalies found in its electronic structure measured at both room temperature and low temperature as well as its high conductivity due to the presence of the surface metallic states have made it a benchmark surface for exploring novel phenomena in supported single-atom-thick, two-dimensional hybrid systems. Among all the studies on the various properties, those focusing surface defects are rather scarce. As the step edges and antiphase boundaries are found to be the more abundant defect features on the Si(111)- $\sqrt{3}\times\sqrt{3}$ -Ag surface, detailed understanding of their structural configurations and associated properties is essential to further unravelling the overall electronic properties of this intriguing surface. Using first-principle total energy calculations, we have determined the equilibrium geometries of typical defect sites associated with step edges and antiphase boundaries observed on the Si(111)- $\sqrt{3}\times\sqrt{3}$ -Ag surface. These large-scale DFT calculations have enabled us to develop equilibrium structural models for a typical step edge and an antiphase boundary, consisting of Ag trimers in one-dimensional trimer chains. Despite the one monolayer coverage of Ag atoms on the terrace regions, the step edge contains more than one monolayer Ag coverage with an Ag:Si ratio of 4:3. This ratio is calculated to be 1:1 in the antiphase boundary chain. The total densities of states have also been calculated for the step edge and antiphase boundary and they are compared with that for the terrace. In all cases, surface states near the Fermi level are observed. Furthermore, the DOS of the mid-gap state found for the step edge model appears to be more intense and closer to the Fermi level than that for the antiphase boundary model and the terraces sites. The corresponding partial DOS spectra for the defect sites reveal different contributions from the 4d states of different Ag atoms and from the s and p states of different Si atoms in the defect region. Although the nature of the surface terraces has been found to be semiconducting, the presence of one-dimensional defects seems to improve the band gap properties that promise applications involving photon absorption and transfer. As these defect sites have also been found to be the most favorable adsorption sites for bio-organic molecules such as cysteine, they are expected to play a crucial role in designing applications in catalysis and chemical sensing. The present work illustrates the viability of using large-scale DFT calculations to model complex surface systems containing defects. Together with experimental results from STM and XPS to reduce the multitude of possible hypothetical structures, these calculations provide a powerful tool to determine the physical structures and their approximate electronic properties.

Chapter 6

Conclusions and Future Work

The surface chemistry of sulfur-containing amino acids on the Si(111)- $\sqrt{3}\times\sqrt{3}$ -Ag surface, particularly the interfacial and growth properties involving not just terrace sites but indeed defect sites, have been investigated by using a three-pronged approach of combining chemical-state information provided by X-ray photoelectron spectroscopy and electronic density of states images from scanning tunneling microscopy with large-scale quantum mechanical calculations based on density functional theory. In particular, we follow the growth evolution of cysteine nanofilm, and study their interfacial interactions with Si(111)- $\sqrt{3}\times\sqrt{3}$ -Ag as well as the intermolecular interactions among the adspecies. The XPS measurements reveal the nature of the molecule-substrate interactions to be covalent bonding mainly through S–Ag linkage while that of molecule-molecule interaction to be zwitterionic. According to STM images, adsorption begins at lower-step edges and antiphase boundaries and expands into unordered coral-reef shaped nanoislands propagating onto the terrace regions. This observation suggests that this template can be used for preferential site functionalization of the surface defects. Furthermore, chemisorption is found to be the prominent adsorption mode for the interfacial layer not only on defects but also on terraces. A combination of two factors are driving the adsorption behavior at room temperature: (1) the high density of step edges and antiphase boundaries compared to the domain sizes of terraces, and (2) the low diffusion barrier of cysteine on Si(111)- $\sqrt{3}\times\sqrt{3}$ -Ag. Unlike cysteine nanofilm growth on Si(111)7 \times 7, formation of a transitional layer is not observed for cysteine film growth at room temperature. Our DFT calculation results further show that the Ag bridge sites are the most favorable adsorption sites on terraces, when compared to other possible sites including Ag and Si threefold hollow and atop sites. In addition, the flat-lying configuration is found to be more energetically favorable for single cysteine adsorbates in our DFT calculations. At elevated temperature, the presence of the cysteine film leads to remarkable transformation of the highly ordered monoatom-thick Ag layer of the Si(111)- $\sqrt{3}\times\sqrt{3}$ -Ag surface into metallic clusters of nanometer sizes by cleavage of Ag–Si bonds and formation of Ag–S and Si–NH bonds. This result suggests the viability of a new approach to modification of the two-dimensional monoatom-thick Si(111)- $\sqrt{3}\times\sqrt{3}$ -Ag surface using sulfur-containing organic adsorbates. Of interest for future work is to determine whether this unique surface chemistry is applicable to other similar intricate two-dimensional metal silicide overlayers, which could provide a general method of fabricating nanoclusters and quantum dots.

After characterizing the effect of the only thiol containing amino acid on Si(111)- $\sqrt{3}\times\sqrt{3}$ -Ag, we investigate the interfacial interactions and growth properties of the other sulfur-containing amino acid,

methionine, at room temperature and at 140 K. This study is especially interesting because it allows us to compare the adsorption properties of the two sulfur-containing amino acids, with a similar back-bone but different side chains (thiol in cysteine and methylthio methylene in methionine), and correspondingly different chemical reactivities, on Si(111)- $\sqrt{3}\times\sqrt{3}$ -Ag. Due to termination of the sulfur atom by a methyl group in its methylthio methylene side chain, methionine, unlike cysteine, does not chemisorb through the sulfur atom on the Si(111)- $\sqrt{3}\times\sqrt{3}$ -Ag surface terraces. Our XPS results show, instead, chemisorption through dehydrogenation of the NH₂ group, which we attribute to adsorption at defects such as step edges and antiphase boundaries. Our XPS results further show that, unlike cysteine adsorbates, methionine prefers chemisorption to Si atoms than Ag atoms. In addition, the chemical state of the methionine film is found to be zwitterionic at low coverages to multilayers. Similar to cysteine films on Si(111)- $\sqrt{3}\times\sqrt{3}$ -Ag but different from methionine growth on Si(111)7 \times 7, the absence of hydrogen bonding features in XPS indicates the absence of a transitional layer. We observe the formation of molecular wires at room temperature, which become more well-defined with short-range alignment at low temperature. These results are corroborated with DFT calculations that show the feasibility of the formation of self-assembled one-dimensional extended dimer rows (as molecular wires).

Molecular size effect is another factor that influences the interfacial interactions and growth properties. To investigate the molecular size effect, we extend our study to the adsorption of glycine, the simplest amino acid, on Si(111)- $\sqrt{3}\times\sqrt{3}$ -Ag. The presence of the metallic Ag 3d features indicates that all three amino acids (methionine, cysteine, and glycine) induce formation of metallic agglomerates (clusters or islands) at elevated temperature. However, the extent and morphology of the induced metallic features appear to depend on the initial coverage of the adsorbates. In the case of physisorbed glycine, the majority of the glycine film is desorbed before annealing, leaving the chemisorbed features at the step edges and antiphase boundaries. Nevertheless, most of the $\sqrt{3}\times\sqrt{3}$ -Ag feature is removed after annealing and could be converted to metallic agglomerates. The adsorbate-induced cluster formation after annealing could be initiated at step edges and phase boundaries as these are the most reactive adsorption sites.

All our experimental results have demonstrated that step edges and antiphase boundaries are the most influential parts of the Si(111)- $\sqrt{3}\times\sqrt{3}$ -Ag surface, and they play an important role in governing the adsorption and growth processes of amino acids. Understanding the geometries and electronic structures of these sites could provide more insights to understanding the overall properties of Si(111)- $\sqrt{3}\times\sqrt{3}$ -Ag. In Chapter 5, we develop the equilibrium geometries of these typical defect sites using large-scale first-principle DFT calculations. We generate three different models based on the Ag:Si ratios of 3:3, 4:3, and 5:3 for the step edge. The Ag₃Si₃ model contains under-coordinated Si atoms at the upper-step and lower-step edges, with the Ag dimer rows along the slope of the step, while the Ag₄Si₃ and Ag₅Si₃

models consist of Ag trimers extended along the slope. To validate our models and to determine the most probable one, we use the STM results of cysteine adsorption at very low coverage as a guide. Under experimental conditions, the observed preferential adsorption of cysteine at lower-step edges at very low coverages could be due to both kinetic and thermodynamic effects at room temperature. In the theoretical modeling based on DFT, however, only thermodynamic effects are considered. Interestingly, the adsorption energies of thiolated cysteine at various plausible adsorption sites on the upper-step and lower-step edges and on the slopes follow a discernible trend in all three models. In the Ag₃Si₃ model, the Si atop site at the upper-step edge is found to be the most favourable adsorption site, which is in marked contrast to the trend found in experiments and can therefore be ruled out. In the Ag₄Si₃ and Ag₅Si₃ models, the Ag dimer sites at the slope are found to be the most favourable adsorption sites, which is more consistent with our STM results. This approach of using cysteine as the probe adsorbate has led us to propose the Ag₄Si₃ model to be the most viable model. The Ag:Si ratio is calculated to be 1:1 for the antiphase boundary with an equilibrium geometry consisting of Ag trimers extended in one dimension. In addition, the total densities of states are calculated for both step edge and antiphase boundary and are compared with those for terraces. The density of states of the mid-gap state associated with the step edge is found to be more intense and closer to the Fermi level. The calculated partial densities of states for the step edge and antiphase boundary reveal the different contributions from Ag and Si atoms of various sites.

The present work has provided a thorough understanding of the surface chemistry of two sulfur-containing amino acids on Si(111)- $\sqrt{3}\times\sqrt{3}$ -Ag and the role of surface defects in the adsorption and film growth processes. This work also opens new doors to constructing Si-based metal cluster nanoarrays and quantum dots using a novel approach of amino-acid-adsorbate mediation. At the same time, the present work provides the basis for investigation into other interesting and definitely more complex surface processes. Some of these future studies could include:

- (1) An immediate follow-up to our surface defect calculations would be to improve our models. For example, increasing the size of the step-edge slab will allow us to investigate the effect of the terrace size on the step edge force field and equilibrium geometry. Furthermore, extending the probe molecule pool to include glycine and methionine (from just cysteine) for the investigation of the adsorption configurations of the three amino acids used in our experiment would be useful because this will enable us to better determine the effect of molecular size and molecular shape on the step edge adsorption.
- (2) Using the total and partial density of states calculation results, we are able to describe some of the surface defect properties. What are other properties that can be calculated for our large-scale system? For example, surface defects have been found to introduce mid-gap states that could

significantly impact the optical properties of the surface. An interesting investigation could be to calculate the surface band structure at defects and their optical properties.

- (3) As the surface defects provide the most favourable adsorption sites for bioorganic molecules, their pertaining applications are likely in the areas of catalysis and chemical sensing. To investigate these potential applications, the photochemical sensing experiments can be performed outside of our ultrahigh vacuum chambers. Before pursuing the chemical sensing experiments, the challenge of surface oxidation must be resolved. Can the Si(111)- $\sqrt{3}\times\sqrt{3}$ -Ag surface structure be maintained in ambient condition? What can be done to bridge the gap between ultrahigh vacuum and ambient condition?
- (4) Highly ordered molecular nanowires of methionine have been observed in low-temperature STM measurements. However, the room-temperature STM measurements could provide more insights into the molecular grating formation at controlled deposition rates and coverages in more practical conditions. In addition, STM measurements should be performed on the as-grown methionine monolayer and multilayer after annealing. These results could provide complementary information needed to identify the interfacial interactions and the morphology of the surface containing the metallic features after annealing.
- (5) The adsorbate-induced metallic nanocluster formation is an important result of this work because it offers a novel approach of using organic adsorbates to modify the two-dimensional single-atom-thick Ag overlayer of Si(111)- $\sqrt{3}\times\sqrt{3}$ -Ag. Additional experiments are required to unravel their formation mechanism as well as to determine the size distribution of the nanoclusters. Moreover, it would be of great interest to investigate the molecular size and reactivity effects, exerted by different organic adsorbates, on the nanocluster morphology after annealing. Is the nanocluster size distribution profile dependent on the functional groups and reactivities of the adsorbates? Is this adsorbate-induced effect merely a chemisorption effect or can physisorption also be a possible option? Can we observe similar phenomenon for other simpler organic molecules (such as other DNA bases)?
- (6) An interesting property of the Si(111)- $\sqrt{3}\times\sqrt{3}$ -Ag surface is its asymmetrical inequivalent triangle (IET) structure, which has been observed at low temperature. In our DFT calculations, we have used the symmetrical alternative, i.e. the honeycomb-chained triangle structure. It would be of interest to investigate the IET structure and to identify their relations to the surface defect models. Do these defects promote the need for the more dynamic HCT structure?
- (7) It has been claimed that IET is the thermal-averaged structure of the IET oscillations at room temperature. In the present work, all the adsorption geometry calculations are based on the HCT

model. It would be interesting to investigate the effect of IET in the adsorption structures. For that purpose, an optimized Ag/Si slab with IET structure must be used to repeat all the calculations to obtain the equilibrium adsorption configurations of all three amino acids.

- (8) The $\sqrt{3}\times\sqrt{3}$ reconstruction phase has been observed for Au, Pt, Pb, In, and Sn. Similar adsorption studies involving cysteine and methionine (and possibly other benchmark amino acids) can also be performed. However, a more interesting question is: Is the metal cluster formation a common phenomenon on metal silicide surfaces with the $\sqrt{3}\times\sqrt{3}$ reconstruction, given the appropriate adsorbates? This information will be very helpful to establishing a more universal approach for constructing (ordered templates of) nanoclusters and quantum dots induced by organic adsorbates.

Bibliography

- (1) Duke, C. B. The Birth and Evolution of Surface Science: Child of the Union of Science and Technology. *Proc. Natl. Acad. Sci.* **2003**, *100*, 3858–3864.
- (2) Somorjai, G. A. Modern Surface Science and Surface Technologies: An Introduction. *Chem. Rev.* **1996**, *96*, 1223–1236.
- (3) Brinkman, W. F.; Haggan, D. E.; Troutman, W. W. A History of the Invention of the Transistor and Where It Will Lead Us. *IEEE J. Solid-State Circuits* **1997**, *32*, 1858–1865.
- (4) Moore, G. E. Cramming More Components onto Integrated Circuits. *Electronics* **1965**, *38*, 114.
- (5) Yates, J. T. A New Opportunity in Silicon-Based Microelectronics. *Science* **1998**, *279*, 335–336.
- (6) Binning, G.; Rohrer, H. 7×7 Reconstruction on Si(111) Resolved in Real Space. *Phys. Rev. Lett.* **1983**, *50*, 119–123.
- (7) Erlandsson, R.; Olsson, L. Force Interaction in Low-Amplitude AC-Mode Atomic Force Microscopy: Cantilever Simulations and Comparison with Data from Si(111) 7×7 . *Appl. Phys. A* **1998**, *66*, S879–S883.
- (8) Takayanagi, K.; Tanishiro, Y. Structure Analysis of Si(111)- 7×7 Reconstructed Surface by Transmission Electron Diffraction. *Surf. Sci.* **1985**, *164*, 367–392.
- (9) Takayanagi, K.; Tanishiro, Y.; Takahashi, M.; Takahashi, S. Structural Analysis of Si(111) 7×7 by UHV-Transmission Electron Diffraction and Microscopy. *J. Vac. Sci. Technol. A Vacuum, Surfaces, Film.* **1985**, *3*, 1502–1506.
- (10) Ahn, J. R.; Yoo, K.; Seo, J. T.; Byun, J. H.; Yeom, H. W. Electronic States of Two-Dimensional Adatom Gas and Nanocluster Array: Na on Si(111) 7×7 . *Phys. Rev. B* **2005**, *72*, 113309.
- (11) Wu, K. Unusual Diffusivity and Clustering of Alkali Metals on the Si(111)- 7×7 Surface. *Sci. Technol. Adv. Mater.* **2005**, *6*, 789–794.
- (12) Wu, K.; Fujikawa, Y.; Nagao, T.; Hasegawa, Y.; Nakayama, K. S.; Xue, Q. K.; Wang, E. G.; Briere, T.; Kumar, V.; Kawazoe, Y.; et al. Na Adsorption on the Si(111)-(7×7) Surface: From Two-Dimensional Gas to Nanocluster Array. *Phys. Rev. Lett.* **2003**, *91*, 126101.
- (13) Watanabe, A.; Naitoh, M.; Nishigaki, S. Local Charge Redistribution at Potassium Adsorption on the Si(111) 7×7 Surface: A Scanning Tunneling Microscopy Study. *Appl. Surf. Sci.* **1999**, *144–145*, 548–553.
- (14) Fan, W. C.; Ignatiev, A. Metal-Adsorbate-Induced Si(111)-(1×3) Reconstruction. *Phys. Rev. B* **1990**, *41*, 3592–3595.
- (15) Jeon, D.; Hashizume, T.; Sakurai, T.; Willis, R. F. Structural and Electronic Properties of Ordered Single and Multiple Layers of Na on the Si(111) Surface. *Phys. Rev. Lett.* **1992**, *69*, 1419–1422.
- (16) Sakamoto, K.; Okuda, T.; Nishimoto, H.; Daimon, H.; Suga, S. Photoemission Study of the Si(111) 3×1 -K Surface. *Phys. Rev. B* **1994**, *50*, 1725–1732.
- (17) Vitali, L.; Ramsey, M. G.; Netzer, F. P. Nanodot Formation on the Si(111)-(7×7) Surface by Adatom Trapping. *Phys. Rev. Lett.* **1999**, *83*, 316–319.
- (18) Li, J. L.; Jia, J. F.; Liang, X. J.; Liu, X.; Wang, J. Z.; Xue, Q. K.; Li, Z. Q.; Tse, J. S.; Zhang, Z.; Zhang, Z.; et al. Spontaneous Assembly of Perfectly Ordered Identical-Size Nanocluster Arrays.

- Phys. Rev. Lett.* **2002**, *88*, 066101.
- (19) Wang, Y. L.; Lai, M. Y. Self-Organized Two-Dimensional Lattice of Magic Clusters. *Phys. Rev. B* **2001**, *64*, 241404.
 - (20) Jia, J. F.; Liu, X.; Wang, J. Z.; Li, J. L.; Wang, X. S.; Xue, Q. K.; Li, Z. Q.; Zhang, Z.; Zhang, S. B. Fabrication and Structural Analysis of Al, Ga, and In Nanocluster Crystals. *Phys. Rev. B* **2002**, *66*, 165412.
 - (21) Hansson, G. V.; Bachrach, R. Z.; Bauer, R. S.; Chiaradia, P. New Models for Metal-Induced Reconstructions on Si(111). *Phys. Rev. Lett.* **1981**, *46*, 1033–1037.
 - (22) Nogami, J.; Park, S.; Quate, C. F. Indium-Induced Reconstructions of the Si(111) Surface Studied by Scanning Tunneling Microscopy. *Phys. Rev. B* **1987**, *36*, 6221–6224.
 - (23) Park, S.; Nogami, J.; Quate, C. F. Metal-induced Reconstructions of the Silicon(111) Surface. *J. Microsc.* **1988**, *152*, 727–734.
 - (24) Wang, D. Y.; Wu, H. Y.; Chen, L. J.; He, W.; Zhan, Q. F.; Cheng, Z. H. Growth of Honeycomb-Symmetrical Mn Nanodots Arrays on Si(111)-7×7 Surfaces. *J. Phys. Condens. Matter* **2006**, *18*, 6357–6363.
 - (25) Wang, D. Y.; Chen, L. J.; He, W.; Zhan, Q. F.; Cheng, Z. H. Preferential Arrangement of Uniform Mn Nanodots on Si(111)-7×7 Surface. *J. Phys. D. Appl. Phys.* **2006**, *39*, 347–350.
 - (26) Zilani, M. A. K.; Xu, H.; Liu, T.; Sun, Y. Y.; Feng, Y. P.; Wang, X. S.; Wee, A. T. S. Electronic Structure of Co-Induced Magic Clusters Grown on Si(111)-(7×7): Scanning Tunneling Microscopy and Spectroscopy and Real-Space Multiple-Scattering Calculations. *Phys. Rev. B* **2006**, *73*, 195415.
 - (27) Zilani, M. A. K.; Sun, Y. Y.; Xu, H.; Peng, G. W.; Feng, Y. P.; Wang, X. S.; Wee, A. T. S. Formation and Stabilization of Fe-Induced Magic Clusters on Si(111)-(7×7) Template. *Surf. Sci.* **2007**, *601*, 2486–2490.
 - (28) Zilani, M. A. K.; Sun, Y. Y.; Xu, H.; Liu, L.; Feng, Y. P.; Wang, X. S.; Wee, A. T. S. Reactive Co Magic Cluster Formation on Si(111)-(7×7). *Phys. Rev. B* **2005**, *72*, 193402.
 - (29) Höpfner, P.; Wisniewski, M.; Sandrock, F.; Schäfer, J.; Claessen, R. Structural Components of the Pt/Si(111)-(√3×√3) Surface from Scanning Tunneling Microscopy. *Phys. Rev. B* **2010**, *82*, 075431.
 - (30) Wawro, A.; Suto, S.; Kasuya, A. STM Studies of PtSi Formation on Si(111) by Solid State Epitaxy. *Phys. Rev. B* **2005**, *72*, 205302.
 - (31) Casalis, L.; Citti, A.; Rosei, R.; Kiskinova, M. STM Study of Superstructures Formed in the Pd/Si(111) System. *Phys. Rev. B* **1995**, *51*, 1954–1957.
 - (32) Zhang, C.; Chen, G.; Wang, K.; Yang, H.; Su, T.; Chan, C. T.; Loy, M. M. T.; Xiao, X. Experimental and Theoretical Investigation of Single Cu, Ag, and Au Atoms Adsorbed on Si(111)-7×7. *Phys. Rev. Lett.* **2005**, *94*, 176104.
 - (33) Wu, Y.; Zhou, Y.; Zhou, C.; Zhan, H.; Kang, J. Atomic Structure and Formation Mechanism of Identically Sized Au Clusters Grown on Si(111)-(7×7) Surface. *J. Chem. Phys.* **2010**, *133*, 124706.
 - (34) Chizhov, I.; Lee, G.; Willis, R. F. STM Study of Room Temperature Adsorption of Au on the Si(111)-(7×7) Surface: Evidence for the Reaction of Au Atoms with Si Rest Atoms. *Appl. Phys. A* **1998**, *66*, S1003–S1006.

- (35) Zhou, Y.; Wu, Q.-H.; Kang, J. STM Study of Au Adsorption on Si(111)-7×7 Surface: Voltage and Temperature Dependence. *J. Nanosci. Nanotechnol.* **2008**, *8*, 3030–3035.
- (36) Zhang, L.; Kim, Y.; Shim, H.; Lee, G. Adsorption of Au Atoms on Si (111)-(7×7) Studied by Using Scanning Tunneling Microscopy. *J. Korean Phys. Soc.* **2009**, *51*, 947–950.
- (37) Zhang, L.; Kim, Y.; Shim, H.; Lee, G. Influence of Substrate Temperature on Submonolayer Au Adsorption on an Si(111)-(7×7) Surface Studied by Scanning Tunneling Microscopy. *J. Phys. Condens. Matter* **2007**, *19*, 486004.
- (38) Zhang, Y. P.; Yang, L.; Lai, Y. H.; Xu, G. Q.; Wang, X. S. Formation of Ordered Two-Dimensional Nanostructures of Cu on the Si(111)-(7×7) Surface. *Surf. Sci.* **2003**, *531*, L378–L382.
- (39) Jarolímek, T.; Mysliveček, J.; Sobotík, P.; Ošť'Ádal, I. Adsorption and Diffusion of Ag Atoms on Si(111)-(7×7) Surface. *Surf. Sci.* **2001**, *482–485*, 386–390.
- (40) Nicholls, J. M.; Salvan, F.; Reihl, B. Surface States of Ordered Au, Ag, and Cu Overlayers on Si(111) Studied by Inverse Photoemission. *Phys. Rev. B* **1986**, *34*, 2945–2948.
- (41) Shibata, A.; Kimura, Y.; Takayanagi, K. In Situ High-Temperature STM Study of the Restructuring on the Si(111)7×7 Surface upon Ag Deposition. *Surf. Sci.* **1994**, *303*, 161–170.
- (42) Zhou, C.; Xue, Q.; Jia, J.; Zhan, H.; Kang, J. Structural and Electronic Properties of Identical-Sized Zn Nanoclusters Grown on Si (111)-(7×7) Surfaces. *J. Chem. Phys.* **2009**, *130*, 024701.
- (43) Wang, Y. L.; Gao, H. J.; Guo, H. M.; Wang, S.; Pantelides, S. T. Bonding Configurations and Collective Patterns of Ge Atoms Adsorbed on Si(111)-(7×7). *Phys. Rev. Lett.* **2005**, *94*, 106101.
- (44) Xie, Z.-X.; Tanaka, K. Tin Atoms Adsorbed on a Si(111)-(7×7) Surface. *Surf. Sci.* **2001**, *479*, 26–32.
- (45) Wang, Y. L.; Guo, H. M.; Qin, Z. H.; Ma, H. F.; Gao, H. J. Toward a Detailed Understanding of Si(111)-7×7 Surface and Adsorbed Ge Nanostructures: Fabrications, Structures, and Calculations. *J. Nanomater.* **2008**, *2008*, 874213.
- (46) Shioda, R.; Kawazu, A.; Baski, A. A.; Quate, C. F.; Nogami, J. Bi on Si(111): Two Phases of the $\sqrt{3}\times\sqrt{3}$ Surface Reconstruction. *Phys. Rev. B* **1993**, *48*, 4895–4898.
- (47) Zhang, T.; Cheng, P.; Li, W. J.; Sun, Y. J.; Wang, G.; Zhu, X. G.; He, K.; Wang, L.; Ma, X.; Chen, X.; et al. Superconductivity in One-Atomic-Layer Metal Films Grown on Si(111). *Nat. Phys.* **2010**, *6*, 104–108.
- (48) Dávila, M. E.; Avila, J.; Asensio, M. C.; Le Lay, G. Complex Behaviors at Simple Semiconductor and Metal/Semiconductor Surfaces. *Surf. Rev. Lett.* **2003**, *10*, 981–1008.
- (49) Zotov, A. V.; Gruznev, D. V.; Utas, O. A.; Kotlyar, V. G.; Saranin, A. A. Multi-Mode Growth in Cu/Si(111) System: Magic Nanoclustering, Layer-by-Layer Epitaxy and Nanowire Formation. *Surf. Sci.* **2008**, *602*, 391–398.
- (50) Rahsepar, F. R.; Zhang, L.; Leung, K. T. Two-Dimensional Self-Assembled Gold Silicide Honeycomb Nanonetwork on Si(111)7×7. *J. Phys. Chem. C* **2014**, *118*, 9051–9055.
- (51) Zegenhagen, J.; Fontes, E.; Grey, F.; Patel, J. R. Microscopic Structure, Discommensurations, and Tiling of Si(111)/Cu-5×5. *Phys. Rev. B* **1992**, *46*, 1860–1863.
- (52) Hötzel, F.; Seino, K.; Huck, C.; Skibbe, O.; Bechstedt, F.; Pucci, A. Metallic Properties of the Si(111)-5×2-Au Surface from Infrared Plasmon Polaritons and Ab Initio Theory. *Nano Lett.* **2015**, *15*, 4155–4160.

- (53) Baski, A. A.; Nogami, J.; Quate, C. F. Si(111)- $\sqrt{3}\times\sqrt{3}$ -Au Reconstruction as Studied by Scanning Tunneling Microscopy. *Phys. Rev. B* **1990**, *41*, 10247–10249.
- (54) Hasegawa, S.; Ino, S. Surface Structures and Conductance at Epitaxial Growths of Ag and Au on the Si(111) Surface. *Phys. Rev. Lett.* **1992**, *68*, 1192–1195.
- (55) Wan, K. J.; Lin, X. F.; Nogami, J. Surface Reconstructions in the Ag/Si(111) System. *Phys. Rev. B* **1993**, *47*, 13700–13712.
- (56) Shibata, A.; Kimura, Y.; Takayanagi, K. On the Restructured Layer of the Si(111)- $\sqrt{3}\times\sqrt{3}$ -Ag Structure Studied by Scanning Tunneling Microscopy. *Surf. Sci.* **1992**, *275*, L697–L701.
- (57) Shibata, A.; Takayanagi, K. Restructuring of the Reconstructed Si(111)- 7×7 Surface by Metal (Au, Ag) Deposition. *Jpn. J. Appl. Phys.* **1993**, *32*, 1385–1388.
- (58) Shibata, A.; Kimura, Y.; Takayanagi, K. Restructuring Process of the Si(111) Surface upon Ag Deposition Studied by In Situ High-Temperature Scanning Tunneling Microscopy. *J. Vac. Sci. Technol. B Microelectron. Nanom. Struct.* **1994**, *12*, 2026–2029.
- (59) McComb, D. W.; Moffatt, D. J.; Hackett, P. A.; Williams, B. R.; Mason, B. F. Scanning-Tunneling-Microscopy Investigation of the Nucleation and Growth of Ag/Si(111)-($\sqrt{3}\times\sqrt{3}$). *Phys. Rev. B* **1994**, *49*, 17139–17148.
- (60) Belianinov, A. A.; Ünal, B.; Lu, N.; Ji, M.; Ho, K. M.; Wang, C. Z.; Tringides, M. C.; Thiel, P. A. Islands and Holes as Measures of Mass Balance in Growth of the ($\sqrt{3}\times\sqrt{3}$)R30° Phase of Ag on Si(111). *Phys. Rev. B* **2010**, *82*, 165429.
- (61) Ding, Y. G.; Chan, C. T.; Ho, K. M. Structure of the ($\sqrt{3}\times\sqrt{3}$)R30° Ag/Si(111) Surface from First-Principles Calculations. *Phys. Rev. Lett.* **1991**, *67*, 1454.
- (62) Sato, N.; Nagao, T.; Hasegawa, S. Si(111)-($\sqrt{3}\times\sqrt{3}$)-Ag Surface at Low Temperatures: Symmetry Breaking and Surface Twin Boundaries. *Surf. Sci.* **1999**, *442*, 65–73.
- (63) Aizawa, H.; Tsukada, M.; Sato, N.; Hasegawa, S. Asymmetric Structure of the Si(111)- $\sqrt{3}\times\sqrt{3}$ -Ag Surface. *Surf. Sci.* **1999**, *429*, L509–L514.
- (64) Zhang, H. M.; Gustafsson, J. B.; Johansson, L. S. O. Surface Atomic Structure of Ag/Si- $\sqrt{3}\times\sqrt{3}$. *Phys. Rev. B* **2006**, *74*, 201304.
- (65) Matsuda, I.; Morikawa, H.; Liu, C.; Ohuchi, S.; Hasegawa, S.; Okuda, T.; Kinoshita, T.; Ottaviani, C.; Cricenti, A.; D'angelo, M.; et al. Electronic Evidence of Asymmetry in the Si(111)- $\sqrt{3}\times\sqrt{3}$ -Ag Structure. *Phys. Rev. B* **2003**, *68*, 085407.
- (66) Hamers, R. J. Formation and Characterization of Organic Monolayers on Semiconductor Surfaces. *Annu. Rev. Anal. Chem.* **2008**, *1*, 707–736.
- (67) Mirkin, C. A.; Taton, T. A. Semiconductors Meet Biology. *Nature* **2000**, *405*, 626–627.
- (68) Niemeyer, C. M.; Mirkin, C. A. Nanobiotechnology. *Small* **2005**, *1*, 356–358.
- (69) Jiang, C. S.; Hasegawa, S.; Ino, S. Surface Conductivity for Au or Ag on Si(111). *Phys. Rev. B* **1996**, *54*, 10389–10392.
- (70) Tong, X.; Jiang, C. S.; Horikoshi, K.; Hasegawa, S. Surface-State Electrical Conduction on the Si(111)- $\sqrt{3}\times\sqrt{3}$ -Ag Surface with Noble-Metal Adatoms. *Surf. Sci.* **2000**, *449*, 125–134.
- (71) Gustafsson, J. B.; Zhang, H. M.; Moons, E.; Johansson, L. S. O. Electron Spectroscopy Studies of PTCDA on Ag/Si(111)- $\sqrt{3}\times\sqrt{3}$. *Phys. Rev. B* **2007**, *75*, 155413.

- (72) Emanuelsson, C.; Johansson, L. S. O.; Zhang, H. M. Photoelectron Spectroscopy Studies of PTCDI on Ag/Si(111)- $\sqrt{3}\times\sqrt{3}$. *J. Chem. Phys.* **2018**, *149*, 044702.
- (73) Yokoyama, T.; Kawasaki, M.; Asari, T.; Ohno, S.; Tanaka, M.; Yoshimoto, Y. Adsorption and Self-Assembled Structures of Sexithiophene on the Si(111)- $\sqrt{3}\times\sqrt{3}$ -Ag Surface. *J. Chem. Phys.* **2015**, *142*, 204701.
- (74) Ohno, S.; Tanaka, H.; Tanaka, K.; Takahashi, K.; Tanaka, M. Electronic Structure of a-Sexithiophene Ultrathin Films Grown on Si(111)- $\sqrt{3}\times\sqrt{3}$ -Ag. *Phys. Chem. Chem. Phys.* **2018**, *20*, 1114–1126.
- (75) Liu, R.; Fu, C.; Perepichka, D. F.; Gallagher, M. C. Supramolecular Structures of Halogenated Oligothiophenes on the Si(111)- $\sqrt{3}\times\sqrt{3}$ -Ag Surface. *Surf. Sci.* **2016**, *647*, 51–54.
- (76) Upward, M. D.; Beton, P. H.; Moriarty, P. Adsorption of Cobalt Phthalocyanine on Ag Terminated Si(111). *Surf. Sci.* **1999**, *441*, 21–25.
- (77) Beggan, J. P.; Krasnikov, S. A.; Sergeeva, N. N.; Senge, M. O.; Cafolla, A. A. Self-Assembly of Ni(II) Porphine Molecules on the Ag/Si(111)-($\sqrt{3}\times\sqrt{3}$)R30° Surface Studied by STM/STS and LEED. *J. Phys. Condens. Matter* **2008**, *20*, 015003.
- (78) Li, Q.; Yamazaki, S.; Eguchi, T.; Kim, H.; Kahng, S. J.; Jia, J. F.; Xue, Q. K.; Hasegawa, Y. Initial Adsorption and Kondo Resonance of 5,10,15,20-Tetrakis(4- Bromophenyl)porphyrin-Co Molecules on Ag/Si(111) Surface Studied by Low-Temperature Scanning Tunneling Microscopy/Spectroscopy. *Jpn. J. Appl. Phys.* **2009**, *48*, 08JB01.
- (79) Baris, B.; Jeannoutot, J.; Luzet, V.; Palmino, F.; Rochefort, A.; Chérioux, F. Noncovalent Bicomponent Self-Assemblies on a Silicon Surface. *ACS Nano* **2012**, *6*, 6905–6911.
- (80) Guaino, P.; Cafolla, A. A.; McDonald, O.; Cart, D.; Sheerin, G.; Hughs, G. Scanning Tunnelling Spectroscopy of Low Pentacene Coverage on the Ag/Si(111)-($\sqrt{3}\times\sqrt{3}$) Surface. *J. Phys. Condens. Matter* **2003**, *15*, S2693–S2698.
- (81) Sheerin, G.; Cafolla, a. a. Self-Assembled Structures of Trimesic Acid on the Ag/Si(111)-($\sqrt{3}\times\sqrt{3}$)R30° Surface. *Surf. Sci.* **2005**, *577*, 211–219.
- (82) Suzuki, T.; Lutz, T.; Payer, D.; Lin, N.; Tait, S. L.; Costantini, G.; Kern, K. Substrate Effect on Supramolecular Self-Assembly: From Semiconductors to Metals. *Phys. Chem. Chem. Phys.* **2009**, *11*, 6498–6504.
- (83) Perdigão, L. M. A.; Staniec, P. A.; Champness, N. R.; Kelly, R. E. A.; Kantorovich, L. N.; Beton, P. H. Experimental and Theoretical Identification of Adenine Monolayers on Ag-Terminated Si(111). *Phys. Rev. B* **2006**, *73*, 195423.
- (84) Tegenkamp, C.; Schmeidel, J.; Pfnür, H. Chemisorption of Ferrocene on Si(111)-Ag $\sqrt{3}$: Frustrated Conformational Flexibility. *Surf. Sci.* **2011**, *605*, 267–271.
- (85) Ozkaya, S.; Birlik Demirel, G. Chemisorption of Thiol-Functionalized Metallocene Molecules on Si(111)- Ag $\sqrt{3}\times\sqrt{3}$ Surface: A Density Functional Theory Study. *Int. J. Quantum Chem.* **2016**, *116*, 35–41.
- (86) Zhao, X.; Rodriguez, J. Photoemission Study of Glycine Adsorption on Cu/Au(111) Interfaces. *Surf. Sci.* **2006**, *600*, 2113–2121.
- (87) Löfgren, P.; Krozer, A.; Lausmaa, J.; Kasemo, B. Glycine on Pt(111): A TDS and XPS Study. *Surf. Sci.* **1997**, *370*, 277–292.
- (88) Barlow, S. M.; Kitching, K. J.; Haq, S.; Richardson, N. V. A Study of Glycine Adsorption on a

- Cu{110} Surface Using Reflection Absorption Infrared Spectroscopy. *Surf. Sci.* **1998**, *401*, 322–335.
- (89) Madden, D. C.; Temprano, I.; Sacchi, M.; Blanco-Rey, M.; Jenkins, S. J.; Driver, S. M. Self-Organized Overlayers Formed by Alanine on Cu{311} Surfaces. *J. Phys. Chem. C* **2014**, *118*, 18589–18603.
- (90) Jone, G.; Jones, L. B.; Thibault-Starzyk, F.; Seddon, E. A.; Raval, R.; Jenkins, S. J.; Held, G. The Local Adsorption Geometry and Electronic Structure of Alanine on Cu{110}. *Surf. Sci.* **2006**, *600*, 1924–1935.
- (91) Barlow, S. M.; Louafi, S.; Le Roux, D.; Williams, J.; Murn, C.; Haq, S.; Raval, R. Polymorphism in Supramolecular Chiral Structures of R- and S-Alanine on Cu(110). *Surf. Sci.* **2005**, *590*, 243–263.
- (92) Barlow, S. M.; Louafi, S.; Le Roux, D.; Williams, J.; Murn, C.; Haq, S.; Raval, R. Supramolecular Assembly of Strongly Chemisorbed Size- and Shape-Defined Chiral Clusters: S- and R-Alanine on Cu(110). *Langmuir* **2004**, *20*, 7171–7176.
- (93) Haq, S.; Massey, A.; Moslemzadeh, N.; Robin, A.; Barlow, S. M.; Raval, R. Racemic versus Enantiopure Alanine on Cu(110): An Experimental Study. *Langmuir* **2007**, *23*, 10694–10700.
- (94) Iwai, H.; Egawa, C. Molecular Orientation and Intermolecular Interaction in Alanine on Cu(001). *Langmuir* **2010**, *26*, 2294–2300.
- (95) Smerieri, M.; Vattuone, L.; Kravchuk, T.; Costa, D.; Savio, L. (S)-Glutamic Acid on Ag(100): Self-Assembly in the Nonzwitterionic Form. *Langmuir* **2011**, *27*, 2393–2404.
- (96) Jones, T. E.; Baddeley, C. J.; Gerbi, A.; Savio, L.; Rocca, M.; Vattuone, L. Molecular Ordering and Adsorbate Induced Faceting in the Ag{110}-(S)-Glutamic Acid System. *Langmuir* **2005**, *21*, 9468–9475.
- (97) Tranca, I.; Smerieri, M.; Savio, L.; Vattuone, L.; Costa, D.; Tielens, F. Unraveling the Self-Assembly of the (S)-Glutamic Acid “Flower” Structure on Ag(100). *Langmuir* **2013**, *29*, 7876–7884.
- (98) Smerieri, M.; Vattuone, L.; Costa, D.; Tielens, F.; Savio, L. Self-Assembly of (S)-Glutamic Acid on Ag(100): A Combined LT-STM and Ab Initio Investigation. *Langmuir* **2010**, *26*, 7208–7215.
- (99) Zhao, X.; Zhao, R. G.; Yang, W. S. Scanning Tunneling Microscopy Investigation of L-Lysine Adsorbed on Cu(001). *Langmuir* **2000**, *16*, 9812–9818.
- (100) Humblot, V.; Méthivier, C.; Raval, R.; Pradier, C. M. Amino Acid and Peptides on Cu(110) Surfaces: Chemical and Structural Analyses of L-Lysine. *Surf. Sci.* **2007**, *601*, 4189–4194.
- (101) Humblot, V.; Méthivier, C.; Pradier, C. M. Adsorption of L-Lysine on Cu(110): A RAIRS Study from UHV to the Liquid Phase. *Langmuir* **2006**, *22*, 3089–3096.
- (102) Kühnle, A.; Linderoth, T. R.; Hammer, B.; Besenbacher, F. Chiral Recognition in Dimerization of Adsorbed Cysteine Observed by Scanning Tunneling Microscopy. *Nature* **2002**, *415*, 891–893.
- (103) Fischer, S.; Papageorgiou, A. C.; Marschall, M.; Reichert, J.; Diller, K.; Klappenberger, F.; Allegretti, F.; Nefedov, A.; Wöll, C.; Barth, J. V. L-Cysteine on Ag(111): A Combined STM and X-Ray Spectroscopy Study of Anchorage and Deprotonation. *J. Phys. Chem. C* **2012**, *116*, 20356–20362.
- (104) Uvdal, K.; Bodö, P.; Liedberg, B. L-Cysteine Adsorbed on Gold and Copper: An X-Ray Photoelectron Spectroscopy Study. *J. Colloid Interface Sci.* **1992**, *149*, 162–173.

- (105) Méthivier, C.; Humblot, V.; Pradier, C.-M. M. L-Methionine Adsorption on Cu(110), Binding and Geometry of the Amino Acid as a Function of Coverage. *Surf. Sci.* **2015**, *632*, 88–92.
- (106) Humblot, V.; Tielens, F.; Luque, N. B.; Hampartsoumian, H.; Méthivier, C.; Pradier, C. M. Characterization of Two-Dimensional Chiral Self-Assemblies L- And D-Methionine on Au(111). *Langmuir* **2014**, *30*, 203–212.
- (107) Schiffrin, A.; Reichert, J.; Pennec, Y.; Auwarter, W.; Alexander Weber-Bargioni; Marschall, M.; Angela, M. D.; Cvetko, D.; Bavdek, G.; Cossaro, A.; et al. Self-Assembly of L-Methionine on cu(111): Steering Chiral Organization by Substrate Reactivity and Thermal Activation. *J. Phys. Chem. C* **2009**, *113*, 12101–12108.
- (108) Schiffrin, A.; Riemann, A.; Auwärter, W.; Pennec, Y.; Weber-Bargioni, A.; Cvetko, D.; Cossaro, A.; Morgante, A.; Barth, J. V. Zwitterionic Self-Assembly of L-Methionine Nanogratings on the Ag(111) Surface. *Proc. Natl. Acad. Sci. U. S. A.* **2007**, *104*, 5279–5284.
- (109) Naitabdi, A.; Humblot, V. Chiral Self-Assemblies of Amino-Acid Molecules: D- and L-Methionine on Au(111) Surface. *Appl. Phys. Lett.* **2010**, *97*, 223112.
- (110) Reichert, J.; Schiffrin, K. A.; Auwa, W.; Weber-bargioni, K. A.; Marschall, M.; Angela, M. D.; Cvetko, D.; Bavdek, G.; Cossaro, A.; Morgante, A.; et al. L-Tyrosine on Ag(111): Universality of the Amino Acid 2D Zwitterionic Bonding Scheme? *ACS Nano* **2010**, *4*, 1218–1226.
- (111) Wang, D.; Xu, Q. M.; Wan, L. J.; Bai, C. L.; Jin, G. Adsorption of Enantiomeric and Racemic Tyrosine on Cu(111): A Scanning Tunneling Microscopy Study. *Langmuir* **2003**, *19*, 1958–1962.
- (112) Seljamäe-Green, R. T.; Simpson, G. J.; Grillo, F.; Greenwood, J.; Francis, S. M.; Schaub, R.; Lacovig, P.; Baddeley, C. J. Assembly of a Chiral Amino Acid on an Unreactive Surface: (S)-Proline on Au(111). *Langmuir* **2014**, *30*, 3495–3501.
- (113) Forster, M.; Dyer, M. S.; Persson, M.; Raval, R. Probing Conformers and Adsorption Footprints at the Single-Molecule Level in a Highly Organized Amino Acid Assembly of (S)-Proline on Cu(110). *J. Am. Chem. Soc.* **2009**, *131*, 10173–10181.
- (114) Chatterjee, A.; Zhang, L.; Leung, K. T. Surface [4+2] Cycloaddition Reaction of Thymine on Si(111)7×7 Observed by Scanning Tunneling Microscopy. *J. Phys. Chem. C* **2013**, *117*, 14677–14683.
- (115) Chatterjee, A.; Zhang, L.; Leung, K. T. Self-Directed Growth of Aligned Adenine Molecular Chains on Si(111)7×7: Direct Imaging of Hydrogen-Bond Mediated Dimers and Clusters at Room Temperature by Scanning Tunneling Microscopy. *Langmuir* **2013**, *29*, 9369–9377.
- (116) Zhang, L.; Chatterjee, A.; Leung, K. T. Three-Stage Growth of Glycine and Glycylglycine Nanofilms on Si(111)7×7 and Their Thermal Evolution in Ultrahigh Vacuum Condition: From Chemisorbed Adstructures to Transitional Adlayer to Zwitterionic Films. *J. Phys. Chem. C* **2011**, *115*, 14155–14163.
- (117) Chatterjee, A.; Zhang, L.; Leung, K. T. Bidentate Surface Structures of Glycylglycine on Si(111)7×7 by High-Resolution Scanning Tunneling Microscopy: Site-Specific Adsorption via N-H and O-H or Double N-H Dissociation. *Langmuir* **2012**, *28*, 12502–12508.
- (118) Chatterjee, A.; Zhang, L.; Leung, K. T. Computational Surface Chemistry of Glycine on Si(111)7×7 and Si(100)2×1: Dissociative Adsorption Through Adduct Formation. *Chem. Phys. Lett.* **2011**, *508*, 219–223.
- (119) Zhang, L.; Chatterjee, A.; Leung, K. T. Hydrogen-Bond-Mediated Biomolecular Trapping: Reversible Catch-and-Release Process of Common Biomolecules on a Glycine-Functionalized

- Si(111)7×7 Surface. *J. Phys. Chem. Lett.* **2010**, *1*, 3385–3390.
- (120) Chatterjee, A.; Zhang, L.; Leung, K. T. Direct Imaging of Hydrogen Bond Formation in Dissociative Adsorption of Glycine on Si(111)7×7 by Scanning Tunneling Microscopy. *J. Phys. Chem. C* **2012**, *116*, 10968–10975.
- (121) Rahsepar, F. R.; Zhang, L.; Farkhondeh, H.; Leung, K. T. Biofunctionalization of Si(111)7×7 by “renewable” L-Cysteine Transitional Layer. *J. Am. Chem. Soc.* **2014**, *136*, 16909–16918.
- (122) Rahsepar, F. R.; Leung, K. T. Self-Organized Supported Clusters of L-Methionine. *J. Phys. Chem. C* **2016**, *120*, 6534–6542.
- (123) Rahsepar, F. R.; Moghimi, N.; Leung, K. T. Surface-Mediated Hydrogen Bonding of Proteinogenic α -Amino Acids on Silicon. *Acc. Chem. Res.* **2016**, *49* (5), 942–951.
- (124) Rahsepar, F. R.; Leung, K. T. Biohybridization of Supported Gold Nanoassemblies on Silicon. *J. Phys. Chem. C* **2018**, *122*, 16113–16121.
- (125) Újfalussy, B.; Lazarovits, B.; Szunyogh, L.; Stocks, G. M.; Weinberger, P. Ab Initio Spin Dynamics Applied to Nanoparticles: Canted Magnetism of a Finite Co Chain along a Pt(111) Surface Step Edge. *Phys. Rev. B* **2004**, *70*, 100404.
- (126) Orita, H.; Inada, Y. DFT Investigation of CO Adsorption on Pt(211) and Pt(311) Surfaces from Low to High Coverage. *J. Phys. Chem. B* **2005**, *109*, 22469–22475.
- (127) Vang, R. T.; Honkala, K.; Dahl, S.; Vestergaard, E. K.; Schnadt, J.; Lægsgaard, E.; Clausen, B. S.; Nørskov, J. K.; Besenbacher, F. Ethylene Dissociation on Flat and Stepped Ni(111): A Combined STM and DFT Study. *Surf. Sci.* **2006**, *600*, 66–77.
- (128) Piccolo, L.; Loffreda, D.; Aires, F. J. C. S.; Deranlot, C.; Jugnet, Y.; Sautet, P.; Bertolini, J. C. The Adsorption of CO on Au(111) at Elevated Pressures Studied by STM, RAIRS and DFT Calculations. *Surf. Sci.* **2004**, *566–568*, 995–1000.
- (129) Hussain, A.; Curulla Ferré, D.; Gracia, J.; Nieuwenhuys, B. E.; Niemantsverdriet, J. W. DFT Study of CO and NO Adsorption on Low Index and Stepped Surfaces of Gold. *Surf. Sci.* **2009**, *603*, 2734–2741.
- (130) Thomsen, L.; Wharmby, M. T.; Riley, D. P.; Held, G.; Gladys, M. J. The Adsorption and Stability of Sulfur Containing Amino Acids on Cu{531}. *Surf. Sci.* **2009**, *603*, 1253–1261.
- (131) Zheng, T.; Wu, C.; Chen, M.; Zhang, Y.; Cummings, P. T. A DFT Study of Water Adsorption on Rutile TiO₂(110) Surface: The Effects of Surface Steps. *J. Chem. Phys.* **2016**, *145*, 044702.
- (132) Yang, P.; Zhang, L. X. A Theoretical Study of Step Edge Geometry on Sapphire(0001) and Its Effect on ZnO Nucleation. *Front. Phys.* **2019**, *14*, 23606.
- (133) Einstein, A. Generation and Conversion of Light with Regard to a Heuristic Point of View , Über Einen Die Erzeugung Und Verwandlung Des Lichtes Betreffenden Heuristischen Gesichtspunkt. *Ann. der Physic* **1905**, *17*, 132–148.
- (134) Nordling, C.; Sokolowski, E.; Siegbahn, K. Precision Method for Obtaining Absolute Values of Atomic Binding Energies. *Phys. Rev.* **1957**, *105*, 1676–1677.
- (135) Binnig, G.; Rohrer, H.; Gerber, C.; Weibel, E. Surface Studies by Scanning Tunneling Microscopy. *Phys. Rev. Lett.* **1982**, *49*, 57–61.
- (136) Wallace, W. E. Mass Spectra. In *NIST Chemistry Webbook, NIST Standard Reference Database Number 69*; Linstrom, P. J., Mallard, W. G., Eds.; National Institute of Standard and Technology:

Gaithersburg MD; 20899.

- (137) Parr, R. G. Density Functional Theory of Atoms and Molecules. In *Horizons of Quantum Chemistry*; Fukui, K., Pullman, B., Eds.; Springer: Dordrecht, 1980; Vol. 3, pp 5–15.
- (138) Dirac, P. A. M. Note on Exchange Phenomena in the Thomas Atom. *Math. Proc. Cambridge Philos. Soc.* **1930**, *26*, 376–385.
- (139) Becke, A. D. Density-Functional Exchange Approximation with Correct Asymptotic Behaviour. *Phys. Rev. A* **1988**, *38*, 3098–3100.
- (140) Perdew, J. P.; Chevary, J. A.; Vosko, S. H.; Jackson, K. A.; Pederson, M. R.; Singh, D. J.; Fiolhais, C. Atoms, Molecules, Solids, and Surfaces: Applications of the Generalized Gradient Approximation for Exchange and Correlation. *Phys. Rev. B* **1992**, *46*, 6671–6687.
- (141) Perdew, J. P.; Burke, K.; Ernzerhof, M. Generalized Gradient Approximation Made Simple. *Phys. Rev. Lett.* **1996**, *77*, 3865–3868.
- (142) Wu, X.; Vargas, M. C.; Nayak, S.; Lotrich, V.; Scoles, G. Towards Extending the Applicability of Density Functional Theory to Weakly Bound Systems. *J. Chem. Phys.* **2001**, *115*, 8748–8757.
- (143) Grimme, S. Accurate Description of van Der Waals Complexes by Density Functional Theory Including Empirical Corrections. *J. Comput. Chem.* **2004**, *25*, 1463–1473.
- (144) Grimme, S. Semiempirical GGA-Type Density Functional Constructed with a Long-Range Dispersion Correction. *J. Comput. Chem.* **2006**, *27*, 1787–1799.
- (145) Grimme, S.; Antony, J.; Ehrlich, S.; Krieg, H. A Consistent and Accurate Ab Initio Parametrization of Density Functional Dispersion Correction (DFT-D) for the 94 Elements H-Pu. *J. Chem. Phys.* **2010**, *132*, 154104.
- (146) Le Lay, G.; Aristov, V. Y.; Seehofer, L.; Buslaps, T.; Al, E. STM and Synchrotron Radiation Studies of “Prototypical” Metal/Semiconductor Systems. *Surf. Sci.* **1994**, *307–309*, 280–294.
- (147) Takahashi, T.; Nakatani, S.; Okamoto, N.; Ishikawa, T.; Kikuta, S. A Study of the Si (111) $\sqrt{3}\times\sqrt{3}$ -Ag Surface by Transmission X-Ray Diffraction and X-Ray Diffraction Topography. *Surf. Sci.* **1991**, *242*, 54–58.
- (148) Takahashi, T.; Nakatani, S.; Okamoto, N.; Ishikawa, T.; Kikuta, S. Study on the Si (111) $\sqrt{3}\times\sqrt{3}$ -Ag Surface Structure by X-Ray Diffraction. *Jpn. J. Appl. Phys.* **1988**, *27*, L753–L755.
- (149) Kirchner, E. J. J.; Baerends, E. J.; Velde, G.; Vlieg, E. A Study on the Si (111)- $\sqrt{3}\times\sqrt{3}$ -Ag System II. Interaction between Substrate and Adsorbate. *Surf. Sci.* **1995**, *330*, 113–125.
- (150) Wandlowski, T.; Lampner, D.; Lindsay, S. M. Structure and Stability of Cytosine Adlayers on Au(111): An in-Situ STM Study. *J. Electroanal. Chem.* **1996**, *404*, 215–226.
- (151) Kawai, T.; Tanaka, H.; Nakagawa, T. Low Dimensional Self-Organization of DNA-Base Molecules on Cu(111) Surfaces. *Surf. Sci.* **1997**, *386*, 124–136.
- (152) Furukawa, M.; Tanaka, H.; Kawai, T. Formation Mechanism of Low-Dimensional Superstructure of Adenine Molecules and Its Control by Chemical Modification: A Low-Temperature Scanning Tunneling Microscopy Study. *Surf. Sci.* **2000**, *445*, 1–10.
- (153) Furukawa, M.; Tanaka, H.; Kawai, T. The Role of Dimer Formation in the Self-Assemblies of DNA Base Molecules on Cu(111) Surfaces: A Scanning Tunneling Microscope Study. *J. Chem. Phys.* **2001**, *115*, 3419–3423.
- (154) Otero, R.; Lukas, M.; Kelly, R. E. A.; Xu, W.; Lægsgaard, E.; Stensgaard, I.; Kantorovich, L. N.;

- Besenbacher, F. Elementary Structural Motifs in a Random Network of Cytosine Adsorbed on a Gold(111) Surface. *Science* **2008**, *319*, 312–315.
- (155) Xu, W.; Kelly, R. E. A.; Otero, R.; Schöck, M.; Lægsgaard, E.; Stensgaard, I.; Kantorovich, L. N.; Besenbacher, F. Probing the Hierarchy of Thymine-Thymine Interactions in Self-Assembled Structures by Manipulation with Scanning Tunneling Microscopy. *Small* **2007**, *3*, 2011–2014.
- (156) Kelly, R. E. A.; Lukas, M.; Kantorovich, L. N.; Otero, R.; Xu, W.; Mura, M.; Lægsgaard, E.; Stensgaard, I.; Besenbacher, F. Understanding the Disorder of the DNA Base Cytosine on the Au(111) Surface. *J. Chem. Phys.* **2008**, *129*, 184707.
- (157) Kelly, R. E. A.; Xu, W.; Lukas, M.; Otero, R.; Mura, M.; Lee, Y. J.; Lægsgaard, E.; Stensgaard, I.; Kantorovich, L. N.; Besenbacher, F. An Investigation into the Interactions between Self-Assembled Adenine Molecules and Au(111) Surface. *Small* **2008**, *4*, 1494–1500.
- (158) Otero, R.; Xu, W.; Lukas, M.; Kelly, R. E. A.; Lægsgaard, E.; Stensgaard, I.; Kjems, J.; Kantorovich, L. N.; Besenbacher, F. Specificity of Watson-Crick Base Pairing on a Solid Surface Studied at the Atomic Scale. *Angew. Chemie* **2008**, *120*, 9819–9822.
- (159) Bald, I.; Wang, Y. G.; Dong, M.; Rosen, C. B.; Ravnsbø, J. B.; Zhuang, G. L.; Gothelf, K. V.; Wang, J. G.; Besenbacher, F. Control of Self-Assembled 2D Nanostructures by Methylation of Guanine. *Small* **2011**, *7*, 939–949.
- (160) Liu, L.; Xia, D.; Klausen, L. H.; Dong, M. The Self-Assembled Behavior of DNA Bases on the Interface. *Int. J. Mol. Sci.* **2014**, *15*, 1901–1914.
- (161) Marti, E. M.; Methivier, C.; Pradier, C. M. (S)-Cysteine Chemisorption on Cu(110), from the Gas or Liquid Phase: An FT-RAIRS and XPS Study. *Langmuir* **2004**, *20*, 10223–10230.
- (162) Canepa, M.; Pelori, P.; Lavagnino, L.; Bisio, F.; Moroni, R.; Terreni, S.; Mattera, L. He* Interaction with Soft Matter Surfaces: Ultra Thin L-Cysteine Films. *Nucl. Instruments Methods Phys. Res. Sect. B* **2007**, *256*, 324–327.
- (163) Luque, N. B.; Vélez, P.; Pötting, K.; Santos, E. Ab Initio Studies of the Electronic Structure of L-Cysteine Adsorbed on Ag(111). *Langmuir* **2012**, *28*, 8084–8099.
- (164) Santos, E.; Avalle, L. B.; Scurtu, R.; Jones, H. L-Cysteine Films on Ag(111) Investigated by Electrochemical and Nonlinear Optical Methods. *Chem. Phys.* **2007**, *342*, 236–244.
- (165) Santos, E.; Avalle, L.; Pötting, K.; Vélez, P.; Jones, H. Experimental and Theoretical Studies of L-Cysteine Adsorbed at Ag(111) Electrodes. *Electrochim. Acta* **2008**, *53*, 6807–6817.
- (166) Schillinger, R.; Šljivančanin, Ž.; Hammer, B.; Greber, T. Probing Enantioselectivity with X-Ray Photoelectron Spectroscopy and Density Functional Theory. *Phys. Rev. Lett.* **2007**, *98*, 136102.
- (167) Kühnle, A.; Molina, L. M.; Linderoth, T. R.; Hammer, B.; Besenbacher, F. Growth of Unidirectional Molecular Rows of Cysteine on Au(110)-(1×2) Driven by Adsorbate-Induced Surface Rearrangements. *Phys. Rev. Lett.* **2004**, *93*, 86101.
- (168) Canepa, M.; Lavagnino, L.; Pasquali, L.; Moroni, R.; Bisio, F.; De Renzi, V.; Terreni, S.; Mattera, L. Growth Dynamics of L-Cysteine SAMs on Single-Crystal Gold Surfaces: A Metastable Deexcitation Spectroscopy Study. *J. Phys. Condens. Matter* **2009**, *21*, 264005.
- (169) Cossaro, A.; Terreni, S.; Cavalleri, O.; Prato, M.; Cvetko, D.; Morgante, A.; Floreano, L.; Canepa, M. Electronic and Geometric Characterization of the L-Cysteine Paired-Row Phase on Au(110). *Langmuir* **2006**, *22*, 11193–11198.
- (170) Gonella, G.; Terreni, S.; Cvetko, D.; Cossaro, A.; Mattera, L.; Cavalleri, O.; Rolandi, R.;

- Morgante, A.; Floreano, L.; Canepa, M. Ultrahigh Vacuum Deposition of L-Cysteine on Au(110) Studied by High-Resolution X-Ray Photoemission: From Early Stages of Adsorption to Molecular Organization. *J. Phys. Chem. B* **2005**, *109*, 18003–18009.
- (171) Höffling, B.; Ortmann, F.; Hannewald, K.; Bechstedt, F. Single Cysteine Adsorption on Au(110): A First-Principles Study. *Phys. Rev. B* **2010**, *81*, 45407.
- (172) Höffling, B.; Ortmann, F.; Hannewald, K.; Bechstedt, F. Interface with Organic Molecules: Cysteine on Au(110). *Phys. Status Solidi* **2010**, *7*, 149–152.
- (173) Kühnle, A.; Linderoth, T. R.; Schunack, M.; Besenbacher, F. L-Cysteine Adsorption Structures on Au(111) Investigated by Scanning Tunneling Microscopy under Ultrahigh Vacuum Conditions. *Langmuir* **2006**, *22*, 2156–2160.
- (174) Kühnle, A.; Linderoth, T. R.; Besenbacher, F. Enantiospecific Adsorption of Cysteine at Chiral Kink Sites on Au(110)-(1×2). *J. Am. Chem. Soc.* **2006**, *128*, 1076–1077.
- (175) Chapman, C. R. L.; Ting, E. C. M.; Kereszti, A.; Paci, I. Self-Assembly of Cysteine Dimers at the Gold Surface: A Computational Study of Competing Interactions. *J. Phys. Chem. C* **2013**, *117*, 19426–19435.
- (176) Buimaga-Iarinca, L.; Morari, C. Effect of Conformational Symmetry upon the Formation of Cysteine Clusters on the Au(110)-(1×1) Surface: A First-Principles Study. *J. Phys. Chem. C* **2013**, *117*, 20351–20360.
- (177) Di Felice, R.; Selloni, A.; Molinari, E. DFT Study of Cysteine Adsorption on Au(111). *J. Phys. Chem. B* **2003**, *107*, 1151–1156.
- (178) Di Felice, R.; Selloni, A. Adsorption Modes of Cysteine on Au(111): Thiolate, Amino-Thiolate, Disulfide. *J. Chem. Phys.* **2004**, *120*, 4906–4914.
- (179) Mateo-Martí, E.; Rogero, C.; Gonzalez, C.; Sobrado, J. M.; De Andrés, P. L.; Martin-Gago, J. A. Interplay between Fast Diffusion and Molecular Interaction in the Formation of Self-Assembled Nanostructures of S-Cysteine on Au(111). *Langmuir* **2010**, *26*, 4113–4118.
- (180) Kühnle, A. Self-Assembly of Organic Molecules at Metal Surfaces. *Curr. Opin. Colloid Interface Sci.* **2009**, *14*, 157–168.
- (181) Fajín, J. L. C.; Gomes, J. R. B.; Cordeiro, M. N. D. S. DFT Study of the Adsorption of D-(L-)Cysteine on Flat and Chiral Stepped Gold Surfaces. *Langmuir* **2013**, *29*, 8856–8864.
- (182) Dobrowolski, J. C.; Rode, J. E.; Sadlej, J. Cysteine Conformations Revisited. *J. Mol. Struct. THEOCHEM* **2007**, *810*, 129–134.
- (183) Bensebaa, F.; Zhou, Y.; Deslandes, Y.; Kruus, E.; Ellis, T. H. XPS Study of Metal-Sulfur Bonds in Metal-Alkanethiolate Materials. *Surf. Sci.* **1998**, *405*, 472–476.
- (184) Briggs, D. D.; Seah, M. P. *Practical Surface Analysis*, 2nd ed.; Wiley: Chichester; Toronto, 1948.
- (185) Dodero, G.; De Michieli, L.; Cavalleri, O.; Rolandi, R.; Oliveri, L.; Daccà, A.; Parodi, R. L-Cysteine Chemisorption on Gold: An XPS and STM Study. *Colloids Surfaces A* **2000**, *175*, 121–128.
- (186) Cavalleri, O.; Gonella, G.; Terreni, S.; Vignolo, M.; Floreano, L.; Morgante, A.; Canepa, M.; Rolandi, R. High Resolution X-Ray Photoelectron Spectroscopy of L-Cysteine Self-Assembled Film. *Phys. Chem. Chem. Phys.* **2004**, *6*, 4042–4046.
- (187) Zubavichus, Y.; Zharnikov, M.; Yang, Y.; Fuchs, O.; Heske, C.; Umbach, E.; Tzvetkov, G.;

- Netzer, F. P.; Grunze, M. Surface Chemistry of Ultrathin Films of Histidine on Gold as Probed by High-Resolution Synchrotron Photoemission. *J. Phys. Chem. B* **2005**, *109*, 884–891.
- (188) Weiss, I. M.; Muth, C.; Drumm, R.; Kirchner, H. O. K. Thermal Decomposition of the Amino Acids Glycine, Cysteine, Aspartic Acid, Asparagine, Glutamic Acid, Glutamine, Arginine and Histidine. *BMC Biophys.* **2018**, *11*, 1–15.
- (189) Stöhr, J.; Gland, J. L.; Kollin, E. B.; Koestner, R. J.; Johnson, A. L.; Muettterties, E. L.; Sette, F. Desulfurization and Structural Transformation of Thiophene on the Pt(111) Surface. *Phys. Rev. Lett.* **1984**, *53*, 2161–2164.
- (190) Qiao, M. H.; Cao, Y.; Tao, F.; Liu, Q.; Deng, J. F.; Xu, G. Q. Electronic and Vibrational Properties of Thiophene on Si(100). *J. Phys. Chem. B* **2000**, *104*, 11211–11219.
- (191) Kaushik, V. K. XPS Core Level Spectra and Auger Parameters for Some Silver Compounds. *J. Electron Spectros. Relat. Phenomena* **1991**, *56*, 273–277.
- (192) Bensebaa, F.; Zhou, Y.; Deslandes, Y.; Kruus, E.; Ellis, T. H. XPS Study of Metal-Sulfur Bonds in Metal-Alkanethiolate Materials. *Surf. Sci.* **1998**, *405*, L472–L476.
- (193) Powell, C. J. Elemental Binding Energies for X-Ray Photoelectron Spectroscopy. *Appl. Surf. Sci.* **1995**, *89*, 141–149.
- (194) Oura, K.; Sumitomo, K.; Kobayashi, T.; Kinoshita, T.; Tanaka, Y.; Shoji, F.; Katayama, I. Adsorption of H on Si(111)- $\sqrt{3}\times\sqrt{3}$ -Ag: Evidence for Ag(111) Agglomerates Formation. *Surf. Sci. Lett.* **1991**, *254*, L460–L464.
- (195) Watanabe, S.; Aono, M.; Tsukada, M. Theoretical Calculations of the Scanning-Tunneling-Microscopy Images of the Si(111)- $\sqrt{3}\times\sqrt{3}$ -Ag Surface. *Phys. Rev. B* **1991**, *44*, 8330–8333.
- (196) McComb, D. W.; Wolkow, R. A.; Hackett, P. A. Defects on the Ag/Si(111)-($\sqrt{3}\times\sqrt{3}$) Surface. *Phys. Rev. B* **1994**, *50*, 18268–18274.
- (197) Venable, J. A. *Introduction to Surface and Thin Film Processes*; Cambridge, 2003.
- (198) Barth, J. V.; Costantini, G.; Kern, K. Engineering Atomic and Molecular Nanostructures at Surfaces. *Nature* **2005**, *437*, 671–679.
- (199) Oura, K.; Ohnishi, H.; Yamamoto, Y.; Katayama, I.; Ohba, Y. Atomic-Hydrogen-Induced Ag Cluster Formation on Si(111)- $\sqrt{3}\times\sqrt{3}$ -Ag Surface Observed by Scanning Tunneling Microscopy. *J. Vac. Sci. Technol. B* **1996**, *14*, 988–991.
- (200) Williams, B. R.; Mason, B. F.; McComb, D. W.; Moffatt, D. J.; Hackett, P. A. A Scanning Tunneling Microscopy Investigation of the Reaction of Hydrogen Atoms with Ag/Si(111)-($\sqrt{3}\times\sqrt{3}$). *Surf. Sci.* **1994**, *313*, L790–L796.
- (201) Ohnishi, H.; Yamamoto, Y.; Katayama, I.; Ohba, Y.; Oura, K. Hydrogen-Induced Ag Cluster Formation on the Si(111)- $\sqrt{3}\times\sqrt{3}$ (R30°)-Ag Surface Observed by Scanning Tunneling Microscopy. *Jpn. J. Appl. Phys.* **1994**, *33*, L1106–L1109.
- (202) Li, B. Q.; Zuo, J. M. Self-Assembly of Epitaxial Ag Nanoclusters on H-Terminated Si(111) Surfaces. *J. Appl. Phys.* **2003**, *94*, 743–748.
- (203) Gronert, S.; O’Hair, R. A. J. Ab Initio Studies of Amino Acid Conformations. 1. The Conformers of Alanine, Serine, and Cysteine. *J. Am. Chem. Soc.* **1995**, *117*, 2071–2081.
- (204) Luo, Y. R. *Comprehensive Handbook of Chemical Bond Energies*; CRC Press: Boca raton, FL, 2007.

- (205) Costa, D.; Pradier, C. M.; Tielens, F.; Savio, L. Adsorption and Self-Assembly of Bio-Organic Molecules at Model Surfaces: A Route towards Increased Complexity. *Surf. Sci. Rep.* **2015**, *70*, 449–553.
- (206) Vuyyuri, S. B.; Hamstra, D. A.; Khanna, D.; Hamilton, C. A.; Markwart, S. M.; Campbell, K. C. M.; Sunkara, P.; Ross, B. D.; Rehemtulla, A. Evaluation of D-Methionine as a Novel Oral Radiation Protector for Prevention of Mucositis. *Clin. Cancer Res.* **2008**, *14*, 2161–2170.
- (207) Humblot, V.; Pradier, C. M. Chiral Recognition of L-Gramicidine on Chiral Methionine-Modified Au(111). *J. Phys. Chem. Lett.* **2013**, *4*, 1816–1820.
- (208) Liu, G.; Rodriguez, J. A.; Dvorak, J.; Hrbek, J.; Jirsak, T. Chemistry of Sulfur-Containing Molecules on Au(111): Thiophene, Sulfur Dioxide, and Methanethiol Adsorption. *Surf. Sci.* **2002**, *505*, 295–307.
- (209) Kuo, K. H.; Shih, J. J.; Liao, Y. H.; Fu, T. W.; Fan, L. J.; Yang, Y. W.; Lin, J. L. Thermal Decomposition of HSCH₂CH₂OH on Cu(111): Identification and Adsorption Geometry of Surface Intermediates. *J. Phys. Chem. B* **2005**, *109*, 5055–5059.
- (210) Cristina, L. J.; Ruano, G.; Salvarezza, R.; Ferrón, J. Thermal Stability of Self-Assembled Monolayers of N-Hexanethiol on Au(111)-(1×1) and Au(001)-(1×1). *J. Phys. Chem. C* **2017**, *121*, 27894–27904.
- (211) Castro, M. E.; White, J. M. Decomposition of Methanethiol on Ni(111): A TPD and SSIMS Study. *Surf. Sci.* **1991**, *257*, 22–32.
- (212) Schmiegel, S. J.; Belton, D. N. Polycrystalline Diamond Film on Si(100) by XPS. *Surf. Sci. Spectra* **1992**, *1*, 329–332.
- (213) Zhao, X.; Yan, H.; Tu, X.; Zhao, R. G.; Yang, W. S. Spillover-Induced Chemisorption of Amino Acid on Silver Surfaces. *Langmuir* **2003**, *19*, 5542–5545.
- (214) Pennec, Y.; Auwärter, W.; Schiffrin, A.; Weber-Bargioni, A.; Riemann, A.; Barth, J. V. Supramolecular Gratings for Tuneable Confinement of Electrons on Metal Surfaces. *Nat. Nanotechnol.* **2007**, *2*, 99–103.
- (215) Riemann, A.; Nelson, B. Molecular Wires Self-Assembled on a Graphite Surface. *Langmuir* **2009**, *25*, 4522–4525.
- (216) Krebs, E.; Grabill, L.; Riemann, A. Amino Acid Nanopatterning on Graphite. *Surf. Sci.* **2018**, *678*, 143–148.
- (217) Schiffrin, A.; Reichert, J.; Auwärter, W.; Jahnz, G.; Pennec, Y.; Weber-Bargioni, A.; Stepanyuk, V. S.; Niebergall, L.; Bruno, P.; Barth, J. V. Self-Aligning Atomic Strings in Surface-Supported Biomolecular Gratings. *Phys. Rev. B* **2008**, *78*, 35424.
- (218) Orpen, A. G.; Brammer, L.; Allen, F. H.; Kennard, O.; Watson, D. G.; Taylor, R. Tables of Bond Lengths Determined by X-Ray and Neutron Diffraction. Part 2. Organometallic Compounds and Co-Ordination Complexes of the D- and F-Block Metals. *J. Chem. Soc. Dalt. Trans.* **1989**, S1–S83.
- (219) Cordero, B.; Gómez, V.; Platero-Prats, A. E.; Revés, M.; Echeverría, J.; Cremades, E.; Barragán, F.; Alvarez, S. Covalent Radii Revisited. *Dalt. Trans.* **2008**, 2832–2838.
- (220) Zhang, L.; Chatterjee, A.; Ebrahimi, M.; Leung, K. T. Hydrogen-Bond Mediated Transitional Adlayer of Glycine on Si (111)7×7 at Room Temperature. *J. Chem. Phys.* **2009**, *130*, 121103.
- (221) Chatterjee, A.; Zhao, L.; Zhang, L.; Pradhan, D.; Zhou, X.; Leung, K. T. Core-Level Electronic

- Structure of Solid-Phase Glycine, Glycyl-Glycine, Diglycyl-Glycine, and Polyglycine: X-Ray Photoemission Analysis and Hartree-Fock Calculations of Their Zwitterions. *J. Chem. Phys.* **2008**, *129*, 105104.
- (222) Zhao, X.; Yan, H.; Zhao, R. G.; Yang, W. S. Physisorption-Induced Surface Reconstruction and Morphology Changes: Adsorption of Glycine on the Au(110) 1×2 Surface. *Langmuir* **2002**, *18*, 3910–3915.
- (223) Chen, Q.; Richardson, N. V. Surface Facetting Induced by Adsorbates. *Prog. Surf. Sci.* **2003**, *73*, 59–77.
- (224) Oura, K.; Naitoh, M.; Yamane, J.; Shoji, F. Hydrogen-Induced Reordering of the Si(111)- $\sqrt{3}\times\sqrt{3}$ -Ag Surface. *Surf. Sci. Lett.* **1990**, *230*, L151–L154.
- (225) Landemark, E.; Karlsson, C. J.; Uhrber, R. I. G. Ideal Unreconstructed Hydrogen Termination of the Si(111) Surface Obtained by Hydrogen Exposure of the $\sqrt{3}\times\sqrt{3}$ -In Surface. *Phys. Rev. B* **1991**, *44*, 1950–1954.
- (226) Saranin, A. A.; Khramtsova, E. A.; Lifshits, V. G. Effect of NH₃ Adsorption on the Atomic Structure of Si(111) $\sqrt{3}\times\sqrt{3}$ -Al and Si(111) $\sqrt{3}\times\sqrt{3}$ -Ag Surfaces. *Surf. Sci.* **1993**, *296*, L21–L26.
- (227) Watanabe, S.; Kondo, Y.; Nakamura, Y.; Nakamura, J. Atomic and Electronic Structure of the Si(111)- $\sqrt{3}\times\sqrt{3}$ -Ag Surface Reexamined Using First-Principles Calculations. *Sci. Technol. Adv. Mater.* **2000**, *1*, 167–172.
- (228) Sweetman, A.; Stannard, A.; Sugimoto, Y.; Abe, M.; Morita, S.; Moriarty, P. Simultaneous Noncontact AFM and STM of Ag:Si(111)-($\sqrt{3}\times\sqrt{3}$)R30°. *Phys. Rev. B - Condens. Matter Mater. Phys.* **2013**, *87*, 75310.
- (229) Ueno, M.; Matsuda, I.; Liu, C.; Hasegawa, S. Step Edges as Reservoirs of Ag Adatom Gas on a Si(111) Surface. *Jpn. J. Appl. Phys.* **2003**, *42*, 4894–4897.
- (230) Krueger, S.; Mönch, W. Electronic and Structural Properties of Steps on Cleaved Semiconductor Surfaces. *Surf. Sci.* **1980**, *99*, 157–164.
- (231) Zhang, H. M.; Sakamoto, K.; Uhrberg, R. I. G. Comprehensive Study of the Metal/Semiconductor Character of Adatom-Induced Ag/Si(111) Reconstructions. *Phys. Rev. B* **2001**, *64*, 245421.
- (232) Uhrberg, R. I. G.; Zhang, H. M.; Balasubramanian, T.; Landemark, E.; Yeom, H. W. Photoelectron Spectroscopy Study of Ag/Si(111) $\sqrt{3}\times\sqrt{3}$ and the Effect of Additional Ag Adatoms. *Phys. Rev. B* **2002**, *65*, 081305.
- (233) Johansson, L. S. O.; Landemark, E.; Karlsson, C. J.; Uhrberg, R. I. G. Fermi-Level Pinning and Surface-State Band Structure of the Si(111)-($\sqrt{3}\times\sqrt{3}$)R30°-Ag. *Phys. Rev. Lett.* **1989**, *63*, 2092–2095.

Appendix A

Cysteine on Si(111)- $\sqrt{3}\times\sqrt{3}$ -Ag

Table A1 Binding energies (in eV) of fitted peak maxima of XPS core-level spectra for O1s, N1s, C1s, and S2s regions and their assignments for cysteine films at increasing exposures and after annealing the as-grown thick cysteine film (obtained with the 3600-s exposure) at 85 °C, 175 °C, and 285 °C.

Core level	Assignment	30 s	60 s	120 s	180 s	240 s	1200 s	3600 s	85 °C	175 °C	285 °C
O 1s	-COO ⁻	531.5	531.5	531.5	531.6	531.6	531.7	532.0	531.9	--	--
	-COOH	532.4	532.5	532.5	532.6	532.6	532.8	--	533.8	532.8	532.8
N 1s	-NH-Si	--	--	--	--	--	--	--	--	399.1	399.0
	-NH ₂	399.5	399.4	399.4	399.5	399.5	--	--	400.0	400.0	400.1
	O-H...N	--	--	--	--	--	--	--	--	401.1	--
	-NH ₃ ⁺	402.0	401.9	401.9	402.0	402.0	401.9	402.0	402.0	--	--
C 1s	-CH ₂ -S-Ag	285.3	285.3	285.3	285.3	285.4	285.2	--	--	285.5	285.1
	-CH ₂ -SH	--	--	--	286.2	286.2	286.2	286.3	286.1	--	--
	-CH ₂ -NH-Si	--	--	--	--	--	--	--	--	286.5	286.3
	-CH ₂ -NH ₂	286.1	286.2	286.1	--	--	--	--	--	--	--
	-CH-NH ₃ ⁺	286.7	287.0	286.7	286.7	286.8	286.8	287.0	287.0	--	--
	-COO ⁻	288.4	288.5	288.4	288.5	288.5	288.5	289.0	288.9	--	--
	-COOH	289.3	289.4	289.4	289.5	289.5	289.3	--	--	289.0	289.2
S 2s	-S-Ag	226.6	226.6	226.4	226.5	226.6	226.6	--	--	226.6	226.6
	-SH	--	--	--	228.5	228.6	228.6	228.6	228.6	228.6	228.6

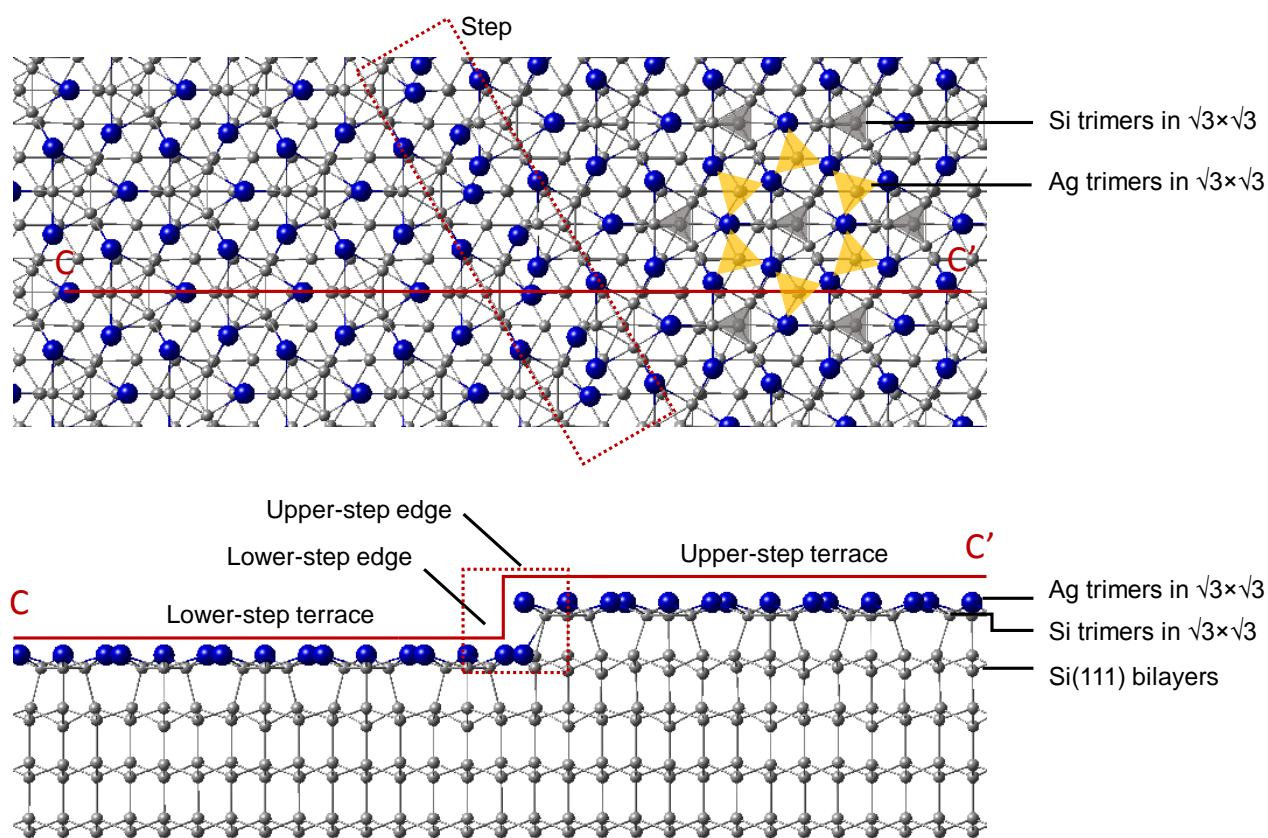


Figure A1 Top view (top) and cross sectional view along the C-C' line (bottom) for an unoptimized model of the Si(111)- $\sqrt{3} \times \sqrt{3}$ -Ag surface illustrating the honeycomb-chained trimer on terraces and a tentative geometrical configuration at the step edge along the [1-21] crystallographic direction. The height of the step edge is equal to the height of a Si(111) bilayer, 3.1 Å. The dangling bonds at the step edge are passivated by Ag atoms in this model. Detailed DFT calculations for structural optimization and analysis of the step edge (and antiphase boundary) will be reported elsewhere.

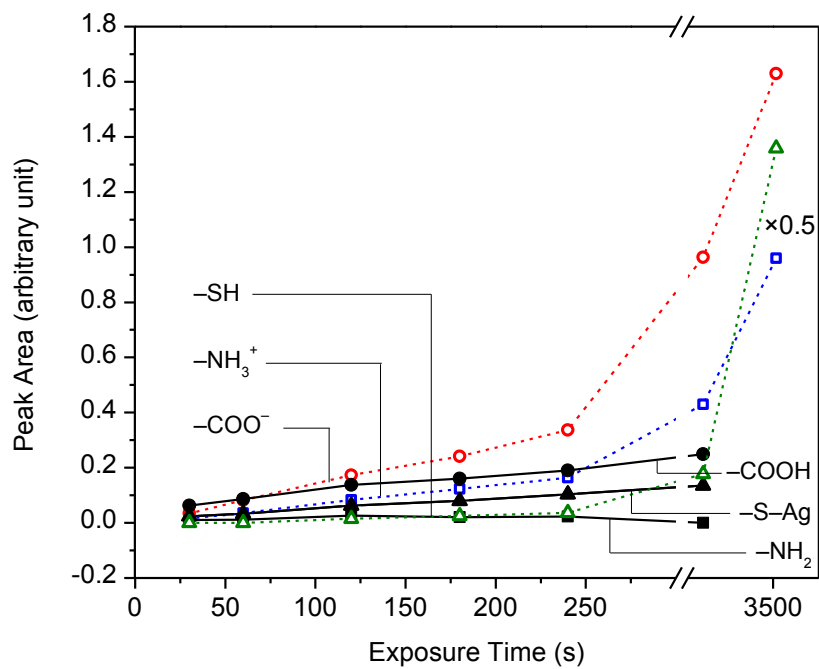


Figure A2 Relative peak areas of O 1s, N 1s, and S 2s features for different cysteine exposures. Solid and dotted lines connecting the respective regular bonding and zwitterionic bonding features are used to guide the eye.

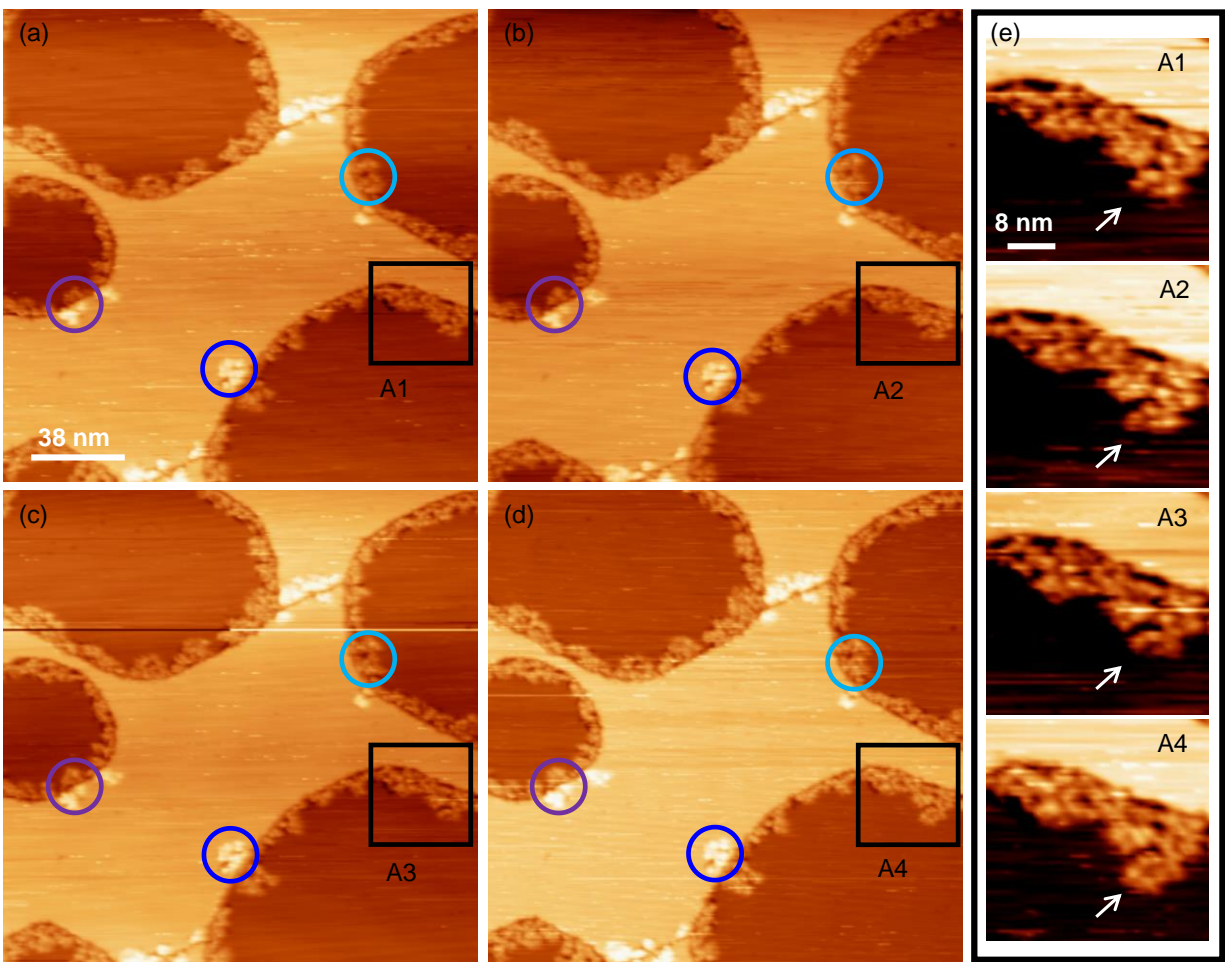


Figure A3 Time-sequence empty-state STM images of the Si(111)- $\sqrt{3}\times\sqrt{3}$ -Ag surface after a 30-s cysteine exposure, collected consecutively with a sample bias of +2 V and a tunneling current of 0.2 nA. The circles and the squares mark the adspecies islands that grow slightly bigger in each image, confirming the mobility of the cysteine adspecies at room temperature. The images in (e) correspond to protrusions found in the magnified areas marked by the squares in images (a-d), which show the addition of bright protrusions at marked locations of the adspecies island.

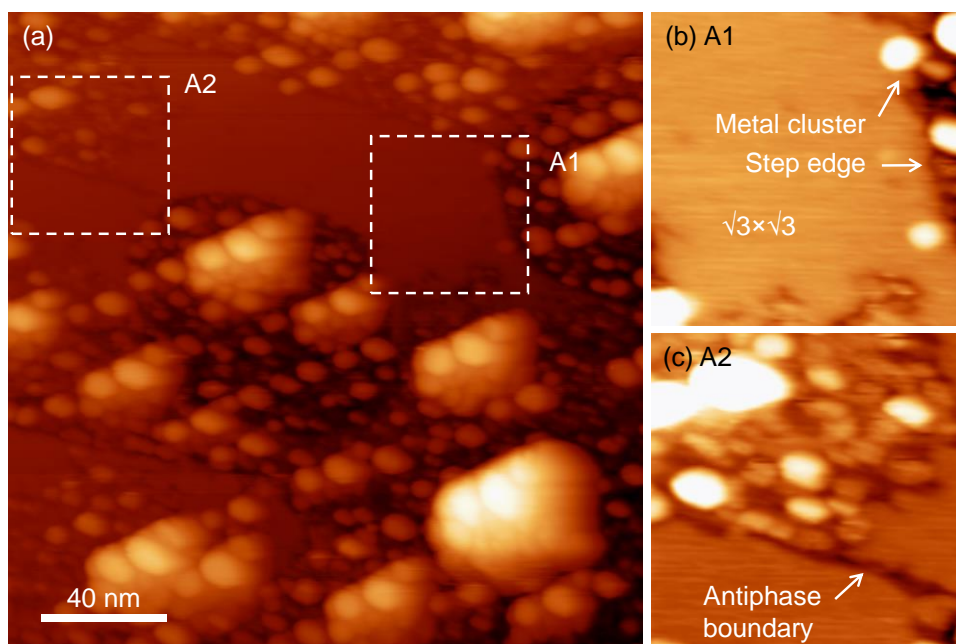


Figure A4 (a) An empty-state STM image obtained with a sample bias of +2 V and a constant tunneling current of 0.2 nA for a Si(111)- $\sqrt{3} \times \sqrt{3}$ -Ag surface after a 240-s cysteine exposure followed by an annealing step at 175 °C. Expanded views of (b) the smooth undisrupted $\sqrt{3} \times \sqrt{3}$ surface terrace and the step edge as in Area A1 and (c) the antiphase boundary in Area A2.

Table A2 Adsorption configurations of thiolated cysteine Conformers A, B, and C on T1 sites of the Si(111)- $\sqrt{3}\times\sqrt{3}$ -Ag model surface before (left) and after full optimization of all the atomic positions (right). The adsorption energies are in unit of eV while the separations $r(X-Y)$ are in units of Å. To better illustrate the adsorption structure, only part of the slab for the model surface is shown for each configuration.

A-T1 → -1.449813 $r(\text{S}-\text{Ag})=2.66$ $r(\text{N}-\text{Ag})=3.59$	A-D1 -2.372746 $r(\text{S}-\text{Ag1})=2.53$ $r(\text{S}-\text{Ag2})=2.57$ $r(\text{N}-\text{Ag})=2.37$	B-T1 → -1.606602 $r(\text{S}-\text{Ag})=2.64$ $r(\text{N}-\text{Ag})=3.75$ $r(\text{HO}-\text{Ag})=3.66$ $r(\text{O}-\text{Ag})=4.19$	B-T1 -2.111299 $r(\text{S}-\text{Ag1})=2.56$ $r(\text{S}-\text{Ag2})=2.62$ $r(\text{N}-\text{Ag})=3.65$ $r(\text{H}-\text{Ag1})=3.08$ $r(\text{O}-\text{Ag1})=3.27$	C-T1 → -1.567911 $r(\text{O}-\text{Ag1})=2.64$ $r(\text{HO}-\text{Ag1})=3.53$ $r(\text{O}-\text{Si})=3.51$	C-T1 -1.777420 $r(\text{S}-\text{Ag1})=2.63$ $r(\text{S}-\text{Ag2})=2.64$ $r(\text{S}-\text{Ag3})=2.63$ $r(\text{O}-\text{Ag})=3.42$

Table A3 Adsorption configurations of thiolated cysteine Conformers A, B, and C on T2 sites of the Si(111)- $\sqrt{3}\times\sqrt{3}$ -Ag model surface before (left) and after full optimization of all the atomic positions (right). The adsorption energies are in unit of eV while the separations $r(X-Y)$ are in units of Å. To better illustrate the adsorption structure, only part of the slab for the model surface is shown for each configuration.

A-T2 \rightarrow -0.904954 $r(\text{S-Si})=3.02$ $r(\text{N-Ag})=3.72$	A-M1 -1.743216 $r(\text{S-Ag1})=2.52$ $r(\text{N-Ag})=2.39$	B-T2 \rightarrow -1.047056 $r(\text{S-Si})=3.04$ $r(\text{S-Ag})=3.02$ $r(\text{N-Ag})=4.01$ $r(\text{HO-Ag1})=3.4$ $r(\text{O-Ag2})=3.98$	B-M1 -1.784698 $r(\text{S-Ag})=2.48$ $r(\text{N-Ag})=5.43$ $r(\text{HO-Ag1})=3.58$ $r(\text{O-Ag2})=2.53$	C-T2 \rightarrow -1.116267 $r(\text{S-Ag})=3.10$ $r(\text{O-Ag1})=3.06$ $r(\text{HO-Ag1})=3.08$	C-D1 -1.663781 $r(\text{S-Ag1})=2.60$ $r(\text{S-Ag2})=2.69$ $r(\text{O-Ag})=3.24$

Table A4 Adsorption configurations of thiolated cysteine Conformers A, B, and C on D1 sites of the Si(111)- $\sqrt{3}\times\sqrt{3}$ -Ag model surface before (left) and after full optimization of all the atomic positions (right). The adsorption energies are in unit of eV while the separations $r(X-Y)$ are in units of Å. To better illustrate the adsorption structure, only part of the slab for the model surface is shown for each configuration.

A-D1 → -1.224351 $r(\text{S}-\text{Ag})=2.59$ $r(\text{N}-\text{Ag})=3.88$	A-D1 -2.355443 $r(\text{S}-\text{Ag1})=2.50$ $r(\text{S}-\text{Ag2})=2.61$ $r(\text{N}-\text{Ag})=2.36$	B-D1 → -1.363309 $r(\text{S}-\text{Ag})=2.64$ $r(\text{N}-\text{Ag})=3.96$ $r(\text{N}-\text{Ag})=4.25$	B-D1 -2.241693 $r(\text{S}-\text{Ag1})=2.61$ $r(\text{S}-\text{Ag2})=2.51$ $r(\text{HO}-\text{Ag1})=3.33$ $r(\text{O}-\text{Ag2})=2.55$	C-D1 → -1.386678 $r(\text{O}-\text{Ag1})=2.60$ $r(\text{O}-\text{Ag1})=3.04$	C-D1 -1.809630 $r(\text{S}-\text{Ag1})=2.63$ $r(\text{S}-\text{Ag2})=3.62$ $r(\text{O}-\text{Ag})=2.95$

Table A5 Adsorption configurations of thiolated cysteine Conformers A, B, and C on D2 sites of the Si(111)- $\sqrt{3}\times\sqrt{3}$ -Ag model surface before (left) and after full optimization of all the atomic positions (right). The adsorption energies are in unit of eV while the separations $r(X-Y)$ are in units of Å. To better illustrate the adsorption structure, only part of the slab for the model surface is shown for each configuration.

A-D2 → -1.037942 $r(\text{S-Si})=2.92$ $r(\text{N-Ag})=3.85$	A-M1 -1.831686 $r(\text{S-Ag})=2.50$ $r(\text{S-Ag})=3.02$ $r(\text{N-Ag})=2.38$	B-D2 → -1.129090 $r(\text{S-Si})=2.90$ $r(\text{N-Ag})=3.88$ $r(\text{HO-Ag1})=3.48$ $r(\text{O-Ag2})=3.90$	B-M1 -1.637997 $r(\text{S-Si})=3.03$ $r(\text{S-Ag})=2.55$ $r(\text{HO-Ag1})=3.24$ $r(\text{O-Ag2})=2.56$	C-D2 → -1.126931 $r(\text{S-Ag})=2.90$ $r(\text{S-Si1})=3.05$ $r(\text{S-Si2})=2.96$ $r(\text{O-Ag})=3.42$	C-M1 -1.369182 $r(\text{S-Ag})=2.58$ $r(\text{S-Si1})=3.25$ $r(\text{S-Si2})=3.14$ $r(\text{O-Ag})=3.37$

Table A6 Adsorption configurations of thiolated cysteine Conformers A, B, and C on D3 sites of the Si(111)- $\sqrt{3}\times\sqrt{3}$ -Ag model surface before (left) and after full optimization of all the atomic positions (right). The adsorption energies are in unit of eV while the separations $r(X-Y)$ are in units of Å. To better illustrate the adsorption structure, only part of the slab for the model surface is shown for each configuration.

A-D3 → -1.058288 $r(\text{S-Si})=2.88$ $r(\text{S-Ag})=3.02$ $r(\text{N-Ag})=4.12$	A-D1 -2.127409 $r(\text{S-Ag1})=2.57$ $r(\text{S-Ag2})=2.57$ $r(\text{N-Ag})=2.47$	B-D3 → -1.205196 $r(\text{S-Si})=2.73$ $r(\text{S-Ag})=2.73$ $r(\text{HO-Ag1})=3.42$ $r(\text{O-Ag1})=4.10$	B-D1 -2.133742 $r(\text{S-Ag1})=2.59$ $r(\text{S-Ag2})=2.51$ $r(\text{HO-Ag1})=2.96$ $r(\text{O-Ag1})=3.06$ $r(\text{N-Ag})=3.67$	C-D3 → -1.172476 $r(\text{S-Ag})=2.69$ $r(\text{S-Si})=2.97$ $r(\text{HO-Ag1})=3.24$	C-D1 -1.721650 $r(\text{S-Ag1})=2.64$ $r(\text{S-Ag2})=2.51$ $r(\text{S-Si})=3.10$ $r(\text{O-Ag})=3.45$

Table A7 Molecular configurations of thiolated cysteine Conformers A, B, and C on M1 sites of the Si(111)- $\sqrt{3}\times\sqrt{3}$ -Ag model surface before (left) and after full optimization of all the atomic positions (right). The adsorption energies are in unit of eV while the separations $r(X-Y)$ are in units of Å. To better illustrate the adsorption structure, only part of the slab for the model surface is shown for each configuration.

A-M1 → -0.719171 $r(\text{S}-\text{Ag})=2.52$ $r(\text{N}-\text{Ag})=4.5$	A-D1 -2.315456 $r(\text{S}-\text{Ag1})=2.50$ $r(\text{S}-\text{Ag2})=2.60$ $r(\text{N}-\text{Ag})=2.37$	B-M1 → -0.826886 $r(\text{S}-\text{Ag})=2.57$ $r(\text{N}-\text{Ag})=4.57$ $r(\text{HO}-\text{Ag})=4.32$ $r(\text{S}-\text{Si})=4.66$	B-D1 -2.095522 $r(\text{S}-\text{Ag1})=2.53$ $r(\text{S}-\text{Ag2})=2.58$ $r(\text{N}-\text{Ag})=3.20$ $r(\text{HO}-\text{Ag1})=3.31$ $r(\text{O}-\text{Ag2})=3.10$	C-M1 → -0.914951 $r(\text{S}-\text{Ag})=2.54$ $r(\text{HO}-\text{Ag})=3.70$	C-D1 -1.968214 $r(\text{S}-\text{Ag1})=2.57$ $r(\text{S}-\text{Ag2})=2.56$ $r(\text{HO}-\text{Ag1})=3.04$

Table A8 Molecular configurations of thiolated cysteine Conformers A, B, and C on M2 sites of the Si(111)- $\sqrt{3}\times\sqrt{3}$ -Ag model surface before (left) and after full optimization of all the atomic positions (right). The adsorption energies are in unit of eV while the separations $r(X-Y)$ are in units of Å. To better illustrate the adsorption structure, only part of the slab for the model surface is shown for each configuration.

A-M2 → -1.055622 $r(\text{S-Si})=2.72$ $r(\text{N-Ag})=4.12$	A-D1 -2.364335 $r(\text{S-Ag1})=2.58$ $r(\text{S-Ag2})=2.52$ $r(\text{S-Si})=3.37$ $r(\text{N-Ag})=2.41$	B-M2 → -1.146309 $r(\text{S-Si})=2.77$ $r(\text{N-Ag})=4.48$ $r(\text{HO-Ag1})=3.67$ $r(\text{O-Ag2})=4.22$	B-D1 -1.858376 $r(\text{S-Si})=2.52$ $r(\text{S-Ag1})=2.82$ $r(\text{S-Ag2})=2.47$ $r(\text{N-Si})=3.94$ $r(\text{HO-Ag1})=3.18$ $r(\text{O-Ag2})=3.17$	C-M2 → -1.147295 $r(\text{S-Si})=2.92$ $r(\text{O-Ag})=3.30$	C-D1 -1.769648 $r(\text{S-Ag1})=2.75$ $r(\text{S-Ag2})=2.50$ $r(\text{O-Ag})=3.11$

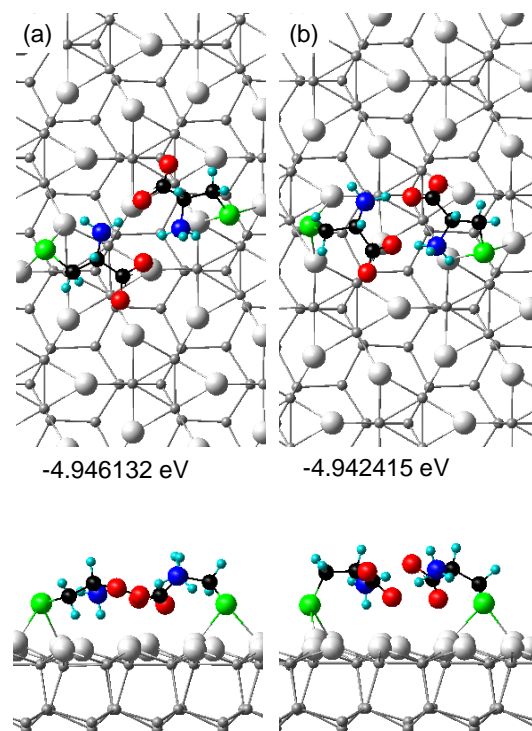


Figure A5 Optimized adsorption configurations of hydrogen-bonded cysteine dimers consisting of (a) two thiolated zwitterionic Conformer A_{ZI}, and (b) two thiolated zwitterionic Conformer B_{ZI}, each adsorbed on the Ag bridge sites of the Si(111)- $\sqrt{3}\times\sqrt{3}$ -Ag model surface. The total adsorption energy of the respective dimer is also indicated. To better illustrate the adsorption structure, only part of the slab for the model surface is shown for each configuration.

Appendix B

Methionine on Si(111)- $\sqrt{3}\times\sqrt{3}$ -Ag

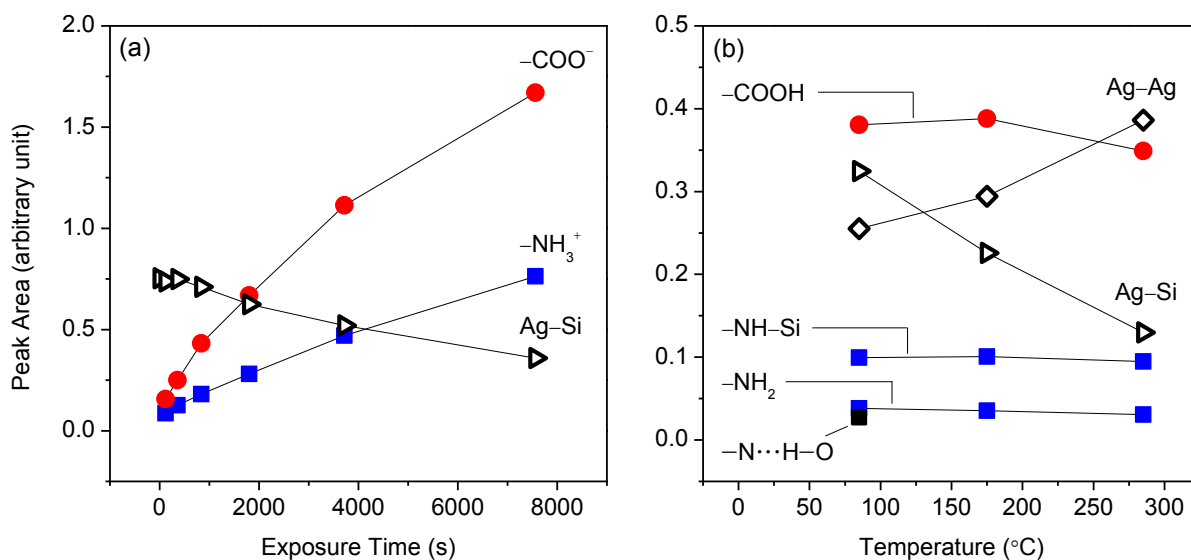


Figure B1 Peak areas of O 1s, N 1s, C 1s, and S 2s features (a) as functions of methionine exposure time on Si(111)- $\sqrt{3}\times\sqrt{3}$ -Ag and (b) annealing of the as-grown 7560-s methionine film at 85, 175, and 285 $^{\circ}\text{C}$.

Table B1 Binding energies (in eV) of fitted peaks for various XPS core-level features and their corresponding assignments for different exposures of L-methionine on Si(111)- $\sqrt{3}\times\sqrt{3}$ -Ag and upon annealing to different temperatures. The notation M represents either Si or Ag or both.

Core level	Assignment	120 s	360 s	840 s	1800 s	3720 s	7560 s	85 °C	175 °C	285 °C
O 1s	-COO ⁻	531.7	531.7	532.7	531.9	532	532	--	--	-
	-COOH	532.6	532.7	532.7	532.6	--	--	532.4	532.5	532.5
N 1s	NH-Si	398.8	398.8	398.8	398.7	398.7	--	398.8	398.7	398.7
	-NH ₂	--	--	--	--	--	--	399.9	399.9	400.1
	O-H...N	--	--	--	--	--	--	401.0	--	--
	-NH ₃ ⁺	401.8	401.8	401.9	402.0	402.0	402.0	--	--	--
C 1s	M-CH _x	--	--	--	--	--	--	--	--	284.2
	-CH ₂ -S-M	--	--	--	--	--	--	--	--	285.4
	-CH ₂ -	285.3	285.5	285.6	285.6	285.6	285.6	285.5	285.4	285.4
	-CH ₂ -S-CH ₃	285.9	285.9	285.9	286.0	286.0	285.9	285.9	285.9	--
	-CH-NH-Si	--	--	--	--	--	--	286.6	286.5	286.3
	-CH-NH ₃ ⁺	286.9	286.9	286.9	286.8	286.9	286.8	--	--	--
	-COO ⁻	288.6	288.7	288.7	288.9	288.9	288.9	--	--	--
	-COOH	--	--	--	--	--	--	289.1	289.1	289.1
S 2s	-S-CH ₃	228.4	228.4	228.4	228.4	228.4	228.4	228.4	228.4	--
	-S-M	--	--	--	--	--	--	--	--	227.2

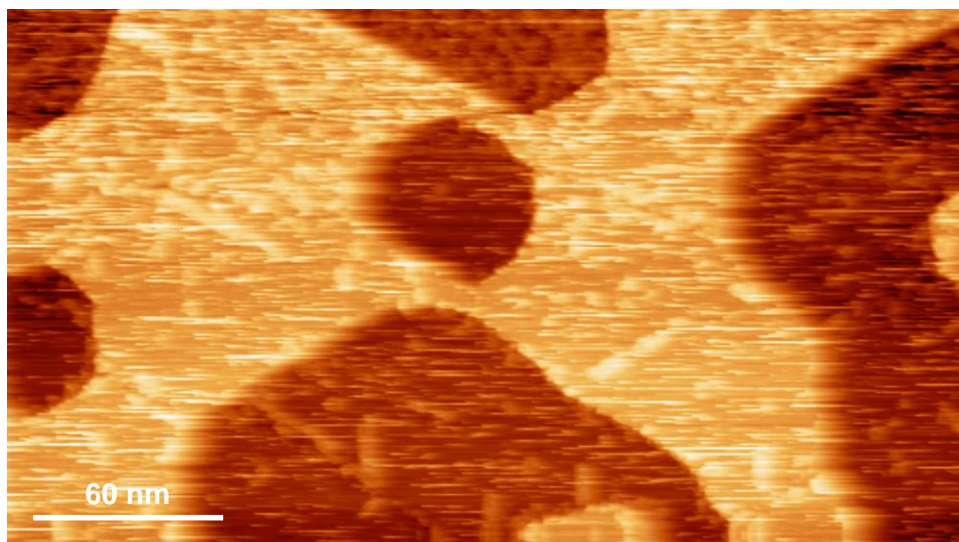


Figure B2 Empty-state STM image of L-methionine with a 20-s exposure on Si(111)- $\sqrt{3}\times\sqrt{3}$ -Ag at room temperature. Despite the somewhat diffuse features caused by the high mobility of the glycine molecules on the surface at room temperature, self-assembly of distinct molecular wires is clearly observed. The image is obtained with a sample bias of +2.0 V and a tunneling current of 0.2 nA at room temperature.

Table B2 Binding energies (in eV) of fitted peaks for various XPS core-level features and their corresponding assignments for glycine on Si(111)- $\sqrt{3}\times\sqrt{3}$ -Ag at different exposures and post-annealing temperatures.

Core level	Assignment	120 s	240 s	720 s	3600 s	85 °C	175 °C	285 °C
O 1s	-COO ⁻	532.1	532.1	532.1	532.1	--	--	--
	-COOH	--	--	--	--	532.6	532.6	532.6
N 1s	NH-Si	--	--	--	--	398.9	398.8	398.8
	-NH ₂	--	--	--	--	400.0	400.0	399.9
	O-H...N	--	--	--	--	401.2	401.3	--
	-NH ₃ ⁺	402.1	402.1	402.1	402.1	402.0	--	--
C 1s	-CH-NH-Si	--	--	--	--	286.5	286.3	286.1
	-CH-NH ₃ ⁺	286.7	286.7	286.7	287.0	--	--	--
	-COO ⁻	289.0	288.8	288.9	289.1	--	--	--
	-COOH	--	--	--	--	289.2	289.1	288.9
	-CH _x	--	--	--	--	--	284.3	284.3

Table B3 Top view of the optimized equilibrium adsorption configurations of methionine monomer at different (initial) adsorption sites M1, D1 and T1, and with different (final) orientations with respect to the surface unit cell. The adsorption energies are in unit of eV while the bond lengths are in unit of Å.

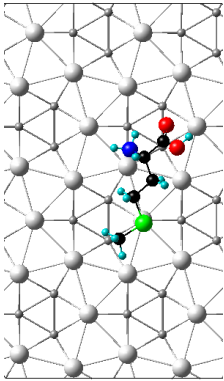
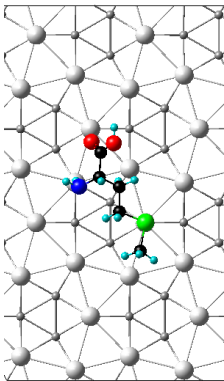
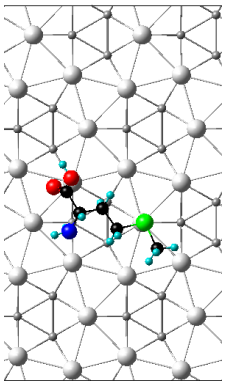
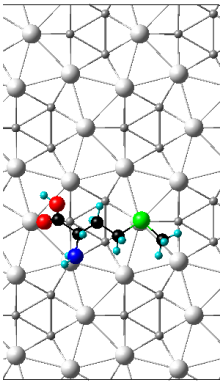
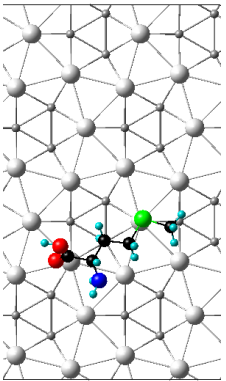
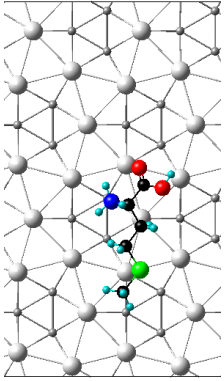
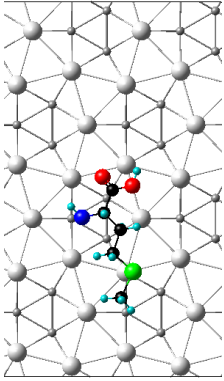
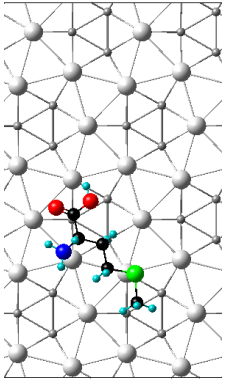
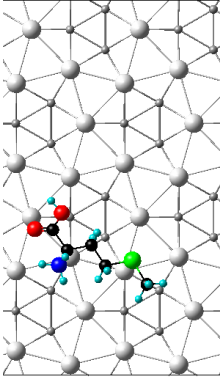
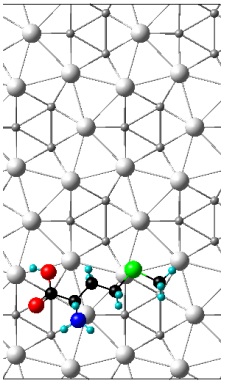
<p>M1-R115 -1.346289 S-Ag = 2.65 N-Ag=2.60</p> 	<p>M1-R70 -1.12584 S-Ag = 2.67 N-Ag=3.55</p> 	<p>M1-R35 -1.275102 S-Ag = 2.63 O-Ag=2.97 N-Ag=3.84 HO-Ag=4.68</p> 	<p>M1-R15 -1.183559 S-Ag = 2.63 O-Ag=3.4 N-Ag=3.50</p> 	<p>M1-R170 -1.298322 S-Ag = 2.62 O-Ag=2.80 N-Ag=3.39</p> 
<p>M1-R105 -1.054912 S-Ag = 2.70 N-Ag=3.16 O-Si=2.90</p> 	<p>M1-R90 -1.239185 S-Ag = 2.63 N-Ag=2.48 O-Si=3.52</p> 	<p>M1-R58 -1.448095 S-Ag = 2.65 N-Ag=2.54 O-Si=2.99 HO-Ag=3.70</p> 	<p>M1-R34 -1.401101 S-Ag = 2.66 N-Ag=2.47 O-Si=2.91</p> 	<p>M1-R0 -1.395298 S-Ag = 2.70 N-Ag=2.48 O-Si=3.52 HO-Ag=3.70</p> 

Table B3 (Continued).

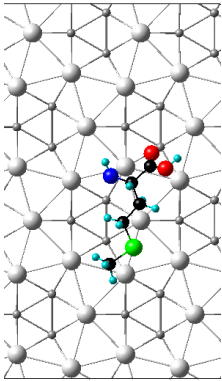
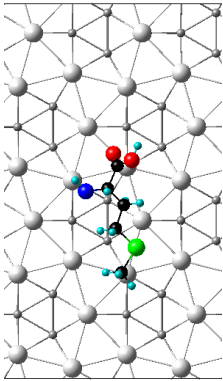
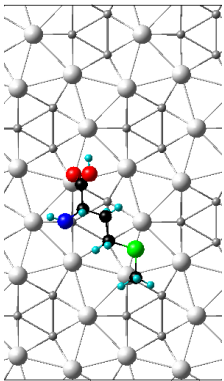
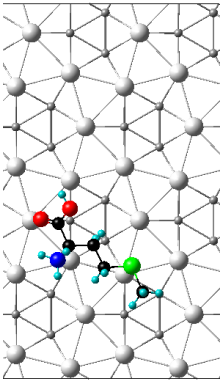
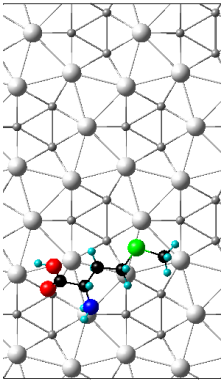
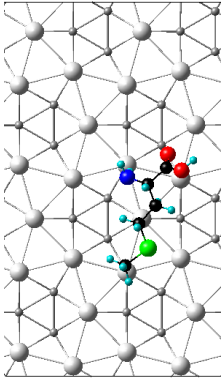
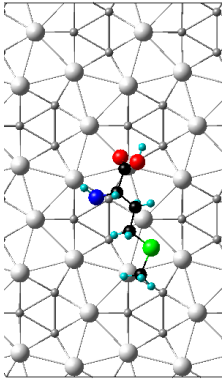
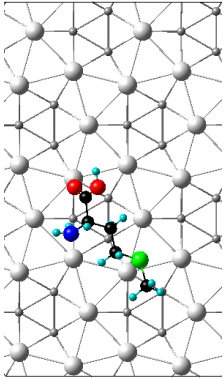
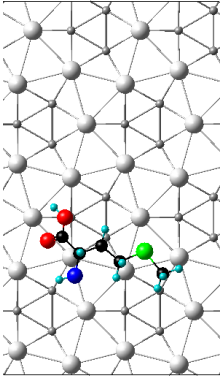
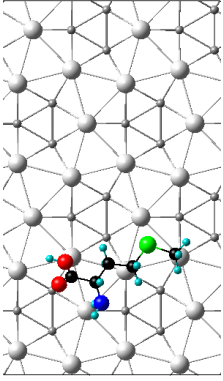
<p>D1-R115 -0.884286 S-Ag1 = 3.38 S-Ag2 = 3.36 N-Ag=2.92 O-Si=3.54</p> 	<p>D1-R92 -0.923402 S-Ag1 = 3.39 S-Ag2 = 3.35 N-Ag=3.63 O-Si=3.07</p> 	<p>D1-R63 -1.014794 S-Ag1 = 3.26 S-Ag2 = 3.26 N-Ag=3.67 O-Si=2.69</p> 	<p>D1-R45 -1.43533 S-Ag1 = 2.63 S-Ag2 = 3.79 N-Ag=2.47 O-Si=2.82</p> 	<p>D1-R170 -0.870855 S-Ag1 = 3.30 S-Ag2 = 3.33 N-Ag=3.62 O-Si=3.97</p> 
<p>T1-R115 -0.858871 S-Ag1 = 3.36 S-Ag2 = 3.43 S-Ag3 = 3.51 N-Ag=3.62 O-Si=3.90</p> 	<p>T1-R85 -0.933543 S-Ag1 = 3.37 S-Ag2 = 3.49 S-Ag3 = 3.54 N-Ag=3.77 O-Ag=2.91</p> 	<p>T1-R60 -1.179683 S-Ag1 = 2.65 S-Ag2 = 3.53 S-Ag3 = 3.51 N-Ag=3.33 O-Ag=2.86</p> 	<p>T1-R23 -1.038002 S-Ag1 = 3.23 S-Ag2 = 3.45 S-Ag3 = 3.49 N-Ag=3.56 O-Ag=3.04</p> 	<p>T1-R170 -0.831463 S-Ag1 = 3.34 S-Ag2 = 3.54 S-Ag3 = 3.54 N-Ag=3.72 O-Si=3.98</p> 

Table B4 Top view of the optimized equilibrium adsorption configurations of methionine antiparallel dimer at different adsorption sites and with different orientations with respect to the surface unit cell. The adsorption energies are in unit of eV while the bond lengths are in unit of Å.

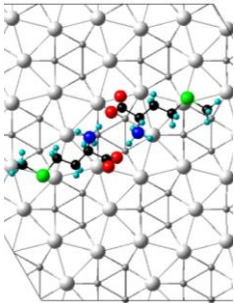
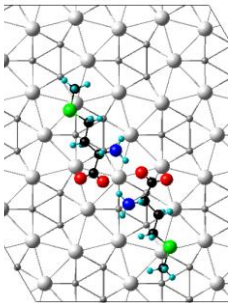
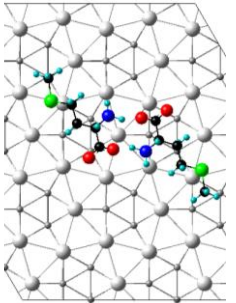
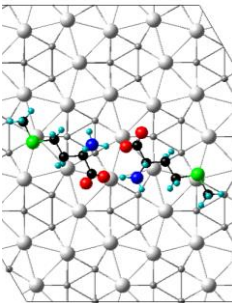
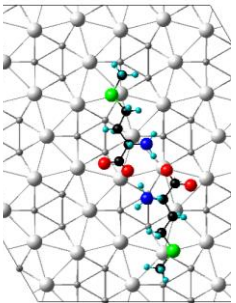
M1-R2-R6 -2.545447 S1-Ag = 2.67 N1-Ag=3.13 O1-Ag=3.15 S2-Ag= 2.93 N2-Ag=3.35 O2-Ag=3.55 S1-S2=12.67 (NH...O) _{ZI} = 1.43-1.48	M1-R84-R88 -2.560705 S1-Ag = 2.66 N1-Ag=3.48 O1-Ag=3.05 S2-Ag= 2.68 N2-Ag=3.29 O2-Ag=2.71 S1-S2=13.08 (NH...O) _{ZI} = 1.57-1.60	M1-R56-R60 -2.476391 S1-Ag = 2.69 N1-Ag=3.18 O1-Ag=2.87 S2-Ag= 2.72 N2-Ag=3.39 O2-Ag=2.76 S1-S2=12.76 (NH...O) _{ZI} = 1.55-1.56	M1-R43-R40 -2.659353 S1-Ag = 2.69 N1-Ag=3.34 O1-Ag=2.45 S2-Ag= 2.66 N2-Si=3.48 O2-Ag=2.97 S1-S2=12.94 (NH...O) _{ZI} = 1.47-1.57	M1-R98-R105 -2.401892 S1-Ag = 2.71 N1-Ag=3.50 O1-Ag=2.74 S2-Ag= 2.69 N2-Ag=3.26 O2-Ag=2.48 S1-S2=12.96 (NH...O) _{ZI} = 1.54-1.59
				

Table B5 Top view of the optimized equilibrium adsorption configurations of methionine parallel dimer at different adsorption sites and with different orientations with respect to the surface unit cell. The adsorption energies are in unit of eV while the bond lengths are in unit of Å.

M1-R105-R105 -2.755241 (S-Ag)1 = 2.66 (N-Si)1=3.66 (O-Ag)1=3.15 (S-Ag)2= 2.71 (N-Ag)2=3.41 (O1-Ag)2=2.89 S1-S2=6.60 NH...O=1.75	M1-R74-R74 -3.055981 (S-Ag)1 = 2.64 (N-Ag)1=3.51 (O-Ag)1=3.44 (S-Ag)2= 2.70 (N-Ag)2=3.18 (O1-Ag)2=2.46 (O2-Ag)2=2.57 S1-S2=6.60 (NH...O) _{ZI} =1.75	M1-R40-R33 -2.546756 (S-Ag)1 = 2.67 (N-Ag)1=3.43 (O-Ag)1=3.32 (S-Ag)2= 2.68 (N-Ag)2=3.37 (O1-Ag)2=3.00 (O2-Ag)2=3.17 S1-S2=6.08 (NH...O) _{ZI} =1.77	M1-R170-R176 -2.685412 (S-Ag)1 = 2.66 (N-Ag)1=3.52 (O-Ag)1=3.39 (S-Ag)2= 2.67 (N-Ag)2=3.48 (O1-Ag)2=3.64 (O2-Ag)2=3.06 S1-S2=6.16 NH...O=2.45

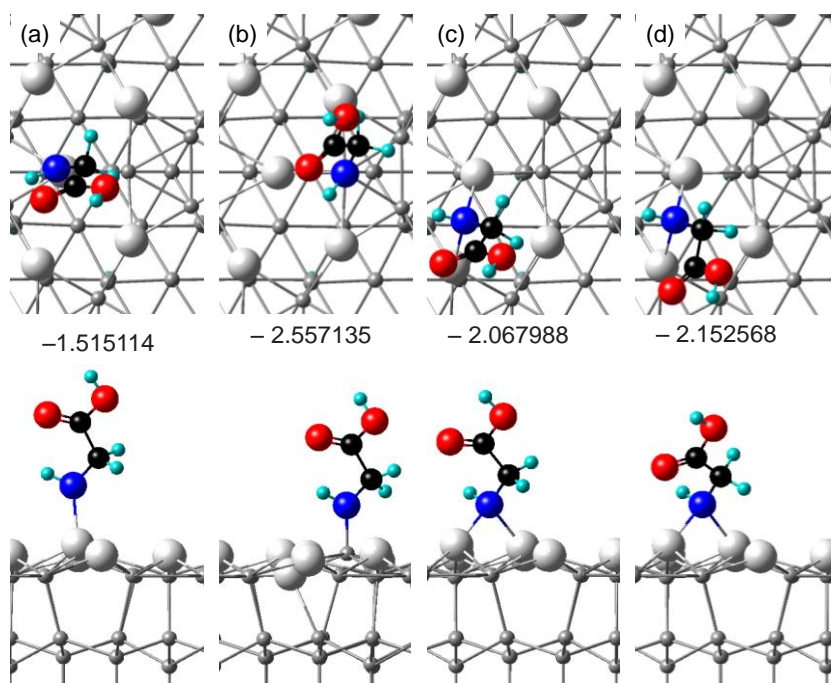


Figure B3 Top and side views of the optimized equilibrium adsorption configurations of glycinate at (a) Ag monomer A1, (b) Si monomer A2, and (c) Ag dimer D1 adsorption sites. The adsorption energies are in unit of eV. A2 appears to be the most favorable adsorption site for glycine bonding through the dissociated amino group in an upright standing configuration. Minor displacements are also observed for the Ag and Si atoms upon chemisorption of glycine.

Appendix C

One-dimensional Surface Defects on Si(111)- $\sqrt{3}\times\sqrt{3}$ -Ag

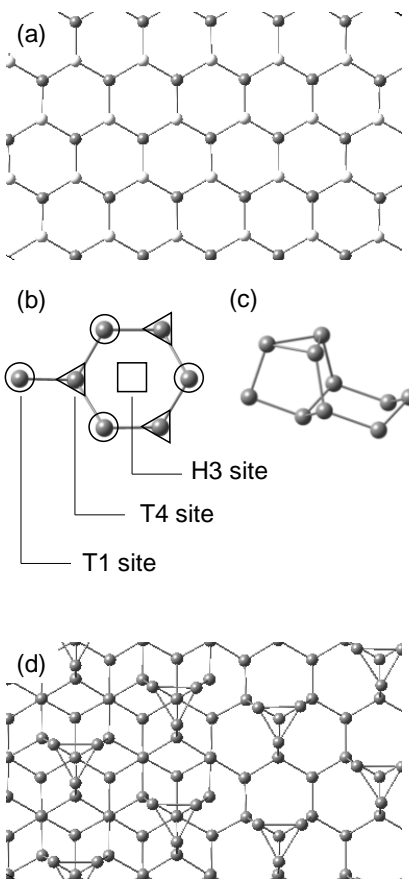


Figure C1 (a) Top view of a Si(111) bilayer. The lighter and darker spheres denote the Si atoms in the top and the bottom layers, respectively. (b) A schematic representation of the major adsorption sites on the Si(111) surface. The square, triangles, and circles denote the H3, T4, and T1 adsorption sites, respectively. (c) A schematic representation of a Si trimer relocated on the T4 adsorption site. (d) A step edge model in which the Si trimers are located on the T4 sites on the upper-step and lower-step terraces of the Si(111) surface.

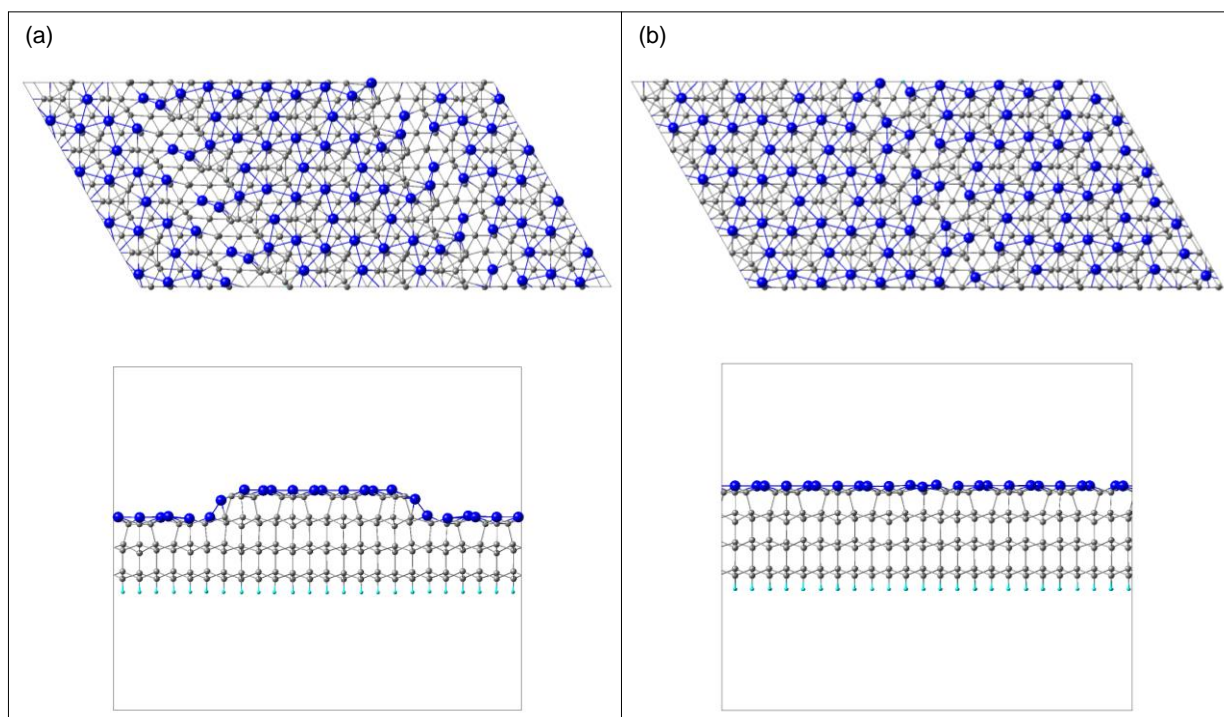


Figure C2 Top views and cross sectional (along the wide side of the slab) views of (a) the step edge slab containing three Si bilayers under the Ag-Si trimers of the upper-step terrace and two Si bilayers under those of the lower-step terraces (576 Si atoms, 96 Ag atoms and 96 H atoms); and (b) the antiphase boundary slab containing three Si bilayers under the Ag-Si trimers. The island model is used to create the step edge slab (672 Si atoms, 96 Ag atoms and 96 H atoms).

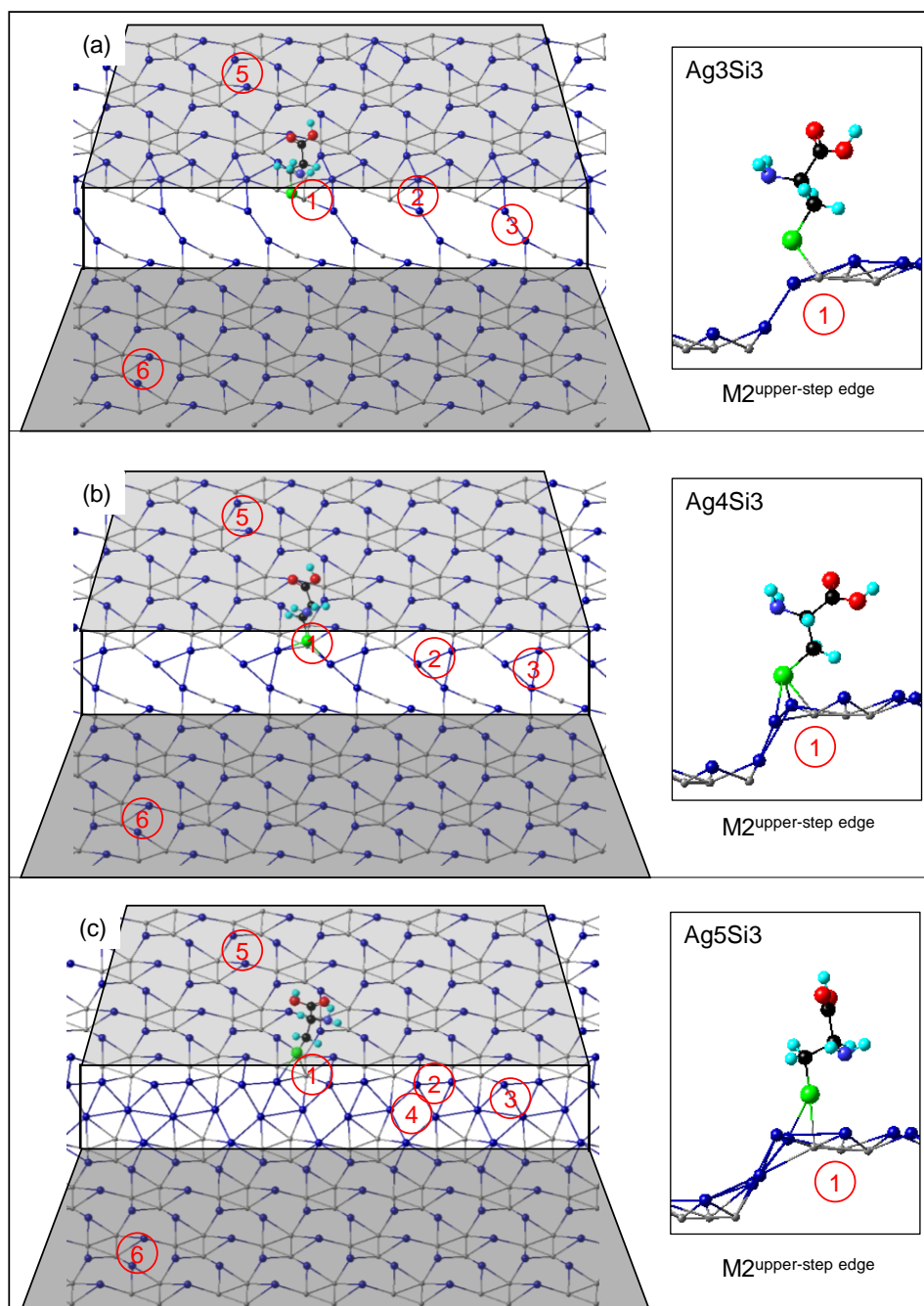


Figure C3 The optimized adsorption geometries of (a) Ag₃Si₃, (b) Ag₄Si₃, and (c) Ag₅Si₃ step edge models showing most possible adsorption sites around the step edge region. Only the topmost layer (Ag–Si trimers) are shown. Only the Ag bridge sites and Si atop sites are considered. The right panels show the adsorption geometry of a single thiolated cysteine adsorbed at the upper-step edge M₂ site on different step edge models. The corresponding adsorption energies are shown in Table C1.

Table C1 Calculated adsorption energies of thiolated cysteine adsorbed at different adsorption sites, through its sulfur atom, for three step edge models with Ag₃Si₃, Ag₄Si₃, and Ag₅Si₃ unit cells. For the structure optimization calculations, the atomic positions of cysteine were relaxed while those of slab were fixed. All the energies are in unit eV.

	Adsorption Site	Ag ₃ Si ₃	Ag ₄ Si ₃	Ag ₅ Si ₃
1	M2 ^{upper-step edge}	-2.513727	-2.175633	-2.222908
2	D1 ^{upper-step edge}	-1.727092	-2.319198	-2.650350
3	D1 ^{slope at site A}	-2.350708	-3.057135	-3.086105
4	D1 ^{slope at site B}	--	--	-3.283988
5	D1 ^{upper-step terrace}	-1.913473	-1.964019	-2.692114
6	D1 ^{lower-step terrace}	-1.927849	-1.764019	-2.753043

The most stable adsorption sites were calculated by placing a single thiolated cysteine molecule at Ag bridge sites (D1) of the upper-step edge, lower-step edge, the step slope, upper-step terrace, and lower-step terrace sites on three different step edge models. The Si atop sites were also calculated for the upper-step edge and lower-step edge sites. There are other possible adsorption sites such as Ag atop and trimer sites of both Ag and Si, however, only D1 and M2 were considered in our calculations as they were found to be the most stable adsorption sites on terraces, according to our calculations in Chapter 3. In all three models, the adsorption does not take place at lower-step edge D1 and M2 sites. Instead, they move to the upper-step edge (in Ag₃Si₃ and Ag₄Si₃ models) and slope D1 sites (in Ag₅Si₃). In the Ag₃Si₃ model, the M2 site at the upper-step edge was found to be the most favorable adsorption sites followed by the Slope D1, upper-step edge D1, and Terrace D1 sites. In the Ag₄Si₃ model, the slope D1 site was found to be the most stable adsorption sites followed by the upper-step D1, the upper-step M2, and the terrace D1 sites. A similar trend was observed for the Ag₅Si₃ model except that the upper-step M2 site is the least stable adsorption site. According to our STM results in Chapter 3, the upper-step edges are not the most preferred adsorption sites on the Si(111)- $\sqrt{3}\times\sqrt{3}$ -Ag surface, therefore the Ag₃Si₃ model cannot describe our experimental results.

Table C2 Calculated adsorption energies of thiolated cysteine adsorbed at different adsorption sites, through its sulfur atom, for the antiphase boundary model. For structure optimization calculations, the atomic positions of cysteine were relaxed while those of slab were fixed. All energies are in unit eV.

Adsorption Site	Ag ₃ Si ₃
M1 ^{chain}	-2.083216
M2 ^{chain}	-1.419904
M2 ^{near-chain}	-1.425848
D1 ^{chain}	-1.544796
D1 ^{near-chain}	-1.586529
T1 ^{chain}	-1.432091
T1 ^{terrace}	-1.897473
T3 ^{chain}	-1.571587